Graduate School Form 9
(Revised 6/03)

PURDUE UNIVERSITY
GRADUATE SCHOOL
Thesis Acceptance

This is to certify that the thesis prepared

By Dionysios C. Aliprantis

Entitled Advances in Electric Machine Modeling and Evolutionary Parameter Identification

Complies with University regulations and meets the standards of the Graduate School for originality and quality

For the degree of Doctor of Philosophy

Signed by the final examining committee:

Scott Sudhoff — Chair
Scott Sudhoff

Oleg Wasynczuk
Oleg Wasynczuk

Chee-Mun Ong
Chee-Mun Ong

Charles Krousgrill
Charles Krousgrill

Approved by: Head of the Graduate Program — Nov 25, 2003 Date

This thesis ☐ is ☒ is not to be regarded as confidential.

Major Professor

Format Approved by:

Chair, Final Examining Committee or Department Thesis Format Advisor

ADVANCES IN ELECTRIC MACHINE MODELING

AND

EVOLUTIONARY PARAMETER IDENTIFICATION

A Thesis

Submitted to the Faculty

of

Purdue University

by

Dionysios C. Aliprantis

In Partial Fulfillment of the

Requirements for the Degree

of

Doctor of Philosophy

December 2003

Στους γονείς μου, Χριστόφορο και Γεωργία

ACKNOWLEDGMENTS

I would like to express my gratitude towards Prof. Scott D. Sudhoff, the major advisor of my Ph.D. studies, who gave me the opportunity to explore my ideas, and guided my research with his innovative and critical thinking. His immense contribution to this work is highly appreciated.

It has been an honor to have Profs. Charles M. Krousgrill, Chee-Mun Ong, and Oleg Wasynczuk serve as members of my graduate advisory committee. The cooperation with Prof. Krousgrill led to my deeper understanding of mechanical vibrations and their effect on induction machines behavior. Prof. Ong's textbook on electric machinery has accompanied me since my first simulation attempts and was widely referenced during the writing of this thesis. Prof. Wasynczuk's earlier work on machine modeling laid the foundations on which this research effort was based. Special thanks to Prof. Paul C. Krause, to whom I am indebted for stimulating my interest in electric machines; he has always inspired me in many different ways.

Many thanks to my friend Brian Kuhn for his daily support during my graduate career. The laboratory setup and acquisition of experimental data would have been impossible without his aid. I thank Prof. Patrick Chapman, and Dr. Steve Glover for their technical expertise and invaluable friendship. I also thank Jaesoo Byoun, Kyle Krueger, Chunki Kwon, Benjamin Loop, and all my fellow graduate students and friends.

I acknowledge the support of my parents, Christopher and Georgia Aliprantis, my sister Faye, and my family here in West Lafayette, Prof. Charalambos D. Aliprantis, Bernadette, Claire and Dionissi. Last, but not least, I thank Sonita Chada, who transformed this difficult journey into an unforgettable experience.

The part of this work concerning the induction machine modeling was supported by ONR (Office of Naval Research), "High Frequency Vibration Analysis of Electric Machinery," under Grant N00014-98-1-01716. The synchronous machine modeling work was funded from NAVSEA (Naval Sea Systems Command) contract N00024-02-NR-60427 "Naval Combat Survivability," as well as from ATI (Advanced Technology Institute)/ONR project "National Naval Responsibility for Naval Engineering: Education and Research for the Electric Naval Engineer," Award 2003-351. Research on evolutionary optimization techniques was funded from ONR contract N00014-02-1-0990 "Polytopic Model Based Stability Analysis and Genetic Design of Electric Warship Power Systems."

TABLE OF CONTENTS

Page

Page

LIST OF TABLES

LIST OF FIGURES

Figure Page

Figure Page

Figure Page

ABSTRACT

Aliprantis, Dionysios C. Ph.D., Purdue University, December, 2003. Advances in Electric Machine Modeling and Evolutionary Parameter Identification. Major Professor: Scott D. Sudhoff.

The design of robust power systems entails extensive use of computer simulations, increasing the demand for high-fidelity electric machine models. In the present study, new dynamic models for induction machines, synchronous machines, and brushless excitation systems are set forth. The models are derived within the orthogonal *qd*-axes theoretical framework. Their formulation is geared towards reflecting the machines' actual operating characteristics, in contrast to conventional models that utilize pre-determined equivalent circuit structures of questionable physical meaning. The proposed induction machine model is developed for power-electronics based applications, where the high-frequency interaction between converter and machine is of particular interest. It represents magnetic saturation in the main and leakage flux paths, and uses an arbitrary linear network to capture the frequency dependence of the rotor circuits. The proposed synchronous machine model is applicable to power system stability studies. It similarly addresses magnetic saturation as well as equivalent circuit issues. The proposed brushless excitation model features an average-value representation of the exciter-machine/rotating-rectifier configuration, and the incorporation of magnetic hysteresis. Novel experimental procedures are devised for characterizing the proposed models which utilize evolutionary optimization techniques as a means for parameter estimation. The models are validated by comparison to experimental results.

1. INTRODUCTION

When designing electric power systems of high complexity and importance, extensive use of computer simulations is a *sine qua non*. Systems whose operation is critical, such as large-scale commercial grids, aircraft power systems, or military ship power and propulsion systems must be studied for a plethora of operating points and contingencies; efficiency, stability and continuity of service are major concerns [1, 2]. These considerations increase the demand for accurate dynamic models of power system components.

The focus of the present study is on rotating electric machinery modeling. In particular, novel models for induction machines, synchronous machines, and brushless excitation systems are set forth. This research was motivated by well-documented deficiencies of existing machine representations—dating from as early as the beginning of the twentieth century [3, 4], which become even more evident from the perspective of modern-day power-electronics based applications.

The intent of this effort was to address conventional models' limitations without sacrificing computational efficiency, amenability to large-scale simulations, and portability. To this end, the proposed models were derived within the orthogonal *qd*-axes theoretical framework [5]. This theory is adequate for predicting the dynamic performance of electric machines by employing relatively low-order models and is conveniently used in the majority of power system studies.

Previous *qd*-axes machine representations are usually based on *ad hoc* equivalent circuit structures, whose complexity grows when it is desirable to take into account additional phenomena. Equivalent circuits may be obtained using physical argumentation and are derived under simplifying assumptions that facilitate the mathematical analysis. However, the physical significance of the equivalent circuit

parameters (resistive, inductive, or capacitive elements) is diminished as the order is increased. In addition, the foreordination of a structure limits the applicability of a model to the specific problem at hand and does not guarantee that the same model would be useful in a different situation. Furthermore, due to the internal complexity of the equivalent circuits, the parameter identification procedure inevitably leads to the formulation of nonlinear problems which require specialized solving algorithms, and whose solution may not be uniquely obtained from experimental measurements at the machine terminals. Hence, equivalent circuit-based models have inherent conceptional and practical disadvantages. Despite being validated through experience, they are not adequately accurate for modern simulation requirements, wherein the most precise representation of reality is desirable.

These considerations steered this research away from the quest for "advanced" equivalent circuits and motivated the pursuit of a fundamentally different modeling philosophy. In particular, the substitution of equivalent circuit structures with arbitrary (that is, lacking a predefined structure) linear networks is proposed herein. These networks may be represented in the frequency domain by transfer functions, or in the time domain by the corresponding state equations. At first glance, these two approaches are mathematically equivalent; however, the arbitrary linear network approach lifts the significant constraints imposed from equivalent circuit-based models. The proposed models become applicable to a broader range of situations; their generalized formulation permits a more faithful representation of the machine's actual operating characteristics and is well suited to modern frequency-domain measurement methods. Furthermore, the complications of the parameter identification procedure are alleviated, since it is considerably easier to identify linear systems' time constants, rather than algebraically convoluted equivalent circuit parameters.

Advanced modeling approaches—such as the ones herein—must incorporate the iron's magnetic nonlinearities. Indeed, the effects of magnetic saturation and hysteresis considerably affect machines' behavior. Hence, the proposed models are not purely linear networks, but they also contain nonlinear inductive branches to rep-

resent saturating/hysteretic flux paths. This work demonstrates a way to integrate these nonlinear elements with the linear networks, in order to derive non-iterative time-domain dynamic models.

A model's derivation must be discussed in conjunction with suitable characterization procedures, allowing extraction of the models' parameter values from experimental data. Clearly, models not accompanied by parameterization methods are incomplete and inept for all practical purposes. Analytical formulas for obtaining parameters of (equivalent-circuit based) machine models [6, 7] may only serve as a first approximation for design purposes; they are not adequately accurate for the needs of dynamic machine modeling. Even finite element analysis, which takes into account the machine's design, has its own limitations that arise from the insufficient knowledge and subsequent mathematical representation of the iron's complicated nonlinear characteristics (including minor-loop excursions). An *experimental* parameter identification procedure is therefore necessary for reproducing the actual observed behavior of electric machines. Traditional experimental procedures that are suitable for existing machine models are insufficient for characterizing more complex models. Hence, novel parameter identification techniques for the induction machine model, the synchronous generator model, and the brushless exciter model have been developed. The procedures only utilize measurements of electrical quantities at the machine terminals, obtained under relatively simple experimental setups. They do not require extra accommodations for internally placed sensors, which might present technical challenges and contribute to increased expenditures.

A significant part of the characterization procedure concerns the analysis of the collected data and aims at fitting the predictions of the model to the observed behavior. This essentially involves solving an optimization problem, where the model's parameters are independent variables that may be adjusted to minimize the prediction error. In this work, we employ evolutionary optimization algorithms for the purposes of parameter identification [8]. As the name implies, these algorithms imitate the evolution of species and nature's unique ability to adapt—and in a sense

"optimize"—the characteristics of organisms to increase their probability of survival. Evolutionary optimization algorithms are increasingly being used in engineering applications, because of their flexibility, simplicity, and ability to produce solutions where other optimization methods fail to do so. Herein, their suitability to electric machine identification problems is demonstrated.

1.1 Thesis Outline

This work begins with a discussion of intrinsic characteristics and advantages of evolutionary algorithms over classical optimization methods, in Chapter 2. Therein, the adopted algorithmic structure and mathematical operators are set forth in detail.

The dissertation continues with the proposed electric machine models. Chapter 3 contains the induction machine model. This model is specifically designed for inverter–machine analysis. It simultaneously represents magnetizing saturation, both stator and rotor leakage saturation, and distributed circuit effects in the rotor, therefore leading to accurate predictions for inverter-induced current and torque ripple. It is thus an ideal tool for the design of quiet electric drives, when the minimization of high-frequency acoustical noise is of particular interest. The model allows for the interaction of supervisory controls, modulation controls, inverter, and machine to be accurately and rapidly studied in an integrated analysis. A set of analytical forms for the leakage and magnetizing characteristics is proposed; this enables the derivation of small- and large-signal steady-state models, that in turn facilitate the experimental method of measuring the model's parameters.

The synchronous machine model, presented in Chapter 4, is an extension of the induction machine model, similarly adopting the arbitrary-linear-network modeling philosophy. This model is recommended for power system stability studies. The equivalent circuit rotor structures found in conventional machine models are replaced by a two-port linear network. Magnetizing path saturation is incorporated in both axes, with a formulation insuring that conditions for conservative magnetic

fields are not violated. A suitable identification procedure is proposed, including a novel experiment that allows the simultaneous determination of the machine's turns ratio and magnetizing path characteristic from measurements at the terminals. The rotor parameters are identified from standstill frequency response tests using genetic algorithms.

In Chapter 5, a brushless excitation system model is set forth. It features an average-value rectifier representation of all rectification modes, and the incorporation of magnetic hysteresis into the d-axis of the excitation using Preisach's theory. The model is a high-fidelity alternative to the widely used IEEE standard exciter representation, ideal for situations where the exciter's response is of particular interest. To characterize the model, a method that utilizes the waveforms of exciter field current and main alternator terminal voltage is proposed. A genetic algorithm is employed to solve the optimization problem of minimizing the model's prediction error during a change in reference voltage level.

2. EVOLUTIONARY OPTIMIZATION

In 1859, Charles Darwin first described a mechanism for the process of evolution, which he termed "natural selection" [9]. According to his theory, the population members of a species are in a constant struggle for existence, since more individuals are produced at each generation than can survive. In such a hostile environment, an individual's chances of survival are increased if it is better adapted to its environment than its competitors. This concept of "survival of the fittest," coupled with the mechanism of random variations (mutations) in the genome, gives rise to the evolution of species. Some mutations result in a profitable change in the organism's traits, while others might have the opposite effect of decreasing its degree of adaptation. Since fitter members have a greater chance of surviving and thus reproducing themselves, the subsequent recombination of genetic material forces the preservation of the useful traits and the suppression of the undesirable ones.

In mathematical terminology, evolution may be viewed as an optimization process. The adaptation of a species to its environment is nature's way of searching a space for the fitness function's maximum value. The fact that nature has been successful in adapting innumerable species to a variety of environments is not mere coincidence. Rather, it implies that evolution is guided by a set of powerful principles, which although being relatively simple, may lead to the development of extremely complex structures [10]. These principles, when deciphered, may be imitated by humans and applied to their own optimization problems.

Since Darwin's seminal work, which founded the biological sciences field of evolutionary genetics, our knowledge has significantly broadened. Based on the discoveries in genetics, mathematicians and engineers have been able to propose a multitude of algorithms that mimic evolution, all gathered under the umbrella of "evolutionary"

optimization. Genetic algorithms [11], evolution strategies [12], evolutionary programming, and genetic programming [13], are examples of algorithms inspired from natural evolution to handle man-made problems [14, 15]. The type of evolutionary algorithm that will be utilized herein is referred to as a genetic algorithm (GA) [16]. Nevertheless, it should be made clear that this GA is not the "canonical" genetic algorithm, although it follows the common structure of genetic algorithms.

The foundations of genetic algorithms where laid out by John Holland and his students at Ann Arbor, Michigan, in the 1960s [17]. In Holland's original work, a theoretical framework was set forth for the use of genetic algorithms as generic adaptation methods in artificial systems. Holland's approach did not consider GAs as function optimizers in the traditional sense [18]; rather, they were methods to "maximize the cumulative payoff of a sequence of trials." In other words, the original GA was a solver of sequential decision processes. However, by means of specialized algorithmic modifications (such as scaling, elitism, etc.), GAs may be transformed into effective function optimizers.

Over the years, genetic algorithms have proven to be efficient for searching through high-dimensional spaces, and have been used extensively as optimization tools when other optimization algorithms are insufficient. Since Holland's probabilistic explanation using the "building-block hypothesis" and the "schema theorem," a significant amount of research has been devoted to explaining why GAs actually perform as well as they do. For example, important theoretical questions that need to be addressed concern their convergence properties: will they locate the optimum [19–21]? If so, how fast? What are the parameters that affect convergence [22]? This research is ongoing, since definite answers have not as yet been obtained [23]. It is not the purpose of this dissertation to expand on these issues. Genetic algorithms are utilized herein as optimization tools, and no contribution is made on evolutionary optimization theory.

2.1 Parameter Identification Using Genetic Algorithms

The model-based parameter estimation process is illustrated in Fig. 2.1. In general, it consists of the following steps [24]:

1. Select a candidate model, parameterized by the parameter vector, $\boldsymbol{\theta} \in \mathbb{R}^n$.

2. Design an "information-rich" experiment, i.e. one whose outcome is sensitive to all the elements of $\boldsymbol{\theta}$.

3. Apply the test signal to the system, gather a data set, Z^N, of N observations, $y(k)$, $k = 1, \ldots, N$, and calculate the predictions of the model, $\hat{y}(k, \boldsymbol{\theta})$.

4. Evaluate a *prediction error*, for example

$$\varepsilon(k, \boldsymbol{\theta}) = y(k) - \hat{y}(k, \boldsymbol{\theta}), \quad k = 1, \ldots, N\,, \tag{2.1}$$

   and an overall prediction error, such as

$$V_N\left(\boldsymbol{\theta}, Z^N\right) = \frac{1}{N}\sum_{k=1}^{N} \ell\left(\varepsilon_F(k, \boldsymbol{\theta})\right)\,, \tag{2.2}$$

   where $\varepsilon_F(\cdot)$ is a filtered version of $\varepsilon(\cdot)$, and $\ell(\cdot)$ is a scalar-valued positive function. Filtering of the observed data allows for attenuation of high-frequency measurement noise, or low-frequency instrumentation drifts.

5. Find the optimal parameter vector, in the sense that the prediction error becomes as small as possible. The best estimate is

$$\boldsymbol{\theta}^\star = \arg\min V_N\left(\boldsymbol{\theta}, Z^N\right)\,. \tag{2.3}$$

6. Validate the model using an alternate experiment.

The minimization of step 5 may be performed using any optimization method, such as gradient or Newton-like algorithms [25]. In this thesis, a genetic algorithm is employed. Evolutionary optimization was preferred over "conventional" hill-climbing optimization on account of the following distinctive characteristics of a GA:

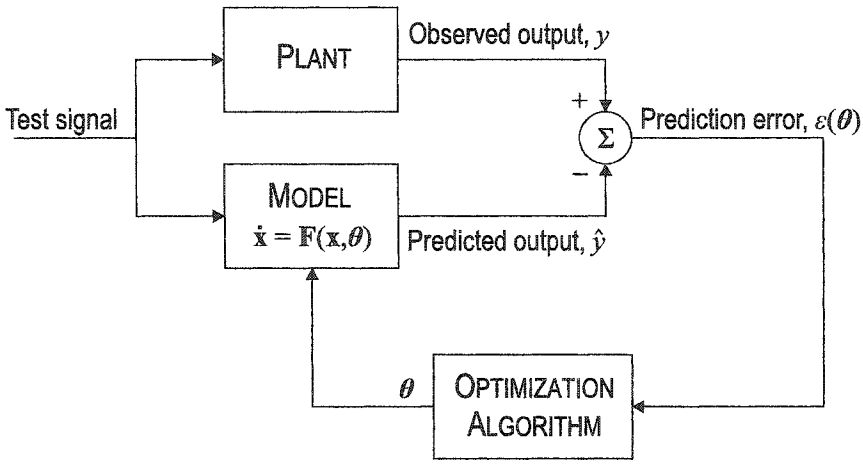

Fig. 2.1. Illustration of the parameter identification process.

- The objective function's gradient or Hessian is not required; GAs only use function values, hence being suitable for non-differentiable or discrete problems.
- The search is guided probabilistically.
- The GA operates on a population of solutions (rather than a single solution).
- An initial guess "close" to the solution is not necessary; population diversity increases the probability of locating the global optimum, rather than getting "stuck" to a suboptimal solution.
- GAs are amenable to parallel computation; function evaluations may be distributed among separate computers.

A model's complexity may be prohibitive for analytically deriving a closed-form objective function expression $V_N(\cdot)$, evaluating its gradient (with respect to the parameters $\boldsymbol{\theta}$), or coming up with an approximate initial parameter set. For these reasons, GAs are highly suitable for parameter identification. However, only a limited number of publications, such as [26–30], contain examples where evolutionary optimization techniques have been applied to electric machine parameter identification.

In summary, the genetic algorithm is used herein to solve the following constrained optimization problem:

$$\begin{aligned} &\text{maximize} && f(\boldsymbol{\theta}) \\ &\text{subject to} && \boldsymbol{\theta} \in \Omega\,. \end{aligned}$$

The function $f : \mathbb{R}^n \to \mathbb{R}^+$ is called the *fitness function*, and attains its maximum when the error is minimum. The domain $\Omega \subset \mathbb{R}^n$ is defined by the minimum and maximum allowable value of the model's parameters (these bounds are usually based on engineering judgment): $\Omega = \{\boldsymbol{\theta} : \theta_i^{\min} \leq \theta_i \leq \theta_i^{\max}, \forall\, i = 1, \ldots, n\}$.

2.2 The Details of the Genetic Algorithm

Genetic algorithms are usually described using terminology borrowed from the field of biology. The GA operates on a set of individuals (parameter sets) called the population, P, which has a fixed size, N_{ind}. By analogy to the encoding of an organism's phenotype (the summation of its visible physical characteristics) into its genotype (the genetic makeup) [31], the members of the population contain encoded versions of the original parameter set values. In this implementation, individuals have a single chromosome with a number of genes equal to the number of parameters in $\boldsymbol{\theta}$. The population is let to evolve for a specific number of generations, N_{gen}.

Traditionally, in "canonical" GAs, the genes were represented using a binary-number (or Gray) encoding of the real parameters. The selection of binary-number encoding is supported from Holland's theory of schemata and the hypothesis of implicit parallelism [11, 17]. However, the use of a real-number encoding has become the standard in modern GA applications, since it offers increased precision and efficiency [13, 32]. The GA used for this work also adopts a real-number encoding.

Herein, two types of genes are defined: linear and exponential. A linear-gene variable θ_i is encoded by

$$y_i = (\theta_i - \theta_i^{\min})/(\theta_i^{\max} - \theta_i^{\min})\,. \tag{2.4}$$

An exponential-gene variable is encoded by

$$y_i = \frac{\ln(\theta_i/\theta_i^{\min})}{\ln(\theta_i^{\max}/\theta_i^{\min})}\,. \tag{2.5}$$

Note that these definitions lead to normalized genes in the range [0–1]. The exponential gene type is used for searching through spaces that span several orders of magnitude. Decoding is achieved through the inverse relations,

$$\theta_i = \theta_i^{\min} + (\theta_i^{\max} - \theta_i^{\min})\, y_i\,, \tag{2.6}$$

or

$$\theta_i = \theta_i^{\min} \left(\frac{\theta_i^{\max}}{\theta_i^{\min}}\right)^{y_i}\,, \tag{2.7}$$

respectively.

As mentioned previously, the GA used herein does not strictly adhere to the structure of a canonical GA. Although it reflects the neo-Darwinian model of organic evolution [8], it is a custom-made version which includes certain features that help accelerate the optimization process. Specifically, our GA implementation has the following structure:

1. *Initialization* (at random).

2. *Evaluation* of the population's fitness, i.e. evaluation of the prediction error and the fitness function $f(\boldsymbol{\theta})$, for all $\boldsymbol{\theta} \in \Omega$.

3. Roulette-wheel *selection* of individuals in the mating pool, pre-conditioned with sigma-truncation [11]. Sigma-truncation consists of ignoring all individuals whose fitness satisfies

$$f' = f - \left[\,\overline{f} - c_{\sigma\text{-tr}}\,\sigma(f)\right] < 0\,, \tag{2.8}$$

where $\overline{f}$ is the average population fitness, $\sigma(f)$ is the standard deviation of the population fitness, and $c_{\sigma\text{-tr}}$ is a constant. During roulette-wheel selection, a mating pool is formed by selecting N_{ind} individuals from the population according to their fitness, with probability of selecting the j-th individual, $p_{\text{sel}}(j) = f'_j / \sum_{k=1}^{N_{\text{ind}}} f'_k$.

4. *Recombination*, i.e. mating of individuals and exchange of their genetic material, by application of the crossover operator, which produces two offspring, o_1 and o_2, from two parents, p_1 and p_2. (Each member of the mating pool has probability p_{mt} of becoming a parent, since $p_{\mathrm{mt}} N_{\mathrm{ind}}/2$ matings take place.) The selected crossover method is simulated binary crossover (SBX) [15, 33], performed on a gene-by-gene basis with parameter η. The offspring are linear combinations of their parents:

$$o_1 = \tfrac{1}{2}[(1+\beta)p_1 + (1-\beta)p_2]\,, \tag{2.9}$$

$$o_2 = \tfrac{1}{2}[(1-\beta)p_1 + (1+\beta)p_2]\,. \tag{2.10}$$

The spread factor β is a random variable, given by

$$\beta = \begin{cases} (2u)^{1/(\eta+1)} & \text{for } u \leq 0.5\,, \\ \dfrac{1}{2(1-u)}^{1/(\eta+1)} & \text{for } u > 0.5\,, \end{cases} \tag{2.11}$$

where $u \in [0,1]$ is a (uniformly distributed) random number. If an offspring happens to be outside the allowable [0,1] range, it is repositioned using the following rule: [1]

$$o' = \begin{cases} o - \lfloor o \rfloor & \text{for } o > 1\,, \\ 1 - (o - \lfloor o \rfloor) & \text{for } o < 0\,. \end{cases} \tag{2.12}$$

5. *Mutation*, i.e. random variations of the genetic material. This is performed by two distinct operators:

   (a) Total mutation, where a gene is changed arbitrarily with probability p_{tm} per gene.

   (b) Partial mutation, where a gene's original value is perturbed according to a normal distribution of standard deviation σ_{pm} with probability p_{pm} per gene. That is, the gene that undergoes mutation is modified in accordance with

$$y_i' = y_i + N(0, \sigma_{\mathrm{pm}})\,, \tag{2.13}$$

[1] The floor function, $\lfloor o \rfloor$, returns the largest integer that is less than or equal to o.

where $N(0, \sigma_{\text{pm}})$ is a random number arising from a zero-mean normal distribution. If $y_i' > 1$, or $y_i' < 0$, then $y_i' = 1$ or $y_i' = 0$, respectively.

6. *Evaluation* of the individuals' fitness $f(\boldsymbol{\theta})$ (only for the newly generated $\boldsymbol{\theta}$).

7. Enforcement of the *elitism* property. The fitness of the current and previous best individuals is compared; if a fitter individual was not generated, the previous best individual is reinserted in the population.

8. *Random search* (a localized search operator in the vicinity of the most fit individual that partially mutates the best individual N_{rs} times according to a normal distribution of standard deviation σ_{rs}). Each gene of the best individual is perturbed by

$$y_i' = y_i \cdot [1 + N(0, \sigma_2)], \tag{2.14}$$

where $\sigma_2 = \sigma_{\text{rs}} u$, and u is a uniformly distributed random number in [0,1]. (A new random number $N(0, \sigma_2)$ is generated for each gene, but the same u is used for all genes of an individual.) If $y_i' > 1$, or $y_i' < 0$, then $y_i' = 1$ or $y_i' = 0$, respectively. The new individuals are evaluated, and if a fitter individual was generated, it replaces the previous best individual in the population.

9. If the current generation is N_{gen}, then stop; else, go to step 3.

These operators are included in an early version of our genetic algorithm optimization toolbox (ENEGAT, ver. 5.4 [16]), which was the one used herein. These routines have now evolved into a more integrated and powerful package [34]. To handle the increased computational demands of multiple function evaluations, a parallel computing environment of 16 machines was developed, named GOPA (Genetic Optimization Processing Array).

3. INDUCTION MACHINE MODELING

3.1 Review of Existing Models

The "standard" qd-axes induction machine model, as described in [5] and depicted in Fig. 3.1, has been extensively used since the early twentieth century [4]. Its derivation is based on a series of assumptions, such as balanced stator and rotor windings with sinusoidal mutual inductance, constant self-inductances, a smooth air-gap, and the absence of saturation, hysteresis, and eddy currents. This model is readily parameterized, easily implemented in time-domain dynamic simulations, and still today widely employed for induction machine studies. However, its accuracy is not sufficient for modern day applications, which involve power-electronic based drive systems and complicated control schemes. The research towards improved induction machine models has thus focused on incorporating the aforementioned details and phenomena that were originally ignored for simplicity, but nonetheless enhance the models' fidelity when accounted for.

Winding function theory [35] is often utilized for taking into account the actual winding distribution of an induction machine. The analysis of a symmetric induction machine having an arbitrary number of stator phases and rotor slots was described

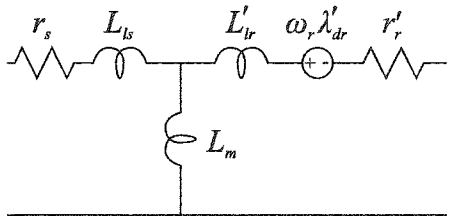

Fig. 3.1. The standard induction machine model equivalent circuit structure (stationary q-axis shown).

in [36–38] using winding functions. If the assumption of sinusoidally distributed windings is dropped, the study of internal faults, such as broken bars or end ring segments, is also possible [39]. With this theory, it was recently proved that a squirrel-cage rotor is equivalent to a set of orthogonal windings (if the stator winding is assumed to be sinusoidally distributed) [40]. The winding function approach also lends itself to the study of mechanical vibrations and audible noise. In general, information about the machine's design specifications is required, and saturation effects are not taken into consideration.

However, representing saturation in induction motors is important, since in modern drive applications the flux is not maintained constant; variation of flux is often used as a means of optimizing a drive's operation [41]. The detuning effects of saturation on field-oriented controllers have been thoroughly examined [42]. By ignoring saturation, "the gain of the slip calculator (i.e. the rotor time constant) is incorrect, the decoupling of flux and torque is disturbed and the field-oriented controller is said to be detuned" [43]. More advanced control schemes vary the flux levels in order to achieve maximum efficiency (for example, by minimizing hysteresis and eddy current losses) [44, 45]. In other applications, the drive's performance is optimized for static or dynamic maximum torque per ampere over a wide speed range [46–48], hence "the calculation of the obtainable torque as well as the design of a control scheme which makes it possible to reach maximum torque over the whole speed range must take the nonlinearity of the magnetization curve into account" [49]. According to [50], where the small-signal stability properties of an induction motor drive were investigated, "perhaps the most important influence of the saturation effect is in the damping of electrical transients." It was found that by adding resistance to the stator terminals, a sustained oscillation was produced under no load. The accuracy in predicting the region of instability was improved by modeling the magnetizing path saturation. Therefore, for all cases where the machine's flux level is variable, magnetizing branch saturation modeling is highly significant [51].

Magnetizing path saturation leads to the phenomenon of cross-magnetization. In [52], the existence of cross-coupling terms between the stator axes, and between stator and rotor axes in quadrature was demonstrated. The physical significance of this effect was questioned in [53], and the issue of cross-saturation has raised controversy in the past, but it is nowadays recognized as an important, experimentally validated phenomenon [54–57].

Main flux path saturation is usually modeled using the nonlinear relationship between magnetizing flux and current. Due to the cylindrical rotor structure of induction machines, magnetizing mmf and flux are collinear, so a single function is sufficient to represent saturation in any direction. This corresponds to replacing the linear magnetizing inductance L_m of Fig. 3.1 by a nonlinear saturating inductance. For instance, the magnetizing flux–current characteristic may be expressed as $\lambda_m = L_m(i_m)\, i_m$, where flux and current are related to their orthogonal qd-axes components by $\lambda_m^2 = \lambda_{md}^2 + \lambda_{mq}^2$, $i_m^2 = i_{md}^2 + i_{mq}^2$. This representation also predicts cross-magnetization effects, like, for example, the influence of q-axis current upon the d-axis flux: $\frac{\partial \lambda_{md}}{\partial i_{mq}} = \frac{\partial [L_m(i_m)\, i_{md}]}{\partial i_{mq}} = \frac{dL_m(i_m)}{di_m} \frac{\partial i_m}{\partial i_{mq}} i_{md} = \frac{dL_m(i_m)}{di_m} \frac{i_{md} i_{mq}}{i_m}$.

Apart from the magnetizing path, the stator and rotor tooth leakage paths may saturate as well [58–61]. This phenomenon is pronounced during the acceleration from rest to rated operating speed, which is accompanied by the flow of large inrush currents and high torque pulsations that may lead to failures in the gear train. In [58], the leakage inductances L_{ls}, L_{lr} of Fig. 3.1 were replaced by nonlinear saturating terms. The model of [58] presents an example of an iterative model, where the resulting equations require iterations "to establish the proper values of saturated magnetizing and leakage fluxes for each time step."

An alternative equivalent circuit structure was proposed in [62–64] (see Fig. 3.2). These models account separately for the saturation of the stator and rotor teeth and cores. They are more accurate than the model representing only the main path saturation, especially in cases of abnormal large-signal disturbances, but they suffer from tedious parameter identification procedures. The saturation dependent

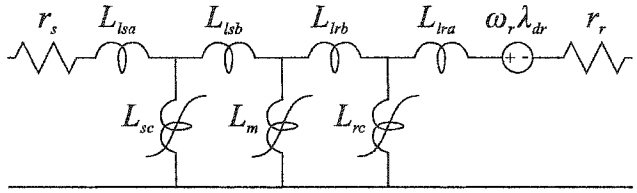

L_{lsa}, L_{lra} = stator and rotor end-winding leakage inductances
L_{sc}, L_{rc} = stator and rotor core inductances
L_{lsb}, L_{lrb} = stator and rotor slot leakage inductances
L_m = magnetizing inductance, which represents the combined reluctances of the stator, rotor teeth, and the air gap

Fig. 3.2. Equivalent induction machine circuit, as proposed by Ojo *et al* (stationary q-axis shown).

parameters may be obtained through finite element analysis, or experimentally using search coils positioned in the air gap. However, the voltages and loads required are much higher than their respective rated values, and the practicality of these methods is questionable. The saturation of the teeth and the stator core distorts the sinusoidal distribution of flux, and causes odd-order flux harmonics to appear in the air-gap [65]. Their impact on machine performance (production of torque ripple and extra copper losses) is minimal, but they generate zero-sequence components in the stator voltage waveforms that may be utilized as a means for locating the air-gap flux.

When simulating ac drives, it is also desirable to represent the induction motor over a wide frequency band, from the slip frequency (a few milli-hertz) up to switching frequencies (tens of kilo-hertz). Although stator winding capacitive effects may become important for high frequencies [66], the part of the machine most sensitive to frequency variations is the rotor (especially squirrel-cage rotors with deep bars) [67]. The skin effect is responsible for the variation of current density inside the rotor bars; when frequency increases, current tends to flow in the portion of the bars closest to the air-gap, thus increasing the resistance and reducing the leakage inductance of the rotor circuits. Models that take into account the deep-bar effect facilitate the design of drives with improved dynamic performance [68]. The rotor

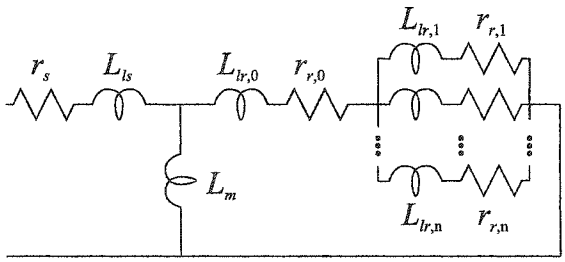

Fig. 3.3. Equivalent induction machine circuit, as proposed by Langheim.

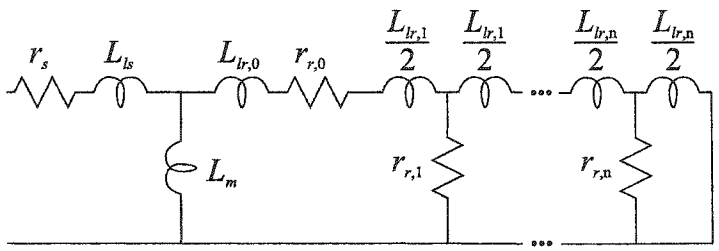

Fig. 3.4. Equivalent induction machine circuit, as proposed by Levy *et al.*

is usually approximated by a ladder network, whose blocks correspond to different sections of the bars (Figs. 3.3, 3.4) [69–71].

The equivalent circuit rotor parameters change with respect to the saturation level of the flux paths. Recent evidence suggests that the variation of rotor bar resistance with current density is relatively minor compared to the corresponding leakage inductance drop [72, 73]. (The saturable nature of the rotor leakage inductance is even more apparent in closed slot designs, due to saturation of the thin rotor bar bridges.) Therefore, the rotor can be adequately modeled by a saturable leakage inductance in series with a linear equivalent circuit, as in Fig. 3.5.

The electromagnetic field distribution around a rotor bar with a simple geometry may be computed analytically. It can be shown that the rotor bar impedance is a function of the square root of frequency. Hence the use of half-order—and in general non-integer order transfer functions—to model the frequency response of the rotor circuits is a logical step [74], potentially leading to models requiring less parameters than integer-order models. This idea has been recently extended to synchronous

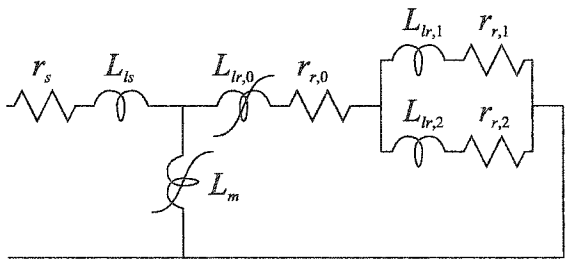

Fig. 3.5. Equivalent induction machine circuit, as proposed by Smith *et al.*

machines models [75], but there is still considerable research to be performed in this area, related in particular to the computation of the time response of such circuits.

Further improvement in squirrel-cage induction machine models is achieved when considering currents flowing between the rotor cage bars due to the absence of insulation from the laminated core [76]. This phenomenon depends on the effective bar-to-bar resistance value, which differs even between motors with identical designs and thus can not be predicted theoretically. The presence of inter-bar currents is responsible for significant variations of locked-rotor torque among nominally identical machines (which affects starting performance). Moreover, inter-bar currents introduce extra losses that cause the deterioration of efficiency under normal operating conditions. In the equivalent circuit proposed in [76] (see Fig. 3.6), the rotor elements are modified by a complex (not real) quantity F, which may be computed from the rotor geometry.

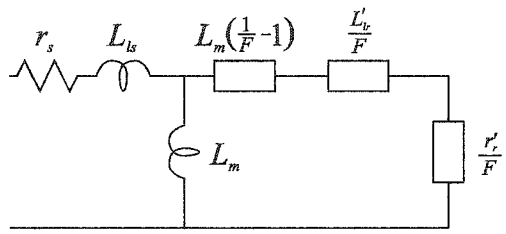

Fig. 3.6. Equivalent induction machine circuit (fundamental field only), as proposed by Williamson and Smith.

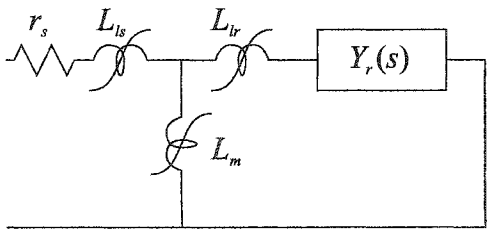

Fig. 3.7. Equivalent circuit structure of the proposed induction machine model.

The power loss mechanism in the iron core is still not well understood [77, 78]. Studies have shown that the classical formulas for hysteresis, eddy and other "anomalous" (excess) losses are not accurate enough, especially in the case of inverter-fed induction motors, where factors such as frequency, loading level and the pulse-width-modulation strategy are important. In any case, the model proposed in this thesis does not explicitly account for iron core losses.

3.2 The Proposed Model—Mathematical Formulation

The proposed model, whose structure is shown in Fig. 3.7, simultaneously includes (1) magnetizing saturation as a function of the q- and d-axis magnetizing flux linkage, (2) both stator and rotor leakage saturation as functions of the stator current, rotor current, and q- and d-axis magnetizing flux linkage, and (3) distributed effects in the rotor. This is done in such a way that the model is completely noniterative at each time step, yielding a high degree of computational efficiency.

In Table 3.1, the features of the different induction machine models are juxtaposed. Notice that the rightmost column corresponds to the features of the proposed model. Apparently, the integration in a single model of main flux path and leakage flux path saturation (as a function of both current and magnetizing flux linkage) with distributed circuit effects in the rotor has not been achieved previously. Furthermore, validation of the established models in the switching frequency range has never been addressed.

Table 3.1
Features of induction machine models.

	[36]	[39]	[40]	[52]	[50]	[51]	[63]	[42]	[65]	[64]	[79]	[69]	[70]	[73]	[80]	[72]	[71]	[58]	[62]	[81]	[82]
Magnetizing path sat.				✓	✓	✓	✓	✓	✓	✓	✓			✓	✓	✓	✓	✓	✓	✓	✓
Leakage sat. (flux)																		✓		✓	✓
Leakage sat. (current)														✓	✓	✓	✓		✓	✓	✓
Cross-saturation				✓		✓		✓			✓				✓	✓	✓	✓			✓
Distributed rotor	✓											✓	✓	✓	✓	✓	✓			✓	✓
High freq. validation																					✓
Spatial harmonics	✓	✓	✓						✓												

3.2.1 Notation

Throughout this analysis, matrix and vector quantities appear in bold font. Vector quantities have subscripts that denote the specific elements of the vector, e.g.

$$\mathbf{f}_{abcx} = [f_{ax}\ f_{bx}\ f_{cx}]^T\ , \tag{3.1}$$

$$\mathbf{f}_{qd0x} = [f_{qx}\ f_{dx}\ f_{0x}]^T\ , \tag{3.2}$$

$$\mathbf{f}_{qdx} = [f_{qx}\ f_{dx}]^T\ . \tag{3.3}$$

Variables without superscripts, such as the ones above, are in an arbitrary reference frame of position θ and angular speed ω. An "r" superscript denotes that a variable is expressed in the rotor reference frame. The electrical rotor position is designated as θ_r, and electrical rotor speed as ω_r. The mechanical quantities are denoted by θ_{rm} and ω_{rm}, while the number of poles is P. The transformation of stationary abc to $qd0$ variables is defined by [5]

$$\mathbf{f}_{qd0s} = \mathbf{K}_s(\theta)\mathbf{f}_{abcs}, \tag{3.4}$$

where

$$\mathbf{K}_s(\theta) = \frac{2}{3}\begin{bmatrix} \cos(\theta) & \cos\left(\theta - \frac{2\pi}{3}\right) & \cos\left(\theta + \frac{2\pi}{3}\right) \\ \sin(\theta) & \sin\left(\theta - \frac{2\pi}{3}\right) & \sin\left(\theta + \frac{2\pi}{3}\right) \\ \frac{1}{2} & \frac{1}{2} & \frac{1}{2} \end{bmatrix}. \tag{3.5}$$

3.2.2 Voltage equations

The stator voltage equations may be expressed in *abc* variables as

$$\mathbf{v}_{abcs} = r_s \mathbf{i}_{abcs} + \frac{d}{dt}\boldsymbol{\lambda}_{abcs}\,, \tag{3.6}$$

where $\mathbf{v}_{abcs}$, $\mathbf{i}_{abcs}$ and $\boldsymbol{\lambda}_{abcs}$ denote the stator winding (phase-to-neutral) voltages, currents flowing into the machine terminals, and flux linkages, respectively, and r_s is the stator winding resistance. Transforming (3.6) to an arbitrary reference frame yields

$$\mathbf{v}_{qd0s} = r_s \mathbf{i}_{qd0s} + \omega \boldsymbol{\lambda}_{dqs} + \frac{d}{dt}\boldsymbol{\lambda}_{qd0s}\,, \tag{3.7}$$

where $\boldsymbol{\lambda}_{dqs} = [\lambda_{ds} \;\; -\lambda_{qs} \;\; 0]^T$. It will be assumed hereafter that the zero sequence variables can be neglected.

The rotor circuits are modeled by two elements connected in series: a nonlinear element, to represent the saturation effects, and a linear element that represents the distributed effects of the rotor. So, the voltage equations of the rotor circuits are

$$\mathbf{0} = \mathbf{e}^r_{qdr} + \frac{d}{dt}\boldsymbol{\lambda}^r_{qdr}\,, \tag{3.8}$$

where e^r_{qr}, e^r_{dr} denote the voltage drop across the linear impedance, and λ^r_{qr}, λ^r_{dr} denote the flux linking the nonlinear part of the rotor circuits.

In the frequency domain, the rotor currents are related to the voltage drops by

$$\tilde{i}^r_{qr}(s) = Y_r(s)\,\tilde{e}^r_{qr}(s), \tag{3.9}$$

$$\tilde{i}^r_{dr}(s) = Y_r(s)\,\tilde{e}^r_{dr}(s), \tag{3.10}$$

where s is the Laplace operator—not to be confused with slip, and the tilde is used to denote dependence on complex frequency. (Later in this chapter, the tilde notation

will be used to represent phasor quantities.) In order to avoid transforming the admittance operator to an arbitrary reference frame, the rotor reference frame is selected for the analysis. The rotor admittance transfer function is of order N_r, and may be expressed as

$$Y_r(s) = Y_{r0}\frac{1 + n_{r1}s + \cdots + n_{r(N_r-1)}s^{N_r-1}}{1 + d_{r1}s + \cdots + d_{rN_r}s^{N_r}}. \tag{3.11}$$

In the time domain, (3.9)–(3.11) may be expressed as

$$\tfrac{d}{dt}\mathbf{x}_q^r = \mathbf{A}_r\mathbf{x}_q^r + \mathbf{B}_r e_{qr}^r\,, \tag{3.12}$$

$$i_{qr}^r = \mathbf{C}_r\mathbf{x}_q^r\,, \tag{3.13}$$

and

$$\tfrac{d}{dt}\mathbf{x}_d^r = \mathbf{A}_r\mathbf{x}_d^r + \mathbf{B}_r e_{dr}^r\,, \tag{3.14}$$

$$i_{dr}^r = \mathbf{C}_r\mathbf{x}_d^r\,. \tag{3.15}$$

For implementation purposes, it is convenient to express the equations in quasi-controller canonical form [83], with the following state matrices,

$$\mathbf{A}_r = \begin{bmatrix} 0 & 1 & 0 & \cdots & 0 & 0 \\ 0 & 0 & 1 & \cdots & 0 & 0 \\ \vdots & \vdots & \vdots & \ddots & \vdots & \vdots \\ 0 & 0 & 0 & \cdots & 1 & 0 \\ 0 & 0 & 0 & \cdots & 0 & 1 \\ -\frac{1}{d_{rN_r}} & -\frac{d_{r1}}{d_{rN_r}} & -\frac{d_{r2}}{d_{rN_r}} & \cdots & -\frac{d_{r(N_r-2)}}{d_{rN_r}} & -\frac{d_{r(N_r-1)}}{d_{rN_r}} \end{bmatrix}, \tag{3.16}$$

$$\mathbf{B}_r = \begin{bmatrix} 0 & \cdots & 0 & \frac{1}{d_{rN_r}} \end{bmatrix}^T, \tag{3.17}$$

$$\mathbf{C}_r = Y_{r0}\begin{bmatrix} 1 & n_{r1} & \cdots & n_{r(N_r-1)} \end{bmatrix}. \tag{3.18}$$

It will be useful to note that

$$\tfrac{d}{dt}i_{qr}^r = \mathbf{C}_r\mathbf{A}_r\mathbf{x}_q^r + \mathbf{C}_r\mathbf{B}_r e_{qr}^r, \tag{3.19}$$

$$\tfrac{d}{dt}i_{dr}^r = \mathbf{C}_r\mathbf{A}_r\mathbf{x}_d^r + \mathbf{C}_r\mathbf{B}_r e_{dr}^r. \tag{3.20}$$

The incorporation of distributed effects in the rotor is one of the most important features of the model. In the low-frequency range, the transfer function (3.11) governs the effective rotor resistance and how it changes with slip frequency. In the switching-frequency region, the transfer function partially replaces the traditional rotor leakage inductance parameter—another portion is taken into account by the nonlinear part. As such, it also mathematically captures the reduction in effective rotor leakage inductance with frequency. This drop-off is one of the most important factors in explaining why switching frequency current ripple is much higher than predicted with previous modeling techniques.

3.2.3 Leakage path magnetics

It is convenient to break the stator flux linkage vectors into leakage and magnetizing flux terms, as

$$\boldsymbol{\lambda}^r_{qds} = \boldsymbol{\lambda}^r_{lqds} + \boldsymbol{\lambda}^r_{mqd}, \tag{3.21}$$

where $\boldsymbol{\lambda}^r_{lqds}$ is the stator leakage flux, and $\boldsymbol{\lambda}^r_{mqd}$ is the magnetizing flux.

The stator leakage flux linkage is a complicated function. Clearly, it depends on the stator current since the leakage flux path utilizes iron in the region of the winding where saturation can occur. It also depends on the rotor current, which serves as an mmf source able to saturate the zigzag leakage flux path. It is reasonable to assume that due to these localized effects, the leakage flux in a given axis is influenced by the stator and rotor current of the same axis. Moreover, since the permeance of the stator teeth is determined by the flux level, it is expected that the stator leakage flux linkage is affected by the magnetizing flux linkage in both axes. The functional form of the leakage flux can be incorporated in the leakage inductance L_{lxs} as

$$\lambda^r_{lxs} = L_{lxs}(i^r_{xs}, i^r_{xr}, \lambda^r_{mq}, \lambda^r_{md})\, i^r_{xs}, \tag{3.22}$$

where "x" can be "q" or "d."

In practical terms, the effect of the current arguments is relatively minor, except during conditions in which the currents are significantly greater than rated. However,

the leakage inductance is significantly affected by the magnetizing flux and decreases quite rapidly as the flux level is increased. An implication of this on drive design is that reduction of flux level will reduce the switching frequency current and torque ripple.

Similarly, the rotor flux linkage equations are expressed in terms of the rotor leakage flux $\boldsymbol{\lambda}^r_{lqdr}$ and the magnetizing flux as

$$\boldsymbol{\lambda}^r_{qdr} = \boldsymbol{\lambda}^r_{lqdr} + \boldsymbol{\lambda}^r_{mqd}\,, \tag{3.23}$$

where the leakage flux linkages are given by

$$\lambda^r_{lxr} = L_{lxr}(i^r_{xs}, i^r_{xr}, \lambda^r_{mq}, \lambda^r_{md})\, i^r_{xr}, \tag{3.24}$$

where again "x" represents either one of the two axes.

3.2.4 Magnetizing path magnetics

The magnetizing flux vector is assumed collinear with the mmf produced by the magnetizing current, i.e. they are related by the scalar function $\Gamma_m(\lambda_m)$, which represents the absolute inverse magnetizing inductance. Hence,

$$\mathbf{i}^r_{mqd} = \Gamma_m(\lambda_m)\, \boldsymbol{\lambda}^r_{mqd}\,, \tag{3.25}$$

$$i_m = \Gamma_m(\lambda_m)\, \lambda_m\,. \tag{3.26}$$

The magnitudes of the current and flux vectors are defined by

$$i_m = \sqrt{(i^r_{md})^2 + (i^r_{mq})^2}\,, \tag{3.27}$$

$$\lambda_m = \sqrt{(\lambda^r_{md})^2 + (\lambda^r_{mq})^2}\,. \tag{3.28}$$

Differentiating (3.25) with respect to time yields

$$\tfrac{d}{dt}\mathbf{i}^r_{mqd} = \boldsymbol{\Gamma}_{mi}(\boldsymbol{\lambda}^r_{mqd})\tfrac{d}{dt}\boldsymbol{\lambda}^r_{mqd}\,, \tag{3.29}$$

where

$$\boldsymbol{\Gamma}_{mi}(\boldsymbol{\lambda}^r_{mqd}) = \begin{bmatrix} \frac{\partial\Gamma_m(\lambda_m)}{\partial\lambda_m}\frac{(\lambda^r_{mq})^2}{\lambda_m} + \Gamma_m(\lambda_m) & \frac{\partial\Gamma_m(\lambda_m)}{\partial\lambda_m}\frac{\lambda^r_{mq}\lambda^r_{md}}{\lambda_m} \\ \frac{\partial\Gamma_m(\lambda_m)}{\partial\lambda_m}\frac{\lambda^r_{mq}\lambda^r_{md}}{\lambda_m} & \frac{\partial\Gamma_m(\lambda_m)}{\partial\lambda_m}\frac{(\lambda^r_{md})^2}{\lambda_m} + \Gamma_m(\lambda_m) \end{bmatrix}. \tag{3.30}$$

The 'i' subscript denotes incremental value.

The incorporation of magnetic saturation is important in order to correctly predict the magnetizing component of the current. In addition, since the effective incremental inductance ($\mathbf{\Gamma}_{mi}^{-1}$) is much lower than the absolute magnetizing inductance, magnetic saturation also contributes to the underestimation of the current ripple in the standard qd-axes induction machine model, although this is not as important an effect as the leakage saturation and distributed effects of the rotor.

3.2.5 Model integration

It is now appropriate to integrate the various submodels into a unified induction machine model. Their equations are combined in the rotor reference frame. A convenient choice of state variables is the set $\mathbf{x} = \left\{\boldsymbol{\lambda}_{mqd}^r, \mathbf{x}_q^r, \mathbf{x}_d^r\right\}$. In this section, an algorithm is set forth to determine the functional dependence of the state variables $\mathbf{x}$ and inputs $\mathbf{u}$ as a differential equation of the form

$$\tfrac{d}{dt}\mathbf{x} = \mathbf{f}(\mathbf{x}, \mathbf{u}), \tag{3.31}$$

which is the fundamental problem in defining any time-domain model. Although the model includes both magnetizing and leakage saturation, this can be done in a completely noniterative fashion.

The first step in this procedure is to calculate the rotor, magnetizing, and stator currents as a function of the states. The rotor currents, i_{qr}^r, i_{dr}^r, are readily calculated in terms of the rotor admittance states, $\mathbf{x}_q^r$, $\mathbf{x}_d^r$, from (3.13) and (3.15), respectively. The magnetizing currents, i_{mq}^r, i_{md}^r, depend on the magnetizing flux states, as can be seen from (3.25) and (3.28). Finally, the stator currents are

$$\mathbf{i}_{qds}^r = \mathbf{i}_{mqd}^r - \mathbf{i}_{qdr}^r \,. \tag{3.32}$$

The next step is to calculate the stator flux linkages, λ_{qs}^r, λ_{ds}^r. From (3.7), their time derivatives are

$$\tfrac{d}{dt}\lambda_{qs}^r = v_{qs}^r - r_s i_{qs}^r - \omega_r \lambda_{ds}^r \,, \tag{3.33}$$

$$\tfrac{d}{dt}\lambda_{ds}^r = v_{ds}^r - r_s i_{ds}^r + \omega_r \lambda_{qs}^r \,. \tag{3.34}$$

Note that these derivatives are computed as an intermediate calculation—they are not integrated since λ^r_{qs} and λ^r_{ds} are not states.

The goal of the ensuing analysis is the formulation of a linear system of equations with the rotor voltages across the linear impedances e^r_{qr} and e^r_{dr}, as well as the time derivatives of the magnetizing flux linkages, $\frac{d}{dt}\lambda^r_{mq}$ and $\frac{d}{dt}\lambda^r_{md}$, taken as unknown.

Differentiation with respect to time of the stator flux linkages (3.21) and (3.22) yields

$$\frac{d}{dt}\lambda^r_{qs} = \left[\frac{\partial L_{lqs}(\cdot)}{\partial i^r_{qs}} i^r_{qs} + L_{lqs}(\cdot)\right]\frac{d}{dt}i^r_{qs} + \left[\frac{\partial L_{lqs}(\cdot)}{\partial i^r_{qr}} i^r_{qs}\right]\frac{d}{dt}i^r_{qr} + \\ + \left[\frac{\partial L_{lqs}(\cdot)}{\partial \lambda^r_{mq}} i^r_{qs} + 1\right]\frac{d}{dt}\lambda^r_{mq} + \left[\frac{\partial L_{lqs}(\cdot)}{\partial \lambda^r_{md}} i^r_{qs}\right]\frac{d}{dt}\lambda^r_{md}\,, \quad (3.35)$$

$$\frac{d}{dt}\lambda^r_{ds} = \left[\frac{\partial L_{lds}(\cdot)}{\partial i^r_{ds}} i^r_{ds} + L_{lds}(\cdot)\right]\frac{d}{dt}i^r_{ds} + \left[\frac{\partial L_{lds}(\cdot)}{\partial i^r_{dr}} i^r_{ds}\right]\frac{d}{dt}i^r_{dr} + \\ + \left[\frac{\partial L_{lds}(\cdot)}{\partial \lambda^r_{mq}} i^r_{ds}\right]\frac{d}{dt}\lambda^r_{mq} + \left[\frac{\partial L_{lds}(\cdot)}{\partial \lambda^r_{md}} i^r_{ds} + 1\right]\frac{d}{dt}\lambda^r_{md}\,. \quad (3.36)$$

A similar set of expressions can be derived from the rotor equations (3.8), (3.23) and (3.24):

$$0 = e^r_{qr} + \left[\frac{\partial L_{lqr}(\cdot)}{\partial i^r_{qs}} i^r_{qr}\right]\frac{d}{dt}i^r_{qs} + \left[\frac{\partial L_{lqr}(\cdot)}{\partial i^r_{qr}} i^r_{qr} + L_{lqr}(\cdot)\right]\frac{d}{dt}i^r_{qr} + \\ + \left[\frac{\partial L_{lqr}(\cdot)}{\partial \lambda^r_{mq}} i^r_{qr} + 1\right]\frac{d}{dt}\lambda^r_{mq} + \left[\frac{\partial L_{lqr}(\cdot)}{\partial \lambda^r_{md}} i^r_{qr}\right]\frac{d}{dt}\lambda^r_{md}\,, \quad (3.37)$$

$$0 = e^r_{dr} + \left[\frac{\partial L_{ldr}(\cdot)}{\partial i^r_{ds}} i^r_{dr}\right]\frac{d}{dt}i^r_{ds} + \left[\frac{\partial L_{ldr}(\cdot)}{\partial i^r_{dr}} i^r_{dr} + L_{ldr}(\cdot)\right]\frac{d}{dt}i^r_{dr} + \\ + \left[\frac{\partial L_{ldr}(\cdot)}{\partial \lambda^r_{mq}} i^r_{dr}\right]\frac{d}{dt}\lambda^r_{mq} + \left[\frac{\partial L_{ldr}(\cdot)}{\partial \lambda^r_{md}} i^r_{dr} + 1\right]\frac{d}{dt}\lambda^r_{md}\,. \quad (3.38)$$

It is necessary to eliminate the dependence of (3.35)–(3.38) on the time derivatives of the stator currents. Using (3.29) and (3.32), we get

$$\frac{d}{dt}\mathbf{i}^r_{qds} = \mathbf{\Gamma}_{mi}(\boldsymbol{\lambda}^r_{mqd})\frac{d}{dt}\boldsymbol{\lambda}^r_{mqd} - \frac{d}{dt}\mathbf{i}^r_{qdr}\,, \quad (3.39)$$

which may be used to obtain

$$\frac{d}{dt}\lambda^r_{qs} = L_{lqsqr}(\cdot)\frac{d}{dt}i^r_{qr} + \\ + \left\{1 + \left[\frac{\partial L_{lqs}(\cdot)}{\partial \lambda^r_{mq}} + \frac{\partial L_{lqs}(\cdot)}{\partial i^r_{qs}}\mathbf{\Gamma}_{mi}(\cdot)_{11}\right] i^r_{qs} + L_{lqs}(\cdot)\mathbf{\Gamma}_{mi}(\cdot)_{11}\right\}\frac{d}{dt}\lambda^r_{mq} + \\ + \left\{\left[\frac{\partial L_{lqs}(\cdot)}{\partial \lambda^r_{md}} + \frac{\partial L_{lqs}(\cdot)}{\partial i^r_{qs}}\mathbf{\Gamma}_{mi}(\cdot)_{12}\right] i^r_{qs} + L_{lqs}(\cdot)\mathbf{\Gamma}_{mi}(\cdot)_{12}\right\}\frac{d}{dt}\lambda^r_{md}\,, \quad (3.40)$$

$$\frac{d}{dt}\lambda^r_{ds} = L_{ldsdr}(\cdot)\frac{d}{dt}i^r_{dr} + \\ + \left\{\left[\frac{\partial L_{lds}(\cdot)}{\partial \lambda^r_{mq}} + \frac{\partial L_{lds}(\cdot)}{\partial i^r_{ds}}\mathbf{\Gamma}_{mi}(\cdot)_{21}\right] i^r_{ds} + L_{lds}(\cdot)\mathbf{\Gamma}_{mi}(\cdot)_{21}\right\}\frac{d}{dt}\lambda^r_{mq} + \\ + \left\{1 + \left[\frac{\partial L_{lds}(\cdot)}{\partial \lambda^r_{md}} + \frac{\partial L_{lds}(\cdot)}{\partial i^r_{ds}}\mathbf{\Gamma}_{mi}(\cdot)_{22}\right] i^r_{ds} + L_{lds}(\cdot)\mathbf{\Gamma}_{mi}(\cdot)_{22}\right\}\frac{d}{dt}\lambda^r_{md}\,, \quad (3.41)$$

$$0 = e^r_{qr} + L_{lqrqr}(\cdot)\frac{d}{dt}i^r_{qr} + \left\{1 + \left[\frac{\partial L_{lqr}(\cdot)}{\partial \lambda^r_{mq}} + \frac{\partial L_{lqr}(\cdot)}{\partial i^r_{qs}}\mathbf{\Gamma}_{mi}(\cdot)_{11}\right] i^r_{qr}\right\}\frac{d}{dt}\lambda^r_{mq} + \\ + \left[\frac{\partial L_{lqr}(\cdot)}{\partial \lambda^r_{md}} + \frac{\partial L_{lqr}(\cdot)}{\partial i^r_{qs}}\mathbf{\Gamma}_{mi}(\cdot)_{12}\right] i^r_{qr}\frac{d}{dt}\lambda^r_{md}\,, \quad (3.42)$$

$$0 = e^r_{dr} + L_{ldrdr}(\cdot)\frac{d}{dt}i^r_{dr} + \left[\frac{\partial L_{ldr}(\cdot)}{\partial \lambda^r_{mq}} + \frac{\partial L_{ldr}(\cdot)}{\partial i^r_{ds}}\mathbf{\Gamma}_{mi}(\cdot)_{21}\right] i^r_{dr}\frac{d}{dt}\lambda^r_{mq} + \\ + \left\{1 + \left[\frac{\partial L_{ldr}(\cdot)}{\partial \lambda^r_{md}} + \frac{\partial L_{ldr}(\cdot)}{\partial i^r_{ds}}\mathbf{\Gamma}_{mi}(\cdot)_{22}\right] i^r_{dr}\right\}\frac{d}{dt}\lambda^r_{md}\,, \quad (3.43)$$

where

$$L_{lqsqr}(\cdot) \triangleq \left[\frac{\partial L_{lqs}(\cdot)}{\partial i^r_{qr}} - \frac{\partial L_{lqs}(\cdot)}{\partial i^r_{qs}}\right] i^r_{qs} - L_{lqs}(\cdot)\,, \quad (3.44)$$

$$L_{ldsdr}(\cdot) \triangleq \left[\frac{\partial L_{lds}(\cdot)}{\partial i^r_{dr}} - \frac{\partial L_{lds}(\cdot)}{\partial i^r_{ds}}\right] i^r_{ds} - L_{lds}(\cdot)\,, \quad (3.45)$$

$$L_{lqrqr}(\cdot) \triangleq \left[\frac{\partial L_{lqr}(\cdot)}{\partial i^r_{qr}} - \frac{\partial L_{lqr}(\cdot)}{\partial i^r_{qs}}\right] i^r_{qr} + L_{lqr}(\cdot)\,, \quad (3.46)$$

$$L_{ldrdr}(\cdot) \triangleq \left[\frac{\partial L_{ldr}(\cdot)}{\partial i^r_{dr}} - \frac{\partial L_{ldr}(\cdot)}{\partial i^r_{ds}}\right] i^r_{dr} + L_{ldr}(\cdot)\,. \quad (3.47)$$

The dependence on the rate of change of the rotor currents is readily eliminated using (3.19) and (3.20):

$$\left\{1 + \left[\frac{\partial L_{lqs}(\cdot)}{\partial \lambda^r_{mq}} + \frac{\partial L_{lqs}(\cdot)}{\partial i^r_{qs}}\mathbf{\Gamma}_{mi}(\cdot)_{11}\right] i^r_{qs} + L_{lqs}(\cdot)\mathbf{\Gamma}_{mi}(\cdot)_{11}\right\}\frac{d}{dt}\lambda^r_{mq} + \\ + \left\{\left[\frac{\partial L_{lqs}(\cdot)}{\partial \lambda^r_{md}} + \frac{\partial L_{lqs}(\cdot)}{\partial i^r_{qs}}\mathbf{\Gamma}_{mi}(\cdot)_{12}\right] i^r_{qs} + L_{lqs}(\cdot)\mathbf{\Gamma}_{mi}(\cdot)_{12}\right\}\frac{d}{dt}\lambda^r_{md} + \\ + L_{lqsqr}(\cdot)\mathbf{C}_r\mathbf{B}_r e^r_{qr} = \frac{d}{dt}\lambda^r_{qs} - L_{lqsqr}(\cdot)\mathbf{C}_r\mathbf{A}_r\mathbf{x}^r_q\,, \quad (3.48)$$

$$\left\{\left[\frac{\partial L_{lds}(\cdot)}{\partial \lambda^r_{mq}} + \frac{\partial L_{lds}(\cdot)}{\partial i^r_{ds}}\mathbf{\Gamma}_{mi}(\cdot)_{21}\right] i^r_{ds} + L_{lds}(\cdot)\mathbf{\Gamma}_{mi}(\cdot)_{21}\right\}\frac{d}{dt}\lambda^r_{mq} + \\ + \left\{1 + \left[\frac{\partial L_{lds}(\cdot)}{\partial \lambda^r_{md}} + \frac{\partial L_{lds}(\cdot)}{\partial i^r_{ds}}\mathbf{\Gamma}_{mi}(\cdot)_{22}\right] i^r_{ds} + L_{lds}(\cdot)\mathbf{\Gamma}_{mi}(\cdot)_{22}\right\}\frac{d}{dt}\lambda^r_{md} + \\ + L_{ldsdr}(\cdot)\mathbf{C}_r\mathbf{B}_r e^r_{dr} = \frac{d}{dt}\lambda^r_{ds} - L_{ldsdr}(\cdot)\mathbf{C}_r\mathbf{A}_r\mathbf{x}^r_d\,, \quad (3.49)$$

$$\left\{1+\left[\frac{\partial L_{lqr}(\cdot)}{\partial \lambda^r_{mq}}+\frac{\partial L_{lqr}(\cdot)}{\partial i^r_{qs}}\mathbf{\Gamma}_{mi}(\cdot)_{11}\right]i^r_{qr}\right\}\frac{d}{dt}\lambda^r_{mq}+$$
$$+\left[\frac{\partial L_{lqr}(\cdot)}{\partial \lambda^r_{md}}+\frac{\partial L_{lqr}(\cdot)}{\partial i^r_{qs}}\mathbf{\Gamma}_{mi}(\cdot)_{12}\right]i^r_{qr}\frac{d}{dt}\lambda^r_{md}+$$
$$+\left[1+L_{lqrqr}(\cdot)\mathbf{C}_r\mathbf{B}_r\right]e^r_{qr}=-L_{lqrqr}(\cdot)\mathbf{C}_r\mathbf{A}_r\mathbf{x}^r_q\,, \quad (3.50)$$

$$\left[\frac{\partial L_{ldr}(\cdot)}{\partial \lambda^r_{mq}}+\frac{\partial L_{ldr}(\cdot)}{\partial i^r_{ds}}\mathbf{\Gamma}_{mi}(\cdot)_{21}\right]i^r_{dr}\frac{d}{dt}\lambda^r_{mq}+$$
$$+\left\{1+\left[\frac{\partial L_{ldr}(\cdot)}{\partial \lambda^r_{md}}+\frac{\partial L_{ldr}(\cdot)}{\partial i^r_{ds}}\mathbf{\Gamma}_{mi}(\cdot)_{22}\right]i^r_{dr}\right\}\frac{d}{dt}\lambda^r_{md}+$$
$$+\left[1+L_{ldrdr}(\cdot)\mathbf{C}_r\mathbf{B}_r\right]e^r_{dr}=-L_{ldrdr}(\cdot)\mathbf{C}_r\mathbf{A}_r\mathbf{x}^r_d\,. \quad (3.51)$$

The solution of (3.48)–(3.51) yields the time derivatives of two of the state variables (the magnetizing flux linkages λ^r_{mq} and λ^r_{md}) and the rotor admittance voltages e^r_{qr} and e^r_{dr}. These latter quantities may then be used in conjunction with (3.12) and (3.14) to calculate the derivatives of the remaining state variables $\mathbf{x}^r_{qr}$ and $\mathbf{x}^r_{dr}$.

The electromagnetic torque of the motor is given by [84]

$$T_e=\tfrac{3}{2}\tfrac{P}{2}(\lambda^r_{md}i^r_{qs}-\lambda^r_{mq}i^r_{ds}). \quad (3.52)$$

Although this formulation is more complicated than the standard qd-axes induction motor model, it largely retains its computational efficiency (although it can have more states depending on the order of the rotor transfer function). In particular, despite the nonlinearities present, the model is completely noniterative at each time step, unlike several other induction motor models that incorporate magnetic saturation. This was accomplished by virtue of an appropriate choice of state variables as well as through the selection of the functional forms for the magnetizing characteristics.

3.3 Parameter Identification Procedure

The workhorses of induction machine parameter estimation have been the "traditional" rotating no-load and locked-rotor tests [7, 85], from which the parameters of the conventional equivalent circuit (Fig. 3.1) may be obtained. If the machine's design is known, these experiments may also be performed on a computer using finite element analysis [86], since the magnetizing and leakage inductances may be calculated from the electromagnetic field. An alternative experimental technique is the method of voltage step tests, where a dc voltage is switched across the machine terminals [87, 88]. In general, these experimental procedures excite the machine in the low-frequency range only. For high-bandwidth modeling, standstill frequency response testing is required [89, 90].

The above procedures are performed off-line, but a variety of methods have been proposed to track the variation of machine parameters on-line from actual operating data [91–93]. On-line identification is particularly useful for field-oriented controllers, where the rotor's time constant is critical, and where for optimal performance (e.g. in terms of maximum torque per ampere), the dependence of all parameters on saturation must be determined and programmed in the controller's logic [94]. Other techniques for time-domain based parameter estimation for the standard qd-axes model (for instance, using free acceleration transients or other information-rich perturbations) have been reported in [26, 28, 95, 96].

Alternatively, parameters may be extracted from steady-state data, such as families of stator current, input impedance, power, or torque versus slip curves [97, 98]. In large power system level studies, when accurate data are not required or known, the equivalent circuits can be approximated from manufacturers' supplied data, e.g. full-load, locked-rotor and breakdown torque values, power factor, full-load amperes, etc. [99, 100]. When more detailed models are adopted, such as the one depicted in Fig. 3.5, parameter identification becomes more complicated. In these cases, it is

impossible to uniquely identify the models' parameters from external measurements only (voltage, current, speed, torque) [101].

It is common practice to lump all different aspects of the iron's nonlinear behavior under the term "saturation" [102]. However, this is not correct and may lead to significant misconceptions. As far as the permeability is concerned, the following terms need to be differentiated, since they signify two distinct behavioral modes of the iron. The *normal* permeability is the ratio B/H and is usually used in large-signal analyses. Under small-signal excitation, minor hysteresis loops are traversed, and the *incremental* permeability, $\Delta B/\Delta H$, should be used. In general, the incremental permeability is a function of the biasing flux density and it is lower than the corresponding normal permeability. It is customarily defined by joining the tips of the minor loop. Therefore, parameter sets estimated from small-signal tests (such as the frequency response experiment) are not rigorously applicable for large-signal studies. Often, no information is provided in regard to how a parameter set has been obtained. In some cases, the steady-state value of magnetizing inductance is altered, in order to reflect its large-signal saturated value; this procedure is just a "practical synthesis." When only a small-signal parameter set is available, then the analyst has no alternative but to use it. Despite all this, there has been evidence to suggest that small-signal parameter sets perform adequately, even for large-signal disturbances [102].

In this section, a suitable parameter identification procedure for the proposed induction machine model is presented. The procedure consists of a combination of rotating tests (under various loading conditions) and standstill frequency response tests. The superscript "r" denoting the rotor reference frame will be dropped for convenience. The machine under test was a Baldor Vector induction motor, type ZDN4115T, rated for 37.3 kW (50 HP), 460 V, 1775 rpm.

3.3.1 Representation of magnetic characteristics

The proposed functional forms are intentionally general, to allow the maximum degree of freedom to the analyst. However, in order to use the model, specific analytical forms for the magnetic characteristics must be defined. A convenient form to use for the magnetization curve is a rational polynomial, since it can represent a wide range of behaviors and because, unlike a simple polynomial, it can remain bounded as the argument approaches infinity. In particular, $\Gamma_m(\lambda_m)$ is taken to be of the form

$$\Gamma_m(\lambda_m) = \frac{\sum_{i=0}^{O_a} a_i(\lambda_m^2)^i}{\sum_{j=0}^{O_b} b_j(\lambda_m^2)^j}\,. \tag{3.53}$$

The polynomial only contains powers of λ_m^2 in order to obtain an even function in λ_m.

It is also necessary to specify the form of the leakage inductance. The model is again quite flexible in form, but herein a simpler representation based on the following two assumptions is used. Firstly, the leakage inductances are primarily a function of the magnitude of the magnetizing flux linkage. For some applications, this assumption is not warranted. For example, if the model is used to study the line-start of large induction machines, the leakage inductance will saturate based on current. However, in drive applications, where large overcurrents do not typically occur, the leakage inductances are hypothesized to be adequately represented as a function of the magnetizing flux linkage only. This hypothesis is vindicated by the accuracy of the results. Upon making this assumption, it is clear that the leakage inductances of the q- and d-axis are equal.

It will be further assumed that the leakage inductance of the stator and rotor are equal. In the presence of linear magnetics, the appropriation of the leakage inductance to the stator or rotor is irrelevant—there is an infinite number of identical equivalent circuits. In the nonlinear case this is not true, but it is reasonable to

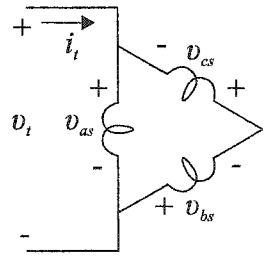

Fig. 3.8. Induction machine test configuration.

expect that the breakdown is not critical [59]. Therefore, it is assumed herein that the stator and rotor leakage inductances are equal, whereupon

$$L_{lqs}(\cdot) = L_{lds}(\cdot) = L_{lqr}(\cdot) = L_{ldr}(\cdot) = L_l(\lambda_m). \tag{3.54}$$

Although the stator and rotor leakage inductances are taken to be equal, part of the rotor leakage inductance is physically represented in $Y_r(s)$. Thus the majority of the leakage inductance is associated with the rotor rather than the stator circuits.

As in the case of the inverse magnetizing inductance, the leakage inductance will be represented as a rational polynomial of the form

$$L_l(\lambda_m) = \frac{\sum_{k=0}^{O_c} c_k(\lambda_m^2)^k}{\sum_{l=0}^{O_d} d_l(\lambda_m^2)^l}. \tag{3.55}$$

3.3.2 Small-signal blocked rotor equivalent circuit

One of the principal experimental tests that will be utilized to characterize the machine is the measurement of the blocked-rotor impedance. For these tests, the machine under test was configured as shown in Fig. 3.8. If the reference frame position is arbitrarily set to be zero, it is readily shown that the test voltage, v_t, and test current, i_t, are related to the stationary q-axis voltages by

$$v_{qs} = v_t\,, \tag{3.56}$$

$$i_{qs} = \tfrac{2}{3} i_t\,. \tag{3.57}$$

In order to measure the small-signal impedance, a dc bias current is used to obtain the appropriate flux level, and the test voltage consists in general of a dc

bias plus a small-signal ac perturbation. Therefore, for the purposes of linearization, variables may be expressed in the form

$$x = x_0 + \Delta x\,. \tag{3.58}$$

The q-axis bias current and the q-axis small-signal input impedance are

$$i_{qs0} = \tfrac{2}{3} i_t\,, \tag{3.59}$$

$$Z_{qs} = \frac{\Delta \tilde{v}_{qs}}{\Delta \tilde{i}_{qs}} = \frac{3}{2}\frac{\Delta \tilde{v}_t}{\Delta \tilde{i}_t}\,, \tag{3.60}$$

respectively; the tilde designates phasor representation. Since all the current is in the q-axis, we have

$$\lambda_m = \lambda_{mq}\,. \tag{3.61}$$

Further, since the dc rotor current i_{dr0} is zero,

$$i_{mq0} = \Gamma_m(\lambda_{mq0})\lambda_{mq0}\,. \tag{3.62}$$

The stage is now set to linearize the dynamic model. First, linearization and Laplace transformation of the q-axis stator and rotor voltage equations (3.7), (3.8), yields

$$\Delta v_{qs} = r_s \Delta i_{qs} + s\Delta\lambda_{qs}\,, \tag{3.63}$$

$$0 = Z_r(s)\Delta i_{qr} + s\Delta\lambda_{qr}\,, \tag{3.64}$$

where $Z_r(s) = 1/Y_r(s)$. Linearization of the flux linkage equations (3.21)–(3.24) yields

$$\Delta\lambda_{qs} = \Delta\lambda_{lqs} + \Delta\lambda_{mq}\,, \tag{3.65}$$

$$\Delta\lambda_{qr} = \Delta\lambda_{lqr} + \Delta\lambda_{mq}\,, \tag{3.66}$$

$$\Delta\lambda_{lqs} = L_l(\lambda_{mq0})\Delta i_{qs} + \frac{\partial L_l(\lambda_{mq0})}{\partial \lambda_m} i_{qs0}\,\Delta\lambda_{mq}\,, \tag{3.67}$$

$$\Delta\lambda_{lqr} = L_l(\lambda_{mq0})\Delta i_{qr}\,, \tag{3.68}$$

where it should be recalled that $i_{qr0} = 0$. Similarly, the linearization of (3.25) yields

$$\Delta\lambda_{mq} = L_{M0}(\Delta i_{qs} + \Delta i_{qr})\,, \tag{3.69}$$

where the incremental inductance is given by

$$L_{M0} = \left[\Gamma_m(\lambda_{mq0}) + \frac{\partial \Gamma_m(\lambda_{mq0})}{\partial \lambda_m}\lambda_{mq0}\right]^{-1} . \tag{3.70}$$

By manipulating these equations, it is readily shown that the small-signal input impedance looking into the q- or the d-axis may be expressed as

$$Z_{qs} = r_s + sL_l(\lambda_{mq0}) + \left[\frac{\partial L_l(\lambda_{mq0})}{\partial \lambda_m} i_{qs0} + 1\right] \frac{sL_{M0}[Z_r(s)+sL_l(\lambda_{mq0})]}{Z_r(s)+s[L_l(\lambda_{mq0})+L_{M0}]} . \tag{3.71}$$

3.3.3 Steady-state equivalent circuit

In addition to the small-signal blocked rotor equivalent circuit, the large-signal equivalent circuit is also valuable for parameter identification purposes. This analysis is valid under the assumption of a fundamental-frequency balanced-set of input voltages.

The derivation begins by noting that the derivative operator in the voltage equations may be replaced by $j(\omega_e - \omega_r)$, since the rotor reference frame is used; ω_e is the electrical frequency and $j = \sqrt{-1}$. Moreover, recall that

$$\tilde{f}_{dx} = j\tilde{f}_{qx} , \tag{3.72}$$

where "x" may be "s" or "r" [5]. With these observations in mind, the steady-state stator voltage equation may be written

$$\tilde{v}_{qs} = r_s\tilde{i}_{qs} + j\omega_e\tilde{\lambda}_{qs} . \tag{3.73}$$

Similarly, the rotor voltage equation becomes

$$0 = Z_r(j\omega_s)\tilde{i}_{qr} + j\omega_s\tilde{\lambda}_{qr} , \tag{3.74}$$

where

$$\omega_s = \omega_e - \omega_r . \tag{3.75}$$

Dividing by the slip,

$$S = \omega_s/\omega_e , \tag{3.76}$$

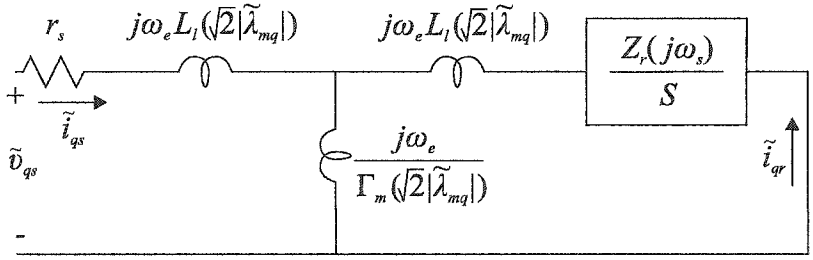

Fig. 3.9. Induction machine steady-state equivalent circuit.

yields

$$0 = \frac{Z_r(j\omega_s)}{S}\tilde{i}_{qr} + j\omega_e\tilde{\lambda}_{qr}\,. \tag{3.77}$$

The flux linkage equations are

$$\tilde{\lambda}_{qs} = \tilde{\lambda}_{lqs} + \tilde{\lambda}_{mq}\,, \tag{3.78}$$

$$\tilde{\lambda}_{qr} = \tilde{\lambda}_{lqr} + \tilde{\lambda}_{mq}\,. \tag{3.79}$$

For balanced, steady-state conditions,

$$\lambda_m = \sqrt{2}|\tilde{\lambda}_{mq}|\,, \tag{3.80}$$

therefore

$$\tilde{\lambda}_{lqs} = L_l(\sqrt{2}|\tilde{\lambda}_{mq}|)\tilde{i}_{qs}\,, \tag{3.81}$$

$$\tilde{\lambda}_{lqr} = L_l(\sqrt{2}|\tilde{\lambda}_{mq}|)\tilde{i}_{qr}\,. \tag{3.82}$$

Finally,

$$\tilde{i}_{mq} = \Gamma_m(\sqrt{2}|\tilde{\lambda}_{mq}|)\tilde{\lambda}_{mq}\,, \tag{3.83}$$

where

$$\tilde{i}_{mq} = \tilde{i}_{qs} + \tilde{i}_{qr}\,. \tag{3.84}$$

Together, these equations suggest the steady-state equivalent circuit of Fig. 3.9.

3.3.4 Measurement of stator flux linkage

The first step in the characterization process is the measurement of the open-circuit stator flux linkage versus magnetizing current. For this study, the machine is fed by a three-phase inverter (at $f_e = 30$ Hz), and driven at synchronous speed. By selecting the time-zero position of the rotor reference frame to be equal to zero, we have $\tilde{f}_{qs} = \tilde{f}_{as}$. From the steady-state model,

$$\tilde{\lambda}_{qs} = \left[L_l(\sqrt{2}|\tilde{\lambda}_{mq}|) + \Gamma_m^{-1}(\sqrt{2}|\tilde{\lambda}_{mq}|)\right] \tilde{i}_{qs} \,. \tag{3.85}$$

Because $\tilde{i}_{mq}$ and $\tilde{\lambda}_{mq}$ are related by (3.83), and because for no-load conditions there is no current flowing in the rotor ($\tilde{i}_{qs} = \tilde{i}_{mq}$), it follows that the above equation can be written in the form

$$\tilde{\lambda}_{qs} = L_{ss}(\sqrt{2}|\tilde{i}_{qs}|)\, \tilde{i}_{qs} \,. \tag{3.86}$$

Hence,

$$|\tilde{\lambda}_{qs,k}| = L_{ss,k}\, |\tilde{i}_{qs,k}| \,, \tag{3.87}$$

where "k" denotes the k-th point in a series of measurements, and where

$$L_{ss,k} = \tfrac{1}{\omega_e} \operatorname{Im}\left\{\tilde{v}_{qs,k}/\tilde{i}_{qs,k}\right\} \,. \tag{3.88}$$

Shown in Fig. 3.10 is a curve representing the best fit to this data, which was determined using quadratic optimization. The test points are plotted as circles. In particular, with the test machine

$$L_{ss}(i) = \frac{9.823 \cdot 10^{-2} + 5.614 \cdot 10^{-4} i^2 + 1.020 \cdot 10^{-7} i^4}{1 + 4.499 \cdot 10^{-3} i^2 + 6.258 \cdot 10^{-6} i^4} \,. \tag{3.89}$$

3.3.5 Measurement of the leakage impedance

The leakage inductance $L_l(\lambda_m)$ is determined by measurement of the blocked-rotor small-signal input impedance, as a function of the q-axis bias current i_{qs0}, using the test set-up depicted in Fig. 3.8. For these conditions, the d-axis is not excited,

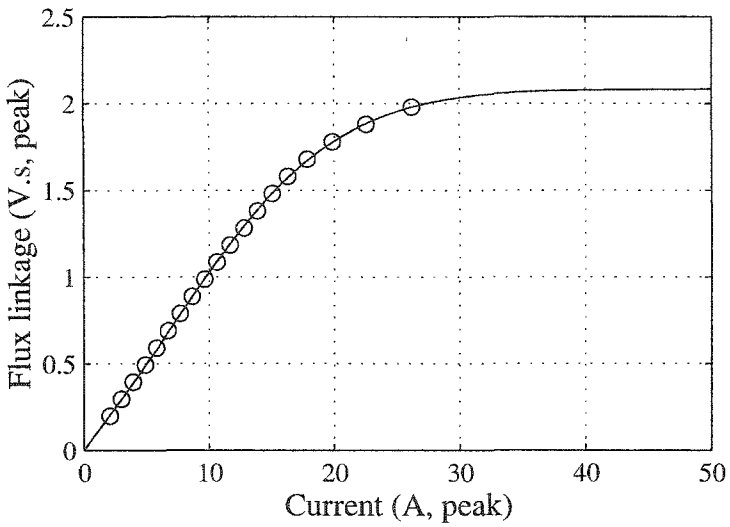

Fig. 3.10. Stator flux linkage versus stator current.

so the q-axis stator current is equal to the magnetizing current, i.e. $i_m = i_{mq} = i_{qs0}$. Moreover, there is no dc current component flowing in the rotor circuits.

The expression for the small-signal input impedance is given by (3.71). However, significant simplification can be made by noting that for practical test conditions

$$\left[\frac{\partial L_l(\lambda_{mq0})}{\partial \lambda_m} i_{qs0} + 1\right] \approx 1, \tag{3.90}$$

and that

$$\frac{sL_{M0}[Z_r(s)+sL_l(\lambda_{mq0})]}{Z_r(s)+s[L_l(\lambda_{mq0})+L_{M0}]} \approx Z_r(s) + sL_l(\lambda_{mq0}), \tag{3.91}$$

whereupon

$$Z_{qs} = r_s + s2L_l(\lambda_{mq0}) + Z_r(s)\,. \tag{3.92}$$

It follows that for a given bias current i_{qs0} the measured leakage inductance may be expressed

$$L_{l,k} = \frac{1}{2\omega_e} \operatorname{Im}\left\{Z_{qs,k} - Z_r(j\omega_e)\right\}, \tag{3.93}$$

where again "k" denotes the k-th data point of this test sequence. In this equation, $Z_r(j\omega_e)$ is unknown. However, its imaginary part may be assigned arbitrarily—subject to the constraint that L_l is always positive. In other words, since these

impedances are in series, moving inductance between Z_r and L_l has little effect on the predictions of the model. For the machine under test, it was assumed that the imaginary part of Z_r was $\mathrm{Im}\{Z_r(j\omega_e)\} = (\omega_e)\,(4.5 \cdot 10^{-3})\ \Omega$, at the frequency used to evaluate the leakage inductance, which was 60 Hz.

It is desirable to characterize $L_{l,k}$ versus the magnetizing flux level. Since there is no dc rotor current, and treating the magnetizing flux as constant, $\lambda_{m,k} = \lambda_{mq0,k}$, we have

$$\lambda_{m,k} = [L_{ss}(i_{qs0,k}) - L_{l,k}]\, i_{qs0,k}\,. \tag{3.94}$$

Rigorously, this expression is not correct. The stator inductance L_{ss} was determined from a large-signal test. On the other hand, $L_{l,k}$ is the incremental inductance from the small-signal blocked rotor test. These quantities are not compatible, and should not be subtracted. However, this operation is not critical since the leakage is small compared to the magnetizing inductance; for the purposes of fitting, we could have completely ignored L_l, or have it set to an arbitrary small value. This compromise is justified by our lack of information about the large-signal leakage inductance.

The best fit to a rational polynomial of L_l versus λ_m is depicted in Fig. 3.11. In the fitting procedure it is important to insure that the leakage inductance function is well behaved for all values of λ_m within a reasonable range. The result was

$$L_l(\lambda_m) = (2.132 \cdot 10^{-3})/(1 + 0.7327\lambda_m^2 - 0.3621\lambda_m^4 + 0.1209\lambda_m^6)\,. \tag{3.95}$$

From this it can be readily established that the maximum value of $\left|\frac{\partial L_l(\lambda_{mq0})}{\partial \lambda_m} i_{qs0}\right|$ is 0.025 for the data points considered, so the assumption (3.90) is valid.

Although the model requires the formulation of the leakage inductance as a function of magnetizing flux linkage, it will be convenient for characterization purposes to express it as a function of magnetizing current also. To this end, Fig. 3.12 depicts L_l versus i_m, where

$$L_l(i_m) = (2.129 \cdot 10^{-3})/(1 + 6.558 \cdot 10^{-3} i_m^2 - 1.966 \cdot 10^{-5} i_m^4 + 5.210 \cdot 10^{-8} i_m^6)\,. \tag{3.96}$$

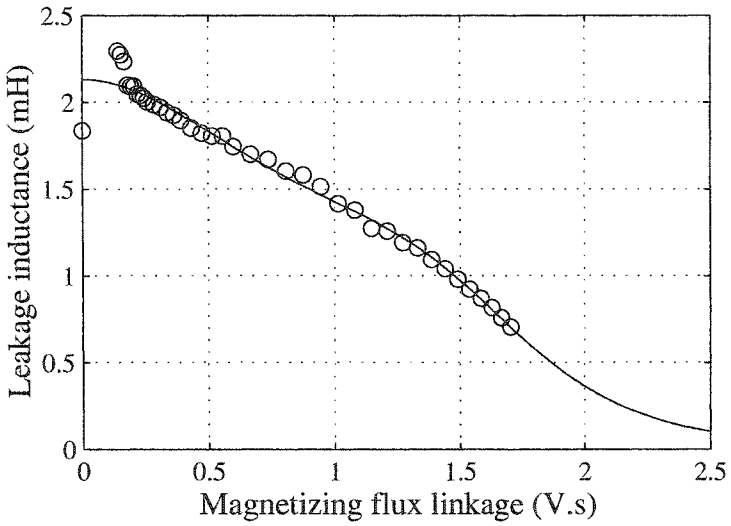

Fig. 3.11. Leakage inductance versus magnetizing flux.

Notice that the equality $L_l(\lambda_m = 0) = L_l(i_m = 0)$ was not strictly enforced during the fitting procedure; this is reflected by the slightly different numerator coefficient. This small discrepancy does not compromise the accuracy of the analysis.

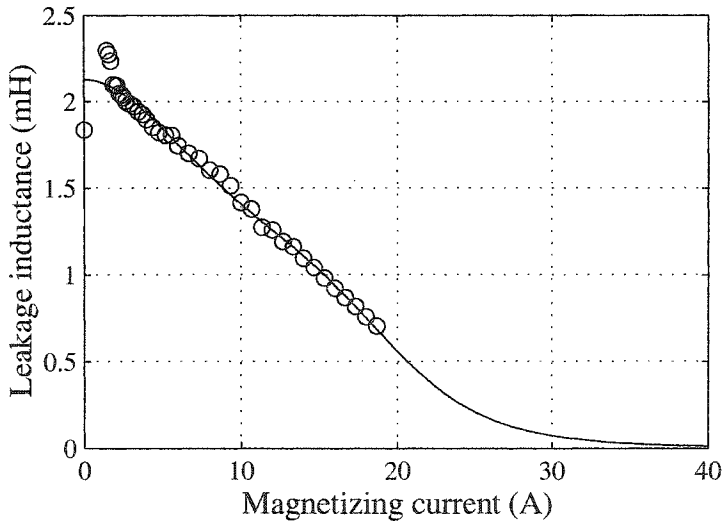

Fig. 3.12. Leakage inductance versus magnetizing current.

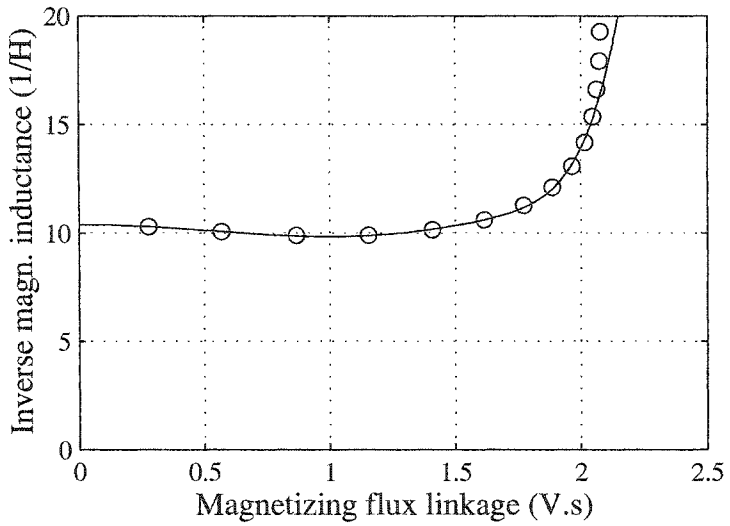

Fig. 3.13. Inverse magnetizing inductance versus magnetizing flux linkage.

3.3.6 Calculation of the magnetizing flux linkage

The next step in the development is the calculation of the function $\Gamma_m(\lambda_m)$. This is done by performing an artificial no-load test, in which the q-axis stator current is varied between zero and some value (close to rated); let the virtual test currents be denoted as $i_{qs,k}$. Keeping in mind the underlying assumptions of (3.94), the functions (3.89) and (3.96) are used to calculate the magnetizing flux

$$\lambda_{mq,k} = [L_{ss}(i_{qs,k}) - L_l(i_{qs,k})]\, i_{qs,k}\,. \tag{3.97}$$

Then,

$$\Gamma_{m,k} = i_{qs,k}/\lambda_{mq,k}\,. \tag{3.98}$$

The fictitious data points along with the best fit to a rational polynomial,

$$\Gamma_m(\lambda_m) = \frac{10.39 - 4.704\lambda_m^2 + 1.648\lambda_m^4 - 0.4258\lambda_m^6 + 4.717\cdot 10^{-2}\lambda_m^8}{1 - 0.3373\lambda_m^2 + 5.088\cdot 10^{-2}\lambda_m^4 - 7.319\cdot 10^{-3}\lambda_m^6 + 7.897\cdot 10^{-4}\lambda_m^8}\,, \tag{3.99}$$

are plotted in Fig. 3.13.

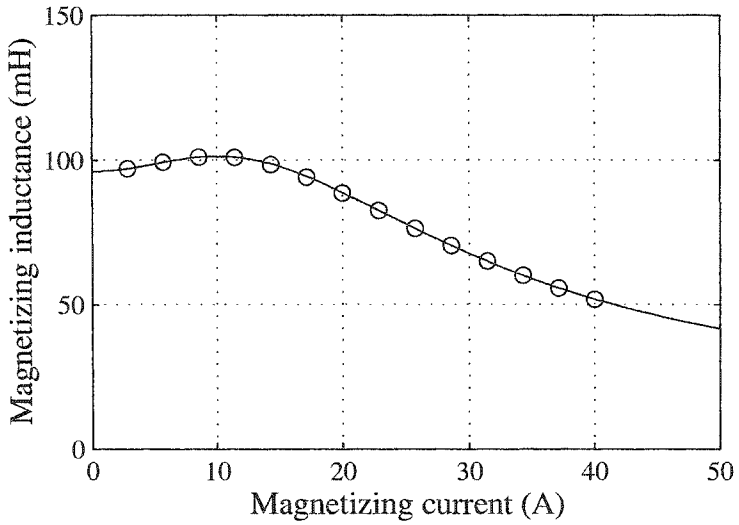

Fig. 3.14. Magnetizing inductance versus magnetizing current.

It is also convenient at this point to derive the magnetizing inductance versus magnetizing current fit, that will be used later. The result,

$$L_m(i_m) = \frac{9.613 \cdot 10^{-2} + 5.478 \cdot 10^{-4} i_m^2 + 9.963 \cdot 10^{-8} i_m^4}{1 + 4.375 \cdot 10^{-3} i_m^2 + 6.113 \cdot 10^{-6} i_m^4 + 1.429 \cdot 10^{-13} i_m^6}\,, \tag{3.100}$$

is plotted in Fig. 3.14. Notice that the equality $\Gamma_m(\lambda_m = 0) = [L_m(i_m = 0)]^{-1}$ was not enforced, since $(9.613 \cdot 10^{-2})^{-1} = 10.40$, but this difference is insignificant. The contribution of the denominators' last term for all reasonable values of current may also be safely neglected, due to its very small coefficient.

3.3.7 Measurement of the low-frequency rotor impedance

In order to characterize the low-frequency rotor impedance, one straightforward method is to operate the machine at a given voltage and allow the slip to vary. This procedure is similar to the one discussed in [103]. From the steady-state equations,

$$j\omega_e \tilde{\lambda}_{mq} = \tilde{v}_{qs} - [r_s + j\omega_e L_l(\lambda_m)]\,\tilde{i}_{qs}\,. \tag{3.101}$$

For the k-th value of slip, S_k, equating the magnitudes of both sides yields

$$\omega_e \lambda_{m,k} = \sqrt{2}\,|\tilde{v}_{qs,k} - [r_s + j\omega_e L_l(\lambda_{m,k})]\,\tilde{i}_{qs,k}|\,, \tag{3.102}$$

where $\lambda_m = \sqrt{2}|\lambda_{mq}|$. This equation can be solved numerically for $\lambda_{m,k}$. Note that the varying-slip experiment creates large disturbances in the rotor, so that, once more, the usage of the incremental leakage inductance is not rigorously correct. The stator resistance of the machine under test was $r_s = 0.22\,\Omega$. The rotor impedance may be calculated from

$$\frac{Z_{r,k}}{S_k} = \frac{j\omega_e \left[\frac{\tilde{v}_{qs,k}}{\tilde{i}_{qs}} - r_s - j\omega_e L_l(\lambda_{m,k})\right]}{j\omega_e - \Gamma_m(\lambda_{m,k})\left[\frac{\tilde{v}_{qs,k}}{\tilde{i}_{qs}} - r_s - j\omega_e L_l(\lambda_{m,k})\right]} - j\omega_e L_l(\lambda_{m,k})\,, \tag{3.103}$$

and the result will be written as a resistance in series with an inductance, i.e.

$$Z_r(j\omega_s) = R_r(\omega_s) + j(\omega_s)L_r(\omega_s)\,. \tag{3.104}$$

The set of values $\left\{f_{s,k}\left(=\frac{\omega_{s,k}}{2\pi}\right), R_{r,k}, L_{r,k}\right\}$ taken during this test procedure is depicted in Fig. 3.15. (For this experiment, the voltage frequency was $f_e = 30.2$ Hz. Since rated slip is $s_{\text{rated}} = (1800 - 1775)/1800 \approx 0.0139$, the rated value of slip frequency is $f_{s,\text{rated}} = s_{\text{rated}} f_e \approx 0.42$ Hz.) As can be seen, at very low frequencies (less than 0.15 Hz), the inductance values are negative. Clearly, at this end the inductance data is unreliable, primarily because the reactance is low compared to the resistance. At a frequency of 0.3 Hz this is no longer a problem, and both resistance and inductance are relatively constant. Ideally, a larger range of slip values would be included in this test. However, the current becomes prohibitively high at larger slips.

Once this data is collected, it could be used to fit a transfer function to the impedance $Z_r(s)$, that would be important in predicting the fundamental component of the waveform. On the other hand, since the data is confined to very low frequencies, it is not sufficient to represent the high-frequency behavior, i.e. the switching-frequency dynamics. Such data is collected using a separate test procedure as described in the next section.

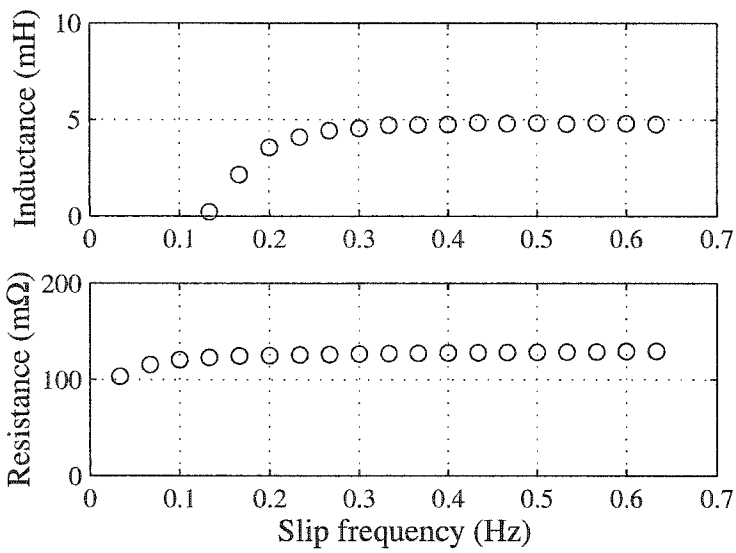

Fig. 3.15. Low-frequency rotor impedance.

3.3.8 Measurement of high-frequency rotor impedance

To measure the rotor impedance at high frequency, it is convenient to perform a standstill frequency response test. The machine is configured as shown in Fig. 3.8; the slip at standstill is unity. From the small-signal input impedance equation, using the approximation (3.90), the rotor impedance may be expressed as

$$Z_{r,k} = \frac{j\omega_{e,k}L_{M0}(i_{qs0,k})\left[Z_{qs,k} - r_s - j\omega_{e,k}L_l(i_{qs0,k})\right]}{j\omega_{e,k}L_{M0}(i_{qs0,k}) - \left[Z_{qs,k} - r_s - j\omega_{e,k}L_l(i_{qs0,k})\right]} - j\omega_{e,k}L_l(i_{qs0,k}). \qquad (3.105)$$

The incremental inductance as a function of current differs from the expression (3.70). In this case, it is given by

$$L_{M0}(i_{qs0,k}) = L_m(i_{qs0,k}) + \frac{dL_m(i_{qs0,k})}{di_m}\, i_{qs0,k}\,, \qquad (3.106)$$

where the previously derived fit of (3.100) is now used.

The high-frequency test results are depicted in Fig. 3.16. Two data sets were taken. The first set was taken with a bias current of $i_{qs0} = 14$ A. The second set was taken with a bias current of $i_{qs0} = 27$ A (rated flux is obtained with $i_{qs0} \approx 19$ A). The upper plot depicts the computed rotor inductance, as well as the total input

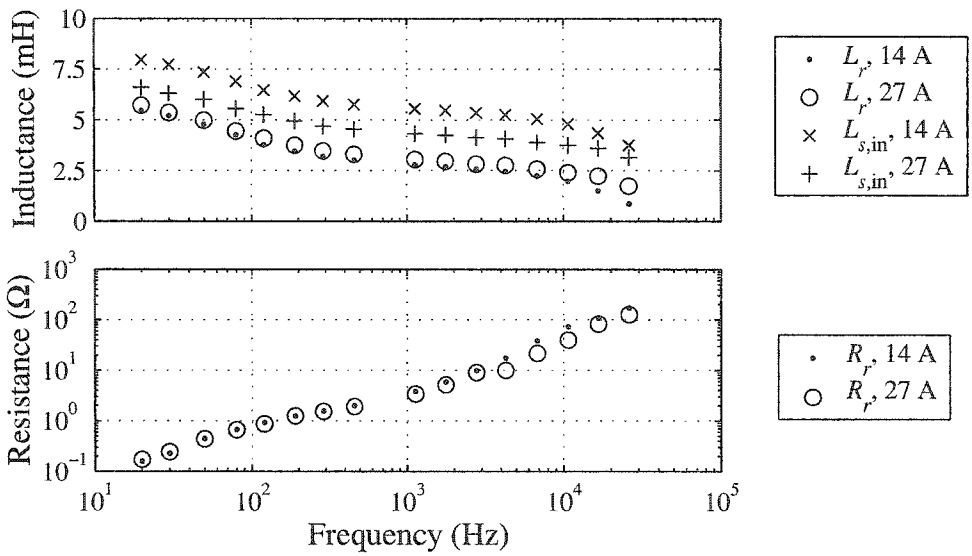

Fig. 3.16. High-frequency rotor impedance.

inductance (at the stator terminals) for the two tests; the lower plot depicts the rotor resistance. As can be seen, the input inductance varies considerably depending upon the flux level, with the higher value of flux yielding the lower apparent inductance. However, it is interesting to observe that the rotor inductance for the two data sets is much closer together. Ideally, they should be identical. This fact does support the ability of the model to incorporate the complicated relationship between flux level, impedance, and frequency. As can also be seen, the resistance points are very close for the two flux levels, over most of the frequency range.

3.3.9 Calculation of the rotor admittance transfer function

The final step in the analysis is the determination of the rotor admittance transfer function. This will be constructed by concatenating the low-frequency with the high-frequency rotor impedance data. The rotor admittance for the k-th point of the set is given by

$$Y_{r,k} = (R_{r,k} + j\omega_{e,k}L_{r,k})^{-1} \ . \tag{3.107}$$

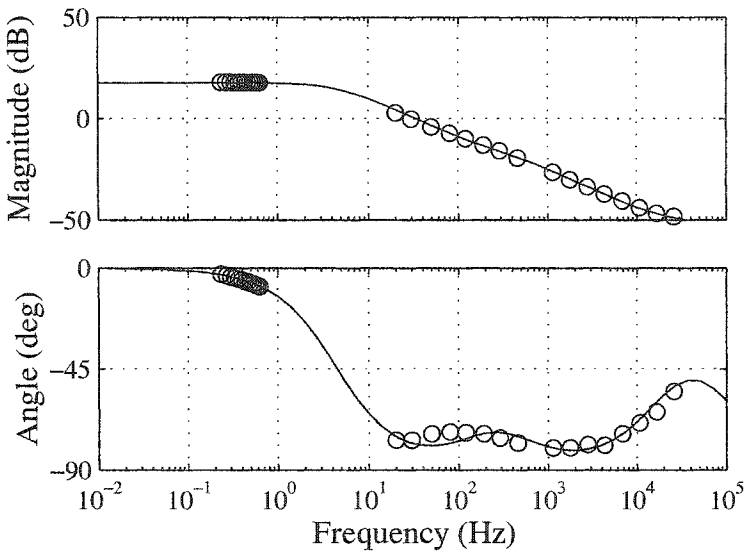

Fig. 3.17. Rotor admittance magnitude (in $\mathrm{dB}\Omega^{-1}$) and phase.

A question arises as to which data set to use for the high-frequency part. For the study herein, the two data sets were simply averaged. However, since best-fit techniques are used to capture the impedance, another approach would have been to simply use both sets of data in the curve fitting procedure. The magnitude and phase of the rotor admittance points, as well as the fitted curve to the frequency response,

$$Y_r(s) = 7.656 \frac{1 + 7.931 \cdot 10^{-4} s + 6.371 \cdot 10^{-9} s^2}{1 + 3.638 \cdot 10^{-2} s + 1.644 \cdot 10^{-5} s^2 + 2.892 \cdot 10^{-11} s^3}, \tag{3.108}$$

are depicted in Fig. 3.17. Note that the stability properties of the computed transfer function must be verified, to ensure that there exist no poles in the right-hand plane.

3.4 Experimental Validation

The predictions of a standard *qd*-axes induction motor model [5] and the model set forth herein were compared with measured waveforms for our four-pole, 460-V, 37-kW, 60-Hz induction motor drive. The inverter was fed from an 800-V dc bus. The modulation strategy used was third harmonic sine-triangle, wherein the amplitude of the third harmonic injection was one sixth of that of the fundamental, and the carrier frequency was 4.88 kHz. The IGBT and diode voltage drops were taken as constants of approximately 1.9 V and 1.3 V, respectively. The delay times from a commanded turn-on of an IGBT to the time it started turning on, and from the commanded turn-off of an IGBT to the time it begins to actually turn off, were 4.35 μs and 2.52 μs, respectively. The turn-on and turn-off times were 145 ns and 320 ns, respectively. The commanded voltage and frequency were 464 V, line-to-line (fundamental rms), and 60 Hz, respectively. For the study shown, the speed was 1790 rpm.

The performance as predicted by the standard *qd*-axes model is depicted in Fig. 3.18. The parameters were obtained from no-load and blocked-rotor tests and were found to be $r_s = 0.22\,\Omega$, $L_{ls} = L'_{lr} = 3.63\,\text{mH}$, $L_M = 88.7\,\text{mH}$ and $r'_r = 0.14\,\Omega$. These values reflect the machine in a relatively cold state, and all studies were conducted at a relatively cold state as well. Variables depicted include the *c*-phase inverter current, the *c*-phase current ripple (the phase current less its fundamental component), the per unit *c*-phase ripple current spectrum (the base current is 67 A), the electromagnetic torque, and the per unit electromagnetic torque ripple spectrum (the base torque is 200 N·m).

The measured performance is illustrated in Fig. 3.19. Therein the air-gap torque was obtained from (3.52), where the variables were calculated by post-processing recorded terminal voltage and current waveforms. Comparing Fig. 3.19 to Fig. 3.18, it is evident that the classical *qd*-axes model drastically underestimates both the peak current and torque ripple by a factor of approximately 1.5–5 over the entire

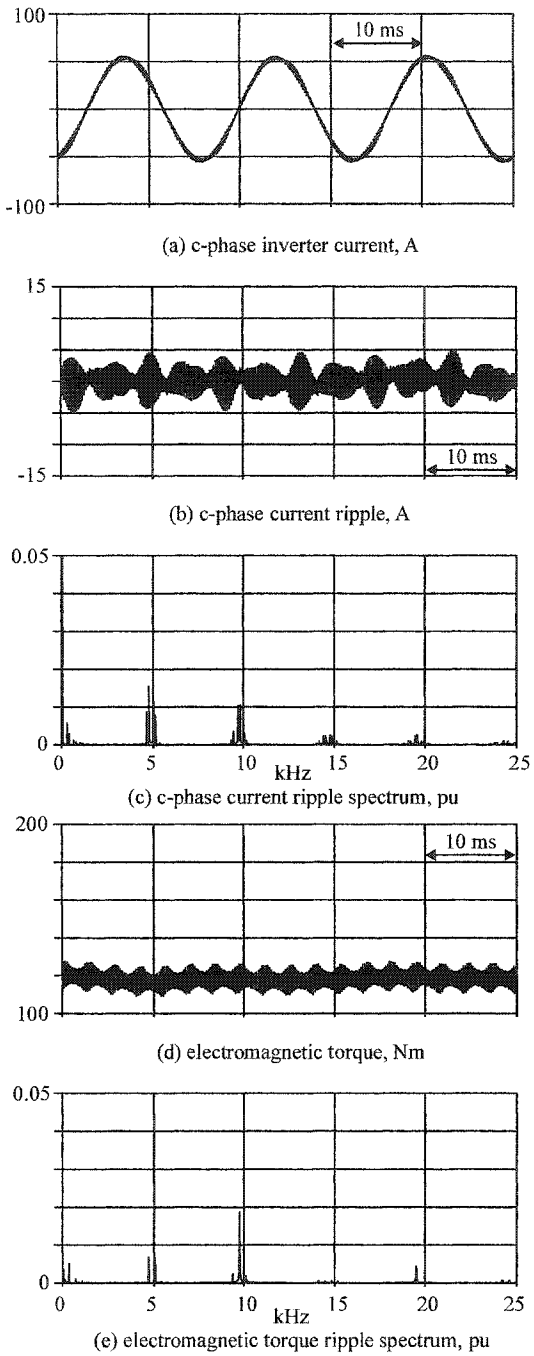

Fig. 3.18. Drive performance predicted by standard model.

frequency range. In addition, the classical model is in error in its prediction of the average torque by approximately 20 N·m. Clearly, the validity of using the standard model to evaluate the power converter/modulator strategy performance or to choose a switching frequency based on the current or torque ripple level requirements is highly questionable.

The performance of the machine as predicted by the proposed model is shown in Fig. 3.20. It can be seen that the performance of the machine and the average torque are much more accurately predicted, over the entire frequency range depicted. The most evident differences between the simulated and predicted waveforms are in low-frequency (less than 2 kHz) spatial effects, such as the 120-Hz component of the torque, which are not represented in this model. The accuracy of the proposed model, both in terms of the fundamental component of the applied waveforms, as well as in terms of switching frequency components, make it ideal to use for combined converter, supervisory control, switch level (modulation) control, and machine simulations.

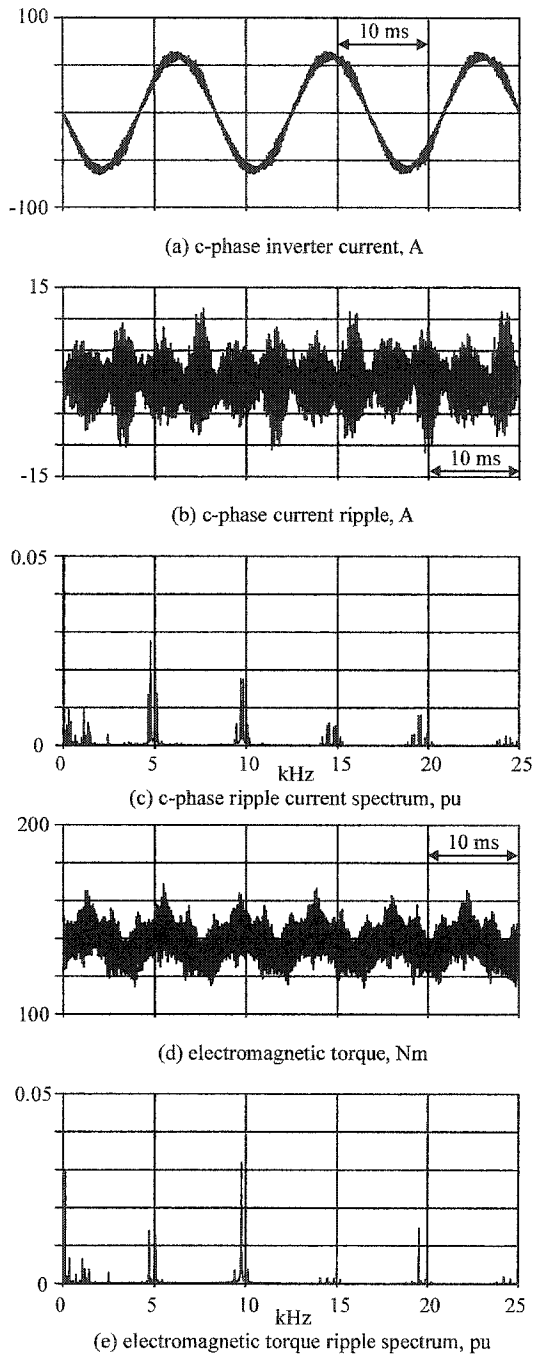

Fig. 3.19. Drive performance as measured.

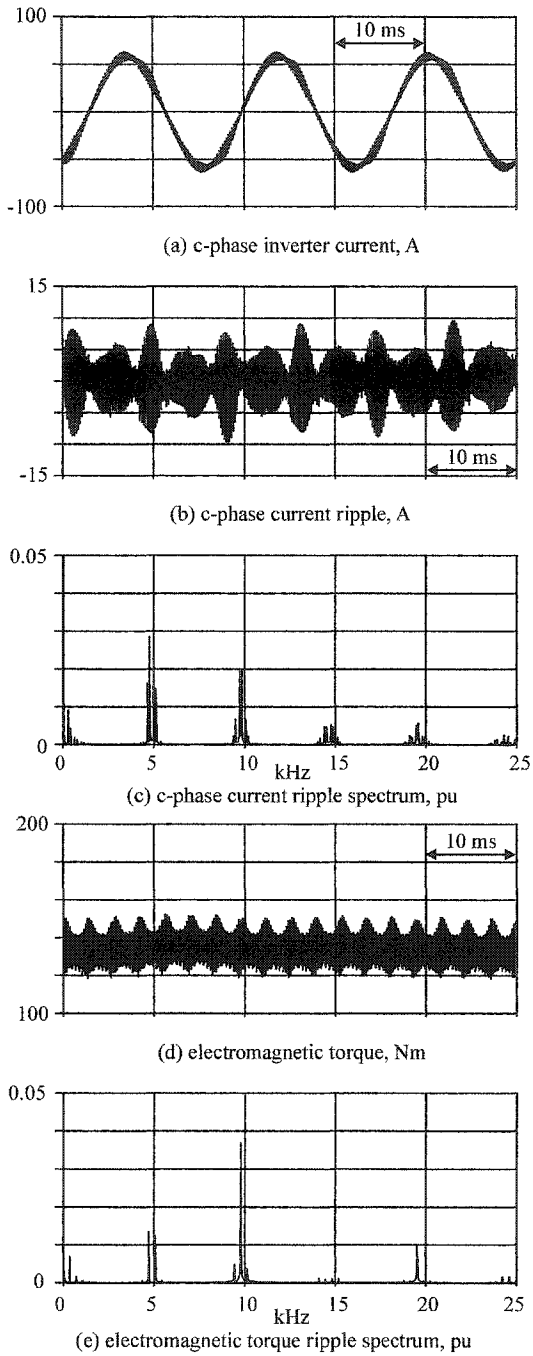

Fig. 3.20. Drive performance as predicted by the proposed model.

3.5 Magnetic Energy Considerations

In this section, the energy storage in the coupling and leakage fields of the proposed induction machine model will be investigated. It will be shown that the coupling field satisfies the conditions of a conservative field. However, the stator and rotor leakage fields are not conservative; this causes an amount of energy to be lost or gained when the states trace an arbitrary closed trajectory.

3.5.1 Math background

We begin by stating the following theorems. For detailed proofs, the reader is referred to any textbook on multi-variable calculus, such as [104].

Theorem 1 *Let* $\mathbf{F} : D \rightarrow \mathbb{R}^n$ *be a vector field, with components* $\mathbf{F}_1, \ldots, \mathbf{F}_n$, *that are continuous throughout some connected region* D *of* $\mathbb{R}^n$, *and* $d\mathbf{R} = [dx_1 \cdots dx_n]^T$. *Then a necessary and sufficient condition for the integral*

$$\int_A^B \mathbf{F} \cdot d\mathbf{R} \tag{3.109}$$

to be independent of the path joining the points A *and* B *is the existence of a differentiable function* f *such that*

$$\mathbf{F} = \nabla f = \left[\frac{\partial f}{\partial x_1} \cdots \frac{\partial f}{\partial x_n} \right]^T \tag{3.110}$$

throughout D.

The independence of the above integral from the path of integration is the defining property of a *conservative* field. If $\mathbf{F}$ has continuous first-order partial derivatives, we can state the following theorem:

Theorem 2 *A necessary and sufficient condition for*

$$\mathbf{F} = \nabla f \tag{3.111}$$

is

$$\frac{\partial \mathbf{F}_i}{\partial x_j} = \frac{\partial \mathbf{F}_j}{\partial x_i}\,, \tag{3.112}$$

for all i, j, that is, the Jacobian matrix of $\mathbf{F}$ is symmetric.

3.5.2 Coupling field

It will be proven that the coupling field is conservative. In other words, the magnetic energy stored in the coupling field is a function of the machine's state only, as defined by the magnetizing flux vector $\boldsymbol{\lambda}^r_{mqd}$. (The remaining states of the model, $\mathbf{x}^r_{qr}$, $\mathbf{x}^r_{dr}$, have no effect on the coupling field energy.)

The electric power supplied to the coupling field is equal to the input power, minus the power lost in the stator resistance, minus the power that supplies the stator and rotor leakage fields, minus the power that is dissipated or stored inside the rotor admittance block (see Fig. 3.7). After manipulation, the electric power supplied to the coupling field may be expressed as

$$P_e = \tfrac{3}{2}\omega_r \left(i^r_{qs}\lambda^r_{md} - i^r_{ds}\lambda^r_{mq}\right) + \tfrac{3}{2}\left(i^r_{mq}\tfrac{d}{dt}\lambda^r_{mq} + i^r_{md}\tfrac{d}{dt}\lambda^r_{md}\right). \tag{3.113}$$

The electrical energy provided to the coupling field is partly stored, and the rest is transferred to the mechanical system. If W_f denotes the coupling field energy and T_e the electromagnetic torque, then the power balance may be written as

$$P_e = \tfrac{d}{dt}W_f + T_e\omega_{rm}\,, \tag{3.114}$$

where the product $T_e\omega_{rm}$ is positive for motor action.

Equating (3.113) and (3.114), and solving for the rate of change of the field energy yields

$$\tfrac{d}{dt}W_f = \left[\tfrac{3}{2}\left(i^r_{qs}\lambda^r_{md} - i^r_{ds}\lambda^r_{mq}\right) - T_e\tfrac{2}{P}\right]\tfrac{d}{dt}\theta_r + \left(\tfrac{3}{2}i^r_{mq}\right)\tfrac{d}{dt}\lambda^r_{mq} + \left(\tfrac{3}{2}i^r_{md}\right)\tfrac{d}{dt}\lambda^r_{md}\,. \tag{3.115}$$

In view of the torque equation (3.52), the first term equals zero, so the differential change of the coupling field energy may be written as

$$dW_f = \tfrac{3}{2}i^r_{mq}\,d\lambda^r_{mq} + \tfrac{3}{2}i^r_{md}\,d\lambda^r_{md}\,. \tag{3.116}$$

By Theorems 1 and 2 (in this case, the vector field is $\mathbf{F} = \frac{3}{2}\left[i^r_{mq}, i^r_{md}\right]^T$, and the independent variables are $\mathbf{x} = \left[\lambda^r_{mq}, \lambda^r_{md}\right]^T$), the coupling field is conservative if and only if

$$\frac{\partial i^r_{mq}}{\partial \lambda^r_{md}} = \frac{\partial i^r_{md}}{\partial \lambda^r_{mq}} \,. \tag{3.117}$$

For the assumed functional forms of the magnetizing currents (3.25), equation (3.117) does indeed hold, as can be readily verified after performing the necessary algebraic manipulations. Therefore, the coupling field is conservative.

3.5.3 Leakage fields

The stator and rotor leakage fields are *not* conservative. This is proved analytically for the rotor leakage field; on the other hand, the equations for the stator leakage field become intractable. However, the non-conservative nature of both fields will be demonstrated through computer simulations. This inconsistency of the proposed model is not critical. The energy that is lost or gained in the leakage fields is negligible compared to the mechanical energy or the energy dissipated in the stator winding resistance.

The power flowing into the rotor leakage field (specifically, the saturating leakage components of both axes) is

$$P_{lr} = \tfrac{3}{2}\left(i^r_{qr}\tfrac{d}{dt}\lambda^r_{lqr} + i^r_{dr}\tfrac{d}{dt}\lambda^r_{ldr}\right). \tag{3.118}$$

Substituting the following relations in (3.118),

$$i^r_{qr} = \mathbf{C}_r\mathbf{x}^r_{qr}\,,\; i^r_{dr} = \mathbf{C}_r\mathbf{x}^r_{dr}\,, \tag{3.119}$$

$$\lambda^r_{lqr} = L_l(\lambda_m)\, i^r_{qr}\,,\; \lambda^r_{ldr} = L_l(\lambda_m)\, i^r_{dr}\,, \tag{3.120}$$

$$\lambda_m = \sqrt{(\lambda^r_{mq})^2 + (\lambda^r_{md})^2}\,, \tag{3.121}$$

and performing the differentiation with respect to time yields

$$\begin{aligned} P_{lr} = {} & \left\{\tfrac{3}{2}\tfrac{\lambda^r_{md}}{\lambda_m}\tfrac{dL_l(\lambda_m)}{\lambda_m}\, i^2_r\right\}\tfrac{d}{dt}\lambda^r_{md} + \left\{\tfrac{3}{2}\tfrac{\lambda^r_{mq}}{\lambda_m}\tfrac{dL_l(\lambda_m)}{\lambda_m}\, i^2_r\right\}\tfrac{d}{dt}\lambda^r_{mq} + \\ & + \left\{\tfrac{3}{2}(\mathbf{C}_r\mathbf{x}^r_{qr})L_l(\lambda_m)\right\}\mathbf{C}_r\tfrac{d}{dt}\mathbf{x}^r_{qr} + \left\{\tfrac{3}{2}(\mathbf{C}_r\mathbf{x}^r_{dr})L_l(\lambda_m)\right\}\mathbf{C}_r\tfrac{d}{dt}\mathbf{x}^r_{dr}\,, \end{aligned} \tag{3.122}$$

where $i^2_r = (i^r_{qr})^2 + (i^r_{dr})^2$.

To prove that the field is not conservative, it suffices to show that one of the symmetry conditions of Theorem 2 does not hold. We will consider the "interaction" between $\frac{d}{dt}\lambda^r_{md}$ and the j-th component of the vector $\frac{d}{dt}\mathbf{x}^r_{qr}$. Hence,

$$\frac{\partial F_{\lambda^r_{md}}}{\partial x^r_{qr,j}} = \frac{3}{2}\frac{\lambda^r_{md}}{\lambda_m}\frac{dL_l(\lambda_m)}{\lambda_m}\left(2i_r\frac{\partial i_r}{\partial x^r_{qr,j}}\right) = 3\frac{\lambda^r_{md}}{\lambda_m}\frac{dL_l(\lambda_m)}{\lambda_m}\, i_r\left(\frac{\partial i_r}{\partial i^r_{qr}}\frac{\partial i^r_{qr}}{\partial x^r_{qr,j}} + \frac{\partial i_r}{\partial i^r_{dr}}\frac{\partial i^r_{dr}}{\partial x^r_{qr,j}}\right) =$$

$$= 3\frac{\lambda^r_{md}}{\lambda_m}\frac{dL_l(\lambda_m)}{\lambda_m}\, i_r\frac{i^r_{qr}}{i_r}C_{r,j} = 3\frac{\lambda^r_{md}}{\lambda_m}\frac{dL_l(\lambda_m)}{\lambda_m} i^r_{qr}C_{r,j}\,, \quad (3.123)$$

where $C_{r,j}$ is the j-th component of the vector $\mathbf{C}_r$. Also,

$$\frac{\partial F_{x^r_{qr,j}}}{\partial \lambda^r_{md}} = C_{r,j}\,\frac{3}{2}\,i^r_{qr}\,\frac{\partial L_l(\lambda_m)}{\partial \lambda^r_{md}} = C_{r,j}\,\frac{3}{2}\,i^r_{qr}\,\frac{dL_l(\lambda_m)}{\lambda_m}\frac{\lambda^r_{md}}{\lambda_m}\,. \quad (3.124)$$

Clearly, $\frac{\partial F_{\lambda^r_{md}}}{\partial x^r_{qr,j}} \neq \frac{\partial F_{x^r_{qr,j}}}{\partial \lambda^r_{md}}$ (they differ by a factor of two), hence the rotor leakage field is not conservative.

3.5.4 A computer simulation study of the coupling and leakage fields

The conservative nature of the coupling field, and the non-conservative nature of the leakage fields are illustrated through a computer simulation (Fig. 3.21). The induction motor is initially at rest. At $t = 0$, it is connected to a voltage source (460 V, line-to-line, rms) and is freely accelerated to synchronous speed (the load torque is assumed zero, and the system inertia is arbitrarily set to $J = 1$ Kg·m^2). Then, after an equilibrium has been reached, a three-phase short-circuit is applied at the machine terminals (at $t = 1.5$ s).

During this transient, all the machine states trace a closed trajectory that starts and ends at the origin. The various field energies are computed as follows: [1]

$$W_{ls} = \frac{3}{2}\int_0^t \left(i^r_{qs}\frac{d}{d\tau}\lambda^r_{lqs} + i^r_{ds}\frac{d}{d\tau}\lambda^r_{lds}\right)\, d\tau\,, \quad (3.125)$$

$$W_{lr} = \frac{3}{2}\int_0^t \left(i^r_{qr}\frac{d}{d\tau}\lambda^r_{lqr} + i^r_{dr}\frac{d}{d\tau}\lambda^r_{ldr}\right)\, d\tau\,, \quad (3.126)$$

[1] The component of energy supplied to the stator leakage field through the voltage terms arising from the transformation to the rotor reference frame turns out to be zero. To see this, substitute $\lambda^r_{lds} = L_l(\lambda_m)\, i^r_{ds}$ and $\lambda^r_{lqs} = L_l(\lambda_m)\, i^r_{qs}$ into $\frac{3}{2}\omega_r(i^r_{qs}\lambda^r_{lds} - i^r_{ds}\lambda^r_{lqs})$.

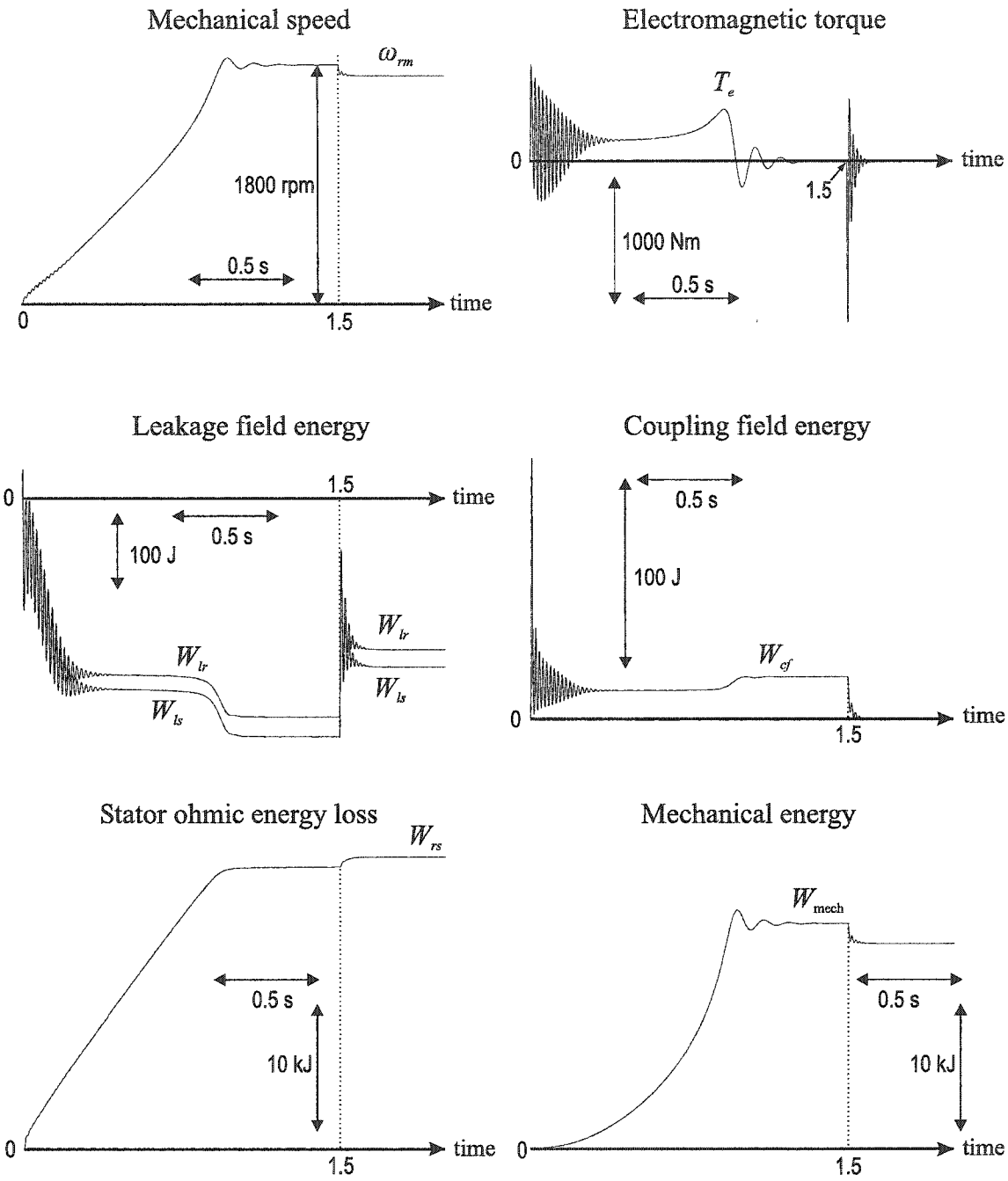

Fig. 3.21. Magnetic field energy study.

$$W_{cf} = \frac{3}{2}\int_0^t \left(i^r_{mq}\frac{d}{d\tau}\lambda^r_{mq} + i^r_{md}\frac{d}{d\tau}\lambda^r_{md}\right)\,d\tau\,, \tag{3.127}$$

$$W_{rs} = \frac{3}{2}\int_0^t r_s\left[\left(i^r_{qs}\right)^2 + \left(i^r_{ds}\right)^2\right]d\tau\,, \tag{3.128}$$

$$W_{\text{mech}} = \int_0^t \left(T_e\omega_{rm}\right)d\tau\,. \tag{3.129}$$

The results plotted in Fig. 3.21 reveal that the coupling field does not consume energy overall, because the energy used to establish it is fully returned to the system at the end of the study ($\Delta W_{cf} = 0$). This is in accordance with the theoretically predicted conservative nature of the coupling field.

However, the behavior of the leakage fields is unpredictable. First, note that the leakage field energy in this study became negative, which would not have been true under the assumption of a linear leakage inductance, where leakage field energy is always positive. [2] Moreover, since the net energy supply is negative ($\Delta W_{lr} \approx -199$ J, $\Delta W_{ls} \approx -222$ J), the leakage fields provided energy back to the system, which is physically impossible. This confirms the hypothesis of a nonconservative stator leakage field, and verifies the analysis for the rotor leakage field.

A word of caution is deemed necessary at this point, since it is not appropriate to compare the leakage field energies with the coupling field energy. For example, one might wonder how it is possible for the leakage energy to be greater (in absolute value terms) than the coupling field energy. The conservative nature of the coupling field implies that W_{cf} corresponds to an energy that is actually stored in the coupling field and is thus fully retrievable. On the other hand, W_{ls} and W_{lr} should not be interpreted as stored energies. Rather, they merely reflect energy consumed or supplied by the nonconservative leakage elements of the proposed model.

Nevertheless, compared to the energy dissipated by the stator resistance and the energy transferred to the shaft, the amount of energy that is gained from the leakage fields is negligible (a few hundred versus several thousand joules). The dynamics of

[2] To see this, substitute $\boldsymbol{\lambda}^r_{lqds} = L^{\text{lin}}_l\,\mathbf{i}^r_{qds}$, $\boldsymbol{\lambda}^r_{lqdr} = L^{\text{lin}}_l\,\mathbf{i}^r_{qdr}$, into (3.125), (3.126), and integrate: $W_{ls} = \frac{3}{2}\frac{1}{2}L^{\text{lin}}_l\,i^2_s > 0$, $W_{lr} = \frac{3}{2}\frac{1}{2}L^{\text{lin}}_l\,i^2_r > 0$.

the system are not seriously affected by the leakage energy. Hence, this inconsistency has only a minor effect on overall system performance.

3.6 Summary

The proposed induction motor model is particularly useful in predicting switching frequency effects. It represents stator and rotor leakage saturation, magnetizing axis saturation, and distributed effects in the rotor circuits, using highly general functional forms. The simultaneous incorporation of these effects, and the high degree of computational efficiency (since the model is non-iterative at each time step) set it apart from other work in this area. Its relative computational speed and the fact that it is readily tied to power electronic converter and controls models make it ideal for studying power-converter/machine interaction as well as other aspects of drive performance, such as the effectiveness of supervisory controls.

A set of analytical forms for the leakage and magnetizing characteristics of the induction machine model has been set forth. Based on these, the standstill small-signal and rotating steady-state large-signal models have been derived and used to facilitate an experimental method of measuring the model's parameters.

Furthermore, an inconsistency of the proposed model which becomes apparent from the viewpoint of magnetic energy storage in the coupling and leakage fields has been identified. Specifically, it was proved that (for the assumed inductance forms) the main path satisfies the constraints of a conservative field, in contrast to the leakage fields that are not conservative. However, the effect of this inconsistency is minor and may be safely neglected under most circumstances.

This work has been published in a peer-reviewed journal [105, 106].

4. SYNCHRONOUS MACHINE MODELING

4.1 Review of Existing Models

Synchronous machines are usually employed as generators connected to a power system. A generator model may be involved in two types of power system stability studies, namely large- and small-disturbance studies. A large disturbance often consists of a fault on the transmission system or the generator itself that the power system must be able to withstand without loss of synchronism. These studies extend to a time period of up to ten seconds, thus termed short-term transient stability studies. On the other hand, a long-term large-disturbance transient stability study runs for time frames on the order of minutes, focusing on the effects of the slower system dynamics, e.g. due to prime mover and energy supply system dynamics, voltage and frequency protection schemes, capacitor switching, or restoration of loads through tap changer action. Small-disturbance stability studies are performed using linearized system equations, to ensure that oscillations are sufficiently damped by the excitation system.

In the current IEEE Standard [107], it is acknowledged that synchronous machines may be accurately modeled by two lumped-parameter equivalent circuits representing the q- and the d-axis, such as the one shown in Fig. 4.1. These models are classified by the number of rotor circuits in each axis; for example, the model with the field winding plus one damper in both d- and q-axis is called model 2.1, the most common combinations being 1.0, 1.1, 2.1, 2.2, 2.3, and 3.3. The number of rotor "damper" branches is selected in accordance with the rotor design. Salient-pole generators with laminated rotors have copper damper bars in the pole faces that are connected with continuous end-rings, forming a squirrel cage amortisseur winding. In this case, model 2.1 is sufficient, since the eddy current effect is suppressed by

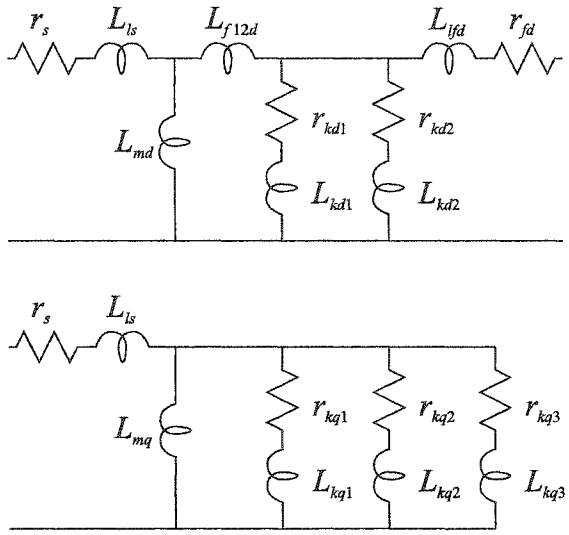

Fig. 4.1. The IEEE Standard model of type 3.3.

the laminated structure of the rotor. However, for machines with solid iron poles, a higher order model should be used to reflect the increased significance of distributed effects in the iron. Round-rotor generators are more complex. Their circumference is slotted to accommodate the field winding, which is held in place by wedges. The wedges' type, i.e. their magnetic properties (usually nonmagnetic), material (steel or aluminum), whether they are segmented or of full length, and other design details can significantly affect the machine's performance. Another important factor is the design of the pole-face, which may have circumferential or longitudinal slots. In these cases, models 2.2, 2.3 or 3.3 are recommended.

The rotor-related part of the equivalent circuits proposed in the Standard differs from other "conventional" equivalent circuits [5, 108], since it contains a "differential leakage" inductance (denoted by L_{f12d} in Fig. 4.1). Its use was proposed by Canay in his seminal paper of 1969 [109], to signify unequal coupling between the rotor windings and the stator, and between the rotor circuits themselves. In view of Fig. 4.2, the field and damper circuits are coupled with the stator with L_{md}, while the coupling between the rotor circuits is $L_{md} + L_{rc}$. A positive L_{rc} indicates better magnetic linkage between field and damper circuit than between stator and individ-

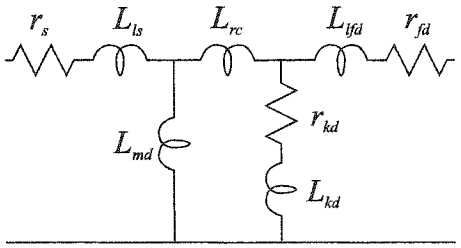

Fig. 4.2. Equivalent d-axis circuit, as proposed by Canay.

ual rotor circuits. This is the case for turbogenerators, because the dampers are also linked to the field through the tooth-top and slot-leakage fields that are common to both. A negative L_{rc} implies worse coupling. This occurs in salient pole machines, where part of the main field is not coupled with the dampers. Although there is clearly no question about the physical significance of this inductance, and despite the repeatedly demonstrated improvement in model predictions, differential leakage is still sometimes ignored by analysts.

A variety of other circuit structures have also been proposed in the literature [110–115]. For instance, in [110], the rotor's d-axis network was represented by three transfer function branches, for which specific forms were proposed, as shown in Fig. 4.3. In [111], ladder networks of a different structure were used to model the solid iron rotor, depicted in Fig. 4.4. Canay [112] and Keyhani [113] utilize additional branches to take into account eddy currents in the slot walls for open field winding conditions (see Fig. 4.5).

New circuits having L_{f12d} equal to zero may be obtained with an appropriate transformation, as was shown by Canay in his original paper, and again by Kirtley in [116]. This corresponds to forcing equal magnetic coupling between all rotor circuits and the stator winding—often called the "equal mutuals" base. However, the equal mutuals base is restricted to the case of three coupled circuits, that is, when the rotor has at most a field winding and one damper [117]. The most unconstrained form of equivalent circuit is one with differential leakage inductances between all damper circuits. Important theoretical results about equivalent circuits were pub-

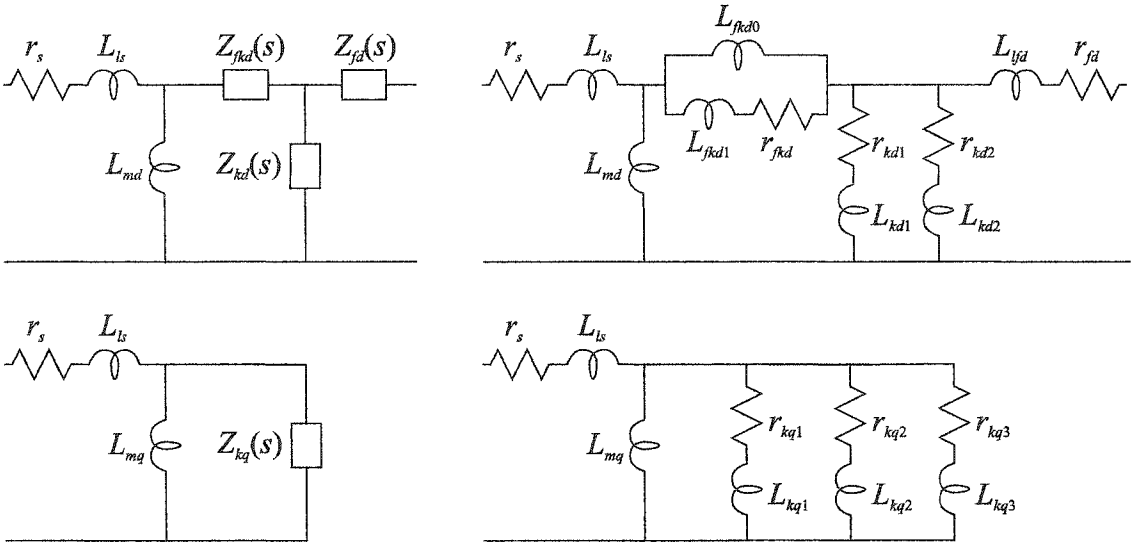

Fig. 4.3. Equivalent circuits, as proposed by Schulz *et al.*

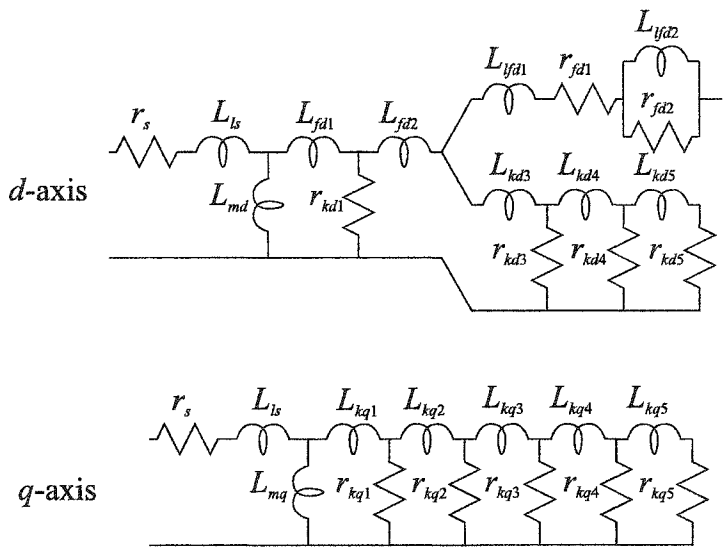

Fig. 4.4. Equivalent "ladder networks," as proposed by Bissig *et al.*

lished in [118, 119], where it was shown that there is no unique RL ladder network representation of a given rotor two-port network with a prescribed impedance matrix.

A further disadvantage of using a mathematical transformation to ensure a specific network structure (one with no differential leakage) is that it causes the new values of the stator leakage and magnetizing inductance to lose their original physical

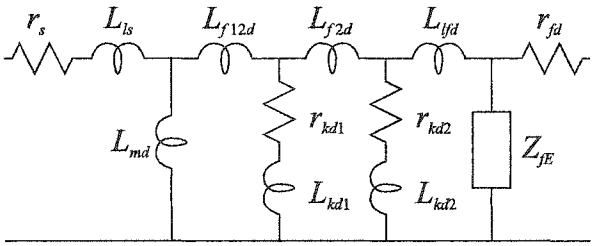

Fig. 4.5. Equivalent d-axis circuit with additional branch Z_{fE} for open field conditions.

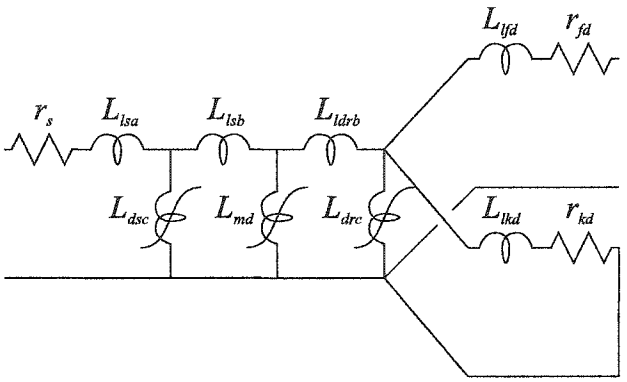

L_{lsa} = stator end-winding leakage inductance (flux path in the air)
L_{dsc}, L_{drc} = stator and rotor core inductances
L_{lsb}, L_{ldrb} = stator and rotor slot leakage inductances (flux path in the iron)
L_{md} = magnetizing inductance, which represents the combined reluctances of the stator teeth, the air gap, and the rotor poles
L_{lfd}, L_{lkd} = field and damper leakage inductances (flux path in the air)

Fig. 4.6. Equivalent d-axis circuit, as proposed by Ojo and Lipo.

meaning. If magnetizing path saturation is to be considered—either by adjusting the magnetizing branch inductance or by replacing it by a nonlinear element—the physical significance of these elements should be preserved [120]. Although some physical significance may be attributed to the parameters of models with up to three "damper" circuits [121], it is gradually lost as the order is further increased, as is recommended for accurate transient stability or subsynchronous resonance studies [122].

Apart from equivalent circuit related problems, synchronous machine research has also focused on the accurate incorporation of magnetic saturation, which has been

shown to considerably affect their operating characteristics [123]. Different methods to model this complicated phenomenon were analyzed in a variety of publications, such as [52, 124–134], usually by modification of the magnetizing inductance in the T-equivalent circuit. A different form of equivalent circuit, derived by considering the flux paths in more detail, was proposed in [124, 128] (see Fig. 4.6). This model independently represents saturation in the teeth and poles, and the stator and rotor cores, and is suitable for studies of asynchronous operation (such as in asynchronous starting) where the levels of core saturation are high.

The incorporation of stator and rotor losses has been reported to have an effect on the machine's dynamic behavior [135]. The losses may be modeled with the addition of short-circuited RL stubs in the equivalent circuit. The parameters of these artificial windings may be determined from core loss measurements. However, the proposed synchronous generator model does not take core loss into account.

4.2 The Proposed Model—Mathematical Formulation

The purpose of this work is to address the aforementioned equivalent circuit issues. In the model that is set forth herein, the equivalent circuit structure of the rotor is replaced by a completely arbitrary linear circuit, a two-port network for the d-axis, and a single branch for the q-axis, as shown in Fig. 4.7. This approach has been adopted from the previous modeling work on induction machines (as discussed in Chapter 3), emphasizing the importance of the rotor's actual input-output behavior rather than the debatable physical meaning of the equivalent circuit parameters. It offers the advantage that once the transfer functions of these linear circuits are determined—using standstill frequency response tests for example, they may be immediately incorporated in the model. It does not require the tedious and time-consuming process of equivalent circuit parameter identification, to which numerous studies have been devoted [136, 137]. Indeed, this problem is highly nonlinear, and the solution algorithms often face convergence issues, accentuated by the

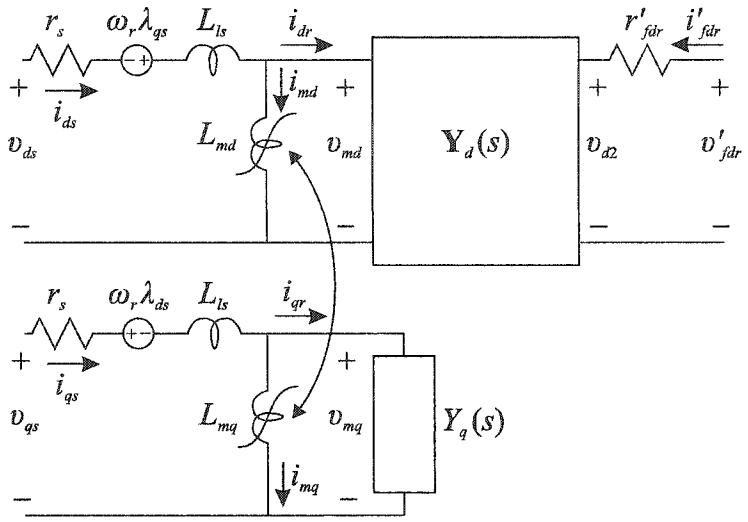

Fig. 4.7. The proposed synchronous machine model.

fact that there is no unique solution. Furthermore, for modern computer simulation software such as Matlab®/Simulink [138] or ACSL® [139], the entry of a specific equivalent circuit structure is not required. Rather, it is more efficient to directly provide a state-space representation of the system to be simulated. The proposed model possesses such a form.

In addition, the proposed model lends itself to the modification of the magnetizing inductances for saturation (and cross-saturation) modeling in both axes. Recent evidence suggests that lumping saturation effects in the magnetizing branch is a reasonable assumption [140, 141], and this hypothesis is further corroborated by our results. Although the leakage flux paths may saturate due to excessive current or by high magnetizing flux levels, synchronous generators are usually operated close to their nominal values of flux, so the leakage inductance may be assumed to remain constant for a wide range of studies. A derivation of the model's torque equation, and restrictions on the magnetizing inductances arising from the assumption of a lossless (conservative) coupling field will be presented in later sections.

From a computer simulation point of view, the proposed model is of the voltage-in, current-out type; the stator and field winding voltages are the inputs, while

the stator and field winding currents are the outputs. The model is computationally efficient in the sense that it is noniterative at each time step, and uses only a minimum number of states obtained from a minimal realization of the measured input-output behavior. It is especially suitable for time-domain dynamic simulations of power systems, as well as for the design and optimization of control schemes.

4.2.1 Notation

Throughout this chapter, matrix and vector quantities appear in bold font. The primed rotor quantities denote referral to the stator through the turns ratio, which is defined as the ratio of stator-to-field turns, $TR = N_s/N_{fdr}$. The analysis takes place in the rotor reference frame; the often used "r" superscript [5] is omitted for convenience. The electrical rotor position, θ_r, and electrical rotor speed, ω_r, are $P/2$ times the mechanical rotor position, θ_{rm}, and mechanical speed, ω_{rm}, where P is the number of poles. The transformation of stationary abc to $qd0$ variables in the rotor reference frame is defined by [5]

$$\mathbf{f}_{qd0s} = \mathbf{K}_s(\theta_r)\mathbf{f}_{abcs}\,, \tag{4.1}$$

where

$$\mathbf{K}_s(\theta_r) = \frac{2}{3}\begin{bmatrix} \cos\theta_r & \cos\left(\theta_r - \frac{2\pi}{3}\right) & \cos\left(\theta_r + \frac{2\pi}{3}\right) \\ \sin\theta_r & \sin\left(\theta_r - \frac{2\pi}{3}\right) & \sin\left(\theta_r + \frac{2\pi}{3}\right) \\ \frac{1}{2} & \frac{1}{2} & \frac{1}{2} \end{bmatrix}. \tag{4.2}$$

4.2.2 Voltage equations

The stator voltage equations may be expressed in abc variables as

$$\mathbf{v}_{abcs} = r_s\mathbf{i}_{abcs} + \frac{d}{dt}\boldsymbol{\lambda}_{abcs}\,, \tag{4.3}$$

where $\mathbf{v}_{abcs}$, $\mathbf{i}_{abcs}$ and $\boldsymbol{\lambda}_{abcs}$ denote stator winding (phase-to-neutral) voltages, currents flowing into the machine terminals, and flux linkages, respectively, and r_s is the stator winding resistance. Transforming (4.3) to the rotor reference frame yields

$$\mathbf{v}_{qd0s} = r_s \mathbf{i}_{qd0s} + \omega_r \boldsymbol{\lambda}_{dqs} + \tfrac{d}{dt}\boldsymbol{\lambda}_{qd0s}\,, \tag{4.4}$$

where $\boldsymbol{\lambda}_{dqs} = \begin{bmatrix} \lambda_{ds} & -\lambda_{qs} & 0 \end{bmatrix}^T$. It will be assumed hereafter that the zero sequence variables can be neglected.

The state equations of the d-axis two-port network (see Fig. 4.7) may be expressed by a linear system of order N_d as

$$\tfrac{d}{dt}\mathbf{x}_d = \mathbf{A}_d\mathbf{x}_d + \mathbf{B}_d \begin{bmatrix} v_{md} \\ v_{d2} \end{bmatrix} = \mathbf{A}_d\mathbf{x}_d + \begin{bmatrix} \mathbf{B}_{d1} & \mathbf{B}_{d2} \end{bmatrix} \begin{bmatrix} v_{md} \\ v_{d2} \end{bmatrix}\,, \tag{4.5}$$

$$\begin{bmatrix} i_{dr} \\ i'_{fdr} \end{bmatrix} = \mathbf{C}_d\,\mathbf{x}_d = \begin{bmatrix} \mathbf{C}_{d1} \\ \mathbf{C}_{d2} \end{bmatrix} \mathbf{x}_d\,, \tag{4.6}$$

where $\mathbf{x}_d \in \mathbb{R}^{N_d \times 1}$, $\mathbf{A}_d \in \mathbb{R}^{N_d \times N_d}$, $\mathbf{B}_d \in \mathbb{R}^{N_d \times 2}$, and $\mathbf{C}_d \in \mathbb{R}^{2 \times N_d}$. The contents of $\mathbf{B}_d$ and $\mathbf{C}_d$ were written as the column vectors, $\mathbf{B}_{d1}, \mathbf{B}_{d2}$, and the row vectors, $\mathbf{C}_{d1}, \mathbf{C}_{d2}$. The magnetizing branch voltages are equal to the derivatives of the corresponding magnetizing flux linkages, which will be computed in the ensuing analysis.

The voltage v_{d2} may be eliminated from the equations, since it is related to the field voltage and current by $v_{d2} = v'_{fdr} - r'_{fdr} i'_{fdr}$. Using this, the following state equation is obtained:

$$\tfrac{d}{dt}\mathbf{x}_d = (\mathbf{A}_d - r'_{fdr}\mathbf{B}_{d2}\mathbf{C}_{d2})\mathbf{x}_d + \begin{bmatrix} \mathbf{B}_{d1} & \mathbf{B}_{d2} \end{bmatrix} \begin{bmatrix} v_{md} \\ v'_{fdr} \end{bmatrix}\,. \tag{4.7}$$

Similarly, the q-axis state equations are

$$\tfrac{d}{dt}\mathbf{x}_q = \mathbf{A}_q\mathbf{x}_q + \mathbf{B}_q v_{mq}\,, \tag{4.8}$$

$$i_{qr} = \mathbf{C}_q\mathbf{x}_q\,, \tag{4.9}$$

where $\mathbf{x}_q \in \mathbb{R}^{N_q \times 1}$, $\mathbf{A}_q \in \mathbb{R}^{N_q \times N_q}$, $\mathbf{B}_q \in \mathbb{R}^{N_q \times 1}$, $\mathbf{C}_q \in \mathbb{R}^{1 \times N_q}$, and N_q is the order of the q-axis system.

It will be useful to derive expressions for the current derivatives. From (4.6)–(4.9):

$$\frac{d}{dt}\begin{bmatrix} i_{dr} \\ i'_{fdr} \end{bmatrix} = \mathbf{C}_d(\mathbf{A}_d - r'_{fdr}\mathbf{B}_{d2}\mathbf{C}_{d2})\mathbf{x}_d + \mathbf{C}_d\mathbf{B}_d \begin{bmatrix} v_{md} \\ v'_{fdr} \end{bmatrix}, \tag{4.10}$$

$$\frac{d}{dt} i_{qr} = \mathbf{C}_q\mathbf{A}_q\mathbf{x}_q + \mathbf{C}_q\mathbf{B}_q v_{mq}\,. \tag{4.11}$$

4.2.3 Rotor transfer functions

In the frequency domain, the rotor currents and voltages are related by the transfer functions

$$\begin{bmatrix} \tilde{i}_{dr} \\ \tilde{i}'_{fdr} \end{bmatrix} = [\mathbf{Y}_d(s)] \begin{bmatrix} \tilde{v}_{md} \\ \tilde{v}_{d2} \end{bmatrix} = \begin{bmatrix} y_{11}(s) & y_{12}(s) \\ y_{12}(s) & y_{22}(s) \end{bmatrix} \begin{bmatrix} \tilde{v}_{md} \\ \tilde{v}_{d2} \end{bmatrix}, \tag{4.12}$$

$$\tilde{i}_{qr} = Y_q(s)\tilde{v}_{mq}\,, \tag{4.13}$$

where $s = j\omega$, and the tilde is used to denote phasor quantities. The elements of $\mathbf{Y}_d(s)$ $(y_{11}(s), y_{12}(s),\ y_{22}(s))$ and $Y_q(s)$ are strictly proper rational polynomial functions of the complex frequency s, of the form

$$y(s) = \frac{n_0 + n_1 s + \cdots + n_{N-1}s^{N-1}}{d_0 + d_1 s + \cdots + d_{N-1}s^{N-1} + d_N s^N}\,. \tag{4.14}$$

The coefficients n_0 and d_0 may not be simultaneously equal to zero, since that would result in a pole–zero cancellation at the origin. This is a representation of a most general form, but a simplified version may be obtained for the d-axis if the physics of the rotor are taken into account.

To this end, Faraday's law is applied to the field winding: $v'_{fdr} = r'_{fdr}i'_{fdr} + d\lambda'_{fdr}/dt$. It can be seen that there is no dc voltage drop besides the ohmic drop of the winding's resistance (which is external to the two-port network). This implies that there exists a direct path for dc current between the primary and secondary sides of the two-port network.

Under this assumption, the constants n_0 of the polynomials will all have the same absolute value, and the system will possess a pole at the origin. To see this, assume that the field side of the admittance block is short-circuited ($\tilde{v}_{d2} = 0$), so that

$$\tilde{i}_{dr} = y_{11}(s)\tilde{v}_{md}\,, \tag{4.15}$$

$$\tilde{i}'_{fdr} = y_{12}(s)\tilde{v}_{md}\,. \tag{4.16}$$

As the frequency approaches zero ($s \to 0$), the hypothesis that at low frequency the two-port network behaves as an ideal series inductor implies that $\tilde{i}_{dr} \to -\tilde{i}'_{fdr}$, so

$$\lim_{s\to 0} y_{11}(s) = -\lim_{s\to 0} y_{12}(s)\,. \tag{4.17}$$

Since the denominator of (4.14) corresponds to the least common denominator of all elements of $\mathbf{Y}_d(s)$, the n_0 element of $y_{11}(s)$ is equal to $-n_0$ of $y_{12}(s)$. Similarly, setting $\tilde{v}_{md} = 0$ and letting the frequency approach zero yields

$$\lim_{s\to 0} y_{12}(s) = -\lim_{s\to 0} y_{22}(s)\,. \tag{4.18}$$

Thus the n_0 element of $y_{12}(s)$ is equal to $-n_0$ of $y_{22}(s)$. This observation, coupled with the fact that these admittances become infinite as $s \to 0$ (again because of the assumption that the network acts as an ideal series inductance at sufficiently low frequency), implies that the d-axis transfer functions must have the following forms:

$$y_{11}(s) = Y_{d0}\frac{1 + \alpha_1 s + \cdots + \alpha_{N_d-1}s^{N_d-1}}{s(1 + \delta_1 s + \cdots + \delta_{N_d-1}s^{N_d-1})}\,, \tag{4.19}$$

$$y_{12}(s) = -Y_{d0}\frac{1 + \beta_1 s + \cdots + \beta_{N_d-1}s^{N_d-1}}{s(1 + \delta_1 s + \cdots + \delta_{N_d-1}s^{N_d-1})}\,, \tag{4.20}$$

$$y_{22}(s) = Y_{d0}\frac{1 + \gamma_1 s + \cdots + \gamma_{N_d-1}s^{N_d-1}}{s(1 + \delta_1 s + \cdots + \delta_{N_d-1}s^{N_d-1})}\,. \tag{4.21}$$

The formulation of the q-axis transfer function is more straightforward, due to the absence of a field winding. In particular, the q-axis transfer function may be expressed as

$$Y_q(s) = Y_{q0}\frac{1 + \epsilon_1 s + \cdots + \epsilon_{N_q-1}s^{N_q-1}}{1 + \zeta_1 s + \cdots + \zeta_{N_q}s^{N_q}}\,. \tag{4.22}$$

In this case, poles and zeros at the origin are not allowed.

4.2.4 Realization theory

The rotor transfer functions are the starting point for the computation of the time-domain state matrices, as used in (4.7) and (4.8). The problem is to determine an internal, state-space description of a linear system, given its external, input-output description. This is the subject of system realization theory [83].

Numerous algorithms exist for deriving a realization. However, for increased computational efficiency, it is desirable to obtain a system of the least possible order, a so-called *minimal* realization. In contrast to the single-input/single-output case, where it is rather straightforward to obtain a realization, the multiple-input/multiple-output case (like the two-port d-axis rotor system) is more complicated. The difficulty arises when determining the minimal realization order. Consider a transfer function written in the form $\mathbf{Y}(s) = \mathbf{N}(s)/m_Y(s)$, where $\mathbf{N}(s)$ is a matrix of polynomials and $m_Y(s)$ is the minimal polynomial of $\mathbf{Y}(s)$. [1] The roots of $m_Y(s)$ constitute a subset of the eigenvalues of the minimal realization; hence, a minimal polynomial with two roots may correspond to a system with a second, third, or fourth order minimal realization.

In the case of the proposed model, the transfer function matrix entries are the functions (4.19)–(4.21), the degree of the minimal polynomial is N_d, and the order of the minimal realization is $2N_d - 1$. This is proved using the following theorem:

> The order of any minimal realization is equal to the degree of the characteristic polynomial, $p_Y(s)$, of the transfer function matrix $\mathbf{Y}(s)$ [83, p. 397]. [2]

It remains to compute $p_Y(s)$, given the functional forms (4.19)–(4.21).

---

[1] The minimal polynomial is defined herein as the monic least common denominator of the transfer function entries. A polynomial is monic when the highest order term has a coefficient of one.

[2] The characteristic polynomial $p_Y(s)$ is defined as the monic least common denominator of all nonzero minors of $\mathbf{Y}(s)$.

Let us write the d-axis transfer function as

$$\mathbf{Y}_d(s) = \frac{1}{m_Y(s)}\mathbf{N}(s) = \frac{1}{m_Y(s)}\begin{bmatrix} n_{11}(s) & n_{12}(s) \\ n_{12}(s) & n_{22}(s) \end{bmatrix}, \tag{4.23}$$

where

$$m_Y(s) = s\left(s^{N_d-1} + \cdots + \delta_{N_d-1}^{-1}\right). \tag{4.24}$$

It is assumed that no common factors exist between $n_{11}(s)$, $n_{12}(s)$, $n_{22}(s)$, and $m_Y(s)$. To obtain $p_Y(s)$, it is necessary to compute all nonzero minors of $\mathbf{Y}_d(s)$. The first order minors are the entries of $\mathbf{Y}_d(s)$, and their monic least common denominator is (by definition) the minimal polynomial $m_Y(s)$. The second order minor is equal to the determinant

$$D(s) = \frac{n_{11}(s)n_{22}(s) - n_{12}^2(s)}{m_Y^2(s)}. \tag{4.25}$$

Taking into account the specified forms of the transfer functions (4.19)–(4.21), it is readily shown that the numerator of $D(s)$ has a root at the origin, which cancels out with one of the two zero roots of $m_Y^2(s)$. Hence,

$$p_Y(s) = s\left(s^{N_d-1} + \cdots + \delta_{N_d-1}^{-1}\right)^2. \tag{4.26}$$

The degree of the characteristic polynomial—the order of the minimal realization—is thus $2N_d - 1$.

An algorithm to obtain a minimal state-space realization from the transfer function matrix is described in Appendix A.

4.2.5 Leakage and magnetizing path magnetics

The stator flux linkage is separated into leakage and magnetizing flux terms as

$$\boldsymbol{\lambda}_{qds} = \boldsymbol{\lambda}_{lqds} + \boldsymbol{\lambda}_{mqd} = L_{ls}\mathbf{i}_{qds} + \boldsymbol{\lambda}_{mqd}, \tag{4.27}$$

where $\boldsymbol{\lambda}_{lqds}$ is the stator leakage flux, and $\boldsymbol{\lambda}_{mqd}$ is the magnetizing flux. The same value of leakage inductance, L_{ls}, is used for both the q- and the d-axis.

The functional forms of main path saturation in the proposed model are similar to [130]. Since in the general case of a salient rotor machine, the mmf and flux vectors are not aligned, the following relations may be assumed for the magnetizing path:

$$i_{mq} = \Gamma_{mq}(\hat{\lambda}_m)\lambda_{mq}\,, \tag{4.28}$$

$$i_{md} = \Gamma_{md}(\hat{\lambda}_m)\lambda_{md}\,. \tag{4.29}$$

The magnitude of the equivalent magnetizing flux vector is defined by

$$\hat{\lambda}_m = \sqrt{\lambda_{md}^2 + \alpha\lambda_{mq}^2}\,, \tag{4.30}$$

where α is a saliency dependent parameter. Differentiating (4.28), (4.29) with respect to time yields

$$\tfrac{d}{dt}\mathbf{i}_{mqd} = \mathbf{\Gamma}_{mi}(\boldsymbol{\lambda}_{mqd})\tfrac{d}{dt}\boldsymbol{\lambda}_{mqd}\,, \tag{4.31}$$

where

$$\mathbf{\Gamma}_{mi}(\boldsymbol{\lambda}_{mqd}) = \begin{bmatrix} \frac{d\Gamma_{mq}(\hat{\lambda}_m)}{d\hat{\lambda}_m}\frac{\alpha\lambda_{mq}^2}{\hat{\lambda}_m} + \Gamma_{mq}(\hat{\lambda}_m) & \frac{d\Gamma_{mq}(\hat{\lambda}_m)}{d\hat{\lambda}_m}\frac{\lambda_{mq}\lambda_{md}}{\hat{\lambda}_m} \\ \frac{d\Gamma_{md}(\hat{\lambda}_m)}{d\hat{\lambda}_m}\frac{\alpha\lambda_{mq}\lambda_{md}}{\hat{\lambda}_m} & \frac{d\Gamma_{md}(\hat{\lambda}_m)}{d\hat{\lambda}_m}\frac{\lambda_{md}^2}{\hat{\lambda}_m} + \Gamma_{md}(\hat{\lambda}_m) \end{bmatrix}. \tag{4.32}$$

The "i" subscript denotes incremental value.

4.2.6 Torque equation

The proposed model's electromagnetic torque equation may be derived by examining the energy balance of the machine's coupling field [5]. The coupling field is created by the magnetizing flux, which links both stator and rotor circuits.

The electric power supplied to the coupling field is equal to the input power, minus the power lost in the stator and field resistances, minus the power that supplies the stator leakage field, minus the power that is dissipated or stored inside the rotor admittance block. Using the equivalent circuit of Fig. 4.7 and (4.27), the electric power supplied to the coupling field may be expressed after manipulation as

$$P_e = \tfrac{3}{2}\omega_r\left(i_{qs}\lambda_{md} - i_{ds}\lambda_{mq}\right) + \tfrac{3}{2}\left(i_{mq}\tfrac{d}{dt}\lambda_{mq} + i_{md}\tfrac{d}{dt}\lambda_{md}\right). \tag{4.33}$$

The electrical energy provided to the coupling field is partly stored, and the rest is transferred to the mechanical system. If W_f denotes the coupling field energy and T_e the electromagnetic torque, then the power balance may be written as

$$P_e = \tfrac{d}{dt} W_f + T_e \omega_{rm} \,, \tag{4.34}$$

where the product $T_e \omega_{rm}$ is positive for motor action. Equating (4.33) and (4.34), and solving for the rate of change of the field energy yields

$$\tfrac{d}{dt} W_f = \left[\tfrac{3}{2} \left(i_{qs} \lambda_{md} - i_{ds} \lambda_{mq} \right) - T_e \tfrac{2}{P} \right] \tfrac{d}{dt} \theta_r + \left(\tfrac{3}{2} i_{mq} \right) \tfrac{d}{dt} \lambda_{mq} + \left(\tfrac{3}{2} i_{md} \right) \tfrac{d}{dt} \lambda_{md} \,. \tag{4.35}$$

Hence, the differential change of the coupling field energy may be written as

$$dW_f = \tfrac{\partial W_f}{\partial \theta_r} d\theta_r + \tfrac{\partial W_f}{\partial \lambda_{mq}} d\lambda_{mq} + \tfrac{\partial W_f}{\partial \lambda_{md}} d\lambda_{md} \,, \tag{4.36}$$

where

$$\tfrac{\partial W_f}{\partial \theta_r} = \tfrac{3}{2} \left(i_{qs} \lambda_{md} - i_{ds} \lambda_{mq} \right) - T_e \tfrac{2}{P} \,, \tag{4.37}$$

$$\tfrac{\partial W_f}{\partial \lambda_{mq}} = \tfrac{3}{2} i_{mq} \,, \tag{4.38}$$

$$\tfrac{\partial W_f}{\partial \lambda_{md}} = \tfrac{3}{2} i_{md} \,. \tag{4.39}$$

The change of coupling field energy from an initial state $\{\theta_{r0}, \lambda_{mq0}, \lambda_{md0}\}$ to an arbitrary final state $\{\theta_r, \lambda_{mq}, \lambda_{md}\}$ is obtained by integrating (4.36):

$$W_f(\theta_r, \lambda_{mq}, \lambda_{md}) = W_{f0} + \int_{\theta_{r0}}^{\theta_r} \left[\tfrac{3}{2} \left(i_{qs} \lambda_{md} - i_{ds} \lambda_{mq} \right) - T_e \tfrac{2}{P} \right] d\theta_r' + \\ + \tfrac{3}{2} \int_{\lambda_{mq0}}^{\lambda_{mq}} i_{mq} \, d\lambda_{mq}' + \tfrac{3}{2} \int_{\lambda_{md0}}^{\lambda_{md}} i_{md} \, d\lambda_{md}' \,. \tag{4.40}$$

Since the field is assumed to be conservative, the integration may be performed over an arbitrary trajectory. Assume that the initial energy is $W_{f0} = 0$, and integrate the first term from θ_{r0} to θ_r, while the fluxes are maintained at zero—which forces T_e to be zero as well. This transition does not change the field energy. Then, consecutively integrate each one of the fluxes from zero to an arbitrary final value, while keeping θ_r and the other flux constant. Recall that the transformation to the

rotor reference frame eliminates the dependence of the magnetizing inductances from the rotor position. The magnetizing currents are independent of θ_r—as in (4.28), (4.29). Therefore, the final value of field energy $W_f(\theta_r, \lambda_{mq}, \lambda_{md})$ is independent of the angular position θ_r, i.e.

$$\frac{\partial W_f}{\partial \theta_r} = 0\,. \tag{4.41}$$

This observation coupled with (4.37) yields the following well-known expression for the electromagnetic torque:

$$T_e = \tfrac{3}{2}\tfrac{P}{2}\left(i_{qs}\lambda_{md} - i_{ds}\lambda_{mq}\right)\,. \tag{4.42}$$

For generator action (and $\omega_r > 0$) the torque will be negative.

4.2.7 Restrictions on the inverse magnetizing inductances

In (4.28) and (4.29), the inverse magnetizing inductances were defined as any arbitrary function of flux. However, to be consistent with the assumption of a lossless coupling field, certain modeling restrictions must be imposed [142, 143].

Specifically, the coupling field's energy expression, which in view of (4.41) has become

$$W_f(\lambda_{mq}, \lambda_{md}) = W_{f0} + \tfrac{3}{2}\int_{\lambda_{mq0}}^{\lambda_{mq}} i_{mq}\, d\lambda'_{mq} + \tfrac{3}{2}\int_{\lambda_{md0}}^{\lambda_{md}} i_{md}\, d\lambda'_{md}\,, \tag{4.43}$$

must satisfy the requirements of a conservative field. A necessary and sufficient condition for this is (see Section 3.5.1)

$$\frac{\partial i_{mq}}{\partial \lambda_{md}} = \frac{\partial i_{md}}{\partial \lambda_{mq}}\,. \tag{4.44}$$

Substitution of (4.28) and (4.29) into (4.44) yields

$$\frac{d\Gamma_{mq}}{d\hat{\lambda}_m}\frac{\lambda_{md}}{\hat{\lambda}_m}\lambda_{mq} = \frac{d\Gamma_{md}}{d\hat{\lambda}_m}\frac{\alpha\lambda_{mq}}{\hat{\lambda}_m}\lambda_{md}\,. \tag{4.45}$$

Cancelling common terms and integrating both sides yields

$$\Gamma_{mq}(\hat{\lambda}_m) = \alpha\Gamma_{md}(\hat{\lambda}_m) + \beta, \quad \beta \in \mathbb{R}\,. \tag{4.46}$$

This restriction has to be enforced during the magnetizing characteristics' curve fitting procedure. Note that it also renders the incremental inverse inductance matrix Γ_{mi} symmetric.

4.2.8 Model integration

The state variables are selected as $\mathbf{x} = \{\boldsymbol{\lambda}_{mqd}, \mathbf{x}_q, \mathbf{x}_d\}$. The goal of the ensuing analysis is the formulation of equations for the time derivatives of the state variables.

First, note that both rotor and magnetizing currents have been previously expressed as functions of the states: the rotor currents are given in terms of the rotor admittance states from (4.6) and (4.9); the magnetizing currents depend on the magnetizing flux states, as seen from (4.28)–(4.30). Hence, the stator currents

$$i_{qs} = i_{mq} + i_{qr}\,, \tag{4.47}$$

$$i_{ds} = i_{md} + i_{dr}\,, \tag{4.48}$$

are also functions of state variables.

Next, the time derivatives of the stator flux linkages are calculated from (4.4),

$$\tfrac{d}{dt}\lambda_{ds} = v_{ds} - r_s i_{ds} + \omega_r \lambda_{qs}\,, \tag{4.49}$$

$$\tfrac{d}{dt}\lambda_{qs} = v_{qs} - r_s i_{qs} - \omega_r \lambda_{ds}\,, \tag{4.50}$$

as functions of state variables and model inputs (the stator voltages). However, they are only evaluated as an intermediate calculation; they are not integrated since $\boldsymbol{\lambda}_{qds}$ are not states.

The differentiation with respect to time of (4.27) yields an alternate expression for the derivatives of the stator flux linkages (cf. (4.49), (4.50)):

$$\tfrac{d}{dt}\lambda_{ds} = L_{ls}\tfrac{d}{dt}(i_{md} + i_{dr}) + \tfrac{d}{dt}\lambda_{md}\,, \tag{4.51}$$

$$\tfrac{d}{dt}\lambda_{qs} = L_{ls}\tfrac{d}{dt}(i_{mq} + i_{qr}) + \tfrac{d}{dt}\lambda_{mq}\,. \tag{4.52}$$

The derivatives of the rotor and magnetizing currents may be evaluated using (4.10), (4.11) and (4.31), so

$$\frac{d}{dt}\lambda_{ds} = L_{ls}\left[\mathbf{\Gamma}_{mi}(\cdot)_{21}\frac{d}{dt}\lambda_{mq} + \mathbf{\Gamma}_{mi}(\cdot)_{22}\frac{d}{dt}\lambda_{md} + \mathbf{C}_{d1}(\mathbf{A}_d - r'_{fdr}\mathbf{B}_{d2}\mathbf{C}_{d2})\mathbf{x}_d + \right.$$
$$\left. + \mathbf{C}_{d1}\mathbf{B}_{d1}\frac{d}{dt}\lambda_{md} + \mathbf{C}_{d1}\mathbf{B}_{d2}v'_{fdr}\right] + \frac{d}{dt}\lambda_{md}\,, \quad (4.53)$$

$$\frac{d}{dt}\lambda_{qs} = L_{ls}\left[\mathbf{\Gamma}_{mi}(\cdot)_{11}\frac{d}{dt}\lambda_{mq} + \mathbf{\Gamma}_{mi}(\cdot)_{12}\frac{d}{dt}\lambda_{md} + \mathbf{C}_q\mathbf{A}_q\mathbf{x}_q + \mathbf{C}_q\mathbf{B}_q\frac{d}{dt}\lambda_{mq}\right] + \frac{d}{dt}\lambda_{mq}\,. \quad (4.54)$$

The following linear system of equations may therefore be formulated:

$$L_{ls}\mathbf{\Gamma}_{mi}(\cdot)_{21}\frac{d}{dt}\lambda_{mq} + \left\{1 + L_{ls}\left[\mathbf{\Gamma}_{mi}(\cdot)_{22} + \mathbf{C}_{d1}\mathbf{B}_{d1}\right]\right\}\frac{d}{dt}\lambda_{md} =$$
$$= \frac{d}{dt}\lambda_{ds} - L_{ls}\mathbf{C}_{d1}[(\mathbf{A}_d - r'_{fdr}\mathbf{B}_{d2}\mathbf{C}_{d2})\mathbf{x}_d + \mathbf{B}_{d2}v'_{fdr}]\,, \quad (4.55)$$

$$\left\{1 + L_{ls}\left[\mathbf{\Gamma}_{mi}(\cdot)_{11} + \mathbf{C}_q\mathbf{B}_q\right]\right\}\frac{d}{dt}\lambda_{mq} + L_{ls}\mathbf{\Gamma}_{mi}(\cdot)_{12}\frac{d}{dt}\lambda_{md} = \frac{d}{dt}\lambda_{qs} - L_{ls}\mathbf{C}_q\mathbf{A}_q\mathbf{x}_q\,, \quad (4.56)$$

where the quantities $\frac{d}{dt}\lambda_{ds}$ and $\frac{d}{dt}\lambda_{qs}$ are obtained from (4.49) and (4.50). The solution of (4.55), (4.56) yields the time derivatives of two of the state variables (the magnetizing flux linkages λ_{mq} and λ_{md}). Apart from being integrated themselves, these derivatives are also inserted in (4.7) and (4.8)—as the magnetizing voltages v_{mq} and v_{md}—for calculating the derivatives of the remaining state variables $\mathbf{x}_d$ and $\mathbf{x}_q$.

4.2.9 External impedance incorporation

The model is flexible enough to allow the incorporation of an external resistance and inductance, connected in series with the field winding. For example, such would be the case of a brushless excitation system, when the detailed model of the exciter–rectifier system is replaced by a nonlinear average-value model. Essentially, this simplification produces a voltage behind reactance representation of the exciter. As was shown in [144], the effective voltage at the generator field has the form

$$v'_{fdr} = E' - R'_e i'_{fdr} - L'_{tr}\frac{d}{dt}i'_{fdr}\,, \quad (4.57)$$

where E' is the voltage behind the effective resistance, R'_e, and the transient inductance, L'_{tr}; the primes denote that all quantities have been referred to the stator.

These voltage drops may be incorporated in the proposed model in a straightforward manner.

In particular, the voltage at the field side of the d-axis admittance block may be written as

$$v_{d2} = E' - (R'_e + r'_{fdr})i'_{fdr} - L'_{tr}\frac{d}{dt}i'_{fdr}\,. \tag{4.58}$$

Using (4.5) and (4.6) this equation becomes

$$v_{d2} = E' - (R'_e + r'_{fdr})\mathbf{C}_{d2}\mathbf{x}_d - L'_{tr}\mathbf{C}_{d2}(\mathbf{A}_d\mathbf{x}_d + \mathbf{B}_{d1}v_{md} + \mathbf{B}_{d2}v_{d2})\,, \tag{4.59}$$

and solving for v_{d2} yields

$$v_{d2} = \kappa[E' - (R'_e + r'_{fdr})\mathbf{C}_{d2}\mathbf{x}_d - L'_{tr}\mathbf{C}_{d2}(\mathbf{A}_d\mathbf{x}_d + \mathbf{B}_{d1}v_{md})]\,, \tag{4.60}$$

where $\kappa = (1 + L'_{tr}\mathbf{C}_{d2}\mathbf{B}_{d2})^{-1}$. After substitution of (4.60) into (4.5), the following modified state equation is obtained:

$$\begin{aligned}\frac{d}{dt}\mathbf{x}_d = &\left[\left(\mathbf{I}_{N_d} - \kappa L'_{tr}\mathbf{B}_{d2}\mathbf{C}_{d2}\right)\mathbf{A}_d - \kappa(r'_{fdr} + R'_e)\mathbf{B}_{d2}\mathbf{C}_{d2}\right]\mathbf{x}_d + \\ &+ \left(\mathbf{I}_{N_d} - \kappa L'_{tr}\mathbf{B}_{d2}\mathbf{C}_{d2}\right)\mathbf{B}_{d1}v_{md} + \kappa\mathbf{B}_{d2}E'\,,\end{aligned} \tag{4.61}$$

where $\mathbf{I}_{N_d}$ denotes the identity matrix of dimension $N_d \times N_d$. The derivatives of the magnetizing flux linkages are given by the solution of the linear system of equations formed by (4.56) and

$$\begin{aligned}&L_{ls}\mathbf{\Gamma}_{mi}(\cdot)_{21}\frac{d}{dt}\lambda_{mq} + \left\{1 + L_{ls}\left[\mathbf{\Gamma}_{mi}(\cdot)_{22} + \mathbf{C}_{d1}\left(\mathbf{I}_{N_d} - \kappa L'_{tr}\mathbf{B}_{d2}\mathbf{C}_{d2}\right)\mathbf{B}_{d1}\right]\right\}\frac{d}{dt}\lambda_{md} \\ &= \frac{d}{dt}\lambda_{ds} - L_{ls}\mathbf{C}_{d1}\left\{\left[\left(\mathbf{I}_{N_d} - \kappa L'_{tr}\mathbf{B}_{d2}\mathbf{C}_{d2}\right)\mathbf{A}_d - \kappa(r'_{fdr} + R'_e)\mathbf{B}_{d2}\mathbf{C}_{d2}\right]\mathbf{x}_d + \kappa\mathbf{B}_{d2}E'\right\},\end{aligned} \tag{4.62}$$

which was obtained by a procedure analogous to the one described in Section 4.2.8.

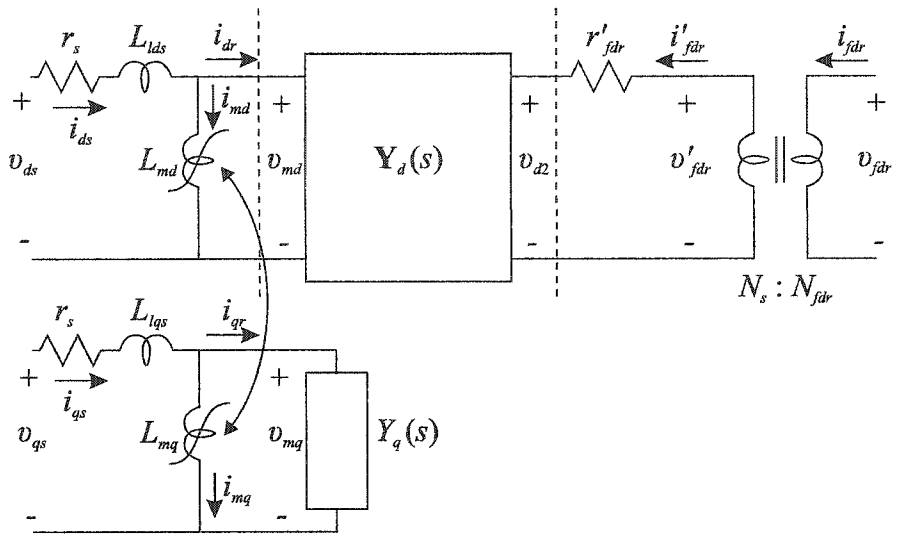

Fig. 4.8. The proposed synchronous machine model (at standstill).

4.3 Parameter Identification Procedure

As discussed in Section 4.1, the current philosophy of synchronous machine modeling for power system studies [107] proposes the use of equivalent circuit structures based on the orthogonal *qd*-axes theory. The pertaining characterization procedure aims at extracting the circuits' resistive and inductive element values [145], which is a difficult optimization problem. In general, the machine has been viewed as a linear network, whose frequency response may be determined from measurements at the terminals (by measuring for instance the operational inductances $L_d(s)$, $L_{afo}(s)$ and the stator-to-field transfer function $sG(s)$, [146–148]).

The modeling perspective presented herein suggests replacing the equivalent circuits with generalized linear networks, as shown in Fig. 4.8. This approach is well suited to standstill frequency response measurements (SSFR), enabling the direct incorporation of the frequency response characteristic in the model, without the intermediate step of finding damper winding circuit element values. In this section, a suitable experimental characterization procedure for the proposed model is described in detail.

In the proposed method, the machine's magnetization characteristic and turns ratio are estimated first. When using a linear machine model, the turns ratio can not be uniquely determined by measurements at the terminals and is usually arbitrarily set to the manufacturer's value. However, the importance of the turns ratio value is increased when adopting a model that explicitly incorporates the nonlinear effect of magnetizing path saturation. In this case, every effort should be made to maintain the physical significance of the model's parameters [120].

The turns ratio determination procedure of [145] is based on extrapolating the ratio of field winding to magnetizing branch voltages at zero frequency using SSFR data; it is thus sensitive to the estimated value of L_{md} and low-frequency noise. This work sets forth a novel testing procedure that utilizes the full range of the magnetizing λ–i curve, and is therefore less sensitive to measurement errors. The method is based on measuring the magnetic nonlinearity of the machine's iron from the armature and field sides. Compared to the commonly used method of voltage step tests [149, 150], the proposed testing procedure is simpler and does not require knowledge of the flux remanence.

The second step in the characterization procedure is the measurement of the rotor's transfer functions. This may be accomplished by performing a series of SSFR tests. Since the SSFR experiment was introduced [151], it has been extensively used in synchronous machine identification [152–158]. However, SSFR testing is not a panacea [111, 159], and it is clearly advantageous to identify the parameters when the machine is under nominal operating conditions [160]. Most of SSFR's inconsistencies stem from the absence of centrifugal forces [161], as well as the use of low current levels which leave the leakage paths atypically biased and the rotor cool. Moreover, minor hysteresis loops are being traversed due to the iron's nonlinear behavior [102, 162]. Consequently, the measured magnetizing inductance corresponds to the incremental permeability of the iron and is thus significantly lower than the one obtained from the magnetizing curve. The proposed method addresses this problem by assuming that all magnetic nonlinearities may be lumped in the mag-

netizing branches, while the linear elements remain unaffected by the saturation level [140, 141]. The model structure lends itself to the separate identification of the magnetizing branch and the rotor circuits. Thus the analyst is offered the option of discarding the measured small-signal magnetizing inductance value and replacing it by a nonlinear saturating element that more closely represents the large-signal magnetizing path behavior.

The proposed experimental procedure is applied to a Leroy–Somer brushless synchronous generator, model LSA 432L7. This is a salient 4-pole machine, rated for 59 kW, 600 V, at 1800 rpm.

4.3.1 Rotor alignment procedures

The characterization procedure for the proposed model requires independent measurements at standstill along the q- and d-axis. The d-axis is conventionally defined as the axis of the field winding, while the q-axis lies 90° ahead for counterclockwise rotation, as shown in Fig. 4.9. The stator-to-rotor reference frame transformation (4.1) is used to translate the original abc variables to qd coordinates. Since the machine is Y-connected, i_{0s} and v_{0s} are zero. The mechanical angle θ_{rm} of the synchronous machine under test is measured with a 12-bit position encoder that gives a resolution of 0.088 mechanical degrees.

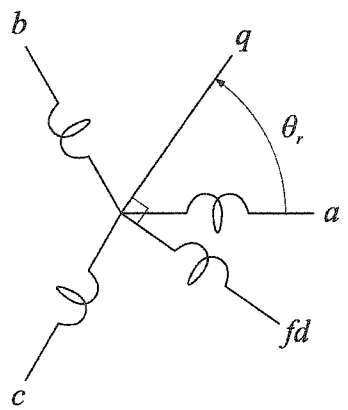

Fig. 4.9. Synchronous generator winding diagram at an arbitrary rotor position θ_r.

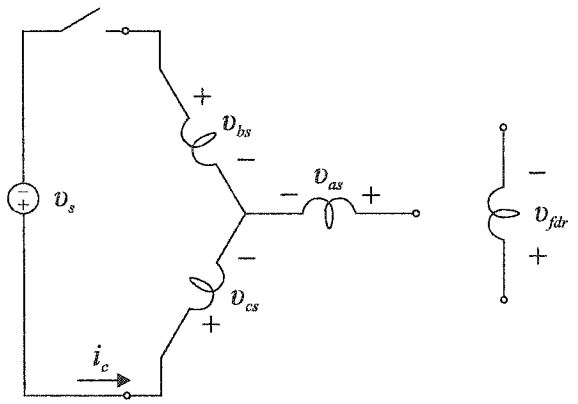

Fig. 4.10. Synchronous generator test configuration. ($\theta_r = 0°$)

The stator is assumed to be geometrically symmetric and slotting is neglected, so the field winding's input impedance is independent of the rotor position θ_r. On the contrary, the armature windings' impedance depends on θ_r, due to the saliency and electrical asymmetry of the rotor. The neutral point is not available, so measurements are taken line-to-line across phases b and c, while phase a is left open. In general, the experiments consist of connecting a voltage source to either the armature or the field winding, and capturing v_{cb}, v_{fd}, i_c and i_{fd}, as shown in Fig. 4.10.

For this test setup, the stator mmf, that would be produced by current flowing in the series-connected b and c phases, is aligned with the corresponding axis. So, alignment with the q-axis may be achieved by exciting the field winding with a sinusoidal signal, measuring the open-circuit line-to-line stator voltage, v_{bc}, and detecting the angle where v_{bc} becomes zero (when $\theta_r = \pm 90°$). To align with the d-axis, we detect the minimums of v_{ac} and v_{ab}, which occur at angles θ_1 and θ_2 (when $\theta_r = 30°$ and $\theta_r = -30°$ respectively); then, the d-axis is aligned at $(\theta_1 + \theta_2)/2$. Alternatively, the location of the d-axis may be determined by measuring the angle where v_{bc} is maximum, but a note of caution is required at this point: the angle of peak voltage may not be accurately detected, as will be shown in the mathematical analysis that follows.

Excitation from the field side with the stator open only involves the d-axis and leaves the q-axis inactive (so that $v_{qs} = 0$ and $i_{qs} = 0$). The inverse of transformation (4.1) [5] yields

$$v_{bs} = \sin\left(\theta_r - \tfrac{2\pi}{3}\right) v_{ds}\,, \tag{4.63}$$

$$v_{cs} = \sin\left(\theta_r + \tfrac{2\pi}{3}\right) v_{ds}\,. \tag{4.64}$$

The measured line-to-line voltage may be related to the d-axis stator voltage by subtracting (4.63) from (4.64), which leads to

$$v_{cb} = \sqrt{3}\cos\theta_r\, v_{ds}\,. \tag{4.65}$$

The d-axis voltage v_{ds} arises from the ac field excitation and is independent of the rotor angle. The change of v_{cb} due to a small rotor angle deviation, $\Delta\theta_r$, is

$$\Delta v_{cb} = -\sqrt{3}\sin\theta_r\, v_{ds}\,\Delta\theta_r\,. \tag{4.66}$$

This observation should clarify the reason why detection of the minimum v_{cb} (at $\theta_r = \pm 90°$, where $\sin\theta_r = \pm 1$) is more reliable than detection of the maximum v_{cb} (at $\theta_r = 0°$, where $\sin\theta_r = 0$).

4.3.2 Resistance measurements

The first step in the characterization procedure is the measurement of the dc values of stator and field winding resistance. Using a four-wire measurement technique, these were determined to be $r_s = 0.108\ \Omega$ and $r_{fdr} = 2.01\ \Omega$ at room temperature. The variation of resistance with temperature is not incorporated in the model.

4.3.3 Magnetizing characteristic and turns ratio identification

The second step of the characterization procedure is the determination of the magnetizing path's λ–i characteristic. This section contains the details of the proposed method, which allows for the simultaneous determination of the turns ratio

and the d-axis magnetizing inductance. The method does not apply to the q-axis, whose characteristic must be obtained from a different type of test, unless test windings exist on the rotor. Herein, the q-axis characterization was performed using step tests.

The proposed procedure consists of alternately exciting the stator and rotor windings (input side), while the other side (output side) is open-circuited. The output voltage and the input current are recorded with a dynamic signal analyzer. The excitation may come from a low-frequency ac source or an adjustable dc voltage source. The source is required to supply a current high enough to saturate the machine. In terms of output power, the equipment need only be rated for the maximum ohmic losses of each winding. When an ac source is used, the experiment consists of measuring full hysteresis loops. When a dc voltage source is available, the voltage is first increased to a point where the magnetizing path may be considered to be saturated; then, the voltage is slowly decreased to zero, and the upper extrados of the hysteresis loop is obtained. [3] In all cases, the tests must be performed at a low frequency in order to ensure that the currents in the rotor circuits are negligible. The terminal quantities may then be directly related to the magnetizing branch variables.

The measured quantities have to be transformed to their respective qd values using (4.1). The rotor is rotated to $\theta_r = 0°$. When exciting the stator side,

$$i_{md} \approx i_{ds} = \tfrac{2}{\sqrt{3}} i_c \,, \tag{4.67}$$

$$\hat{\lambda}_m = \lambda_{md} \approx \lambda'_{fdr} = TR \cdot \lambda_{fdr} = TR \int v_{fdr}\, dt \,. \tag{4.68}$$

When exciting the rotor side,

$$i_{md} \approx i'_{fdr} = \tfrac{2}{3} \tfrac{1}{TR} i_{fdr} \,, \tag{4.69}$$

$$\lambda_{md} = \tfrac{1}{\sqrt{3}} \lambda_{cb} = \tfrac{1}{\sqrt{3}} \int v_{cb}\, dt \,. \tag{4.70}$$

The integration of the voltage in (4.68) and (4.70) is performed numerically. If full hysteresis loops are measured, then appropriate integration constants may be found

[3] The term *extrados* refers to the exterior curve of an arch—cf. the arch formed by a hysteresis loop.

such that the loops become symmetric around the origin. If the excitation is of the dc type, then the integration constants are unknown. However, they may be determined, for example, by requiring that the magnetizing flux characteristic (or its extrapolation) intersects the origin.

Similarly, for the q-axis step tests, the rotor is rotated and locked at $\theta_r = 90°$, and

$$i_{mq} \approx i_{qs} = \tfrac{2}{\sqrt{3}} i_c \,, \tag{4.71}$$

$$\lambda_{qs} = \lambda_{lqs} + \lambda_{mq} = \tfrac{1}{\sqrt{3}} \int (v_{cb} - 2r_s i_c) dt \,, \tag{4.72}$$

$$\hat{\lambda}_m = \sqrt{\alpha}\, \lambda_{mq} \,. \tag{4.73}$$

In this measurement, an "output" side does not exist; the voltage sensor is transferred to the input. The magnetizing flux linkage is estimated by subtracting the stator leakage flux component from the overall flux. This leakage inductance is obtained from the d-axis SSFR test (and so the d-axis is characterized first.)

The fundamental idea behind the procedure is to exploit the magnetic nonlinearity properties of the machine's iron. Specifically, two d-axis magnetization curves, $\lambda_{md}(TR)$ vs. i_{md} and λ_{md} vs. $i_{md}(TR)$ may be measured by exciting the machine from the armature and the field side, respectively. Each experiment contains a variable that is directly measurable and one that depends on the turns ratio. The turns ratio is a free parameter that is adjusted until a value is found for which the two nonlinear saturation curves coincide. The procedure will fail for linear curves. The curvature introduced by saturation is essential.

This process is illustrated in Fig. 4.11. The experimental equipment available consisted of (i) an ac source, whose current capabilities only allowed the machine to be saturated from the field side, and (ii) a dc source that was capable of saturating the machine from the stator side. First, a hysteresis loop was obtained using a 10 mHz ac source. Next, the upper extrados curve was obtained using the dc source. The field-excitation hysteresis loop remains fixed with respect to the flux linkage axis, but varies with respect to the current axis, in accordance with (4.69) and (4.70). The

stator-excitation extrados changes in the opposite way, i.e. it remains constant with respect to the current axis but varies with respect to flux, as in (4.67) and (4.68). Its dc offset is adjusted for each value of the turns ratio so that it coincides with the hysteresis loop close to the origin. There exists a single value of the turns ratio that minimizes the distance of the two curves. This value is quite accurately determined by trial-and-error. For this example, $TR = 0.087$.

The following rational polynomial expression for the d-axis inverse magnetizing inductance may be derived by a least-squares fitting technique:

$$\Gamma_{md}(\hat{\lambda}_m) = 10^3 \cdot \frac{1 - 1.122\hat{\lambda}_m + 0.3348\hat{\lambda}_m^2}{29.20 - 32.48\hat{\lambda}_m + 9.261\hat{\lambda}_m^2} \,. \tag{4.74}$$

This expression is valid for $\hat{\lambda}_m < \hat{\lambda}_{m1} = 1.6$ V·s. For greater values, the rational function diverges, and an appropriate continuation is defined so that the flux linkage increases linearly with current with the same slope as at $\hat{\lambda}_{m1}$.

The q-axis function, i.e. the parameters α, β of (4.46), may then be estimated from (4.74) using the value of leakage inductance obtained from the (autonomous) d-axis SSFR-based procedure described in the next section (0.97 mH). This yields

$$\Gamma_{mq}(\hat{\lambda}_m) = -6.580 + 2.461\, \Gamma_{md}(\hat{\lambda}_m) \,. \tag{4.75}$$

The fits of these functional forms to measured data are illustrated in Fig. 4.12.

4.3.4 Rotor identification

The third step in the characterization procedure is extraction of the rotor transfer functions, $\mathbf{Y}_d(s)$ and $Y_q(s)$, from SSFR measurements at the machine terminals. Due to the small-signal nature of the SSFR test, the magnetic materials are traversing minor loops of their respective B–H curves. If all the tests are performed under no magnetization bias, the incremental permeabilities will keep constant throughout the tests. The values estimated for the magnetizing inductances are not valid for normal operating conditions and will be discarded. It is assumed that the rotor circuits are

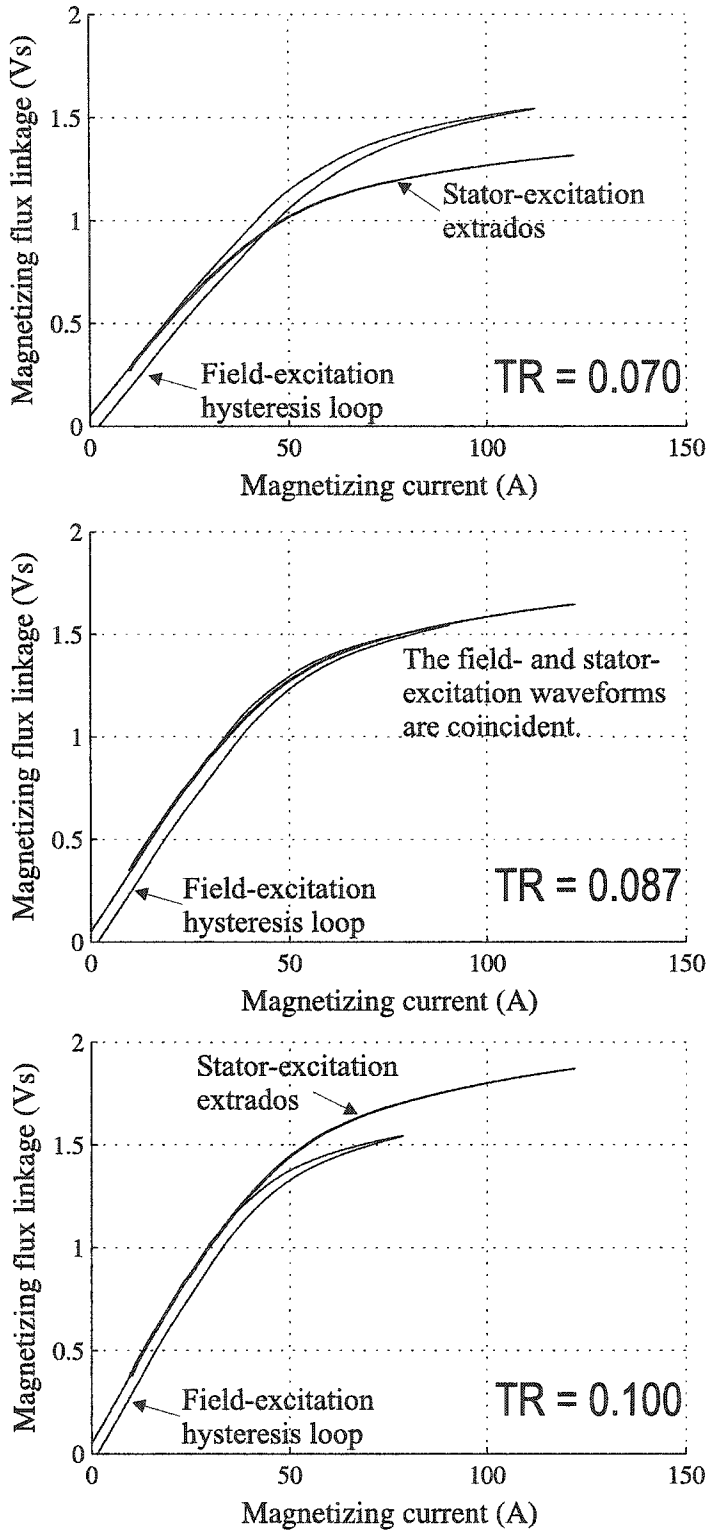

Fig. 4.11. Illustration of the turns ratio determination process.

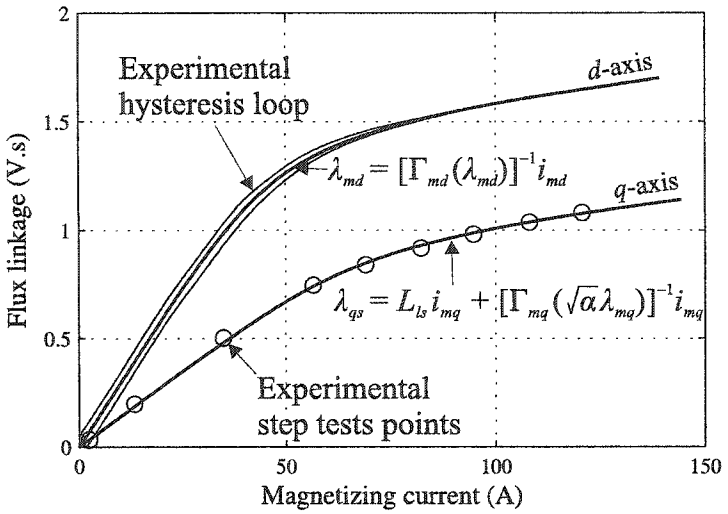

Fig. 4.12. Magnetization curves: λ_{md} vs. i_{md}, and λ_{qs} vs. i_{mq}.

independent of magnetizing flux. Model validation studies [140, 141] indicate that this is a workable assumption.

The elements of $\mathbf{Y}_d(s)$ ($y_{11}(s)$, $y_{12}(s)$, $y_{22}(s)$), and $Y_q(s)$ are strictly proper rational polynomial functions of the complex frequency. Their equations are repeated here for convenience:

$$y_{11}(s) = Y_{d0} \frac{1 + \alpha_1 s + \cdots + \alpha_{N_d-1} s^{N_d-1}}{s(1 + \delta_1 s + \cdots + \delta_{N_d-1} s^{N_d-1})}, \tag{4.76}$$

$$y_{12}(s) = -Y_{d0} \frac{1 + \beta_1 s + \cdots + \beta_{N_d-1} s^{N_d-1}}{s(1 + \delta_1 s + \cdots + \delta_{N_d-1} s^{N_d-1})}, \tag{4.77}$$

$$y_{22}(s) = Y_{d0} \frac{1 + \gamma_1 s + \cdots + \gamma_{N_d-1} s^{N_d-1}}{s(1 + \delta_1 s + \cdots + \delta_{N_d-1} s^{N_d-1})}, \tag{4.78}$$

$$Y_q(s) = Y_{q0} \frac{1 + \epsilon_1 s + \cdots + \epsilon_{N_q-1} s^{N_q-1}}{1 + \zeta_1 s + \cdots + \zeta_{N_q} s^{N_q}}. \tag{4.79}$$

Setting $s = j\omega$, the transfer functions (4.76)–(4.79) relate the rotor currents and voltages in the frequency-domain by

$$\begin{bmatrix} \tilde{i}_{dr} \\ \tilde{i}'_{fdr} \end{bmatrix} = [\mathbf{Y}_d(s)] \begin{bmatrix} \tilde{v}_{md} \\ \tilde{v}_{d2} \end{bmatrix} = \begin{bmatrix} y_{11}(s) & y_{12}(s) \\ y_{12}(s) & y_{22}(s) \end{bmatrix} \begin{bmatrix} \tilde{v}_{md} \\ \tilde{v}_{d2} \end{bmatrix}, \tag{4.80}$$

$$\tilde{i}_{qr} = Y_q(s)\, \tilde{v}_{mq}, \tag{4.81}$$

where the tilde denotes phasor quantities. After manipulation, the internal rotor quantities are related to measurable terminal quantities by

$$\begin{bmatrix} \tilde{i}_{ds} - \frac{1}{sL_{md}}\left[\tilde{v}_{ds} - (r_s + sL_{ls})\tilde{i}_{ds}\right] \\ \tilde{i}'_{fdr} \end{bmatrix} = \begin{bmatrix} y_{11}(s) & y_{12}(s) \\ y_{12}(s) & y_{22}(s) \end{bmatrix} \begin{bmatrix} \tilde{v}_{ds} - (r_s + sL_{ls})\tilde{i}_{ds} \\ \tilde{v}'_{fdr} - r'_{fdr}\tilde{i}'_{fdr} \end{bmatrix}, \tag{4.82}$$

$$\tilde{i}_{qs} - \frac{1}{sL_{mq}}\left[\tilde{v}_{qs} - (r_s + sL_{ls})\tilde{i}_{qs}\right] = Y_q(s)\left[\tilde{v}_{qs} - (r_s + sL_{ls})\tilde{i}_{qs}\right]. \tag{4.83}$$

Parameter set uniqueness properties

It is useful to know whether a given rotor model may be uniquely parameterized, since, if not, the identification algorithm may converge to a different parameter set every time it is executed. This section addresses the uniqueness properties of the proposed synchronous machine model. The existence of multiple equivalent parameter sets will be shown using the methodology outlined in [119].

The model under consideration is shown in Fig. 4.8. Under small-signal conditions, the magnetizing branch inductances become linear elements, and the model represents a purely linear circuit. In general, the q-axis leakage inductance is not equal to the d-axis leakage inductance.

The stator and field winding resistances may be accurately measured (at dc), and will thus be considered as known. The turns ratio is also known. Hence, the parameters to complete the characterization of the d-axis are L_{lds}, L_{md}, and the rotor two-port network transfer functions. The goal of this analysis is to demonstrate what conditions must be satisfied between two parameter sets, so that the d-axis exhibits identical behavior. The results may be summarized in the following theorem, whose proof is given in Appendix B:

Theorem 3 *If two d-axis networks are equivalent, then the following conditions between their parameters are satisfied (the superscript '$\star$' is used to denote the parameters of the second network):*

$$TR\, L^{\star}_{md} = TR^{\star} L_{md}\,, \tag{4.84}$$

$$L_{lds} + L_{md} = L^{\star}_{lds} + L^{\star}_{md}\,, \tag{4.85}$$

and

$$\mathbf{Z}^{\star}_{d}(s) = \left(\frac{TR^{\star}}{TR}\right)^{2} \begin{bmatrix} z_{11}(s) + s\frac{TR}{TR^{\star}}(L_{lds} - L^{\star}_{lds}) & z_{12}(s) \\ z_{21}(s) & z_{22}(s) \end{bmatrix}. \tag{4.86}$$

Equation (4.86) implies that the rotor impedance parameters (given by the inverse of the admittance matrix, $\mathbf{Z}_d(s) = \mathbf{Y}_d^{-1}(s)$) must all be scaled by the factor $(TR^{\star}/TR)^2$, with the exception of $z^{\star}_{11}(s)$, which contains one additional term. This term may be accounted for by adding an external inductance,

$$L_{\text{ext}} = \left(\frac{TR^{\star}}{TR}\right)(L_{lds} - L^{\star}_{lds}) = \left(\frac{TR^{\star}}{TR}\right)^{2} L_{md} - L^{\star}_{md}\,, \tag{4.87}$$

in series between the magnetizing branch and the two-port network.

If the turns ratio were unknown, there would be an infinite number of equivalent parameter sets. However, if it is fixed to its measured (from the aforementioned procedure) value, then the network is unique. Hence, the identification procedure should ideally converge to the same parameter set each time.

The q-axis is completely characterized by L_{lqs}, L_{mq} and $Y_q(s)$. In this case, the following theorem holds (for a proof refer to Appendix B):

Theorem 4 *If two q-axis networks are equivalent, then their parameters must satisfy:*

$$L_{lqs} + L_{mq} = L^{\star}_{lqs} + L^{\star}_{mq}\,, \tag{4.88}$$

$$Z^{\star}_{q}(s) = \left(\frac{L^{\star}_{mq}}{L_{mq}}\right)^{2} Z_q(s) + \left[\frac{(L^{\star}_{mq})^2}{L_{mq}} - L^{\star}_{mq}\right] s\,. \tag{4.89}$$

To force a unique solution, the leakage inductance is set to a pre-specified value, which due to lack of better information is arbitrarily equal to the d-axis value, i.e. $L_{lqs} = L_{lds} = L_{ls}$.

Identification algorithm and experimental results

To accurately capture the d-axis rotor dynamics, multiple SSFR experiments are required. SSFR experiments were conducted using the following test setups: (i) exciting the field winding side with the stator terminals open-circuited, (ii) exciting the stator side with the field open, and (iii) exciting the stator side with the field shorted. For these tests, the following transfer functions were measured (the subscript indicates the setup number):

$$\left(\tilde{v}_{ds}/\tilde{i}'_{fdr}\right)_{(\mathrm{i})} = -\frac{y_{12}(s)\, sL_{md}}{y_{22}(s)+D(s)\, sL_{md}}\,, \tag{4.90}$$

$$\left(\tilde{v}'_{fdr}/\tilde{i}'_{fdr}\right)_{(\mathrm{i})} = r'_{fdr} + \frac{1+y_{11}(s)\, sL_{md}}{y_{22}(s)+D(s)\, sL_{md}}\,, \tag{4.91}$$

$$\left(\tilde{v}_{ds}/\tilde{i}_{ds}\right)_{(\mathrm{ii})} = r_s + sL_{ls} + \frac{y_{22}(s)\, sL_{md}}{y_{22}(s)+D(s)\, sL_{md}}\,, \tag{4.92}$$

$$\left(\tilde{v}'_{fdr}/\tilde{i}_{ds}\right)_{(\mathrm{ii})} = -\frac{y_{12}(s)\, sL_{md}}{y_{22}(s)+D(s)\, sL_{md}}\,, \tag{4.93}$$

$$\left(\tilde{v}_{ds}/\tilde{i}_{ds}\right)_{(\mathrm{iii})} = r_s + sL_{ls} + \frac{[1+r'_{fdr}y_{22}(s)]\, sL_{md}}{1+r'_{fdr}y_{22}(s)+[y_{11}(s)+r'_{fdr}D(s)]\, sL_{md}}\,, \tag{4.94}$$

$$\left(\tilde{i}'_{fdr}/\tilde{i}_{ds}\right)_{(\mathrm{iii})} = \frac{y_{12}(s)\, sL_{md}}{1+r'_{fdr}y_{22}(s)+[y_{11}(s)+r'_{fdr}D(s)]\, sL_{md}}\,, \tag{4.95}$$

where $D(s) = y_{11}(s)\, y_{22}(s) - y_{12}^2(s)$ is the determinant of $\mathbf{Y}_d(s)$. These equations were obtained by manipulation of (4.82).

The q-axis is a single-port network, so only its input impedance is measurable:

$$\tilde{v}_{qs}/\tilde{i}_{qs} = r_s + sL_{ls} + \frac{sL_{mq}}{1+Y_q(s)\, sL_{mq}}\,. \tag{4.96}$$

To quantify the difference between a series of measured and estimated data points, an appropriate error function must be defined. The one used herein takes into account the difference in both magnitude and angle of the complex quantities. Let x denote a transfer function for which $\{\hat{x}_k\}$ is the set of measured data, and $\{x_k\}$ the

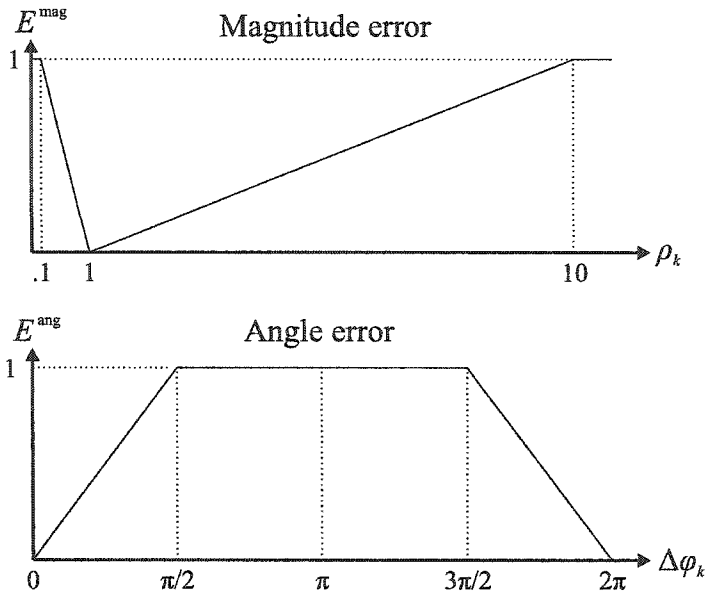

Fig. 4.13. Plots of the normalized magnitude and angle error functions.

corresponding set of predicted data for $k = 1, \ldots, N$ points. A normalized magnitude error is defined based on $\rho_k = |\hat{x}_k/x_k|$ by

$$E^{\text{mag}}(\rho_k) = \begin{cases} \frac{\min\{\rho_k, 10\}-1}{9} & \text{if } \rho_k \geq 1, \\ \frac{1-\max\{\rho_k, 0.1\}}{0.9} & \text{if } \rho_k < 1. \end{cases} \tag{4.97}$$

Also, a normalized angle difference error is defined based on $\Delta\phi_k = |\angle\hat{x}_k - \angle x_k|$ by

$$E^{\text{ang}}(\Delta\phi_k) = \begin{cases} \frac{\min\{\Delta\phi_k, \pi/2\}}{\pi/2} & \text{if } \Delta\phi_k \in [0, \pi], \\ \frac{\min\{2\pi-\Delta\phi_k, \pi/2\}}{\pi/2} & \text{if } \Delta\phi_k \in [\pi, 2\pi]. \end{cases} \tag{4.98}$$

These error functions return a value from 0 to 1, and all errors outside the specified bounds are mapped to 1, as shown in Fig. 4.13.

The total prediction error for a transfer function is computed by averaging the length and angle errors:

$$E(x) = \frac{1}{2N}\sum_{k=1}^{N}\left[E^{\text{mag}}(\rho_k) + E^{\text{ang}}(\Delta\phi_k)\right]. \tag{4.99}$$

In this example, the summations were taken over all points in the frequency range 10 mHz–1 kHz. The total d-axis error is the mean error of the three experimental setups, i.e.

$$E_d = \tfrac{1}{3}\left[E_{d(\mathrm{i})} + E_{d(\mathrm{ii})} + E_{d(\mathrm{iii})}\right] , \tag{4.100}$$

where

$$E_{d(\mathrm{i})} = \tfrac{1}{2}\left\{E\left[\left(\tilde{v}_{ds}/\tilde{i}'_{fdr}\right)_{(\mathrm{i})}\right] + E\left[\left(\tilde{v}'_{fdr}/\tilde{i}'_{fdr}\right)_{(\mathrm{i})}\right]\right\} , \tag{4.101}$$

$$E_{d(\mathrm{ii})} = \tfrac{1}{2}\left\{E\left[\left(\tilde{v}_{ds}/\tilde{i}_{ds}\right)_{(\mathrm{ii})}\right] + E\left[\left(\tilde{v}'_{fdr}/\tilde{i}_{ds}\right)_{(\mathrm{ii})}\right]\right\} , \tag{4.102}$$

$$E_{d(\mathrm{iii})} = \tfrac{1}{2}\left\{E\left[\left(\tilde{v}_{ds}/\tilde{i}_{ds}\right)_{(\mathrm{iii})}\right] + E\left[\left(\tilde{i}'_{fdr}/\tilde{i}_{ds}\right)_{(\mathrm{iii})}\right]\right\} . \tag{4.103}$$

The q-axis error is

$$E_q = E\left(\tilde{v}_{qs}/\tilde{i}_{qs}\right) . \tag{4.104}$$

The goal of the parameter identification procedure is a set of parameters that minimize the prediction errors. One way to achieve this would be to use least squares fitting. Examination of (4.82) and (4.83) reveals that if L_{ls}, L_{md} and L_{mq} are known, a linear system may be formed having the coefficients of the transfer functions as unknowns. The number of rows (proportional to the number of experimental points) would be much larger than the number of unknown parameters, and a solution would be obtained in the least squares sense. Values for L_{ls}, L_{md} and L_{mq} could be iteratively provided, for example by a simple random search, or by a brute-force enumerative search, until the minimization of the prediction error.

However, such a formulation leads to extremely ill-conditioned least-squares problems. Due to the formation of Vandermonde matrix blocks in the system matrix, the condition number increases rapidly with the system order as well as range of frequencies [163]. For a single-input/single-output system, an appropriate weighting function may be selected to obtain a reasonable fit over a wide frequency range [148,153]—a procedure which is time-consuming, sensitive to the experimental data, and that requires an experienced analyst. For multiple-input/multiple-output systems, the weighting function technique is not readily applicable. Hence, the least squares method can prove highly problematic.

As an alternative, genetic algorithms may be utilized. For mapping the parameters to be identified to the genes of the GA, it is convenient to factor the transfer functions (4.76)–(4.79) as follows:

$$y_{11}(s) = Y_{d0}\frac{(1+\tau_{\alpha 1}s)\cdots(1+\tau_{\alpha(N_d-1)}s)}{s(1+\tau_{\delta 1}s)\cdots(1+\tau_{\delta(N_d-1)}s)}, \tag{4.105}$$

$$y_{12}(s) = -Y_{d0}\frac{(1+\tau_{\beta 1}s)\cdots(1+\tau_{\beta(N_d-1)}s)}{s(1+\tau_{\delta 1}s)\cdots(1+\tau_{\delta(N_d-1)}s)}, \tag{4.106}$$

$$y_{22}(s) = Y_{d0}\frac{(1+\tau_{\gamma 1}s)\cdots(1+\tau_{\gamma(N_d-1)}s)}{s(1+\tau_{\delta 1}s)\cdots(1+\tau_{\delta(N_d-1)}s)}, \tag{4.107}$$

$$Y_q(s) = Y_{q0}\frac{(1+\tau_{\epsilon 1}s)\cdots(1+\tau_{\epsilon(N_q-1)}s)}{(1+\tau_{\zeta 1}s)\cdots(1+\tau_{\zeta N_q}s)}. \tag{4.108}$$

This is done because it is easier to set a search range for time constants than polynomial coefficients. Herein, it is assumed that all time constants are real. If this is not the case, then it is straightforward to modify the parameterization in such a way as to accommodate complex conjugate pairs [164]. Since the minimal polynomial orders are not known beforehand, it is assumed that $N_d = 2$ and $N_q = 1$. If the GA would fail to provide a satisfactory fit, then N_d, N_q would be increased [165]. However, these values were adequate for our case.

Two GA studies need to be run—one for each axis. The parameter values for the d-axis GA (see Section 2.2) were set to: $N_{\text{ind}} = 200$, $N_{\text{gen}} = 1500$, $\eta = 2$, $c_{\sigma\text{-tr}} = 1.0$, $p_{\text{mt}} = 0.6$, $p_{\text{tm}} = 0.00714$ $(= 1/7/20)$, $\sigma_{\text{pm}} = 0.3$, $p_{\text{pm}} = 0.0286$ $(= 1/7/5)$, $N_{\text{rs}} = 50$, $\sigma_{\text{rs}} = 0.01$. For the q-axis GA, the parameter values were: $N_{\text{ind}} = 100$, $N_{\text{gen}} = 200$, $\eta = 2$, $c_{\sigma\text{-tr}} = 2.0$, $p_{\text{mt}} = 0.6$, $p_{\text{tm}} = 0.00667$ $(= 1/3/50)$, $\sigma_{\text{pm}} = 0.3$, $p_{\text{pm}} = 0.0167$ $(= 1/3/20)$, $N_{\text{rs}} = 25$, $\sigma_{\text{rs}} = 0.01$. The fitness is defined as the inverse of the errors (4.100) and (4.104), i.e. $f = 1/E_d$ or $f = 1/E_q$, accordingly.

The study-specific GA settings are listed in Table 4.1. The evolution of the d- and q-axis GAs is displayed in Figs. 4.14 and 4.15. The GA was always able to generate a highly fit individual, with approximately the same genes, as expected from the uniqueness properties of the networks. The parameter set shown corresponds to the highest fitness among several evolutions. The magnetizing inductances were

Table 4.1
List of GA variables and settings for synchronous generator characterization.

	variable	units	gene type	min.	max.	result
d-axis	L_{md}	mH	lin.	5	30	14.26
	L_{ls}	mH	exp.	0.01	5	0.97
	Y_{d0}	1/H	lin.	10	2000	1239.6
	$\tau_{\alpha 1}$	ms	exp.	0.1	10^4	18.25
	$\tau_{\beta 1}$	ms	exp.	0.1	10^4	12.87
	$\tau_{\gamma 1}$	ms	exp.	0.1	10^4	9.24
	$\tau_{\delta 1}$	ms	exp.	0.1	10^4	1.57
q-axis	L_{mq}	mH	lin.	5	30	8.75
	Y_{q0}	1/H	exp.	0.01	100	5.82
	$\tau_{\zeta 1}$	ms	exp.	0.01	10^4	1.46

considerably lower than the ones obtained from the step tests. This is attributed to the incremental permeability of the iron for the small-signal SSFR test; their estimated values are hereafter discarded.

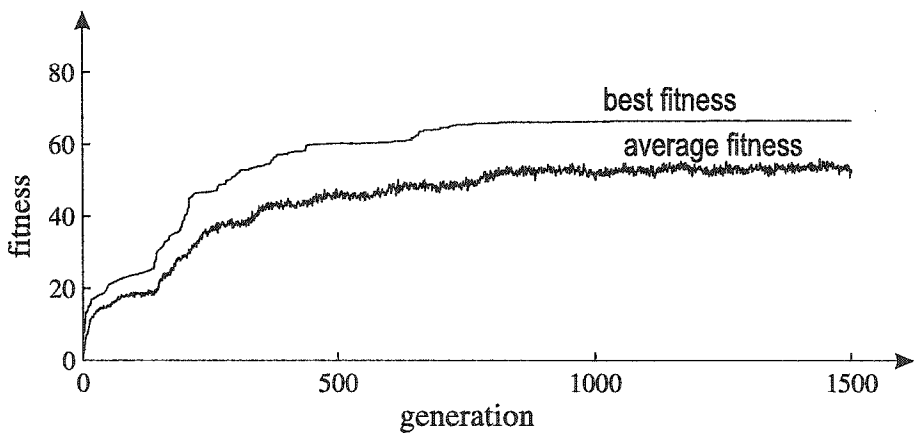

Fig. 4.14. Plot of fitness vs. generation number for the d-axis GA.

The SSFR experimental points, and the fitted curves are shown in Fig. 4.16. Data was taken as high as 10 kHz, where parasitic capacitive effects become evident, so the fitting was constrained to 1 kHz. The errors, as defined in (4.101)–(4.104), were: $E_{d(\mathrm{i})} = 0.0168$, $E_{d(\mathrm{ii})} = 0.0098$, $E_{d(\mathrm{iii})} = 0.0185$ and $E_q = 0.0084$. The algorithm was sufficiently robust not to be affected from noise at the low-frequency end.

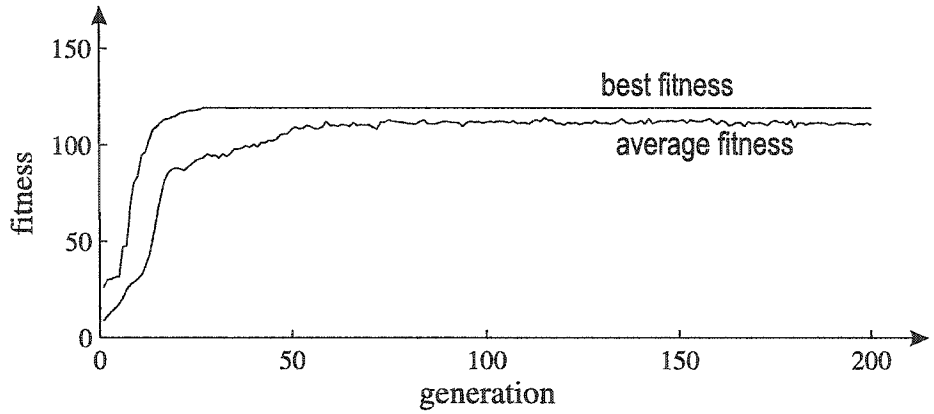

Fig. 4.15. Plot of fitness vs. generation number for the q-axis GA.

For instance, measurements (a) and (d) should be identical—assuming the system is linear, and indeed the estimated responses are. However, the low-frequency data of experiment (a) were contaminated with noise. This example underlines the importance of performing multiple experiments and appropriately utilizing all available data.

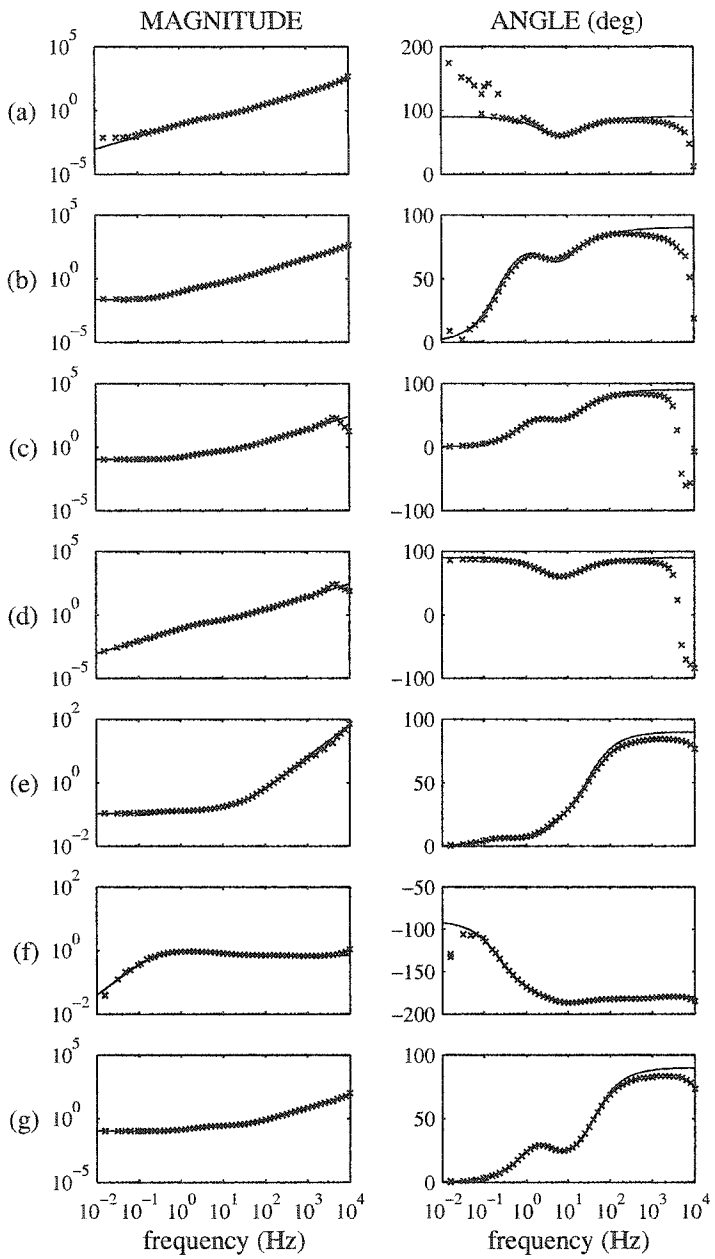

Fig. 4.16. The SSFR measurements and estimates.

(a): $\left(\tilde{v}_{ds}/\tilde{i}'_{fdr}\right)_{\text{(i)}}$, (b): $\left(\tilde{v}'_{fdr}/\tilde{i}'_{fdr}\right)_{\text{(i)}}$,
(c): $\left(\tilde{v}_{ds}/\tilde{i}_{ds}\right)_{\text{(ii)}}$, (d): $\left(\tilde{v}'_{fdr}/\tilde{i}_{ds}\right)_{\text{(ii)}}$,
(e): $\left(\tilde{v}_{ds}/\tilde{i}_{ds}\right)_{\text{(iii)}}$, (f): $\left(\tilde{i}'_{fdr}/\tilde{i}_{ds}\right)_{\text{(iii)}}$,
(g): $\left(\tilde{v}_{qs}/\tilde{i}_{qs}\right)$

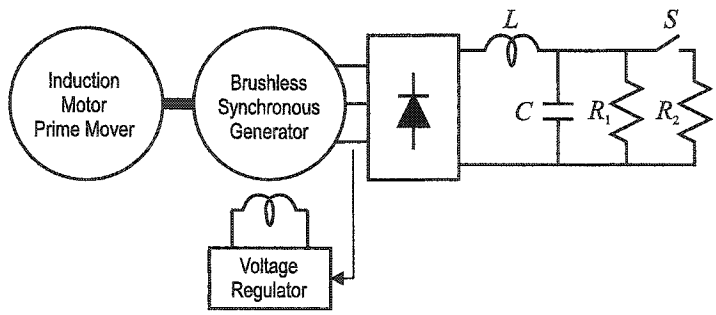

Fig. 4.17. Experimental setup of the synchronous generator model validation study.

4.4 Experimental Validation

The proposed synchronous generator model is validated using the experimental setup depicted in Fig. 4.17; therein, the generator is feeding a nonlinear rectifier load. The generator's prime mover is a field-oriented induction motor drive system that is programmed to maintain constant rated speed (its mathematical model is described in Appendix C). The voltage regulator uses a proportional–integral control strategy to maintain the commanded voltage (560 V line-to-line, fundamental rms) at the generator terminals; the brushless exciter's field current is controlled with a hysteresis modulator (this model is described in Appendix D). The generator is loaded with an uncontrolled rectifier that feeds a resistive load through an LC filter. The load parameters are: $L = 7.5$ mH, $C = 500$ μF, $R_1 = R_2 = 32.5\,\Omega$. The brushless exciter is represented by the model that is set forth later in this dissertation.

For the first experiment, the switch S is closed so that the total resistive load is $R = 16.3\,\Omega$. The generator's voltage reference is modified according to the profile shown in Fig. 4.18. The envelope is computed from the synchronous reference frame voltages, [4] $v_{\text{ll,env}} = \sqrt{3\left[\left(v_{qs}^{e}\right)^2 + \left(v_{ds}^{e}\right)^2\right]}$. Each of the seven trapezoid shaped blocks

[4]For a three-phase balanced voltage set, $[(v_{qs}^{e})^2 + (v_{ds}^{e})^2]^{\frac{1}{2}}$ attains a constant value, equal to the peak of the line-to-neutral voltage. Therefore, in this case $v_{\text{ll,env}}$ is also a constant that corresponds to the peak of the line-to-line voltages. However, in practice, the terminal voltages are not purely sinusoidal, thus creating ripple in the qd-axes synchronous voltages, which in turn reflects on the waveform of $v_{\text{ll,env}}$.

is characterized by a different slope (the same for rise and fall) and peak voltage: (1) 20000 V/s, 560 V; (2)–(4) 2000 V/s, 560 V, 420 V, 280 V respectively; (5)–(7) 400 V/s, 560 V, 420 V, 280 V respectively. [Note: the above voltage values correspond to rms quantities.]

This series of commanded voltage steps creates an extended period of significant disturbances, and tests the validity of the model for large-transients simulations. The actual voltage exhibits an overshoot, which is more pronounced for the faster slew rate steps. Moreover, due to the exciter's magnetically hysteretic behavior, it does not fall to zero. The predictions for mechanical speed (Fig. 4.19) are in excellent agreement with the experimental results. Finally, detailed voltage and current waveforms are depicted in Fig. 4.20. Since the proposed model is based on the *qd*-axes theory, higher harmonics attributable to the machine's design are not represented. This reflects on the voltage waveforms of Fig. 4.18, wherein the experimental waveform contains more ripple than the simulated waveform. However, harmonics that are caused by the nonlinearity of the load are predicted accurately.

The second experiment involves sudden load changes. Initially, the switch S is open; at $t = t_1$ it is closed, and at $t = t_2$ it is opened again. In Fig. 4.21, a low-pass filtered version of the line-to-line voltage "envelope" is depicted. On average, the simulated and experimental waveforms are similar. As discussed above, the experimental voltage includes higher-order harmonics caused by slot effects. The mechanical speed waveforms are illustrated in Fig. 4.22.

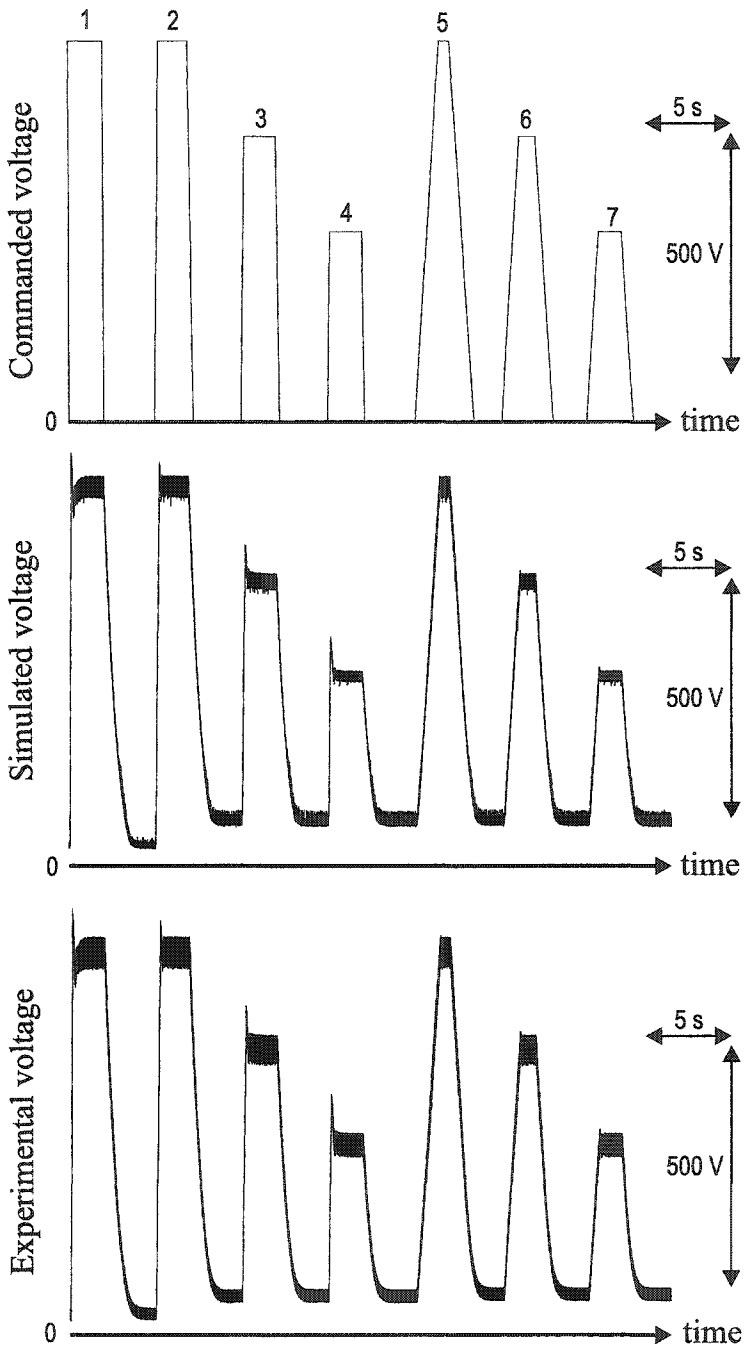

Fig. 4.18. Plots of the commanded and actual line-to-line voltage "envelopes," for a series of reference voltage steps.

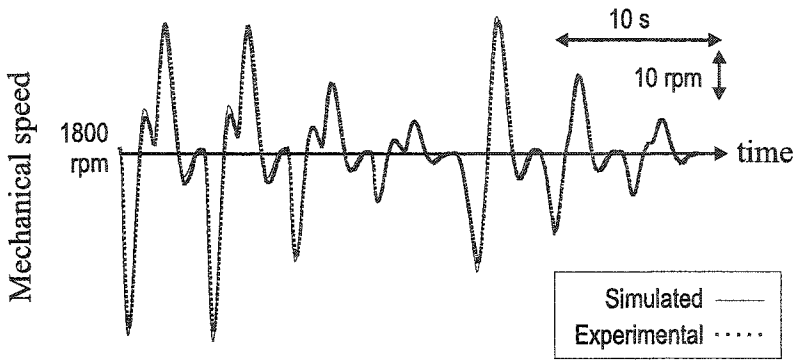

Fig. 4.19. Shaft speed variation around the commanded value of 1800 rpm, during a series of reference voltage steps.

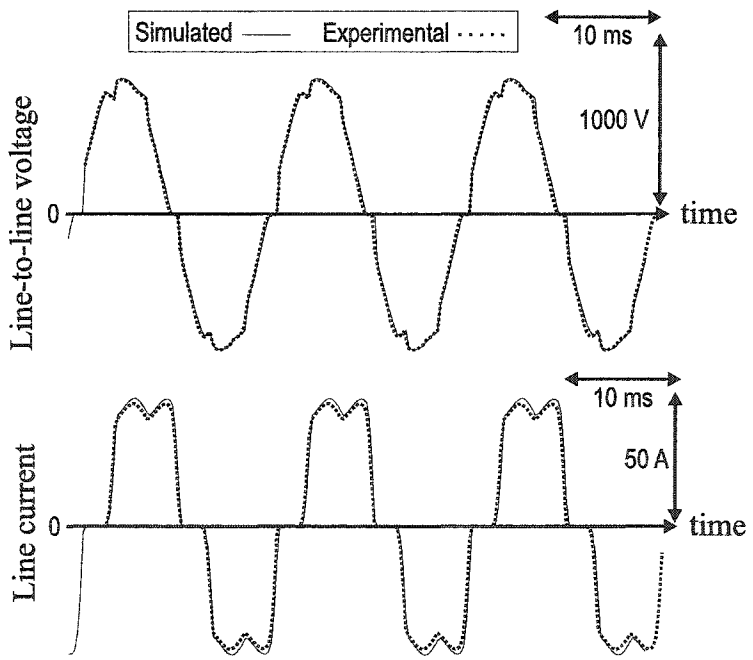

Fig. 4.20. Steady-state voltage and current waveforms (560 V, line-to-line, rms).

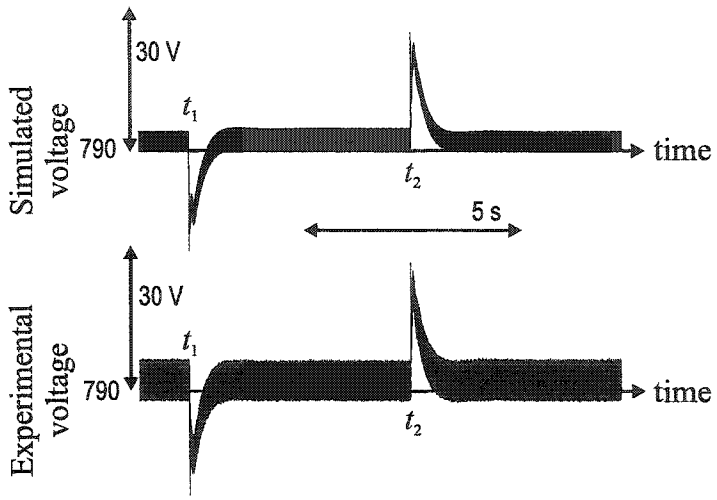

Fig. 4.21. Line-to-line voltage "envelope," during a step load change. [Low-pass filtered; $\tau_f = 2.65$ ms.]

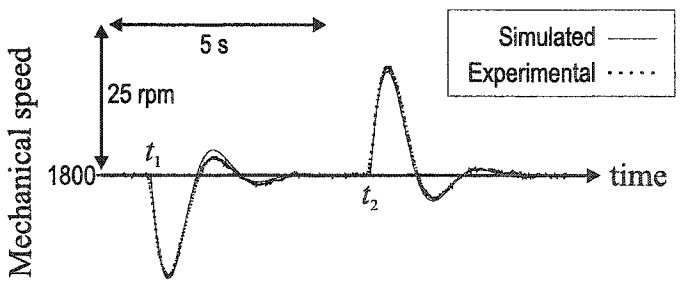

Fig. 4.22. Shaft speed variation around the commanded value of 1800 rpm, during a step load change.

4.5 Summary

An integrated perspective on synchronous machine modeling, using arbitrary transfer function representations that replace the rotor's equivalent circuit structures, has been presented. This approach offers several advantages, such as the direct incorporation of frequency response results into the model—without further consideration of equivalent circuit parameter identification—and accurate representation of magnetic saturation effects. The model retains the computational efficiency of the qd-axes theoretical framework and is suitable for small- and large-signal time-domain simulations of power systems.

A suitable experimental characterization procedure for the proposed model has been proposed. The procedure consists of magnetizing curve tests and frequency response tests. Both experiments are performed off-line at standstill and are relatively easy to carry out. As part of this procedure, a novel method for extracting the turns ratio from the magnetizing curve data has been set forth. It was shown how the transfer functions of the rotor circuits as well as the stator leakage inductance may be extracted from manipulation of the SSFR, using a genetic algorithm to solve the nonlinear optimization problem.

This work is pending publication in a peer-reviewed journal [166, 167].

5. BRUSHLESS EXCITATION MODELING

5.1 Introduction

Brushless excitation of synchronous generators offers increased reliability and reduced maintenance requirements [168, 169]. In these systems, both the exciter machine and the rectifier are mounted on the same shaft as the main alternator (Fig. 5.1). Since the generator's output voltage is regulated by controlling the exciter's field current, the exciter is an integral part of a generator's control loop and has significant impact on a power system's dynamic behavior.

In this section, a brushless exciter model suitable for time-domain simulations of power systems is set forth. The analysis follows the common approach of decoupling the main generator from the exciter–rectifier. Because of the large inductance of a generator's field winding, the field current is slow-varying [170, 171]. Therefore, the

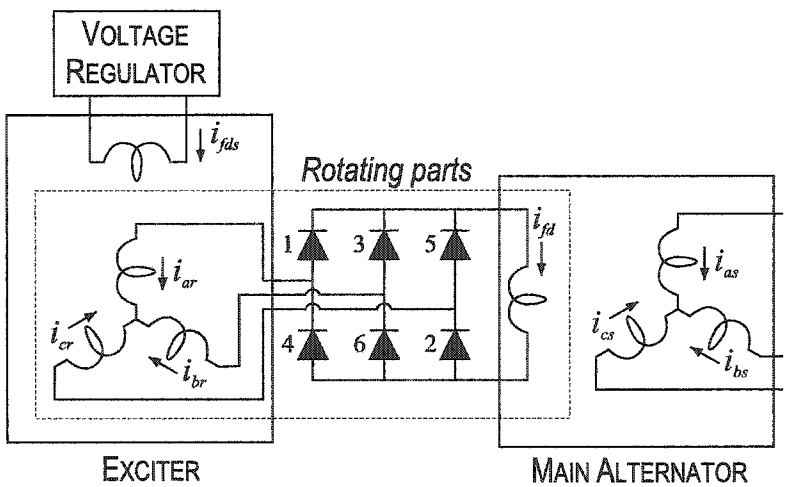

Fig. 5.1. Schematic of a brushless synchronous generator.

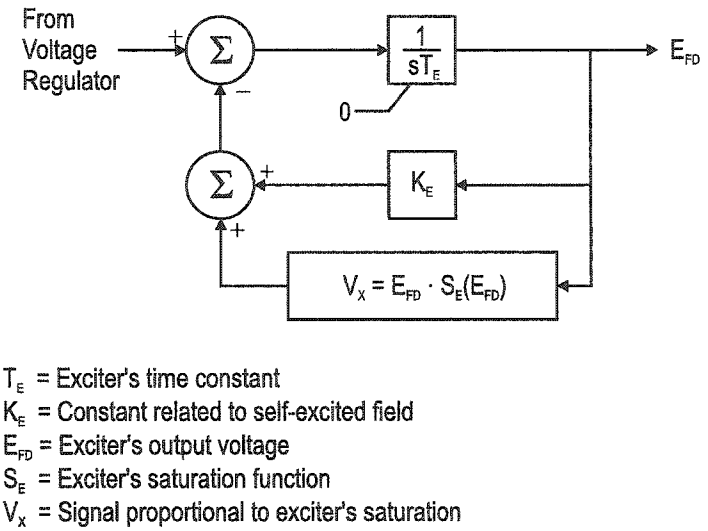

Fig. 5.2. The IEEE Standard AC5A brushless exciter.

modeling problem may be reduced to that of a synchronous machine (the exciter) connected to a rectifier load.

For power system studies, detailed waveforms of rotating rectifier quantities are usually not important (unless, for example, diode failures [172] or estimation of winding losses are of interest). Moreover, avoiding the simulation of the internal rectifier increases computational efficiency and reduces modeling complexity [173, 174]. The machine–rectifier configuration may be viewed as an ac voltage source in series with a constant commutating inductance [175]; however, this overly simplified model does not accurately capture the system's operational characteristics [176–180]. The widely used brushless exciter model proposed by IEEE (see Fig. 5.2) represents the exciter as a first-order system [181]; it was originally devised for small-signal analyses and its applicability to large-disturbance studies remains questionable [182]. An average-value machine–rectifier model that allows linking of a *qd*-axes machine model to dc quantities was derived in [183]. This model is based on the actual physical structure of an electric machine and maintains its validity during large-transient simulations.

In this work, the theory of [183] (which covered only mode I operation) is extended to all three rectification modes [184]. This is necessary for brushless excitation systems, because the exciter's armature current—directly related to the generator's field current—is strongly linked to power system dynamics [170]. During transients, the rectifier's operation may vary from mode I to the complete short-circuit occurring at the end of mode III [173]. The exciter–rectifier configuration is analyzed on an average-value basis in a later section.

The incorporation of ferromagnetic hysteresis is an additional feature of the proposed model. Brushless synchronous generators may use the exciter's remanent magnetism to facilitate self-starting, when no other source is available to power the voltage regulator. However, the magnetization state directly affects the level of excitation required to maintain a commanded voltage at the generator terminals. Hence, representation of hysteresis enhances the model's fidelity with respect to the voltage regulator variables.

Hysteresis is modeled herein using Preisach's theory [185–189], using the so-called classical Preisach model (which describes "static" hysteresis, where the speed of the field's variation has no effect on branching). Preisach's theory has been employed for modeling magnetic cores in power electronic applications [190–196]; it has also been applied in finite element analyses of electric machines [197–203], usually from the viewpoint of iron loss computation.

The Preisach model guarantees that minor loops close to the previous reversal point [204–206]. This property is essential for accurate representation of the exciter's magnetizing path behavior. Hysteresis models that do not predict closed minor loops, such as the widely used Jiles–Atherton model [207–213], are not appropriate. To see this, consider a brushless generator connected to a nonlinear load that induces terminal current ripple. This ripple transfers to the exciter's magnetizing branch current, and in the "steady-state" a minor loop trajectory is traced on the λ–i plane. If the loop is not closed, the flux can drift away from the correct operating point.

We begin with a notational and model overview. Next, a brief review of Preisach's theory is set forth. Then model development begins in earnest, with the development of the Preisach hysteresis model, a reduced-order machine model, and the rotating-rectifier average-value model. We conclude with a validation of the model by comparison to experimental results.

5.2 Notation and Model Overview

Throughout this work, matrix and vector quantities appear in bold font. The primed stator quantities denote referral to the rotor through the turns ratio, which is defined as the ratio of armature-to-field turns, $TR = N_r/N_{fds}$. The electrical rotor position, θ_r, and speed, ω_r, are $P/2$ times the mechanical rotor position, θ_{rm}, and speed, ω_{rm}, where P is the number of poles. The analysis takes place in the stator reference frame (since the field winding in the exciter machine is located on the stator). The transformation of rotating abc to stationary $qd0$ variables is defined by [5]

$$\mathbf{f}^s_{qd0r} = \mathbf{K}^s_r(\theta_r)\mathbf{f}_{abcr}\,, \tag{5.1}$$

where [1]

$$\mathbf{K}^s_r(\theta_r) = \frac{2}{3}\begin{bmatrix} \cos\theta_r & \cos\left(\theta_r + \frac{2\pi}{3}\right) & \cos\left(\theta_r - \frac{2\pi}{3}\right) \\ -\sin\theta_r & -\sin\left(\theta_r + \frac{2\pi}{3}\right) & -\sin\left(\theta_r - \frac{2\pi}{3}\right) \\ \frac{1}{2} & \frac{1}{2} & \frac{1}{2} \end{bmatrix}. \tag{5.2}$$

Since a neutral connection is not present, $f_{0r} = 0$.

The components of the proposed excitation model are shown in Fig. 5.3. The exciter model connects to the main alternator model through the field voltage, v_{fd}, and current, i_{fd}; it also requires ω_{rm}. The voltage regulator model provides the voltage to the exciter's field winding, v_{fds}, and receives the current, i_{fds}. The exciter

[1] The minus sign in the second row and the apparent interchange of the second and third columns from Park's transformation (as defined in [5]) arises from using a counter-clockwise positive direction for rotor position coupled with the location of the ac windings on the rotor.

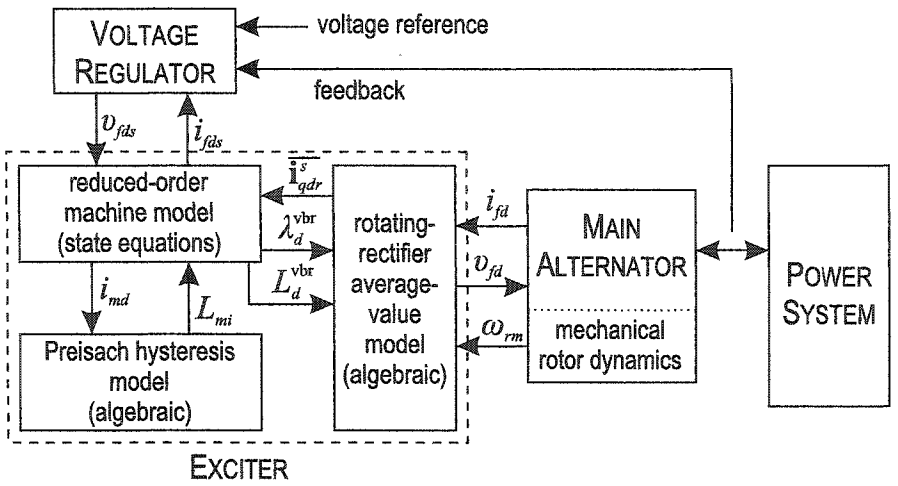

Fig. 5.3. Interconnection block diagram (input–output relationships) for the proposed exciter model.

model is comprised of three separate models, namely, the rotating-rectifier average-value model, the Preisach hysteresis model, and the reduced-order machine model.

The rotating-rectifier average-value model computes the average currents flowing in the exciter armature, $\overline{\mathbf{i}^s_{qdr}}$, based on i_{fd}, the voltage-behind-reactance (VBR) d-axis flux linkage, λ_d^{vbr}, and the (varying) VBR d-axis inductance, L_d^{vbr}. (The q-axis VBR inductance is also used, but is considered constant.) These voltage-behind-reactance quantities are computed from the reduced-order machine model. The hysteresis model performs the computations and bookkeeping required to use Preisach's hysteresis theory. Its only input is the d-axis magnetizing current, i_{md}; its output is the incremental magnetizing inductance, L_{mi}, that represents the slope of the hysteresis loop at a given instant. The integrations of the state equations are performed inside the reduced-order machine model block. The states are i_{fds} and the d-axis magnetizing flux, λ_{md}. The aforementioned variables will be defined formally in the ensuing analysis. Notice that the proposed model is applicable whether hysteresis is represented or not; in case of a linear magnetizing path, the hysteresis block is replaced by a constant inductance term.

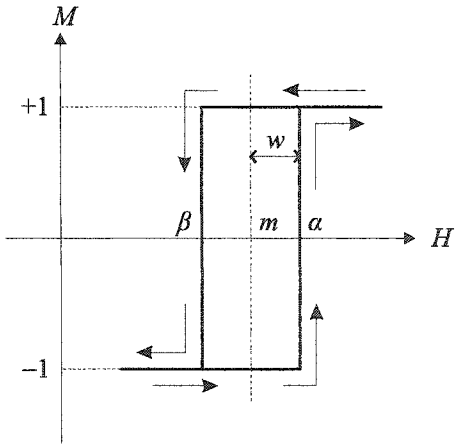

Fig. 5.4. Elementary hysteresis loop.

5.3 Hysteresis Modeling Using Preisach's Theory

Preisach's theory of hysteresis is based on the concept of elementary magnetic dipoles (also called hysterons). By definition, each dipole assumes either a positive or a negative magnetization state, in accordance with the history of the magnetic field. These simple hysteresis operators may be defined by their "up" and "down" switching values, α and β, respectively. Equivalently, they may be defined by a mean value, $m = (\alpha + \beta)/2$, and a loop width, $w = (\alpha - \beta)/2$. Their magnetizing characteristic forms a rectangular loop, as shown in Fig. 5.4. The action of the simple hysteresis operator on the field intensity, $H(t)$, is an elementary magnetization denoted as $\gamma_{\alpha\beta}H(t) = \pm 1$ or $\delta_{mw}H(t) = \pm 1$.

A simplistic physical interpretation of hysterons arises from the domain wall motion inside the material [214]. In general, domain wall motion is impeded by imperfections in the crystal structure—such as inclusions of nonmagnetic matter. In the presence of an applied field, a wall will initially bend in such a way as to maximize the volume of domains parallel to the field, while still remaining attached to the restraining inclusion. However, a field threshold exists past which the wall will be able to "snap" away from the obstacle and progress to the next one in its way.

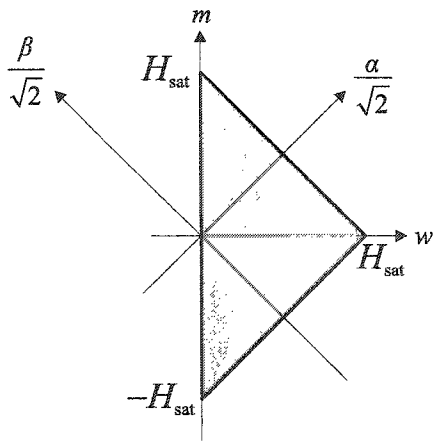

Fig. 5.5. The Preisach function domain.

The behavior of a ferromagnetic material may be thought to arise from a statistical distribution of hysterons. The function which describes the density of hysterons is known as the Preisach function. It is defined on $\mathbb{R}^2$ and is denoted by $\mu(\alpha, \beta)$ or $\nu(m, w)$, depending on which set of coordinates is used. The Preisach function is zero everywhere except on the domain $\mathcal{D}$ of Fig. 5.5. To explain the shape of this region, it is first noted that $w > 0$ (since loops with $a < b$ may not exist). The other constraints originate from the observation that a finite applied field, H_{sat}, will fully saturate the material. Thus all dipoles must obey $m + w < H_{\text{sat}}$. Consideration of saturation in the opposite direction yields $m - w > -H_{\text{sat}}$. These three inequalities lead to the triangular domain depicted in Fig. 5.5.

The total magnetization of the material may be obtained by taking into account the contribution of all elementary dipoles, integrating over $\mathcal{D}$:

$$M(t) = \iint\limits_{\alpha \geq \beta} \mu(\alpha, \beta)\, \gamma_{\alpha\beta} H(t)\, d\alpha\, d\beta = \iint\limits_{w \geq 0} \nu(m, w)\, \delta_{mw} H(t)\, dm\, dw\,. \tag{5.3}$$

The domain $\mathcal{D}$ is divided in two parts: the upper part, $\mathcal{D}^{(-)}$, corresponds to dipoles with negative magnetization; the lower part, $\mathcal{D}^{(+)}$, corresponds to positive magnetization. The magnetization is thus

$$M(t) = \iint\limits_{\mathcal{D}^{(+)}} \mu(\alpha, \beta)\, d\alpha\, d\beta - \iint\limits_{\mathcal{D}^{(-)}} \mu(\alpha, \beta)\, d\alpha\, d\beta\,. \tag{5.4}$$

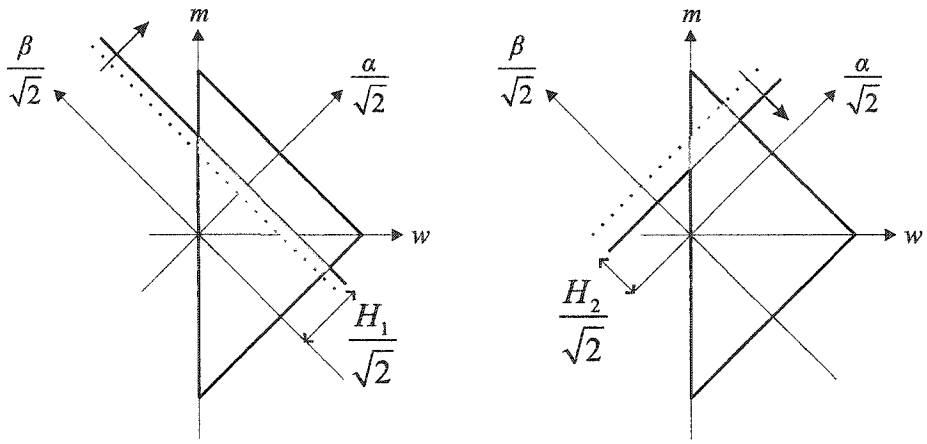

(a) Increasing magnetic field (b) Decreasing magnetic field

Fig. 5.6. Visualization of Preisach diagrams.

The formation of the domain's boundary may be visualized using the Preisach diagram, as shown in Fig. 5.6. First, assume that the magnetic field has the value H_1 and is increasing, forcing all dipoles with upper switching point $\alpha = H_1$ to switch to the plus state. The switching action is graphically equivalent to the creation of a sweeping front, represented by a line perpendicular to the α-axis, that moves towards increasing α. The shaded area that the front sweeps past becomes part of $\mathcal{D}^{(+)}$. When the field is decreasing, dipoles with lower switching point $\beta = H_2$ are forced to switch to the negative state. A new front is created, this time perpendicular to the β-axis and moving towards decreasing β, claiming area from $\mathcal{D}^{(+)}$ and adding it to $\mathcal{D}^{(-)}$.

To illustrate this process, assume that a decreasing ac field, as shown in Fig. 5.7, is imposed on the material. Therein the notation $h_x = H_x/\sqrt{2}$ is utilized for the extrema of the field intensity. The resulting boundary is formed by orthogonal line segments, and is often termed a "staircase" boundary. The boundary, $\mathcal{B}$, is defined by the reversal points of the magnetic field. For the example of Fig. 5.7, the points $H_1, \ldots, H_5$ are sufficient to describe the shape of the boundary. In order to denote the reversal points' type, that is, whether they are upper or lower turning points, the following notation may be used: $\mathcal{B} = \{^{H_1}\ _{H_2}\ ^{H_3}\ _{H_4}\ ^{H_5}\}$. Note that $H_{k+2} < H_k$, for the

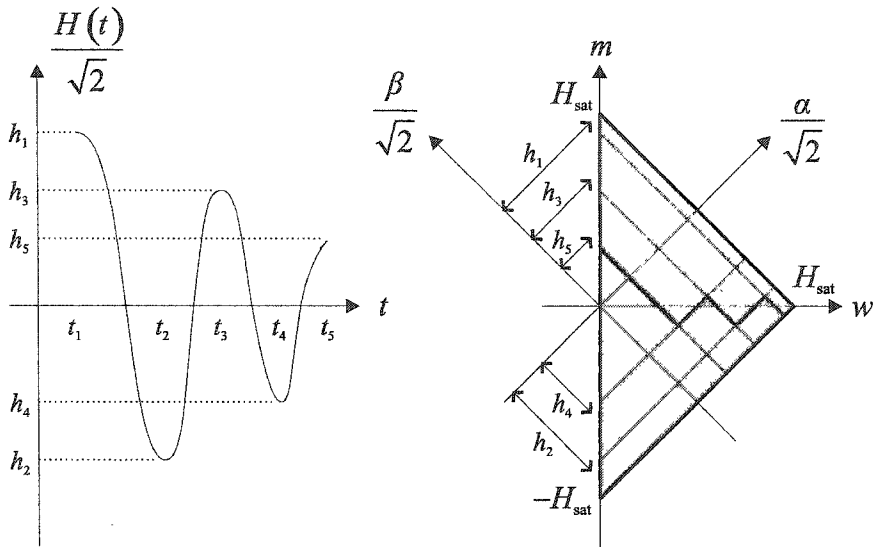

Fig. 5.7. Illustration of boundary formation.

upper points, and $H_{k+2} > H_k$, for the lower points. The boundary may always be described by a sequence of points, $\mathcal{B} = \{^{H_1}{}_{H_2}{}^{H_3} \cdots\}$ or $\mathcal{B} = \{_{H_1}{}^{H_2}{}_{H_3} \cdots\}$. The first case implies that the material was initially negatively saturated; the second case corresponds to an initially positively saturated medium.

The following symmetry condition is characteristic of most materials:

$$\nu(m, w) = \nu(-m, w)\,. \tag{5.5}$$

If the ac field of Fig. 5.7 is initially large enough to fully saturate the material, and if it decays at a relatively slow rate, an ac-demagnetization process takes place; the boundary will eventually approximate the w-axis, i.e. $\mathcal{D}^{(+)} = \mathcal{D}^{(-)}$. Equation (5.4), coupled with the assumed symmetry condition, predicts that the material will become demagnetized, $M = 0$. The boundary in this special case (where the material is initially demagnetized), is denoted $\mathcal{B} = \{0\,^{H_1}{}_{H_2}{}^{H_3} \cdots\}$, for $H_1 > 0$, or $\mathcal{B} = \{0\,_{H_1}{}^{H_2}{}_{H_3} \cdots\}$, for $H_1 < 0$.

The magnetization history may be reconstructed once the set of points defining the boundary is given. In other words, the reversal points act as the material's memory. However, this memory may be erased by an appropriate magnetic field.

For example, consider the sequence of points $\mathcal{B} = \{^{H_1}{}_{H_2}{}^{H_3}{}_{H_4}{}^{H_5}\}$ of Fig. 5.7. The magnetic field reached a local maximum H_3, decreased to H_4 and started increasing again—the current value of the magnetic field is $H = H_5$. As long as $H \leq H_3$, it can be seen from Fig. 5.8 (a) that the positive and negative domains are $\mathcal{D}^{(+)} = (\mathrm{AB\Gamma\Delta EZ\Lambda}) = (\Theta\Gamma\Delta\mathrm{EZ\Lambda}) + (\mathrm{AB\Theta})$ and $\mathcal{D}^{(-)} = (\mathrm{AIKZE\Delta\Gamma B}) = (\Theta\mathrm{IKZE\Delta\Gamma B}) - (\mathrm{AB\Theta})$, respectively. According to (5.4) the magnetization is

$$M(t) = \iint\limits_{(\Theta\Gamma\Delta\mathrm{EZ\Lambda})} \mu(\alpha,\beta)\, d\alpha\, d\beta - \iint\limits_{(\Theta\mathrm{IKZE\Delta\Gamma B})} \mu(\alpha,\beta)\, d\alpha\, d\beta + 2\iint\limits_{(\mathrm{AB\Theta})} \mu(\alpha,\beta)\, d\alpha\, d\beta\,. \quad (5.6)$$

The division of $\mathcal{D}$ into $(\Theta\Gamma\Delta\mathrm{EZ\Lambda})$ and $(\Theta\mathrm{IKZE\Delta\Gamma B})$ corresponds to the division at time $t = t_4$. After t_4, the magnetization is increasing and may be expressed

$$M(t) = M(t_4) + 2\int_{H_4}^{H}\int_{H_4}^{\alpha} \mu(\alpha,\beta)\, d\beta\, d\alpha\,, \quad (5.7)$$

where the integration over $(\mathrm{AB\Theta})$ has been expressed in terms of α, β. When $H > H_3$—as in Fig. 5.8 (b), the positive and negative domains change to $\mathcal{D}^{(+)} = (\mathrm{A'\Delta'EZ\Lambda}) = (\mathrm{MEZ\Lambda}) + (\mathrm{A'\Delta'M})$ and $\mathcal{D}^{(-)} = (\mathrm{A'IKZE\Delta'}) = (\mathrm{MIKZE}) - (\mathrm{A'\Delta'M})$. The magnetization is now

$$M(t) = M(t_2) + 2\int_{H_2}^{H}\int_{H_2}^{\alpha} \mu(\alpha,\beta)\, d\beta\, d\alpha\,. \quad (5.8)$$

As can be seen, $M(t)$ depends on H_2, and the information that was contained in the reversal points H_3, H_4 has been erased by the sweeping front. This behavior constitutes a basic property of the Preisach model, called the *deletion* or *wiping-out* property.

Generalizing the preceding analysis, the magnetization in the case of a magnetic field that has increased from H_0 to H without passing previous reversal points, may be expressed as

$$M^u(t) = M(t_0) + 2\int_{H_0}^{H}\int_{H_0}^{\alpha} \mu(\alpha,\beta)\, d\beta\, d\alpha\,, \quad (5.9)$$

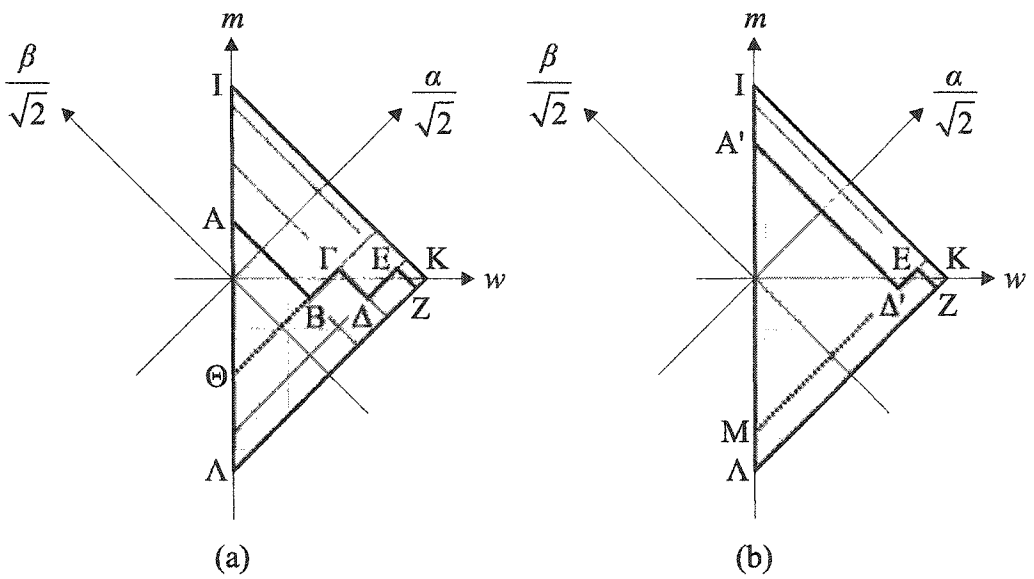

Fig. 5.8. Illustration of the deletion property of the Preisach model.

where $M(t_0)$ is the initial magnetization, and the superscript 'u' is used to denote an "upwards" moving field. Similarly, in the case of a "downwards" moving field that has not passed previous reversal points, we may write (using the superscript 'd')

$$M^d(t) = M(t_0) - 2\int_H^{H_0}\int_\beta^{H_0} \mu(\alpha,\beta)\,d\alpha\,d\beta\,. \tag{5.10}$$

If the material is demagnetized, the M–H curve that will be traced is called the initial curve. In this case, the magnetization is

$$M^{iu}(t) = 2\int_0^{H}\int_{-\alpha}^{\alpha} \mu(\alpha,\beta)\,d\beta\,d\alpha\,, \tag{5.11}$$

or

$$M^{id}(t) = -2\int_H^{0}\int_\beta^{-\beta} \mu(\alpha,\beta)\,d\alpha\,d\beta\,. \tag{5.12}$$

An expression for the susceptibility, which is defined as the slope of the hysteresis curve, i.e.

$$\chi = dM/dH\,, \tag{5.13}$$

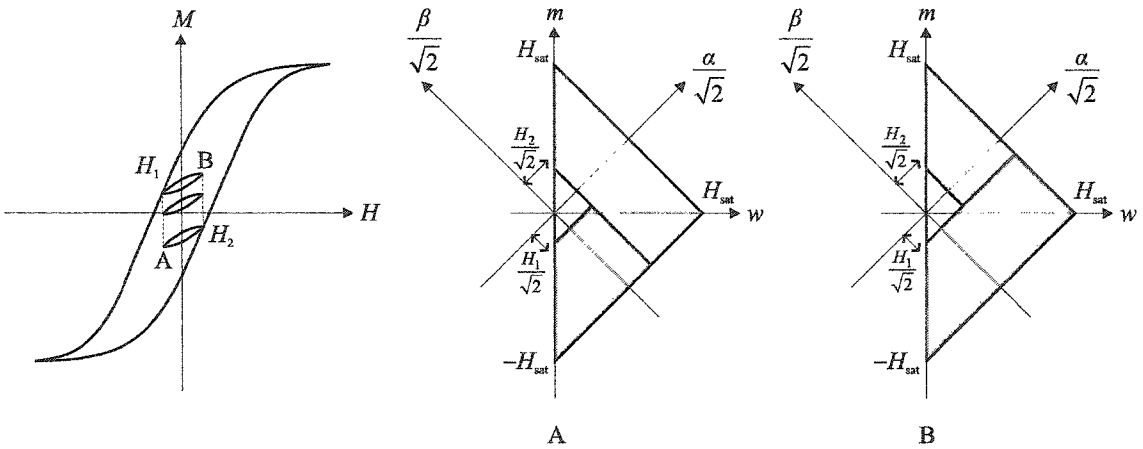

Fig. 5.9. Congruency of minor loops in the Preisach model.

may now be readily obtained by applying the fundamental theorem of calculus. Hence,

$$\chi^u = 2 \int_{H_0}^{H} \mu(H, \beta)\, d\beta\,, \tag{5.14}$$

$$\chi^d = 2 \int_{H}^{H_0} \mu(\alpha, H)\, d\alpha\,, \tag{5.15}$$

$$\chi^{iu} = 2 \int_{-H}^{H} \mu(H, \beta)\, d\beta\,, \tag{5.16}$$

$$\chi^{id} = 2 \int_{H}^{-H} \mu(\alpha, H)\, d\alpha\,. \tag{5.17}$$

Note that the susceptibility is zero at the reversal points and at the origin of the initial curve, and it is nonnegative everywhere else.

A *minor loop* is the loop of the M–H plane which is traced when the magnetic field oscillates between any two values, H_1 and H_2, in contrast to the *major loop* which is traced when the field oscillates between $-H_{\rm sat}$ and $H_{\rm sat}$. It should be clear from the preceding analysis that the Preisach model predicts the formation of closed minor loops (according to the deletion property). In addition, the Preisach model has

the *congruency* property, which is portrayed in Fig. 5.9. Therein, loops A, B start from the upwards and downwards parts of the major hysteresis loop, respectively. The congruency property states that the shape of the minor loops depends only on the reversal points, and is independent of the material's magnetization history. This can be readily proven using (5.9)–(5.10) or by geometric considerations. The deletion and congruency properties are necessary and sufficient for a process to be described by a Preisach-type model [189].

5.3.1 Specification of the Preisach function

Herein it is assumed that the statistical distribution of hysterons is Gaussian, i.e.

$$\nu(m,w) = \frac{M_s}{2\pi\sigma_m\sigma_w} \exp\left\{-\frac{1}{2}\left[\frac{(w-\overline{w})^2}{\sigma_w^2} + \frac{m^2}{\sigma_m^2}\right]\right\} . \tag{5.18}$$

M_s is a constant with dimensions of magnetization. The σ_m and σ_w terms represent the corresponding standard deviations, while $\overline{w}$ denotes the hysterons' width mean value.

By making use of the relations $\alpha = m + w$ and $\beta = m - w$, the integration of the Preisach function with respect to the (α, β) variables may be transformed to an integration with respect to the (m, w) variables. Specifically, integrating over an arbitrary domain Ω (of either positive or negative magnetization),

$$\iint_{\Omega} \mu(\alpha,\beta)\, d\alpha\, d\beta = \iint_{\Omega} \mu(\alpha(m,w),\beta(m,w)) \left|\frac{\partial(\alpha,\beta)}{\partial(m,w)}\right| dm\, dw\,, \tag{5.19}$$

where $\left|\frac{\partial(\alpha,\beta)}{\partial(m,w)}\right|$ denotes the absolute value of the Jacobian of the transformation, which (the Jacobian) is the determinant

$$\frac{\partial(\alpha,\beta)}{\partial(m,w)} = \begin{vmatrix} \frac{\partial\alpha}{\partial m} & \frac{\partial\alpha}{\partial w} \\ \frac{\partial\beta}{\partial m} & \frac{\partial\beta}{\partial w} \end{vmatrix} = \begin{vmatrix} 1 & 1 \\ 1 & -1 \end{vmatrix} = -2\,. \tag{5.20}$$

Therefore,

$$\iint_{\Omega} \mu(\alpha,\beta)\, d\alpha\, d\beta = 2 \iint_{\Omega} \mu(\alpha(m,w),\beta(m,w))\, dm\, dw\,, \tag{5.21}$$

which, in view of (5.3), implies

$$\nu(m,w) = 2\mu(\alpha,\beta)\,. \tag{5.22}$$

Hence,

$$\mu(\alpha,\beta) = \frac{M_s}{4\pi\sigma_m\sigma_w}\exp\left\{-\frac{\sigma_m^2(\alpha-\beta-2\overline{w})^2+\sigma_w^2(\alpha+\beta)^2}{8\sigma_w^2\sigma_m^2}\right\}\,. \tag{5.23}$$

Since $\nu(m,w) > 0$ for all $m,w \in \mathbb{R}$, the triangular Preisach domain extends to infinity; however, for $w > \overline{w} + 3\sigma_w$ or $|m| > 3\sigma_m$, $\nu(m,w)$ is practically zero. The magnetization at saturation may be obtained by integrating (5.18) over the right-half Preisach plane, $w > 0$: [2]

$$M_{\text{sat}} = \tfrac{1}{2}M_s\left[1+\text{erf}\left(\frac{\overline{w}}{\sqrt{2}\,\sigma_w}\right)\right]\,. \tag{5.24}$$

To determine the susceptibility of an increasing magnetic field, as given by (5.14), it is convenient to rewrite (5.23) as follows:

$$\mu(\alpha,\beta) = \frac{M_s}{4\pi\sigma_m\sigma_w}\exp\left\{-\frac{(\gamma\alpha+\beta+\delta\overline{w})^2}{2\tau^2}-\frac{(\alpha-\overline{w})^2}{2\sigma^2}\right\}\,, \tag{5.25}$$

where $\sigma = \sqrt{\sigma_w^2+\sigma_m^2}$, $\tau = 2\sigma_w\sigma_m/\sigma$, $\gamma = (\sigma_w^2-\sigma_m^2)/\sigma^2$, $\delta = 1-\gamma = (2\sigma_m^2)/\sigma^2$. Then, the susceptibility becomes

$$\chi^u = \frac{M_s}{\sqrt{2\pi}\,\sigma}\exp\left\{-\frac{(H-\overline{w})^2}{2\sigma^2}\right\}\left\{\text{erf}\left[\frac{(\gamma+1)H+\delta\overline{w}}{\sqrt{2}\,\tau}\right]-\text{erf}\left[\frac{\gamma H+H_0+\delta\overline{w}}{\sqrt{2}\,\tau}\right]\right\}\,. \tag{5.26}$$

Similarly, for a decreasing magnetic field, write (5.23) as

$$\mu(\alpha,\beta) = \frac{M_s}{4\pi\sigma_m\sigma_w}\exp\left\{-\frac{(\alpha+\gamma\beta-\delta\overline{w})^2}{2\tau^2}-\frac{(\beta+\overline{w})^2}{2\sigma^2}\right\}\,, \tag{5.27}$$

to obtain

$$\chi^d = \frac{M_s}{\sqrt{2\pi}\,\sigma}\exp\left\{-\frac{(H+\overline{w})^2}{2\sigma^2}\right\}\left\{\text{erf}\left[\frac{H_0+\gamma H-\delta\overline{w}}{\sqrt{2}\,\tau}\right]-\text{erf}\left[\frac{(\gamma+1)H-\delta\overline{w}}{\sqrt{2}\,\tau}\right]\right\}\,. \tag{5.28}$$

The susceptibility of the initial curve is given by

$$\chi^{iu} = \frac{M_s}{\sqrt{2\pi}\,\sigma}\exp\left\{-\frac{(H-\overline{w})^2}{2\sigma^2}\right\}\left\{\text{erf}\left[\frac{(\gamma+1)H+\delta\overline{w}}{\sqrt{2}\,\tau}\right]-\text{erf}\left[\frac{(\gamma-1)H+\delta\overline{w}}{\sqrt{2}\,\tau}\right]\right\}\,, \tag{5.29}$$

and

$$\chi^{id} = \frac{M_s}{\sqrt{2\pi}\,\sigma}\exp\left\{-\frac{(H+\overline{w})^2}{2\sigma^2}\right\}\left\{\text{erf}\left[\frac{(\gamma-1)H-\delta\overline{w}}{\sqrt{2}\,\tau}\right]-\text{erf}\left[\frac{(\gamma+1)H-\delta\overline{w}}{\sqrt{2}\,\tau}\right]\right\}\,. \tag{5.30}$$

[2]The error function is defined by $\text{erf}(x) = \frac{2}{\sqrt{\pi}}\int_0^x e^{-\xi^2}\,d\xi$.

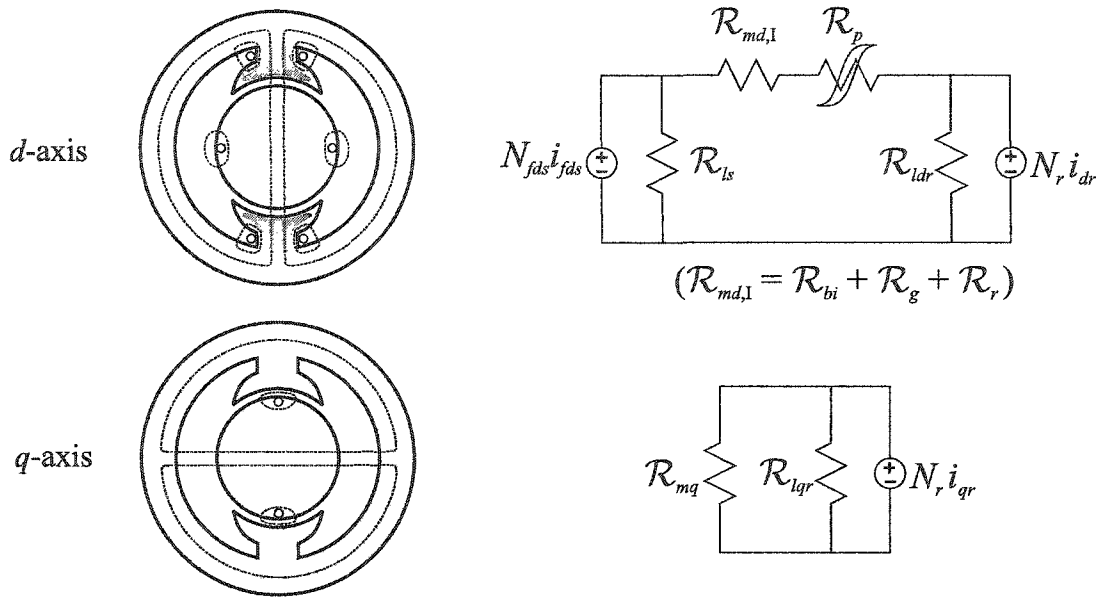

Fig. 5.10. Simplified diagram of exciter's magnetic flux paths, and the corresponding magnetic equivalent circuits.

5.4 The Proposed Model—Mathematical Formulation

The exciter's magnetic equivalent circuit is depicted in Fig. 5.10. The d-axis main flux path reluctance is comprised of the stator back-iron reluctance, $\mathcal{R}_{bi}$, the pole iron reluctance, $\mathcal{R}_p$, the air-gap reluctance, $\mathcal{R}_g$, and the rotor body reluctance, $\mathcal{R}_r$. In the proposed model, it is assumed that all hysteretic magnetic effects are concentrated in the region of the poles; hence, magnetic nonlinearities are incorporated into $\mathcal{R}_p$. All other reluctances are considered to be linear, including the reluctances of the leakage flux paths, $\mathcal{R}_{ls}$ and $\mathcal{R}_{ldr}$. The q-axis magnetic paths are also considered to be linear.

The magnetic equivalent circuit of Fig. 5.10 is translated to the electrical T-equivalent circuit of Fig. 5.11. The exciter machine does not have damper windings. As in [183], a reduced-order machine model is utilized, wherein the (average) armature currents are injected by the rectifier model. The state variables are selected to be λ_{md} and i'_{fds}. There are no states associated with the q-axis, because its equation

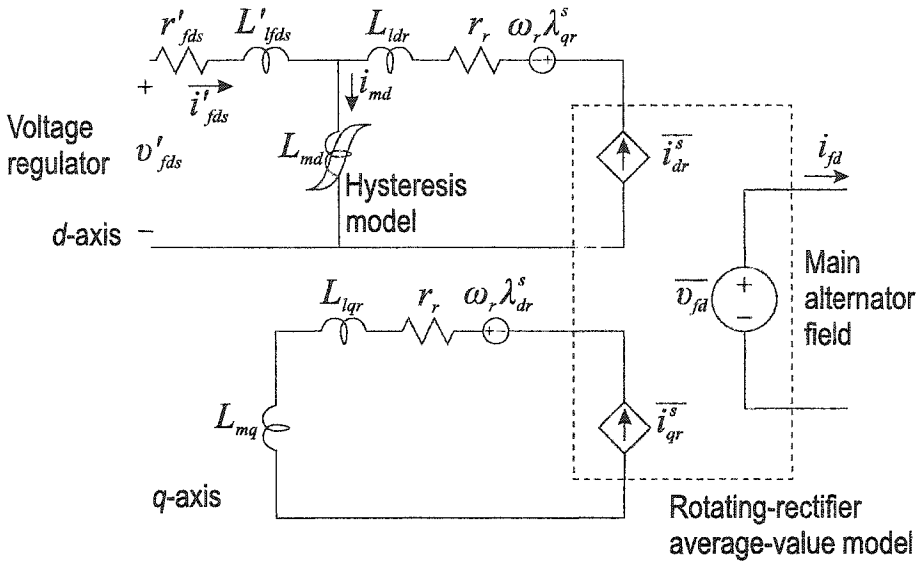

Fig. 5.11. Exciter's equivalent circuit and interface mechanism to the voltage regulator and main alternator models.

is purely algebraic. The hysteresis model determines the incremental magnetizing inductance. In the following sections, the sub-models are presented in detail.

5.4.1 The hysteresis model

For the purposes of machine modeling, it is convenient to work with electrical rather than field quantities. Hence, by analogy to $B = \mu_0(H + M)$, the machine's d-axis magnetizing flux linkage is written as the sum of a linear and a hysteretic component,

$$\lambda_{md} = L_{m,\text{sat}}\, i_{md} + \lambda_{md,M}\,. \tag{5.31}$$

The Preisach model is now expressed in terms of the magnetization component of flux linkage, $\lambda_{md,M}$, and the magnetizing current, i_{md} (instead of the magnetization, M, and the magnetic field, H). The inductance $L_{m,\text{sat}}$ corresponds to the slope of the magnetizing characteristic at saturation.

The hysteresis model's input is the magnetizing current, i_{md}, and its output is the incremental inductance,

$$L_{mi} = d\lambda_{md,M}/di_{md}\,. \tag{5.32}$$

It will be useful to note that by combining (5.31) and (5.32),

$$\tfrac{d}{dt}\lambda_{md} = (L_{m,\mathrm{sat}} + L_{mi})\tfrac{d}{dt}i_{md}\,. \tag{5.33}$$

The susceptibility expressions (5.26)–(5.30) are translated in terms of electrical quantities to the following incremental inductance equations:

$$L^{u}_{mi} = \tfrac{\lambda_{Ms}}{\sqrt{2\pi}\,\sigma}\exp\left\{-\tfrac{(i_{md}-\overline{w})^2}{2\sigma^2}\right\}\left\{\mathrm{erf}\left[\tfrac{(\gamma+1)i_{md}+\delta\overline{w}}{\sqrt{2}\,\tau}\right] - \mathrm{erf}\left[\tfrac{\gamma i_{md}+i_{md0}+\delta\overline{w}}{\sqrt{2}\,\tau}\right]\right\}, \tag{5.34}$$

$$L^{d}_{mi} = \tfrac{\lambda_{Ms}}{\sqrt{2\pi}\,\sigma}\exp\left\{-\tfrac{(i_{md}+\overline{w})^2}{2\sigma^2}\right\}\left\{\mathrm{erf}\left[\tfrac{\gamma i_{md}+i_{md0}-\delta\overline{w}}{\sqrt{2}\,\tau}\right] - \mathrm{erf}\left[\tfrac{(\gamma+1)i_{md}-\delta\overline{w}}{\sqrt{2}\,\tau}\right]\right\}, \tag{5.35}$$

$$L^{iu}_{mi} = \tfrac{\lambda_{Ms}}{\sqrt{2\pi}\,\sigma}\exp\left\{-\tfrac{(i_{md}-\overline{w})^2}{2\sigma^2}\right\}\left\{\mathrm{erf}\left[\tfrac{(\gamma+1)i_{md}+\delta\overline{w}}{\sqrt{2}\,\tau}\right] - \mathrm{erf}\left[\tfrac{(\gamma-1)i_{md}+\delta\overline{w}}{\sqrt{2}\,\tau}\right]\right\}, \tag{5.36}$$

$$L^{id}_{mi} = \tfrac{\lambda_{Ms}}{\sqrt{2\pi}\,\sigma}\exp\left\{-\tfrac{(i_{md}+\overline{w})^2}{2\sigma^2}\right\}\left\{\mathrm{erf}\left[\tfrac{(\gamma-1)i_{md}-\delta\overline{w}}{\sqrt{2}\,\tau}\right] - \mathrm{erf}\left[\tfrac{(\gamma+1)i_{md}-\delta\overline{w}}{\sqrt{2}\,\tau}\right]\right\}, \tag{5.37}$$

where λ_{Ms} is a constant with dimensions of flux linkage. The appropriate equation is selected based on the direction of change of the magnetizing current. Since the exciter's complete magnetic history is unknown, it is assumed that it is initially demagnetized. From (5.34)–(5.37), $L_{mi} = 0$ at the reversal points and at the origin of the initial curve, and $L_{mi} > 0$ everywhere else. L_{mi} thus depends only on i_{md0}, i_{md}, and the direction of change of i_{md} (in accordance with the congruency property).

The Preisach model constantly monitors the direction of change of i_{md}, and adds the reversal points to a last-in-first-out stack. The crossing of a previous reversal point signifies a minor loop closure. In this case, the two points that define this minor loop are deleted from the stack (as dictated by the deletion property).

5.4.2 The reduced-order machine model

This model is termed 'reduced-order' because the (fast) transients associated with the rotor windings are neglected. Its inputs are the qd-axes rotor currents

(which will be approximated by their average value), $\overline{i^s_{qdr}}$, [3] the exciter's field winding voltage, v_{fds}, and the incremental inductance, L_{mi}. In this block, the integrations for the two states, i'_{fds} and λ_{md} are performed. Outputs are the magnetizing current, $i_{md} = \overline{i^s_{dr}} + i'_{fds}$, the VBR d-axis flux linkage, λ^{vbr}_d, and the VBR d-axis inductance, L^{vbr}_d.

In this model, an overbar is used to emphasize the approximation of a quantity by its fast-average value (its average over the previous 60 degrees). Often, in such cases, it is appropriate to average the entire model thereby yielding a formalized average-value model. However, because of the nonlinearities involved with the hysteresis model, formal averaging of the model would prove awkward. Therefore, the interpretation applicable herein is that quantities indicated as instantaneous (without overbars) are also being approximated by their fast-average value.

The description of the reduced-order machine model begins with the field winding flux linkage,

$$\lambda'_{fds} = L'_{lfds} i'_{fds} + \lambda_{md} \,. \tag{5.38}$$

Substitution of (5.33) and the currents' relationship, $i'_{fds} = i_{md} - \overline{i^s_{dr}}$, into (5.38) and consideration of the field voltage equation,

$$v'_{fds} = r'_{fds} i'_{fds} + \tfrac{d}{dt}\lambda'_{fds} \,, \tag{5.39}$$

yields

$$(L'_{lfds} + L_{m,\text{sat}} + L_{mi}) \tfrac{d}{dt} i_{md} = v'_{fds} - r'_{fds} i'_{fds} + L'_{lfds} \tfrac{d}{dt} \overline{i^s_{dr}} \,. \tag{5.40}$$

The inductance term of the left-hand side is positive since $L_{mi} \geq 0$. Hence, the sign of the right-hand side determines the magnetizing current's direction of change and which expression for L_{mi} is to be selected from (5.34)–(5.37). The state equations may be obtained from (5.33), (5.39) and (5.40):

$$\tfrac{d}{dt}\lambda_{md} = \tfrac{L_{m,\text{sat}} + L_{mi}}{L'_{lfds} + L_{m,\text{sat}} + L_{mi}} \left(v'_{fds} - r'_{fds} i'_{fds} + L'_{lfds} \tfrac{d}{dt} \overline{i^s_{dr}} \right) \,, \tag{5.41}$$

[3] The q-axis current is not utilized by the reduced-order machine model, since its dynamic behavior only involves the d-axis. However, $\overline{i^s_{qr}}$ is computed for completeness.

and

$$\frac{d}{dt}i'_{fds} = \left[v'_{fds} - r'_{fds}i'_{fds} - (L_{m,\text{sat}} + L_{mi})\frac{d}{dt}\overline{i^s_{dr}}\right] / (L'_{lfds} + L_{m,\text{sat}} + L_{mi})\,. \tag{5.42}$$

The derivative $d\overline{i^s_{dr}}/dt$ is estimated from the variation of $\overline{i^s_{dr}}$. It is convenient to approximate it by the following relationship, written in the frequency domain:

$$s\,\overline{i^s_{dr}} \approx \frac{s}{\tau_i s + 1}\,\overline{i^s_{dr}}\,. \tag{5.43}$$

If τ_i is relatively small (so that $\tau_i s+1 \approx 1$), a good low-frequency estimate is obtained. This approximation is justified by the slow-varying nature of i_{fd} and consequently of $\overline{i^s_{dr}}$. Equation (5.43) is readily translated into a time-domain differential equation, and the problematic numerical differentiation of $\overline{i^s_{dr}}$ is thus avoided. Herein, we set $\tau_i = 0.5$ ms.

The exciter's electromagnetic torque may be computed from the well-known expression, $T_e = (3P/4)(\lambda_{mq}\,\overline{i^s_{dr}} - \lambda_{md}\,\overline{i^s_{qr}})$. However, since the exciter is a small machine relative to the main alternator, its torque is assumed negligible herein.

The armature voltage equations must be expressed in voltage-behind-reactance form to be compatible with the rotating-rectifier average-value model. In the VBR model, the rotor flux linkages are expressed

$$\lambda^s_{qr} = L^{\text{vbr}}_q\, i^s_{qr}\,, \tag{5.44}$$

$$\lambda^s_{dr} = L^{\text{vbr}}_d\, i^s_{dr} + \lambda^{\text{vbr}}_d\,, \tag{5.45}$$

where

$$L^{\text{vbr}}_q = L_{lqr} + L_{mq}\,, \tag{5.46}$$

$$L^{\text{vbr}}_d = L_{ldr} + \left[(L_{m,\text{sat}} + L_{mi})^{-1} + (L'_{lfds})^{-1}\right]^{-1}\,, \tag{5.47}$$

and

$$\lambda^{\text{vbr}}_d = \lambda_{md} - i^s_{dr} / \left[(L_{m,\text{sat}} + L_{mi})^{-1} + (L'_{lfds})^{-1}\right]\,. \tag{5.48}$$

These equations hold for fast current transients, hence the overbar notation is not appropriate.

In VBR form, λ_d^{vbr} is essentially constant for fast transients. In particular, if for fast transients (such as commutation processes) we assume that the field flux linkage is constant, then it can be shown that λ_d^{vbr} is constant as well. Upon neglecting the rotor resistance, the VBR voltage equations may be expressed

$$v_{qr}^s \approx -\omega_r L_d^{\text{vbr}} i_{dr}^s + L_q^{\text{vbr}} \tfrac{d}{dt} i_{qr}^s + E_q^{\text{vbr}}\,, \tag{5.49}$$

$$v_{dr}^s \approx \omega_r L_q^{\text{vbr}} i_{qr}^s + L_d^{\text{vbr}} \tfrac{d}{dt} i_{dr}^s\,, \tag{5.50}$$

with $E_q^{\text{vbr}} = -\omega_r \lambda_d^{\text{vbr}}$.

5.4.3 The rotating-rectifier average-value model

This section contains the derivation of the rotating-rectifier average-value model, which computes the average currents flowing in the exciter armature, $\overline{\mathbf{i}_{qdr}^s}$, from i_{fd}, the VBR d-axis flux linkage, λ_d^{vbr}, and the VBR d-axis inductance, L_d^{vbr}. (The computation also uses the VBR q-axis inductance, L_q^{vbr}, which is assumed constant herein.) The analysis is based on the classical separation of a rectifier's operation in three distinct modes [184]. This type of rectifier modeling is valid for a constant (or slow-varying) dc current.

The transformation of the no-load versions of (5.49), (5.50) to the rotor reference frame yields the following three-phase voltage set:

$$e_{ar} = E\cos\theta_r\,, \tag{5.51}$$

$$e_{br} = E\cos(\theta_r + \tfrac{2\pi}{3})\,, \tag{5.52}$$

$$e_{cr} = E\cos(\theta_r - \tfrac{2\pi}{3})\,, \tag{5.53}$$

where $E = E_q^{\text{vbr}}$. [4] It is useful to define a voltage angle θ_{ev} so that the a-phase voltage attains its maximum value when $\theta_{ev} = 0$, i.e. $e_{ar} = |E| \cos \theta_{ev}$. The voltage and rotor angles are thus related by

$$\delta = \theta_r - \theta_{ev} = \begin{cases} \pi & \text{for } E < 0\,, \\ 0 & \text{for } E \geq 0\,. \end{cases} \tag{5.54}$$

Because of symmetry, it is only necessary to consider a 60° interval (for a six-pulse bridge). Consider the interval which begins when valve 6 (see Fig. 5.1) starts conducting (at $\theta_{ev} = \alpha$, where α is a phase delay [5]), and ends at $\theta_{ev} = \alpha + \pi/3$. During this interval, current is commutated from valve 2 to valve 6 (phase c to phase b); if the diode resistance is negligible, a line-to-line short-circuit between phases b and c is in effect, so $v_{br} - v_{cr} = 0$. (v_{xr} denotes the line-to-neutral voltage of winding x.) If the rotor's resistance is also neglected, Faraday's law implies

$$\lambda_{br} - \lambda_{cr} = C\,, \tag{5.55}$$

where C is a constant. This relationship will prove useful in the analysis that follows.

The next observation is that the average rectifier output voltage may be expressed

$$\overline{v_{dc}} = \frac{3}{\pi} \int_{\alpha}^{\alpha+\pi/3} (v_{ar} - v_{br})\, d\theta_{ev}\,, \tag{5.56}$$

which may be approximated as

$$\begin{aligned} \overline{v_{dc}} &\approx \frac{3}{\pi} \int_{\alpha}^{\alpha+\pi/3} \left(\tfrac{d}{dt}\lambda_{ar} - \tfrac{d}{dt}\lambda_{br}\right)\, d\theta_{ev} \\ &\approx \frac{3}{\pi}\, \omega_r \left[(\lambda_{ar} - \lambda_{br})_{\theta_{ev}=\alpha+\frac{\pi}{3}} - (\lambda_{ar} - \lambda_{br})_{\theta_{ev}=\alpha}\right]\,. \end{aligned} \tag{5.57}$$

Neglecting armature resistance makes the analysis far more tractable. As it turns out, the inaccuracy involved in this assumption can be largely mitigated using a correction term which will be defined in a later section.

[4] The standard numbering of the diodes (Fig. 5.1) corresponds to the order of conduction in the case of an *abc* phase sequence. However, in this case, a reverse *acb* phase sequence is obtained, and the diodes conduct in a different order.

[5] This α should not be confused with the symbol that was used in the Preisach model section to denote the hysterons' upper switching point.

The *abc* flux linkages may be related to the phase currents and the VBR flux linkage by transforming (5.44), (5.45) using (5.1), (5.54). After manipulation,

$$\lambda_{ar}(\theta_{ev}) - \lambda_{br}(\theta_{ev}) = \tfrac{2}{\sqrt{3}} \left\{ L_q^{\text{vbr}} \sin(\theta_{ev} + \tfrac{\pi}{3}) \left[\cos\theta_{ev}, \cos(\theta_{ev} + \tfrac{2\pi}{3}), \cos(\theta_{ev} - \tfrac{2\pi}{3}) \right] - \right.$$
$$\left. - L_d^{\text{vbr}} \cos(\theta_{ev} + \tfrac{\pi}{3}) \left[\sin\theta_{ev}, \sin(\theta_{ev} + \tfrac{2\pi}{3}), \sin(\theta_{ev} - \tfrac{2\pi}{3}) \right] \right\} \mathbf{i}_{abcr}(\theta_{ev}) +$$
$$+ \sqrt{3} \lambda_d^{\text{vbr}} \cos(\delta + \theta_{ev} + \tfrac{\pi}{3}) , \quad (5.58)$$

$$\lambda_{br}(\theta_{ev}) - \lambda_{cr}(\theta_{ev}) = \tfrac{2}{\sqrt{3}} \left\{ -L_q^{\text{vbr}} \sin\theta_{ev} \left[\cos\theta_{ev}, \cos(\theta_{ev} + \tfrac{2\pi}{3}), \cos(\theta_{ev} - \tfrac{2\pi}{3}) \right] + \right.$$
$$\left. + L_d^{\text{vbr}} \cos\theta_{ev} \left[\sin\theta_{ev}, \sin(\theta_{ev} + \tfrac{2\pi}{3}), \sin(\theta_{ev} - \tfrac{2\pi}{3}) \right] \right\} \mathbf{i}_{abcr}(\theta_{ev}) -$$
$$- \sqrt{3} \lambda_d^{\text{vbr}} \cos(\delta + \theta_{ev}) = C . \quad (5.59)$$

To proceed further, the rectification mode must be considered.

Mode I operation

Mode I operation (Fig. 5.12) may be separated into the commutation and conduction sub-intervals. The commutation lasts for less than 60 electrical degrees ($0 \leq u < \pi/3$), where u denotes the commutation angle. During the commutation interval ($0 \leq \theta_{ev} < u$), three diodes are conducting (1, 2 and 6); during the conduction interval ($u \leq \theta_{ev} < \pi/3$), only two diodes are conducting (1 and 6). The *abc* currents are

$$\mathbf{i}_{abcr}(\theta_{ev}) = \begin{cases} [-i_{dc},\ i_6,\ i_{dc} - i_6]^T & \text{for } 0 \leq \theta_{ev} < u , \\ [-i_{dc},\ i_{dc},\ 0]^T & \text{for } u \leq \theta_{ev} < \tfrac{\pi}{3} , \end{cases} \quad (5.60)$$

where $i_{dc} = i_{fd}$ is the current flowing out of the rectifier and into the generator field, and i_6 is the (positive, anode-to-cathode) current flowing through diode 6; $i_6(\theta_{ev})$ increases from $i_6(0) = 0$ to $i_6(u) = i_{dc}$.

The average dc voltage may be computed from (5.57), after substituting (5.60) into (5.58); this sequence of operations yields

$$\overline{v_{dc}} = \tfrac{3}{\pi} \omega_r \left(\sqrt{3} \left| \lambda_d^{\text{vbr}} \right| - L_d^{\text{vbr}} i_{dc} \right) . \quad (5.61)$$

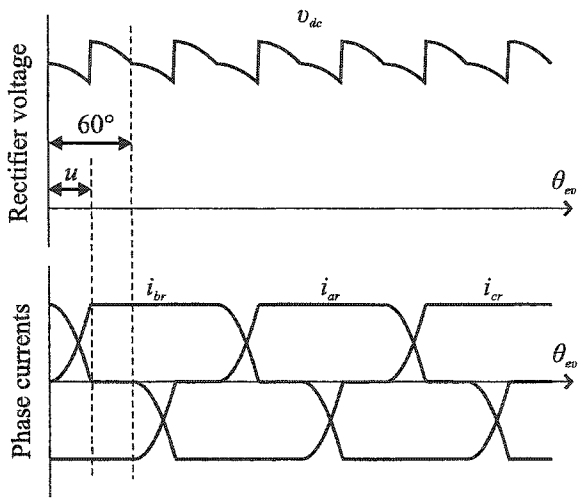

Fig. 5.12. Mode I operation.

The term $(3/\pi)\,\omega_r L_d^{\text{vbr}}$ represents the effective commutating resistance for mode I operation.

Substitution of (5.60) into (5.59) yields

$$2i_6\left(L_d^{\text{vbr}}\cos^2\theta_{ev}+L_q^{\text{vbr}}\sin^2\theta_{ev}\right)- \\ -2i_{dc}\left[L_d^{\text{vbr}}\cos(\theta_{ev}-\tfrac{\pi}{3})\cos\theta_{ev}+L_q^{\text{vbr}}\sin(\theta_{ev}-\tfrac{\pi}{3})\sin\theta_{ev}\right]- \\ -\sqrt{3}\lambda_d^{\text{vbr}}\cos(\delta+\theta_{ev})=C\,. \quad (5.62)$$

Evaluating this expression at $\theta_{ev}=0$ and $\theta_{ev}=u$, we obtain

$$C=\sqrt{3}\left|\lambda_d^{\text{vbr}}\right|-L_d^{\text{vbr}}\,i_{dc}\,, \quad (5.63)$$

and

$$C=\sqrt{3}\left|\lambda_d^{\text{vbr}}\right|\cos u+\left[\tfrac{1}{2}\left(L_d^{\text{vbr}}+L_q^{\text{vbr}}\right)+\left(L_d^{\text{vbr}}-L_q^{\text{vbr}}\right)\cos\left(2u+\tfrac{\pi}{3}\right)\right]i_{dc}\,, \quad (5.64)$$

respectively. By equating (5.63), (5.64), the following nonlinear equation is obtained, which may be solved numerically for the commutation angle u:

$$g^{\text{I}}(u)\triangleq\sqrt{3}\left|\lambda_d^{\text{vbr}}\right|(1-\cos u)- \\ -\left[\tfrac{1}{2}\left(3L_d^{\text{vbr}}+L_q^{\text{vbr}}\right)+\left(L_d^{\text{vbr}}-L_q^{\text{vbr}}\right)\cos\left(2u+\tfrac{\pi}{3}\right)\right]i_{dc}=0\,. \quad (5.65)$$

Knowledge of u and C (from (5.63)) allows the computation of the average qd-axes rotor currents. Equation (5.62) is solved for i_6 and substituted into (5.60), which is transformed using (5.1). The currents of the first sub-interval (denoted by the superscript '(i)') are thus:

$$\mathbf{i}_{qdr}^{s,(\mathrm{i})}(\theta_{ev}) = \frac{2\sqrt{3}}{3}\begin{bmatrix} i_{dc}\sin(\delta+\theta_{ev}-\frac{\pi}{3}) - i_6(\theta_{ev})\sin(\delta+\theta_{ev}) \\ i_{dc}\cos(\delta+\theta_{ev}-\frac{\pi}{3}) - i_6(\theta_{ev})\cos(\delta+\theta_{ev}) \end{bmatrix} . \tag{5.66}$$

Their average value is

$$\overline{\mathbf{i}_{qdr}^{s,(\mathrm{i})}} = \frac{3}{\pi}\int_0^u \mathbf{i}_{qdr}^{s,(\mathrm{i})}(\theta_{ev})\, d\theta_{ev} . \tag{5.67}$$

This integral is difficult to evaluate analytically, so it is evaluated numerically, e.g. using Simpson's rule [183, 215]. On the other hand, the average value of the conduction sub-interval currents (denoted by the superscript '(ii)') may be computed analytically:

$$\overline{\mathbf{i}_{qdr}^{s,(\mathrm{ii})}} = \frac{2\sqrt{3}}{\pi} i_{dc}\begin{bmatrix} \cos(\delta+\frac{2\pi}{3}) - \cos(\delta+u+\frac{\pi}{3}) \\ -\sin(\delta+\frac{2\pi}{3}) + \sin(\delta+u+\frac{\pi}{3}) \end{bmatrix} . \tag{5.68}$$

The total qd-axes currents average value is

$$\overline{\mathbf{i}_{qdr}^{s}} = \overline{\mathbf{i}_{qdr}^{s,(\mathrm{i})}} + \overline{\mathbf{i}_{qdr}^{s,(\mathrm{ii})}} . \tag{5.69}$$

Mode II operation

In mode II operation (Fig. 5.13), the commutation angle is 60 degrees, but commutation is auto-delayed by the angle α ($0 \le \alpha \le \pi/6$). There are always three diodes conducting, and the abc currents are

$$\mathbf{i}_{abcr}(\theta_{ev}) = [-i_{dc},\, i_6,\, i_{dc} - i_6]^T \quad \text{for } \alpha \le \theta_{ev} < \alpha + \tfrac{\pi}{3} . \tag{5.70}$$

The current i_6 increases from $i_6(\alpha) = 0$ to $i_6(\alpha + \pi/3) = i_{dc}$.

The average dc voltage is computed similarly to mode I by substituting (5.70) into (5.58) and (5.57):

$$\overline{v_{dc}} = \frac{3}{\pi}\omega_r\left\{\sqrt{3}\left|\lambda_d^{\mathrm{vbr}}\right|\cos\alpha - \left[\tfrac{1}{2}\left(L_d^{\mathrm{vbr}} + L_q^{\mathrm{vbr}}\right) + \left(L_d^{\mathrm{vbr}} - L_q^{\mathrm{vbr}}\right)\sin\left(2\alpha+\tfrac{\pi}{6}\right)\right] i_{dc}\right\} . \tag{5.71}$$

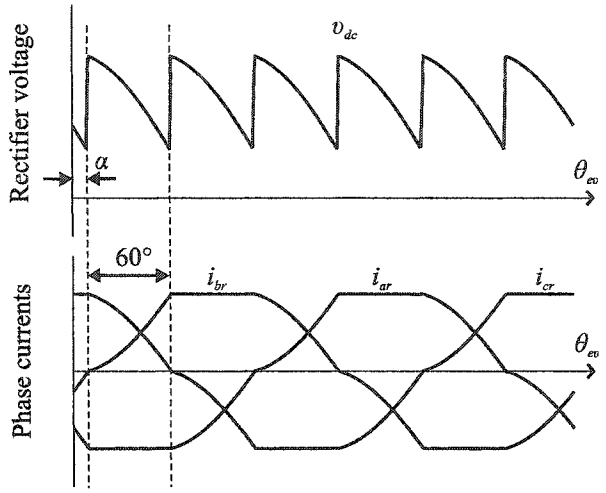

Fig. 5.13. Mode II operation.

The commutating resistance now depends on α, as well as the VBR qd-axes inductances.

Evaluating (5.59) at $\theta_{ev} = \alpha$ and $\theta_{ev} = \alpha + \pi/3$, and equating the two results yields the following nonlinear equation, which is solved numerically for α:

$$g^{\mathrm{II}}(\alpha) \triangleq -\sqrt{3}\left|\lambda_d^{\mathrm{vbr}}\right| \sin\left(\alpha + \tfrac{\pi}{6}\right) + \\ + \left[L_d^{\mathrm{vbr}} + L_q^{\mathrm{vbr}} - \left(L_d^{\mathrm{vbr}} - L_q^{\mathrm{vbr}}\right) \cos\left(2\alpha + \tfrac{\pi}{3}\right)\right] i_{dc} = 0\,. \quad (5.72)$$

The expression (5.66) for $\mathbf{i}_{qdr}^{s,(\mathrm{i})}(\theta_{ev})$ is valid throughout commutation, and the average qd-axes currents are

$$\overline{\mathbf{i}_{qdr}^{s}} = \tfrac{3}{\pi} \int_{\alpha}^{\alpha+\frac{\pi}{3}} \mathbf{i}_{qdr}^{s,(\mathrm{i})}(\theta_{ev})\, d\theta_{ev}\,. \quad (5.73)$$

Mode III operation

In mode III operation (Fig. 5.14), commutation is delayed by $\alpha = \pi/6$, and $\pi/3 < u \leq 2\pi/3$. This mode may be split into two sub-intervals. During the interval $\pi/6 \leq \theta_{ev} < u - \pi/6$, two commutations are taking place simultaneously; four diodes are conducting (3, 1, 2 and 6), and a three-phase short-circuit is applied to the exciter, so $v_{dc} = 0$. At $\theta_{ev} = \pi/6$, the commutation of diode 1 is at a

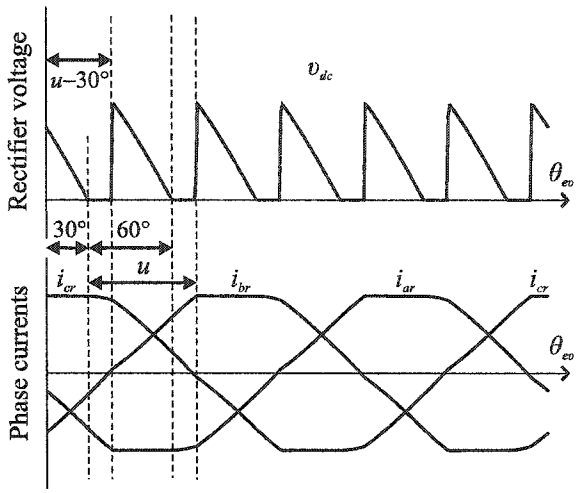

Fig. 5.14. Mode III operation.

further commutation stage than the commutation of diode 6, which is just starting ($i_1(\pi/6) = i_\alpha$, $i_6(\pi/6) = 0$). At $\theta_{ev} = u - \pi/6$, the commutation of diode 3 to diode 1 finishes ($i_1(u - \pi/6) = i_{dc}$); the current of diode 6 has increased to $i_6(u - \pi/6) = i_\mu$. During $u - \pi/6 \leq \theta_{ev} < \pi/2$, there are three diodes conducting (1, 2 and 6), and a line-to-line short circuit is imposed on the exciter. Due to symmetry considerations, $i_6(\pi/2) = i_\alpha$. The *abc* currents are

$$\mathbf{i}_{abcr}(\theta_{ev}) = \begin{cases} [-i_1,\ -i_{dc} + i_1 + i_6,\ i_{dc} - i_6]^T & \text{for } \frac{\pi}{6} \leq \theta_{ev} < u - \frac{\pi}{6}\,, \\ [-i_{dc},\ i_6,\ i_{dc} - i_6]^T & \text{for } u - \frac{\pi}{6} \leq \theta_{ev} < \frac{\pi}{2}\,. \end{cases} \tag{5.74}$$

During the first sub-interval, $\lambda_{ar}(\theta_{ev}) - \lambda_{br}(\theta_{ev}) = C_1$ and $\lambda_{br}(\theta_{ev}) - \lambda_{cr}(\theta_{ev}) = C$. Inserting the corresponding part of (5.74) into (5.58) and (5.59),

$$\begin{aligned} 2(i_{dc} - i_6)\left[L_d^{\text{vbr}} \cos(\theta_{ev} + \tfrac{\pi}{3}) \cos\theta_{ev} + L_q^{\text{vbr}} \sin(\theta_{ev} + \tfrac{\pi}{3}) \sin\theta_{ev}\right] - \\ - 2i_1\left[L_d^{\text{vbr}} \cos^2(\theta_{ev} + \tfrac{\pi}{3}) + L_q^{\text{vbr}} \sin^2(\theta_{ev} + \tfrac{\pi}{3})\right] + \\ + \sqrt{3}\lambda_d^{\text{vbr}} \cos(\delta + \theta_{ev} + \tfrac{\pi}{3}) = C_1\,, \end{aligned} \tag{5.75}$$

$$- 2(i_{dc} - i_6)\left[L_d^{\text{vbr}} \cos^2\theta_{ev} + L_q^{\text{vbr}} \sin^2\theta_{ev}\right] +$$
$$+ 2i_1\left[L_d^{\text{vbr}} \cos(\theta_{ev} + \tfrac{\pi}{3}) \cos\theta_{ev} + L_q^{\text{vbr}} \sin(\theta_{ev} + \tfrac{\pi}{3}) \sin\theta_{ev}\right] -$$
$$- \sqrt{3}\lambda_d^{\text{vbr}} \cos(\delta + \theta_{ev}) = C\,, \quad (5.76)$$

respectively. Substitution of the values of i_1 and i_6 at the three separating angles, $\theta_{ev} = \pi/6$, $\theta_{ev} = u - \pi/6$ and $\theta_{ev} = \pi/2$, into (5.62), (5.75) and (5.76), yields

$$i_\alpha = \left[3\left|\lambda_d^{\text{vbr}}\right| + \left(L_q^{\text{vbr}} - 3L_d^{\text{vbr}}\right) i_{dc}\right] / (2L_q^{\text{vbr}})\,, \quad (5.77)$$

$$C = 3\left|\lambda_d^{\text{vbr}}\right| - 3L_d^{\text{vbr}}\, i_{dc}\,, \quad (5.78)$$

$$i_\mu(u) = \left[\tfrac{1}{2}\left(L_d^{\text{vbr}} + L_q^{\text{vbr}}\right) + \left(L_d^{\text{vbr}} - L_q^{\text{vbr}}\right)\cos 2u\right]^{-1} \cdot$$
$$\cdot \left\{C - \sqrt{3}\left|\lambda_d^{\text{vbr}}\right| \cos(u + \tfrac{\pi}{6}) - \left[\tfrac{1}{2}\left(L_d^{\text{vbr}} + L_q^{\text{vbr}}\right) -\right.\right.$$
$$\left.\left. - \left(L_d^{\text{vbr}} - L_q^{\text{vbr}}\right) \sin\left(2u + \tfrac{\pi}{6}\right)\right] i_{dc}\right\}, \quad (5.79)$$

$$g^{\text{III}}(u) \triangleq \left[L_d^{\text{vbr}} + L_q^{\text{vbr}} + \left(L_d^{\text{vbr}} - L_q^{\text{vbr}}\right)\cos(2u - \tfrac{\pi}{3})\right] i_\mu(u) -$$
$$- \left[\tfrac{1}{2}\left(L_d^{\text{vbr}} + L_q^{\text{vbr}}\right) + \left(L_d^{\text{vbr}} - L_q^{\text{vbr}}\right)\sin(2u - \tfrac{\pi}{6})\right] i_{dc} +$$
$$+ \sqrt{3}\left|\lambda_d^{\text{vbr}}\right| \cos(u - \tfrac{\pi}{6}) - C = 0\,. \quad (5.80)$$

Equation (5.80) is solved numerically for u. Using (5.77)–(5.79) in conjunction with (5.57), it can be shown that

$$\overline{v_{dc}} = \tfrac{3}{\pi}\,\omega_r \left(3\left|\lambda_d^{\text{vbr}}\right| - 3L_d^{\text{vbr}}\, i_{dc}\right)\,. \quad (5.81)$$

Analytic formulas for the commutating currents during the first sub-interval may be obtained by solving the linear system formed by (5.75) and (5.76):

$$i_1(\theta_{ev}) = \left[C/(3L_d^{\text{vbr}} L_q^{\text{vbr}})\right]\left[\tfrac{1}{2}\left(L_d^{\text{vbr}} + L_q^{\text{vbr}}\right) + \left(L_d^{\text{vbr}} - L_q^{\text{vbr}}\right)\sin(2\theta_{ev} + \tfrac{\pi}{6})\right] -$$
$$- \left(\lambda_d^{\text{vbr}}/L_d^{\text{vbr}}\right)\sin(\delta + \theta_{ev})\,, \quad (5.82)$$

$$i_6(\theta_{ev}) = i_{dc} + \left[C/(3L_d^{\text{vbr}} L_q^{\text{vbr}})\right]\left[\tfrac{1}{2}\left(L_d^{\text{vbr}} + L_q^{\text{vbr}}\right) - \left(L_d^{\text{vbr}} - L_q^{\text{vbr}}\right)\cos 2\theta_{ev}\right] +$$
$$+ \left(\lambda_d^{\text{vbr}}/L_d^{\text{vbr}}\right)\sin(\delta + \theta_{ev} + \tfrac{\pi}{3})\,. \quad (5.83)$$

The average first sub-interval qd-axes currents may thus be evaluated analytically. After manipulation,

$$\overline{\mathbf{i}_{qdr}^{s,(\mathrm{i})}} = \begin{bmatrix} \frac{4C}{\pi L_q^{\mathrm{vbr}}} \sin(\delta + \frac{u}{2} + \frac{\pi}{6}) \sin(\frac{\pi}{6} - \frac{u}{2}) \\ \frac{4C}{\pi L_d^{\mathrm{vbr}}} \cos(\delta + \frac{u}{2} + \frac{\pi}{6}) \sin(\frac{\pi}{6} - \frac{u}{2}) + \frac{3\lambda_d^{\mathrm{vbr}}}{\pi L_d^{\mathrm{vbr}}} \left(\frac{\pi}{3} - u\right) \end{bmatrix} . \tag{5.84}$$

The second sub-interval qd-axes currents, $\mathbf{i}_{qdr}^{s,(\mathrm{ii})}(\theta_{ev})$, are given by (5.66) and may be evaluated by numerical integration:

$$\overline{\mathbf{i}_{qdr}^{s,(\mathrm{ii})}} = \frac{3}{\pi} \int_{u-\frac{\pi}{6}}^{\frac{\pi}{2}} \mathbf{i}_{qdr}^{s,(\mathrm{ii})}(\theta_{ev})\, d\theta_{ev} . \tag{5.85}$$

Determining the mode of operation

Determination of the mode of operation is the first step of the averaging sub-routine and it guides the algorithm to the correct set of formulas. At the boundary between modes I and II, both nonlinear relations $g^{\mathrm{I}}(u = \pi/3)$ and $g^{\mathrm{II}}(\alpha = 0)$ yield

$$i_{dc}^{\mathrm{I\text{–}II}} = \sqrt{3}\, |\lambda_d^{\mathrm{vbr}}| / (L_d^{\mathrm{vbr}} + 3L_q^{\mathrm{vbr}}) . \tag{5.86}$$

At the boundary between modes II and III, the evaluation of $g^{\mathrm{II}}(\alpha = \pi/6)$ and $g^{\mathrm{III}}(u = \pi/3)$ yields

$$i_{dc}^{\mathrm{II\text{–}III}} = 3\, |\lambda_d^{\mathrm{vbr}}| / (3L_d^{\mathrm{vbr}} + L_q^{\mathrm{vbr}}) . \tag{5.87}$$

At the point of complete short-circuit occurring at the edge of mode III (denoted by mode IV), $g^{\mathrm{III}}(u = 2\pi/3)$ becomes

$$i_{dc}^{\mathrm{III\text{–}IV}} = |\lambda_d^{\mathrm{vbr}}| / L_d^{\mathrm{vbr}} . \tag{5.88}$$

This mode separation is valid if the boundaries are well-ordered. Note that $i_{dc}^{\mathrm{III\text{–}IV}} > i_{dc}^{\mathrm{II\text{–}III}}$ is always true; on the other hand, $i_{dc}^{\mathrm{II\text{–}III}} > i_{dc}^{\mathrm{I\text{–}II}}$ is satisfied only for the following range of VBR inductance parameters:

$$L_d^{\mathrm{vbr}} / L_q^{\mathrm{vbr}} < \tfrac{3\sqrt{3}-1}{3-\sqrt{3}} \approx 3.3 . \tag{5.89}$$

At first glance, (5.89) imposes a significant constraint on the model parameters. However, in the proposed model L_d^{vbr} assumes values closer to a leakage inductance,

while L_q^{vbr} is dominated by a magnetizing inductance term. Hence, it is generally expected that (5.89) will be satisfied for all "reasonable" inductance values.

Solving the nonlinear equations

According to the operation mode, a numerical solution to one of the nonlinear equations (5.65), (5.72) or (5.80) needs to be obtained. Recall that a continuous function $g(x)$ has a root $x_0 \in [a, b]$ if $g(a)\, g(b) \leq 0$. In this case, it suffices to show: (i) $g^{\text{I}}(0)\, g^{\text{I}}(\pi/3) \leq 0$, (ii) $g^{\text{II}}(0)\, g^{\text{II}}(\pi/6) \leq 0$, and (iii) $g^{\text{III}}(\pi/3)\, g^{\text{III}}(2\pi/3) \leq 0$.

For mode I operation, where $0 \leq i_{dc} \leq i_{dc}^{\text{I–II}}$, it may be shown that

$$g^{\text{I}}(0) = -2L_d^{\text{vbr}}\, i_{dc} \leq 0\,, \tag{5.90}$$

$$g^{\text{I}}(\tfrac{\pi}{3}) = \tfrac{\sqrt{3}}{2}|\lambda_d^{\text{vbr}}| - \tfrac{1}{2}(L_d^{\text{vbr}} + 3L_q^{\text{vbr}})\, i_{dc} \geq 0\,. \tag{5.91}$$

For mode II, $i_{dc}^{\text{I–II}} < i_{dc} \leq i_{dc}^{\text{II–III}}$, and

$$g^{\text{II}}(0) = -\tfrac{\sqrt{3}}{2}|\lambda_d^{\text{vbr}}| + \tfrac{1}{2}(L_d^{\text{vbr}} + 3L_q^{\text{vbr}})\, i_{dc} > 0\,, \tag{5.92}$$

$$g^{\text{II}}(\tfrac{\pi}{6}) = -\tfrac{3}{2}|\lambda_d^{\text{vbr}}| + \tfrac{1}{2}(3L_d^{\text{vbr}} + L_q^{\text{vbr}})\, i_{dc} \leq 0\,. \tag{5.93}$$

For mode III, $i_{dc}^{\text{II–III}} < i_{dc}$, and

$$g^{\text{III}}(\tfrac{\pi}{3}) = (3L_d^{\text{vbr}}/L_q^{\text{vbr}})\left[\tfrac{3}{2}|\lambda_d^{\text{vbr}}| - \tfrac{1}{2}(3L_d^{\text{vbr}} + L_q^{\text{vbr}})i_{dc}\right] < 0\,, \tag{5.94}$$

$$g^{\text{III}}(\tfrac{2\pi}{3}) = 6\left(|\lambda_d^{\text{vbr}}| - L_d^{\text{vbr}}\, i_{dc}\right) \geq 0\,. \tag{5.95}$$

Hence, a solution to all three equations will always exist. Further algebraic manipulations—not shown herein—reveal that the solution is unique. It may thus be obtained with arbitrary precision in a finite number of steps using the bisection algorithm [215].

Incorporating resistive losses

The model's accuracy may be improved by taking into account the resistive losses of the armature and the voltage drop of the rotating rectifier diodes. Their incor-

poration affects the magnitude of the brushless exciter steady-state field current, as well as the transient behavior of the synchronous generator.

In the previous sections, the armature resistance and the diodes were ignored. The rigorous incorporation of these terms in the model would entail considerable modifications and possibly would make the algebra intractable. Hence, to simplify the analysis, the computation of the losses is decoupled from the computation of the average dc voltage. Thus the average voltage applied across the main generator field is

$$\overline{v_{fd}} = \overline{v_{dc}} - \overline{v_{\text{loss}}} \,. \tag{5.96}$$

The average voltage loss, $\overline{v_{\text{loss}}}$, is computed by averaging the drop across diodes 1 and 6, and the ohmic drop of the armature's resistance, that is,

$$\overline{v_{\text{loss}}} = \left(\overline{v_{d1}} - r_r \overline{i_a}\right) + \left(\overline{v_{d6}} + r_r \overline{i_b}\right) \,. \tag{5.97}$$

A diode's voltage–current characteristic is represented herein by the following function:

$$v_d(i_d) = a i_d + (b i_d)^c \,. \tag{5.98}$$

The parameters a, b and c are obtained with a curve-fitting procedure.

5.4.4 Model summary

In summary, the algorithm proceeds as follows:

1. Initialize model; assume material is demagnetized.
2. Compute $\overline{di^s_{dr}}/dt$ from (5.43).
3. Determine the direction of change of i_{md} using (5.40), and check for reversal of direction. In case of direction reversal, add a point to the magnetic history stack.
4. Detect crossing of a previous reversal point (minor loop closure). In this case, delete two points from the history stack.

5. Compute L_{mi} using one of (5.34)–(5.37).

6. Compute λ_d^{vbr} from (5.48).

7. Determine δ from (5.54).

8. Determine the mode of operation, using (5.86)–(5.88).

9. If mode I:

   (a) Compute $\overline{v_{dc}}$ from (5.61).

   (b) Solve (5.65) for u.

   (c) Compute average currents from (5.66)–(5.69).

   If mode II:

   (a) Solve (5.72) for α.

   (b) Compute $\overline{v_{dc}}$ from (5.71).

   (c) Compute average currents from (5.66), (5.73).

   If mode III:

   (a) Compute $\overline{v_{dc}}$ from (5.81).

   (b) Solve (5.80) for u.

   (c) Compute average currents from (5.84), (5.85).

10. Compute $\overline{v_{fd}}$ from (5.96), (5.97).

11. Compute $d\lambda_{md}/dt$ from (5.41).

12. Compute di'_{fds}/dt from (5.42).

13. Go to step (2).

Steps (3)–(5) are specific to the Preisach model. If a linear magnetizing inductance is used instead, set $L_{mi} = 0$ and $L_{m,\text{sat}} = L_{md}$.

5.5 Parameter Identification Procedure

The exciter is a synchronous machine whose "standard" qd-axes model may be characterized independently by a variety of methods [145]. When no slip rings are installed to enable measurement of the rotating armature's quantities, the characterization must be performed at standstill. However, standstill measurements do not always correspond to actual operating characteristics. For example, the main flux magnetic path may behave differently when rotating. Furthermore, exciter machines are often designed with as little as one slot per pole per phase (as is the case for the machine under test herein), which results in nonsinusoidal winding inductances that require detailed modeling and complicated parameter identification procedures [174].

Alternately, if the performance of the exciter–generator system is examined as a whole, a simpler average-value model (such as the one proposed herein) may be adopted. The model may then be characterized by utilizing the generator's input–output characteristics while rotating. Assuming that the main alternator's model and parameter set are known, this section sets forth a method to extract the exciter's parameters from the measurable quantities, namely, the main alternator voltage and the exciter field winding current.

In general, every parameter estimation procedure aims at finding an optimal parameter vector, in the sense that the model's prediction error becomes as small as possible (refer to Section 2.1). Identification techniques that are applicable to the IEEE exciter model or, in general, to other linear/linearized time-invariant models [216, 217] are not applicable to the proposed exciter model because this model includes a memory operator—the Preisach hysteresis model. Therefore, its response depends on the time history, and it must be characterized by minimizing a time-domain based error, as in [218–220]. In this work, a genetic algorithm (GA) is employed for solving this optimization problem.

The parameters that need to be identified are:

- The exciter's field winding resistance, r_{fds}.

- The exciter's field winding leakage inductance, L_{lfds}.
- The exciter's armature winding resistance, r_r.
- The exciter's d-axis armature winding leakage inductance, L_{ldr}.
- The exciter's armature-to-field turns ratio, TR.
- The parameters that characterize the exciter's d-axis magnetizing branch. These are related to the Preisach model representation. The selected Preisach function is parameterized by four parameters, namely, λ_{Ms}, σ_w, σ_m, $\overline{w}$. Also required is the slope of the magnetizing curve at saturation, $L_{m,\mathrm{sat}}$.
- The exciter's voltage-behind-reactance q-axis inductance, $L_q^{\mathrm{vbr}} = L_{lqr} + L_{mq}$.
- The v–i characteristic of the rotating rectifier diodes.

The resistances, diode characteristic, and turns ratio may be measured at standstill, by disconnecting exciter and rectifier from the main generator. The remaining eight parameters will be identified from the system's time-domain response.

This section describes the experimental identification procedure as applied to the exciter machine of a 59-kW, 600-V, Leroy–Somer brushless synchronous generator, model LSA-432L7—the system described in Chapter 4. Its exciter is an eight-pole machine, whose field is rated for 12 V, 2.5 A.

5.5.1 Resistance measurements

The first step in the characterization procedure is the measurement of the dc values of armature and field winding resistance. Using a four-wire measurement technique, these were determined to be $r_r = 0.121\ \Omega$ and $r_{fds} = 4.69\ \Omega$ at room temperature. The variation of resistance with temperature is not incorporated in the model.

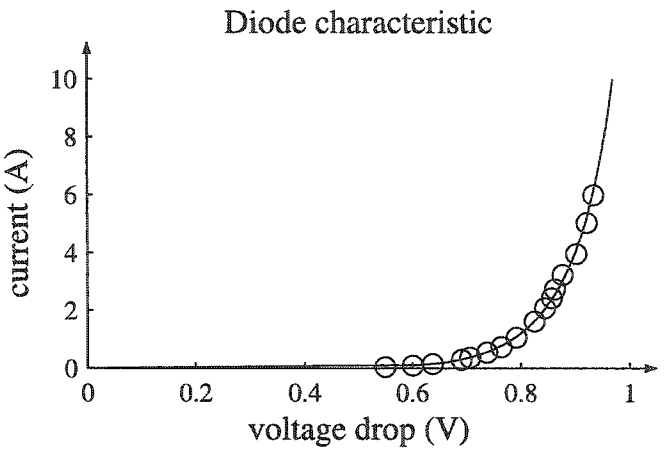

Fig. 5.15. Static i–v diode characteristic: measured points and fitted curve.

5.5.2 Diodes characterization

The diodes' static voltage–current characteristic is represented by the following function:

$$v_d(i_d) = ai_d + (bi_d)^c \,. \tag{5.99}$$

The parameters a, b and c are obtained with a curve-fitting procedure to experimental points: $a = -4.61 \cdot 10^{-3}$, $b = 0.114$, $c = 0.109$. The data points and fitted curve are displayed in Fig. 5.15.

5.5.3 Turns ratio measurement

The turns ratio is determined with the technique outlined in Section 4.3.3. This method consists of alternately exciting the exciter's field and armature windings (input side) with an ac source, while the other side (output side) is open-circuited. The output voltage and the input current are recorded with a dynamic signal analyzer and are processed to obtain hysteresis loops. The tests must be performed at a low frequency in order to ensure that the eddy currents in the rotor circuits are negligible. Herein, the hysteresis loops were obtained at 5 Hz.

The rotor is rotated so that current flowing in the series combination of phases c–b (with phase a open) produces an mmf aligned with the d-axis. When exciting the armature side, terminal quantities are related to qd-axes variables by

$$i_{md} \approx i^s_{dr} = \tfrac{2}{\sqrt{3}} i_c \,, \tag{5.100}$$

$$\lambda_{md} \approx \lambda'_{fds} = TR \cdot \lambda_{fds} = TR \int v_{fds}\, dt \,. \tag{5.101}$$

When exciting the field side,

$$i_{md} \approx i'_{fds} = \tfrac{2}{3} \tfrac{1}{TR} i_{fds} \,, \tag{5.102}$$

$$\lambda_{md} = \tfrac{1}{\sqrt{3}} \lambda_{cb} = \tfrac{1}{\sqrt{3}} \int v_{cb}\, dt \,. \tag{5.103}$$

The integration of the voltage in (5.101) and (5.103) is performed numerically. Appropriate integration constants are found such that the loops become symmetric around the origin.

The fundamental idea behind the procedure is to exploit the magnetic nonlinearity properties of the machine's iron. Specifically, different d-axis loops, $\lambda_{md}(TR)$ vs. i_{md} and λ_{md} vs. $i_{md}(TR)$ may be measured by exciting the machine from the armature and the field side, respectively. Each experiment contains a variable that is directly measurable and one that depends on the turns ratio. The turns ratio is a free parameter that is adjusted until a value is found for which the distance between the curves is minimized. This value is quite accurately determined by trial-and-error. For this machine, $TR = 0.070$ (see Fig. 5.16).

5.5.4 Evolutionary time-domain parameter estimation

In the proposed procedure, the generator is disconnected from the power system and is rotated at 1800 rpm under no-load conditions. The voltage reference is modified according to the profile shown in Fig. 5.17; this profile is the same as the one of Fig. 4.18, on page 99. These perturbations force the exciter to operate in all three rectification modes and create large variations in its magnetization state,

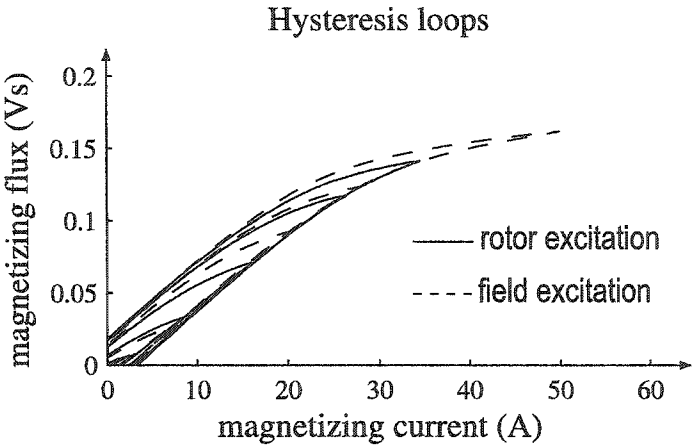

Fig. 5.16. Hysteresis loop match for $TR = 0.070$.

so that the experiment contains enough information for characterizing the model. The quantities of the internal rotating parts (Fig. 5.1) are not measurable because slip rings were not installed. Therefore, the model is characterized based on terminal quantities only, namely the synchronous generator voltage and the exciter's field current command, i^*_{fds}. (In the test system, the actual current closely follows the commanded current.) The GA searches for the parameter set that minimizes the difference between measured and predicted time-domain data. Each individual of the population, i.e. each parameter set, is evaluated by a computer simulation.

In order to quantify the difference between the measured and predicted waveforms, appropriate error functions must be defined. Since it is virtually impossible to achieve perfect synchronization between experimental and simulated ac voltages, the error is based on their envelopes. The "envelope" of the line-to-line voltage is defined (as in Section 4.4) by

$$v_{\text{ll,env}} = \sqrt{3\left[\left(v^e_{qs}\right)^2 + \left(v^e_{ds}\right)^2\right]}\,. \tag{5.104}$$

The difference at time sample $t_k, k = 1, \ldots, N$ between simulated and experimental waveforms is

$$\Delta v(t_k) = \min\{|v^{\text{sim}}_{\text{ll,env}}(t_k) - v^{\text{exp}}_{\text{ll,env}}(t_k)|, b_v\}\,, \tag{5.105}$$

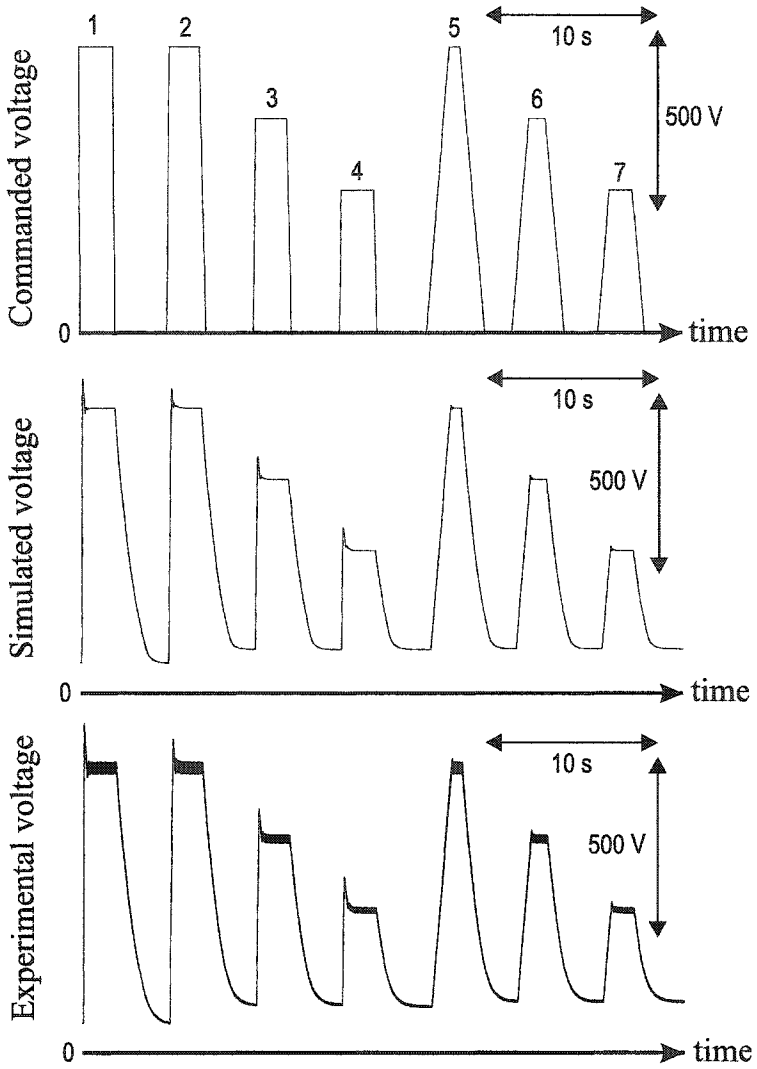

Fig. 5.17. Plots of the commanded and actual line-to-line voltage "envelope"—no load.

$$\Delta i(t_k) = \min\{|i_{fds}^{*,\mathrm{sim}}(t_k) - i_{fds}^{*,\mathrm{exp}}(t_k)|, b_i\}\,, \tag{5.106}$$

for the voltage and current, respectively. The constants $b_v = 100$ V and $b_i = 0.5$ A are upper bounds. The error takes into account the maximum and average difference: [6]

$$E_v = \tfrac{1}{2}\left\{\max[\Delta v(t_k)] + \mathrm{mean}[\Delta v(t_k)]\right\}\,, \tag{5.107}$$

$$E_i = \tfrac{1}{2}\left\{\max[\Delta i(t_k)] + \mathrm{mean}[\Delta i(t_k)]\right\}\,. \tag{5.108}$$

[6] If $x_k, k = 1, \ldots, N$ are the data points of x, then $\mathrm{mean}(x) = (1/N)\sum_{k=1}^{N} x_k$.

Table 5.1
List of GA variables and settings for exciter characterization.

variable	units	gene type	min.	max.	result
λ_{Ms}	Vs	exp.	0.1	2	0.952
$L_{m,\mathrm{sat}}$	mH	exp.	0.5	5	3.37
$\overline{w}$	A	lin.	−50	0	−16.7
σ_w	A	exp.	4	40	10.1
σ_m	A	exp.	4	40	15.9
L_q^{vbr}	mH	exp.	1	5	2.31
L_{ldr}	mH	exp.	0.1	1	0.490
L'_{lfds}	mH	exp.	0.1	1	0.861

The fitness is obtained by a weighted sum of the two errors,

$$f = \frac{b_v + w_i b_i}{E_v + w_i E_i} \geq 1\,, \tag{5.109}$$

where the weight, $w_i = 1000$, is used to compensate for the small magnitude of the field current compared to the terminal voltage. The experimental waveforms were sampled every $\Delta t = 1$ ms; the simulated traces were saved at the same rate.

The study-specific GA settings are listed in Table 5.1. The remaining GA parameter values were set to: $N_{\mathrm{ind}} = 100$, $N_{\mathrm{gen}} = 100$, $\eta = 2$, $c_{\sigma\text{-tr}} = 2.0$, $p_{\mathrm{mt}} = 0.6$, $p_{\mathrm{tm}} = 0.00625$ $(= 1/8/20)$, $\sigma_{\mathrm{pm}} = 0.3$, $p_{\mathrm{pm}} = 0.025$ $(= 1/8/5)$, $N_{\mathrm{rs}} = 25$, $\sigma_{\mathrm{rs}} = 0.1$. To accelerate the evolution process, the simulations were performed in a parallel computing environment. The evaluations were distributed among a cluster of eight computers (having AMD processors running at 1.67 GHz), and, for 100 generations, approximately 12 hours were required.

The evolution of a representative GA run is displayed in Fig. 5.18. At the specified number of generations, the GA has reached a "plateau," where the fitness increases only incrementally. The achieved fitness (as defined by (5.109)) was $f = 6.26$. The parameter values of the best individual are contained in Table 5.1. It is possible that, if the GA had run for a larger number of generations, then a fitter individual might have been obtained. However, since the predictions of the model with the obtained parameter set were satisfactory, the GA was terminated.

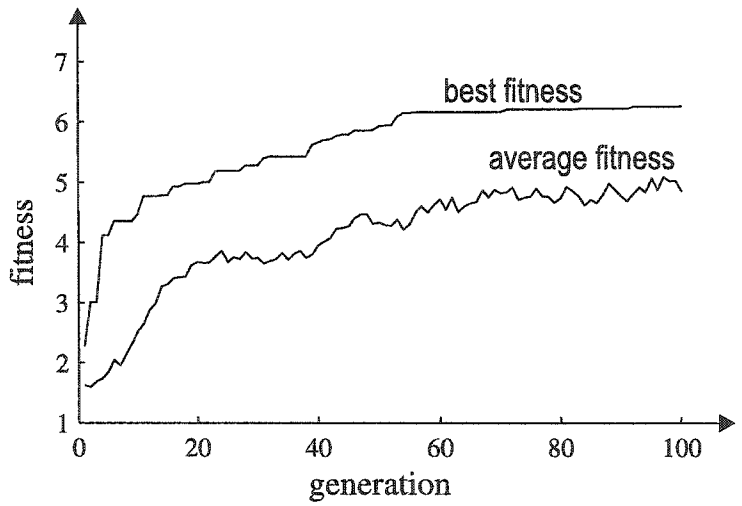

Fig. 5.18. Plot of fitness vs. generation number for the exciter GA.

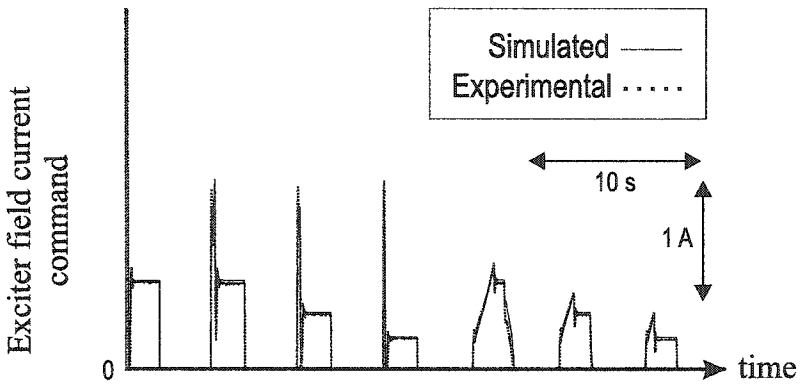

Fig. 5.19. Plot of the simulated and experimental exciter field current command—no load.

The experimental and simulated waveforms of terminal voltage and exciter field current command are illustrated in Fig. 5.17 and Fig. 5.19, respectively. A plot of the obtained Preisach function is shown in Fig. 5.20.

5.6 Experimental Validation

The generator is loaded with an uncontrolled rectifier that feeds a resistive load through an LC filter, as shown in Fig. 5.21. The load parameters are: $L = 7.5$ mH,

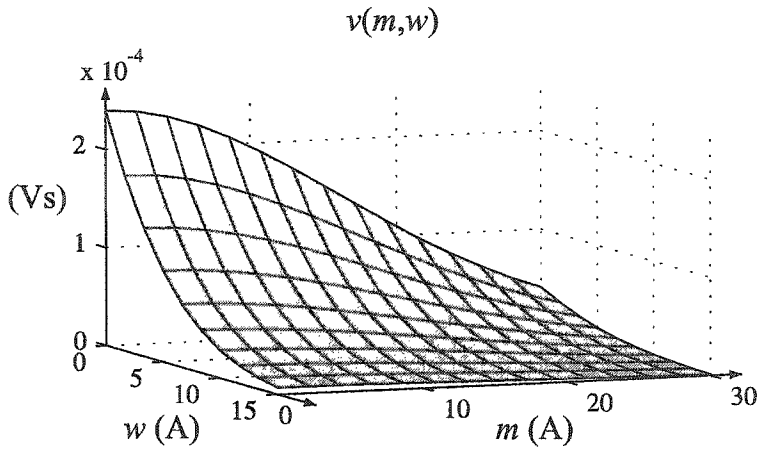

Fig. 5.20. Preisach function plot for $w > 0$ and $m > 0$. This function is symmetric with respect to the w-axis.

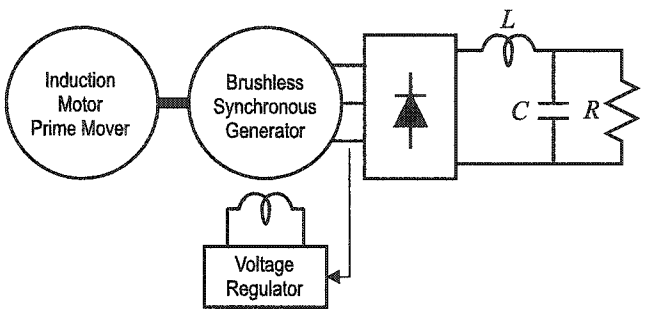

Fig. 5.21. Experimental setup of the exciter model validation study.

$C = 500\ \mu\text{F}$, $R = 16.3\,\Omega$. The quantities of the internal rotating parts (Fig. 5.1) are not measurable because slip rings were not installed. Hence, the model is judged based on terminal quantities only, namely the synchronous generator voltage and the exciter's field current.

In this case study, the generator's voltage reference is modified according to the profile shown in Fig. 4.18, on page 99. This series of commanded voltage steps creates an extended period of significant disturbances and tests the model's validity for large-transients simulations. The terminal voltage exhibits an overshoot, which is more pronounced for the faster slew-rate steps. Moreover, due to the exciter's magnetically hysteretic behavior, it does not fall to zero. The varying levels of remanence

in the exciter machine reflect on the magnitude of the voltage and are captured fairly accurately. The standard IEEE model [181] does not predict hysteretic effects. The higher ripple in the experimental voltage waveform is attributed to slot effects, not incorporated in the synchronous machine model (see Chapter 4). Simulated vs. experimental waveforms of the exciter's field current command are shown in Fig. 5.22; these correspond to the seven command steps of Fig. 4.18. The first plot depicts a situation where the controller's current limit (3 A) is reached. Such nonlinear control strategies may not be studied using the IEEE model, which does not calculate the exciter's field current. The proposed model is able to predict both steady-state values and transient behavior. From Figs. 4.18 and 5.22 it can be seen that the simulated terminal voltage and field current are in good agreement with the measured quantities for this loaded case, even though the parameter identification was conducted using no-load data.

The corresponding variation of rectification mode is depicted in Fig. 5.23. Under steady-state conditions, the exciter operates in mode II; however, the auto-delay angle α varies with operating point. During transients, operation in all modes takes place. Therefore, a simple mode I model would have been insufficient to predict this behavior. The observed rapid mode alternations and ripple in the waveforms of u and α result from the ripple in the main alternator field current, which in turn is caused by the rectifier load on the main alternator.

An illustration of hysteretic behavior is shown in Fig. 5.24; the depicted transient corresponds to the first trapezoid of Fig. 4.18. The upper right hand plot depicts the magnetization component of the magnetizing flux vs. magnetizing current, $\lambda_{md,M}(i_{md})$; the upper left and lower right plots depict $\lambda_{md,M}(t)$ and $i_{md}(t)$, respectively. The $i_{md}(t)$ plot has been rotated 90° clockwise. As can be seen, the trajectories move through four "steady-state" points, labelled A, B, C, and D (D $\neq$ A). These points do not lie on a straight line. This complex behavior could not have been captured by a linear magnetization model (where $\lambda_{md} = L_{md}\, i_{md}$).

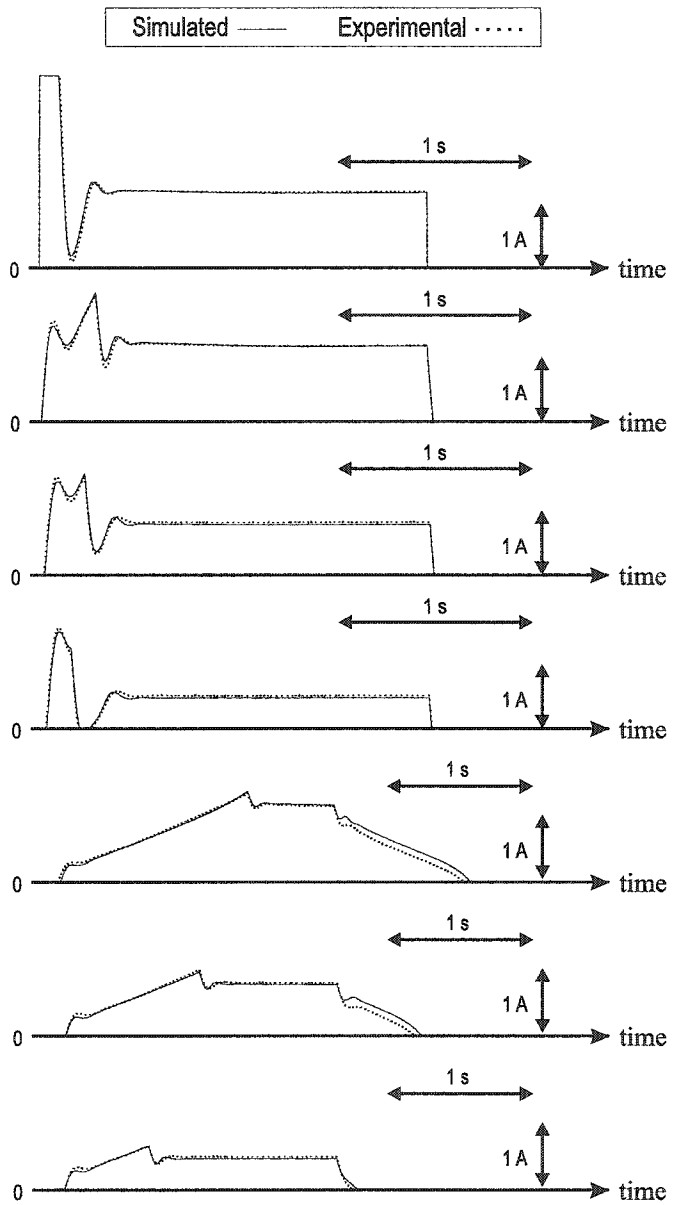

Fig. 5.22. Plots of the commanded exciter field current.

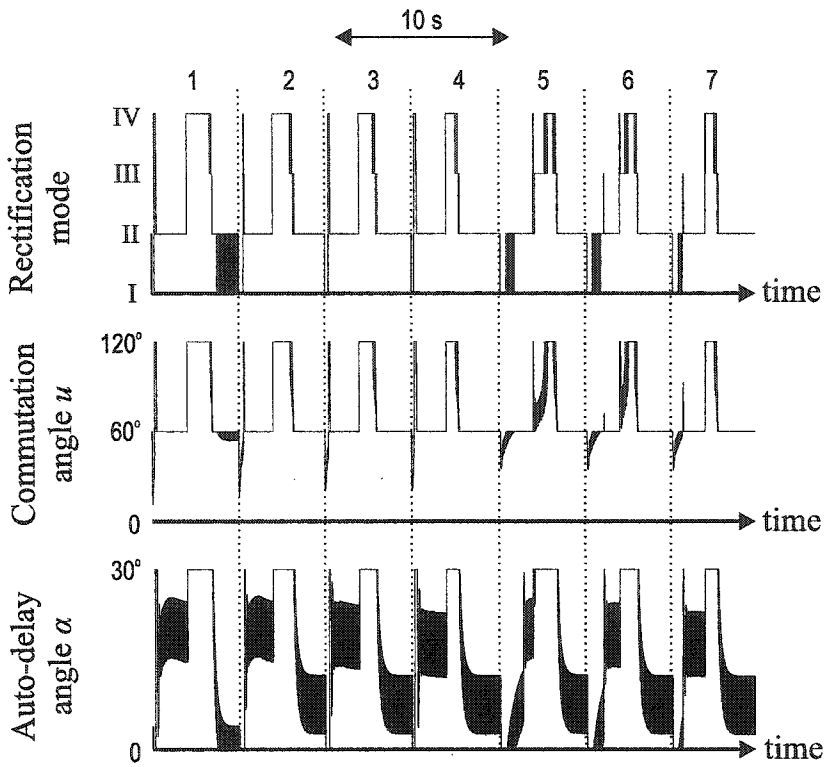

Fig. 5.23. Variation of rectification mode, commutation angle, and auto-delay angle.

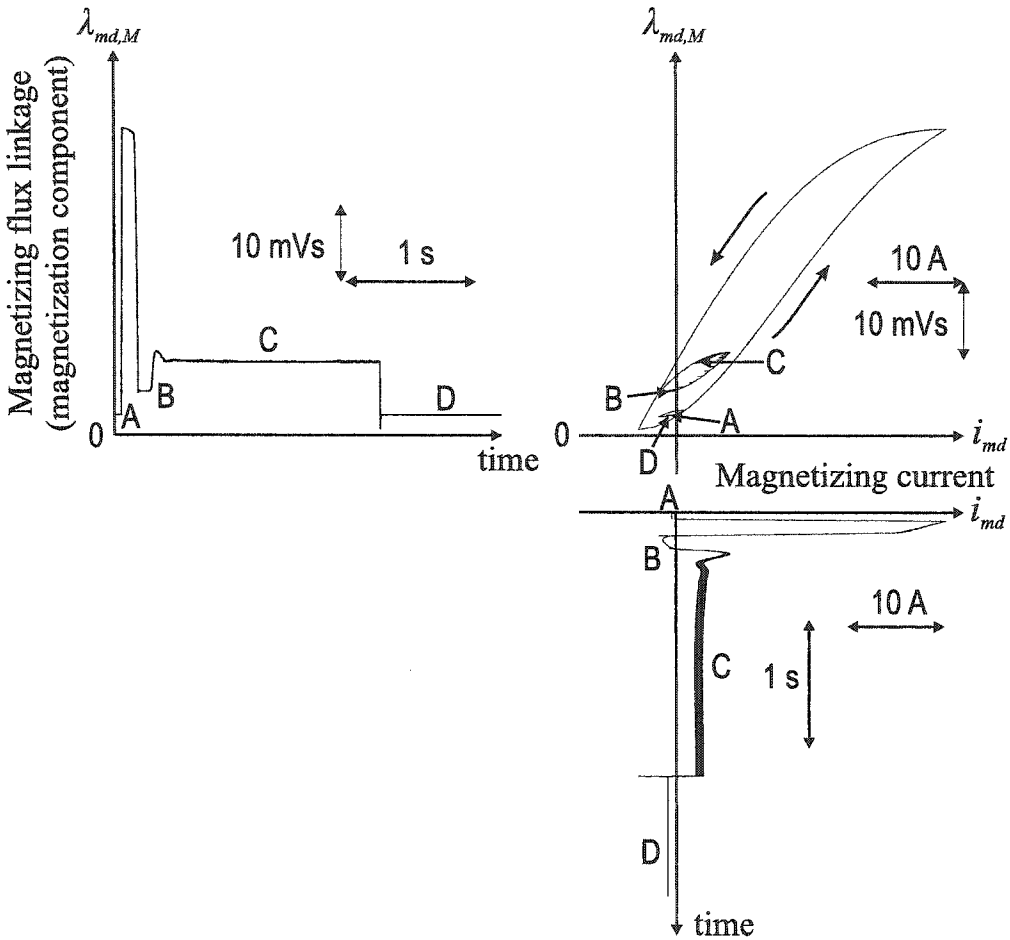

Fig. 5.24. Illustration of hysteresis.

In order to "initialize" the magnetic state, the commanded voltage is stepped from 0 V to 560 V and then back to 0 V at 20000 V/s (not shown in Fig. 4.18). The exciter's flux is forced to a higher than normal level (see Fig. 5.24). According to the deletion property, the previous magnetic history is erased. Furthermore, on account of the congruency property, the return path depends only on the reversal point on the λ_{md}–i_{md} curve. Hence, this initialization procedure is guaranteed to bring the material back to the same state, regardless of the previous operating history. This theoretically predicted behavior was experimentally verified.

5.7 Summary

The described brushless exciter model was successfully evaluated against experimental results. The modeling of all rectification modes, the prediction of the exciter's field current, and the representation of magnetic hysteresis, are important features that are not included in the standard IEEE exciter model. The proposed model is thus a high-fidelity alternative for large-disturbance simulations, where a computationally efficient exciter representation is necessary. Hence, it is recommended for transient stability studies and voltage regulator design.

The model was successfully parameterized using genetic algorithms. The GA minimized an error based on the time-domain difference between the observed and simulated waveforms of the synchronous generator system. The proposed experiment was relatively easy to carry out; it did not require the installation of slip rings for monitoring internal rotating quantities, and was performed at no load.

This work is pending publication in a peer-reviewed journal [221, 222].

6. CONCLUSIONS

This research ultimately resulted in a new class of electric machine models, ideal for dynamic simulations of modern power systems. The proposed models are differentiated from previous work in this area because of their underlying modeling philosophy, based on the realization that pre-defined equivalent circuit structures may not be sufficient for accurately reproducing the machines' actual behavior. Rather, what is required is the generalization of existing representations by means of arbitrary linear networks, whose complexity and parameters are eventually decided from experimental observations. The successful integration of nonlinear elements and generic linear systems to obtain highly accurate, computationally efficient mathematic formulations is a major contribution of this thesis.

The proposed induction and synchronous machine models both adhere to the aforementioned principles. Compared to existing models, they offer enhanced capabilities of simultaneously incorporating magnetic saturation effects and increased order rotor representations. The proposed brushless excitation model does not embrace such detailed machine descriptions, since the exciter is in essence a "secondary" machine used to drive the main alternator. However, the exciter's significance with respect to the power system's stability properties can not be underrated, and this work has thus focused on faithfully recreating its exact input–output relationship. This model outperforms the widely used IEEE standard model by being valid for large-disturbance transient studies, by calculating the exciter's field current, and by representing magnetic hysteresis.

In parallel with the theoretical model descriptions, appropriate experimental characterization procedures have been designed and presented in detail. In particular, the application of evolutionary optimization algorithms to the parameter identi-

fication process has been found to be straightforward and highly effective. Evolutionary algorithms are significantly simpler, more flexible, and more efficient for large-dimensional problems, such as the simulation-based prediction-error-minimization problem, than traditional optimization methods. A significant part of this research was devoted to the development of a collection of genetic optimization routines and the setting up of a parallel computing environment, which have proven instrumental for identifying the proposed models' parameters.

The proposed approach to electric machine modeling suggests several new research avenues. It is reasonable that the next step should be the modeling of additional machines using the proposed representations, and their characterization with the suggested methods. It would be interesting to apply the synchronous machine model to solid-iron rotor generators, that traditionally have been described by high-order rotor representations, or for performing subsynchronous resonance studies. The amount of experience thus gained would more clearly reveal the proposed models' capabilities as well as their limitations, and eventually would lead to more advanced modeling approaches, even for other electric machine types.

The induction machine model lends itself to the design of novel drive control schemes, that will take into consideration the high-bandwidth rotor behavior as well as the magnetizing and leakage saturation, in order to achieve improved steady-state and dynamic performance (for instance, the maximization of torque per stator ampere). From a theoretical point of view, the minor inconsistency related to the non-conservative nature of the leakage magnetic fields requires further investigation; it may be possible to resolve this by adopting alternate forms of leakage inductance. Once this issue has been addressed, the derivation of new synchronous generator models with saturable leakage paths will also be attainable.

As far as the exciter model is concerned, a further improvement would be the inclusion of damper windings, and the subsequent derivation of an average-value model. Alternatively, one could concentrate on improving the Preisach hysteresis

model, for example by incorporation of hysteresis along the q-axis as well, or the utilization of more advanced "dynamic" Preisach models.

Perhaps the most significant disadvantage of qd-axes models is the difficulty of incorporating iron core losses. However, it might be possible to achieve this by transforming the (nonlinear, but single-valued) magnetizing branches into hysteretic elements, as was done within the proposed exciter model. Of course, since hysteresis loss is dependent on the ac frequency, the analysis would have to be performed in the reference frame of the actual physical magnetic field; for example, in an induction machine the rotor "sees" a magnetic field alternating at slip frequency, while in the stator, the field varies at the electrical frequency. Hence, the challenge would be to extend the orthogonal axes theory so that the combination of two reference frames (frequencies) in a single model becomes feasible.

In regard to model parameterization, it should be possible to emulate the experimental procedures using finite element or magnetic equivalent circuit analyses. This would require very accurate iron models, also able to predict minor-loop excursions for recreating the machine's small-signal behavior (the Preisach model might prove useful in this case). Indeed, parameterization from the design stage offers significant advantages, such as lower costs and optimal designs for the specific application at hand (perhaps using evolutionary algorithms). In addition, the possibility to extract the models' parameters from on-line data presents numerous opportunities for future research.

The investigation of more advanced (in terms of convergence speed and efficiency) evolutionary optimization techniques should be continued. The tremendous potential of genetic algorithms (and other evolutionary optimization methods) for parameter estimation has not yet been fully exploited. Genetic algorithms offer a great flexibility to the analyst. In general, a variety of available information about a system (be it in the frequency-domain, the time-domain, or a combination of both) may be readily incorporated in a fitness function. Furthermore, GAs not only provide means for characterizing complex models, such as the ones herein, but should

also encourage the derivation and utilization of more detailed and state-of-the-art models that would otherwise have been intractable to parameterize.

LIST OF REFERENCES

LIST OF REFERENCES

[1] (2002, Jan.) Electrical power networks efficiency and security control challenge problem, EPNES. ONR. [Online]. Available: http://www.usna.edu/EPNES/ONR_Control_Challenge.pdf

[2] The eastern interconnection power outage of august 14–15, 2003. U.S. Department of Energy, Office of Electric Transmission & Distribution. [Online]. Available: http://www.electricity.doe.gov/2003_blackout.htm

[3] R. H. Park, "Two-reaction theory of synchronous machines. Generalized method of analysis—Part I," *AIEE Transactions*, vol. 48, no. 3, pp. 716–730, July 1929.

[4] H. C. Stanley, "An analysis of the induction machine," *AIEE Trans.*, vol. 57, pp. 751–757, 1938.

[5] P. C. Krause, O. Wasynczuk, and S. D. Sudhoff, *Analysis of Electric Machinery.* New York: IEEE Press, 1995.

[6] M. Kostenko and L. Piotrovsky, *Electrical Machines*, 3rd ed. Moscow: Mir Publishers, 1974, vol. I–II.

[7] P. L. Alger, *Induction Machines. Their Behavior and Uses.* Basel, Switzerland: Gordon and Breach, 1995.

[8] T. Bäck, U. Hammel, and H.-P. Schwefel, "Evolutionary computation: Comments on the history and current state," *IEEE Trans. Evol. Comput.*, vol. 1, no. 1, pp. 3–17, Apr. 1997.

[9] C. Darwin, *The Origin of Species.* New York: Oxford University Press, 1998.

[10] W. Atmar, "Notes on the simulation of evolution," *IEEE Trans. Neural Networks*, vol. 5, no. 1, pp. 130–147, Jan. 1994.

[11] D. E. Goldberg, *Genetic Algorithms in Search, Optimization, and Machine Learning.* Boston: Addison–Wesley, 1989.

[12] H.-P. Schwefel, *Evolution and Optimum Seeking.* New York: John Wiley & Sons, 1995.

[13] Z. Michalewicz, *Genetic Algorithms + Data Structures = Evolution Programs.* New York: Springer, 1996.

[14] M. Gen and R. Cheng, *Genetic Algorithms & Engineering Optimization.* New York: John Wiley & Sons, 2000.

[15] K. Deb, *Multi-Objective Optimization using Evolutionary Algorithms.* Chichester: John Wiley & Sons, 2001.

[16] S. D. Sudhoff, "Energy Systems Analysis Consortium (ESAC) Non-Encoded Genetic Algorithm Toolbox (ENEGAT)," School of Electrical and Computer Engr., Purdue Univ., West Lafayette, IN, 47907, 2003.

[17] J. H. Holland, *Adaptation in Natural and Artificial Systems.* Cambridge, Massachusetts: The MIT Press, 1998.

[18] K. A. D. Jong, "Genetic algorithms are NOT function optimizers," in *Foundations of Genetic Algorithms 2*, L. D. Whitley, Ed. Morgan Kaufmann, 1993, pp. 5–17.

[19] D. E. Goldberg, "Simple genetic algorithms and the minimal, deceptive problem," in *Genetic Algorithms and Simulated Annealing*, L. Davis, Ed. Pitman, London; Morgan Kaufmann, Los Altos, California, 1987, pp. 74–88.

[20] L. Booker, "Improving search in genetic algorithms," in *Genetic Algorithms and Simulated Annealing*, L. Davis, Ed. Pitman, London; Morgan Kaufmann, Los Altos, California, 1987, pp. 61–73.

[21] G. Rudolph, "Convergence analysis of canonical genetic algorithms," *IEEE Trans. Neural Networks*, vol. 5, no. 1, pp. 96–101, Jan. 1994.

[22] J. D. Schaffer, "Some effects of selection procedures on hyperplane sampling by genetic algorithms," in *Genetic Algorithms and Simulated Annealing*, L. Davis, Ed. Pitman, London; Morgan Kaufmann, Los Altos, California, 1987, pp. 89–103.

[23] D. E. Goldberg, *The Design of Innovation. Lessons from and for Competent Genetic Algorithms.* Boston: Kluwer Academic Publishers, 2002.

[24] L. Ljung, *System Identification: Theory for the User.* New Jersey: Prentice–Hall, 1987.

[25] E. K. P. Chong and S. H. Żak, *An Introduction to Optimization.* New York: John Wiley & Sons, 1996.

[26] F. Alonge, F. D'Ippolito, G. Ferrante, and F. M. Raimondi, "Parameter identification of induction motor model using genetic algorithms," *IEE Proc., Control Theory Appl.*, vol. 145, no. 6, pp. 587–593, Nov. 1998.

[27] K. S. Huang, W. Kent, Q. H. Wu, and D. R. Turner, "Parameter identification of an induction machine using genetic algorithms," in *Proc. International Symposium on Computer Aided Control System Design*, vol. 1. IEEE, 1999, pp. 510–515.

[28] H. Razik, C. Defranoux, and A. Rezzoug, "Identification of induction motor using a genetic algorithm and a quasi-Newton algorithm," in *Proc. Power Electronics Congress CIEP.* IEEE, Oct. 2000, pp. 65–70.

[29] R. Escarela-Perez, T. Niewierowicz, and E. Campero-Littlewood, "Synchronous machine parameters from frequency-response finite-element simulations and genetic algorithms," *IEEE Trans. Energy Conversion*, vol. 16, no. 2, pp. 198–203, June 2001.

[30] B. P. Loop and S. D. Sudhoff, "Switched reluctance machine model using inverse inductance characterization," *IEEE Trans. Ind. Applicat.*, vol. 39, no. 3, pp. 743–751, May/June 2003.

[31] E. J. Gardner, M. J. Simmons, and D. P. Snustad, *Principles of Genetics*, 8th ed. New York: John Wiley & Sons, 1991.

[32] A. H. Wright, "Genetic algorithms for real parameter optimization," in *Foundations of Genetic Algorithms*, G. J. E. Rawlins, Ed. Morgan Kaufmann, 1991, pp. 205–218.

[33] K. Deb and R. B. Agrawal, "Simulated binary crossover for continuous search space," Indian Institute of Technology, Kanpur, Tech. Rep., Nov. 1994.

[34] S. D. Sudhoff, "Genetic Optimization and Systems Engineering Tool (GOSET)," School of Electrical and Computer Engr., Purdue Univ., West Lafayette, IN, 47907, 2003.

[35] N. L. Schmitz and D. W. Novotny, *Introductory Electromechanics*. New York: Ronald Press Company, 1965.

[36] H. R. Fudeh and C. M. Ong, "Modeling and analysis of induction machines containing space harmonics. Part I: Modeling and transformation," *IEEE Trans. Power App. Syst.*, vol. 102, no. 8, pp. 2608–2615, Aug. 1983.

[37] ——, "Modeling and analysis of induction machines containing space harmonics. Part II: Analysis of asynchronous and synchronous actions," *IEEE Trans. Power App. Syst.*, vol. 102, no. 8, pp. 2616–2620, Aug. 1983.

[38] ——, "Modeling and analysis of induction machines containing space harmonics. Part III: Three-phase cage rotor induction machines," *IEEE Trans. Power App. Syst.*, vol. 102, no. 8, pp. 2621–2628, Aug. 1983.

[39] X. Luo, Y. Liao, H. A. Toliyat, A. El-Antably, and T. A. Lipo, "Multiple coupled circuit modeling of induction machines," *IEEE Trans. Ind. Applicat.*, vol. 31, no. 2, pp. 311–318, Mar./Apr. 1995.

[40] A. R. Muñoz and T. A. Lipo, "Complex vector model of the squirrel-cage induction machine including instantaneous rotor bar currents," *IEEE Trans. Ind. Applicat.*, vol. 35, no. 6, pp. 1332–1340, Nov./Dec. 1999.

[41] E. Levi and M. Wang, "Online identification of the mutual inductance for vector controlled induction motor drives," *IEEE Trans. Energy Conversion*, vol. 18, no. 2, pp. 299–305, June 2003.

[42] P. Vas and M. Alaküla, "Field-oriented control of saturated induction machines," *IEEE Trans. Energy Conversion*, vol. 5, no. 1, pp. 218–224, Mar. 1990.

[43] R. D. Lorenz and D. W. Novotny, "Saturation effects in field-oriented induction machines," *IEEE Trans. Ind. Applicat.*, vol. 26, no. 2, pp. 283–289, Mar./Apr. 1990.

[44] D. S. Kirschen, D. W. Novotny, and T. A. Lipo, "Optimal efficiency control of an induction motor drive," *IEEE Trans. Energy Conversion*, vol. 2, no. 1, pp. 70–76, Mar. 1987.

[45] R. D. Lorenz and S.-M. Yang, "Efficiency-optimized flux trajectories for closed-cycle operation of field-orientation induction machine drives," *IEEE Trans. Ind. Applicat.*, vol. 28, no. 3, pp. 574–580, May/June 1992.

[46] I. T. Wallace, D. W. Novotny, R. D. Lorenz, and D. M. Divan, "Increasing the dynamic torque per ampere capability of induction machines," *IEEE Trans. Ind. Applicat.*, vol. 30, no. 1, pp. 146–153, Jan./Feb. 1994.

[47] ——, "Verification of enhanced dynamic torque per ampere capability in saturated induction machines," *IEEE Trans. Ind. Applicat.*, vol. 30, no. 5, pp. 1193–1201, Sept./Oct. 1994.

[48] O. Wasynczuk, S. D. Sudhoff, K. A. Corzine, J. L. Tichenor, P. C. Krause, I. G. Hansen, and L. M. Taylor, "A maximum torque per ampere control strategy for induction motor drives," *IEEE Trans. Energy Conversion*, vol. 13, no. 2, pp. 163–169, June 1998.

[49] H. Grotstollen and J. Wiesing, "Torque capability and control of a saturated induction motor over a wide range of flux weakening," *IEEE Trans. Ind. Electron.*, vol. 42, no. 4, pp. 374–381, Aug. 1995.

[50] Y.-K. He and T. A. Lipo, "Computer simulation of an induction machine with spatially dependent saturation," *IEEE Trans. Power App. Syst.*, vol. 103, no. 4, pp. 707–714, Apr. 1984.

[51] R. J. Kerkman, "Steady-state and transient analyses of an induction machine with saturation of the magnetizing branch," *IEEE Trans. Ind. Applicat.*, vol. 21, no. 1, pp. 226–234, Jan./Feb. 1985.

[52] J. E. Brown, K. P. Kovács, and P. Vas, "A method of including the effects of main flux path saturation in the generalized equations of A.C. machines," *IEEE Trans. Power App. Syst.*, vol. 102, no. 1, pp. 96–103, Jan. 1983.

[53] K. P. Kovács, "On the theory of cylindrical rotor A.C. machines, including main flux saturation," *IEEE Trans. Power App. Syst.*, vol. 103, no. 4, pp. 754–761, Apr. 1984.

[54] P. Vas, K. E. Hallenius, and J. E. Brown, "Cross-saturation in smooth-air-gap electrical machines," *IEEE Trans. Energy Conversion*, vol. 1, no. 1, pp. 103–112, Mar. 1986.

[55] A. M. El-Serafi, A. S. Abdallah, M. K. El-Sherbiny, and E. H. Badawy, "Experimental study of the saturation and the cross-magnetizing phenomenon in saturated synchronous machines," *IEEE Trans. Energy Conversion*, vol. 3, no. 4, pp. 815–823, Dec. 1988.

[56] A. M. El-Serafi and J. Wu, "Determination of the parameters representing the cross-magnetizing effect in saturated synchronous machines," *IEEE Trans. Energy Conversion*, vol. 8, no. 3, pp. 333–342, Sept. 1993.

[57] E. Levi and V. A. Levi, "Impact of dynamic cross-saturation on accuracy of saturated synchronous machine models," *IEEE Trans. Energy Conversion*, vol. 15, no. 2, pp. 224–230, June 2000.

[58] T. A. Lipo and A. Consoli, "Modeling and simulation of induction motors with saturable leakage reactances," *IEEE Trans. Ind. Applicat.*, vol. 20, no. 1, pp. 180–189, Jan./Feb. 1984.

[59] A. M. A. Mahmoud and R. W. Menzies, "A complete time domain model of the induction motor for efficiency evaluation," *IEEE Trans. Energy Conversion*, vol. 1, no. 1, pp. 68–76, Mar. 1986.

[60] A. Keyhani and H. Tsai, "IGSPICE simulation of induction machines with saturable inductances," *IEEE Trans. Energy Conversion*, vol. 4, no. 1, pp. 118–125, Mar. 1989.

[61] J. Faiz and A. R. Seifi, "Dynamic analysis of induction motors with saturable inductances," *Electric Power Systems Research*, vol. 34, pp. 205–210, 1995.

[62] G. R. Slemon, "Modelling of induction machines for electric drives," *IEEE Trans. Ind. Applicat.*, vol. 25, no. 6, pp. 1126–1131, Nov./Dec. 1989.

[63] J. O. Ojo, A. Consoli, and T. A. Lipo, "An improved model of saturated induction machines," *IEEE Trans. Ind. Applicat.*, vol. 26, no. 2, pp. 212–221, Mar./Apr. 1990.

[64] C. R. Sullivan and S. R. Sanders, "Models for induction machines with magnetic saturation of the main flux path," *IEEE Trans. Ind. Applicat.*, vol. 31, no. 4, pp. 907–917, July/Aug. 1995.

[65] J. C. Moreira and T. A. Lipo, "Modeling of saturated ac machines including air gap flux harmonic components," *IEEE Trans. Ind. Applicat.*, vol. 28, no. 2, pp. 343–349, Mar./Apr. 1992.

[66] Z. Zhao, M. Kendig, and D. Rogovin, "Modeling, simulation, and analysis of stator windings of induction machines in high frequencies," in *Proc. Industry Applications Society Annual Meeting*, vol. 1. IEEE, 1998, pp. 259–264.

[67] Z. Zhang, G. E. Dawson, and T. R. Eastham, "Evaluation of dynamic parameters and performance of deep-bar induction machines," in *Proc. Industry Applications Society Annual Meeting.* IEEE, 1994, pp. 62–66.

[68] R. W. A. A. De Doncker, "Field-oriented controllers with rotor deep bar compensation circuits," *IEEE Trans. Ind. Applicat.*, vol. 28, no. 5, pp. 1062–1071, Sept./Oct. 1992.

[69] J. Langheim, "Modelling of rotorbars with skin effect for dynamic simulation of induction machines," in *Proc. Industry Applications Society Annual Meeting.* IEEE, 1989, pp. 38–44.

[70] W. Levy, C. F. Landy, and M. D. McCulloch, "Improved models for the simulation of deep bar induction motors," *IEEE Trans. Energy Conversion*, vol. 5, no. 2, pp. 393–400, June 1990.

[71] O. V. Thorsen and M. Dalva, "Development and industrial application of a practical model for simulation of saturated deep bar induction machines," in *Proc. Industry Applications Society Annual Meeting*, vol. 1. IEEE, 1994, pp. 137–142.

[72] A. C. Smith, R. C. Healey, and S. Williamson, "A transient induction motor model including saturation and deep bar effect," *IEEE Trans. Energy Conversion*, vol. 11, no. 1, pp. 8–15, Mar. 1996.

[73] N. Retière, A. Foggia, D. Roye, and P. Mannevy, "Deep-bar induction motor model for large transient analysis under saturated conditions," in *Proc. International Electric Machines and Drives Conference.* IEEE, 1997, pp. MD1–3.1–3.3.

[74] N. M. Retière and M. S. Ivanès, "An introduction to electric machine modeling by systems of non-integer order. Application to double-cage induction machine," *IEEE Trans. Energy Conversion*, vol. 14, no. 4, pp. 1026–1032, Dec. 1999.

[75] D. Riu, N. Retière, and M. Ivanès, "Turbine generator modeling by non-integer order systems," in *Proc. International Electric Machines and Drives Conference.* IEEE, 2001, pp. 185–187.

[76] S. Williamson and A. C. Smith, "Equivalent circuits for cage induction motors with inter-bar currents," *IEE Proc.–Electr. Power Appl.*, vol. 149, no. 3, pp. 173–183, May 2002.

[77] C. A. Hernández-Arámburo, T. C. Green, and A. C. Smith, "Assessment of power losses of an inverter-driven induction machine with its experimental validation," in *Proc.* 37^{th} *Industry Applications Society Annual Meeting.* IEEE, Oct. 2002.

[78] Y. Chen and P. Pillay, "An improved formula for lamination core loss calculations in machines operating with high frequency and high flux density excitation," in *Proc.* 37^{th} *Industry Applications Society Annual Meeting.* IEEE, Oct. 2002.

[79] E. Levi, "A unified approach to main flux saturation modelling in D-Q axis models of induction machines," *IEEE Trans. Energy Conversion*, vol. 10, no. 3, pp. 455–461, Sept. 1995.

[80] I. Boldea and S. A. Nasar, "A general equivalent circuit (GEC) of electric machines including crosscoupling saturation and frequency effects," *IEEE Trans. Energy Conversion*, vol. 3, no. 3, pp. 689–695, Sept. 1988.

[81] S.-I. Moon, A. Keyhani, and S. Pillutla, "Nonlinear neural-network modeling of an induction machine," *IEEE Trans. Contr. Syst. Technol.*, vol. 7, no. 2, pp. 203–211, Mar. 1999.

[82] D. C. Aliprantis, "Advances in electric machine modeling and evolutionary parameter identification," Ph.D. dissertation, Purdue University, West Lafayette, IN, Dec. 2003.

[83] P. J. Antsaklis and A. N. Michel, *Linear Systems.* New York: McGraw–Hill, 1997.

[84] S. D. Sudhoff, D. C. Aliprantis, B. T. Kuhn, and P. L. Chapman, "An advanced induction machine model for predicting inverter–machine interaction," in *Proc. Power Electronics Specialists Conference*, vol. 4. IEEE, June 2001, pp. 2043–2052.

[85] *Test Procedure for Polyphase Induction Motors and Generators*, IEEE Std. 112, 1996.

[86] D. Dolinar, R. D. Weerdt, R. Belmans, and E. M. Freeman, "Calculation of two-axis induction motor model parameters using finite elements," *IEEE Trans. Energy Conversion*, vol. 12, no. 2, pp. 133–142, June 1997.

[87] S.-I. Moon and A. Keyhani, "Estimation of induction machine parameters from standstill time-domain data," *IEEE Trans. Ind. Applicat.*, vol. 30, no. 6, pp. 1609–1615, Nov./Dec. 1994.

[88] A. Stanković, E. R. Benedict, V. John, and T. A. Lipo, "A novel method for measuring induction machine magnetizing inductance," in *Proc. Industry Applications Society Annual Meeting.* IEEE, Oct. 1997, pp. 234–238.

[89] J. R. Willis, G. J. Brock, and J. S. Edmonds, "Derivation of induction motor models from standstill frequency response tests," *IEEE Trans. Energy Conversion*, vol. 4, no. 4, pp. 608–615, Dec. 1989.

[90] A. Ganji, P. Guillaume, R. Pintelon, and P. Lataire, "Induction motor dynamic and static inductance identification using a broadband excitation technique," *IEEE Trans. Energy Conversion*, vol. 13, no. 1, pp. 15–20, Mar. 1998.

[91] J. Holtz and T. Thimm, "Identification of the machine parameters in a vector-controlled induction motor drive," *IEEE Trans. Ind. Applicat.*, vol. 27, no. 6, pp. 1111–1118, Nov./Dec. 1991.

[92] L.-C. Zai, C. L. DeMarco, and T. A. Lipo, "An extended Kalman filter approach to rotor time constant measurement in PWM induction motor drives," *IEEE Trans. Ind. Applicat.*, vol. 28, no. 1, pp. 96–104, Jan./Feb. 1992.

[93] H. B. Karayaka, M. N. Marwali, and A. Keyhani, "Induction machine parameter tracking from test data via PWM inverters," in *Proc. Industry Applications Society Annual Meeting.* IEEE, 1997, pp. 227–233.

[94] N. R. Klaes, "Parameter identification of an induction machine with regard to dependencies on saturation," *IEEE Trans. Ind. Applicat.*, vol. 29, no. 6, pp. 1135–1140, Nov./Dec. 1993.

[95] S. R. Shaw and S. B. Leeb, "Identification of induction motor parameters from transient stator current measurements," *IEEE Trans. Ind. Electron.*, vol. 46, no. 1, pp. 139–149, Feb. 1999.

[96] K. S. Huang, Q. H. Wu, and D. R. Turner, "Effective identification of induction motor parameters based on fewer measurements," *IEEE Trans. Energy Conversion*, vol. 17, no. 1, pp. 55–60, Mar. 2002.

[97] R. R. Bishop and G. G. Richards, "Identifying induction machine parameters using a genetic optimization algorithm," in *Proc. Southeastcon.* IEEE, Apr. 1990, pp. 476–479.

[98] E. B. Souza Filho, A. M. N. Lima, and C. B. Jacobina, "Characterization of induction machines with a genetic algorithm," in *Proc. International Electric Machines and Drives Conference IEMDC.* IEEE, 1999, pp. 446–448.

[99] P. Pillay, R. Nolan, and T. Haque, "Application of genetic algorithms to motor parameter determination for transient torque calculations," *IEEE Trans. Ind. Applicat.*, vol. 33, no. 5, pp. 1273–1282, Sept./Oct. 1997.

[100] P. Nangsue, P. Pillay, and S. E. Conry, "Evolutionary algorithms for induction motor parameter determination," *IEEE Trans. Energy Conversion*, vol. 14, no. 3, pp. 447–453, Sept. 1999.

[101] F. Córcoles, J. Pedra, M. Salichs, and L. Sainz, "Analysis of the induction machine parameter identification," *IEEE Trans. Energy Conversion*, vol. 17, no. 2, pp. 183–190, June 2002.

[102] S. H. Minnich, "Small signals, large signals, and saturation in generator modelling," *IEEE Trans. Energy Conversion*, vol. 1, no. 1, pp. 94–102, Mar. 1986.

[103] M. Akbaba, M. Taleb, and A. Rumeli, "Improved estimation of induction machine parameters," *Electric Power Systems Research*, vol. 34, pp. 65–73, 1995.

[104] G. B. Thomas, *Calculus and Analytic Geometry*, 4th ed. Addison-Wesley, 1968.

[105] S. D. Sudhoff, D. C. Aliprantis, B. T. Kuhn, and P. L. Chapman, "An induction machine model for predicting inverter–machine interaction," *IEEE Trans. Energy Conversion*, vol. 17, no. 2, pp. 203–210, June 2002.

[106] ——, "Experimental characterization procedure for use with an advanced induction machine model," *IEEE Trans. Energy Conversion*, vol. 18, no. 1, pp. 48–56, Mar. 2003.

[107] *Guide for Synchronous Generator Modeling Practices in Stability Analyses*, IEEE Std. 1110, Nov. 1991.

[108] C.-M. Ong, *Dynamic Simulation of Electric Machinery Using Matlab®/Simulink.* Ney Jersey: Prentice Hall, 1998.

[109] I. M. Canay, "Causes of discrepancies on calculation of rotor quantities and exact equivalent diagrams of the synchronous machine," *IEEE Trans. Power App. Syst.*, vol. 88, no. 7, pp. 1114–1120, July 1969.

[110] R. P. Schulz, W. D. Jones, and D. N. Ewart, "Dynamic models of turbine generators derived from solid rotor equivalent circuits," *IEEE Trans. Power App. Syst.*, vol. 92, no. 3, pp. 926–933, May/June 1973.

[111] H. Bissig, K. Reichert, and T. S. Kulig, "Modelling and identification of synchronous machines, a new approach with an extended frequency range," *IEEE Trans. Energy Conversion*, vol. 8, no. 2, pp. 263–271, June 1993.

[112] I. M. Canay, "Determination of the model parameters of machines from the reactance operators $x_d(p), x_q(p)$ (evaluation of standstill frequency response test)," *IEEE Trans. Energy Conversion*, vol. 8, no. 2, pp. 272–279, June 1993.

[113] A. Keyhani and H. Tsai, "Identification of high-order synchronous generator models from SSFR test data," *IEEE Trans. Energy Conversion*, vol. 9, no. 3, pp. 593–603, Sept. 1994.

[114] S. Pillutla and A. Keyhani, "Neural network based modeling of round rotor synchronous generator rotor body parameters from operating data," *IEEE Trans. Energy Conversion*, vol. 14, no. 3, pp. 321–327, Sept. 1999.

[115] H. B. Karayaka, A. Keyhani, G. T. Heydt, B. L. Agrawal, and D. A. Selin, "Neural network based modeling of a large steam turbine-generator rotor body parameters from on-line disturbance data," *IEEE Trans. Energy Conversion*, vol. 16, no. 4, pp. 305–311, Dec. 2001.

[116] J. L. Kirtley, "On turbine-generator rotor equivalent circuits," *IEEE Trans. Power Syst.*, vol. 9, no. 1, pp. 262–271, Feb. 1994.

[117] M. R. Harris, P. J. Lawrenson, and J. M. Stephenson, *Per-Unit Systems with Special Reference to Electrical Machines.* Cambridge, Great Britain: Cambridge University Press, in association with the Institution of Electrical Engineers, 1970.

[118] J. Verbeeck, R. Pintelon, and P. Guillaume, "Determination of synchronous machine parameters using network synthesis techniques," *IEEE Trans. Energy Conversion*, vol. 14, no. 3, pp. 310–314, Sept. 1999.

[119] J. Verbeeck, R. Pintelon, and P. Lataire, "Relationships between parameter sets of equivalent synchronous machine models," *IEEE Trans. Energy Conversion*, vol. 14, no. 4, pp. 1075–1080, Dec. 1999.

[120] I. Kamwa and P. Viarouge, "On equivalent circuit structures for empirical modeling of turbine-generators," *IEEE Trans. Energy Conversion*, vol. 9, no. 3, pp. 579–592, Sept. 1994.

[121] I. M. Canay, "Physical significance of sub-subtransient quantities in dynamic behaviour of synchronous machines," *IEE Proc., Part B*, vol. 135, no. 6, pp. 334–340, Nov. 1988.

[122] P. L. Dandeno and M. R. Iravani, "Third order turboalternator electrical stability models with applications to subsynchronous resonance studies," *IEEE Trans. Energy Conversion*, vol. 10, no. 1, pp. 78–86, Mar. 1995.

[123] R. G. Harley, D. J. N. Limebeer, and E. Chirricozzi, "Comparative study of saturation methods in synchronous machine models," *IEE Proc., Part B*, vol. 127, no. 1, pp. 1–7, Jan. 1980.

[124] G. R. Slemon, "Analytical models for saturated synchronous machines," *IEEE Trans. Power App. Syst.*, vol. 90, no. 2, pp. 409–417, Mar./Apr. 1971.

[125] R. S. Ramshaw and G. Xie, "Nonlinear model of nonsalient synchronous machines," *IEEE Trans. Power App. Syst.*, vol. 103, no. 7, pp. 1809–1815, July 1984.

[126] G. Xie and R. S. Ramshaw, "Nonlinear model of synchronous machines with saliency," *IEEE Trans. Energy Conversion*, vol. 1, no. 3, pp. 198–204, Sept. 1986.

[127] F. P. de Mello and L. N. Hannett, "Representation of saturation in synchronous machines," *IEEE Trans. Power Syst.*, vol. 1, no. 4, pp. 8–18, Nov. 1986.

[128] J. O. Ojo and T. A. Lipo, "An improved model for saturated salient pole synchronous motors," *IEEE Trans. Energy Conversion*, vol. 4, no. 1, pp. 135–142, Mar. 1989.

[129] J. Tamura and I. Takeda, "A new model of saturated synchronous machines for power system transient stability simulations," *IEEE Trans. Energy Conversion*, vol. 10, no. 2, pp. 218–224, June 1995.

[130] S.-A. Tahan and I. Kamwa, "A two-factor saturation model for synchronous machines with multiple rotor circuits," *IEEE Trans. Energy Conversion*, vol. 10, no. 4, pp. 609–616, Dec. 1995.

[131] H. Tsai, A. Keyhani, J. A. Demcko, and D. A. Selin, "Development of a neural network based saturation model for synchronous generator analysis," *IEEE Trans. Energy Conversion*, vol. 10, no. 4, pp. 617–624, Dec. 1995.

[132] K. A. Corzine, B. T. Kuhn, S. D. Sudhoff, and H. J. Hegner, "An improved method for incorporating magnetic saturation in the q-d synchronous machine model," *IEEE Trans. Energy Conversion*, vol. 13, no. 3, pp. 270–275, Sept. 1998.

[133] S. Pillutla and A. Keyhani, "Neural network based saturation model for round rotor synchronous generator," *IEEE Trans. Energy Conversion*, vol. 14, no. 4, pp. 1019–1025, Dec. 1999.

[134] H. B. Karayaka, A. Keyhani, B. L. Agrawal, D. A. Selin, and G. T. Heydt, "Identification of armature, field, and saturated parameters of a large steam turbine-generator from operating data," *IEEE Trans. Energy Conversion*, vol. 15, no. 2, pp. 181–187, June 2000.

[135] I. Boldea and S. A. Nasar, "Unified treatment of core losses and saturation in the orthogonal-axis model of electric machines," *IEE Proc., Part B*, vol. 134, no. 6, pp. 355–363, Nov. 1987.

[136] L. Salvatore and M. Savino, "Experimental determination of synchronous machine parameters," *IEE Proc., Part B*, vol. 128, no. 4, pp. 212–218, July 1981.

[137] I. M. Canay, "Modelling of alternating-current machines having multiple rotor circuits," *IEEE Trans. Energy Conversion*, vol. 8, no. 2, pp. 280–296, June 1993.

[138] The MathWorks, Inc., *Simulink Reference*, Natick, MA, 2002.

[139] AEgis Technologies Group, Inc., *Advanced Continuous Simulation Language (ACSL) Reference Manual*, Huntsville, AL, 1999.

[140] J. Verbeeck, R. Pintelon, and P. Lataire, "Influence of saturation on estimated synchronous machine parameters in standstill frequency response tests," *IEEE Trans. Energy Conversion*, vol. 15, no. 3, pp. 277–283, Sept. 2000.

[141] N. Dedene, R. Pintelon, and P. Lataire, "Estimation of a global synchronous machine model using a multiple-input multiple-output estimator," *IEEE Trans. Energy Conversion*, vol. 18, no. 1, pp. 11–16, Mar. 2003.

[142] J. A. Melkebeek and J. L. Willems, "Reciprocity relations for the mutual inductances between orthogonal axis windings in saturated salient-pole machines," *IEEE Trans. Ind. Applicat.*, vol. 26, no. 1, pp. 107–114, Jan./Feb. 1990.

[143] P. W. Sauer, "Constraints on saturation modeling in AC machines," *IEEE Trans. Energy Conversion*, vol. 7, no. 1, pp. 161–167, Mar. 1992.

[144] S. D. Sudhoff, K. A. Corzine, H. J. Hegner, and D. E. Delisle, "Transient and dynamic average-value modeling of synchronous machine fed load-commutated converters," *IEEE Trans. Energy Conversion*, vol. 11, no. 3, pp. 508–514, Sept. 1996.

[145] *Test Procedures for Synchronous Machines*, IEEE Std. 115, Dec. 1995.

[146] S. D. Umans, J. A. Mallick, and G. L. Wilson, "Modeling of solid rotor turbogenerators. Part I: Theory and techniques," *IEEE Trans. Power App. Syst.*, vol. 97, no. 1, pp. 269–277, Jan./Feb. 1978.

[147] Y. Jin and A. M. El-Serafi, "A "three transfer functions" approach for the standstill frequency response test of synchronous machines," *IEEE Trans. Energy Conversion*, vol. 5, no. 4, pp. 740–749, Dec. 1990.

[148] I. Kamwa, P. Viarouge, H. Le-Huy, and E. J. Dickinson, "Three-transfer-function approach for building phenomenological models of synchronous machines," *IEE Proc., Part C*, vol. 141, no. 2, pp. 89–98, Mar. 1994.

[149] P. J. Turner, A. B. J. Reece, and D. C. Macdonald, "The D.C. decay test for determining synchronous machine parameters: Measurement and simulation," *IEEE Trans. Energy Conversion*, vol. 4, no. 4, pp. 616–623, Dec. 1989.

[150] E. S. Boje, J. C. Balda, R. G. Harley, and R. C. Beck, "Time-domain identification of synchronous machine parameters from simple standstill tests," *IEEE Trans. Energy Conversion*, vol. 5, no. 1, pp. 164–175, Mar. 1990.

[151] W. Watson and G. Manchur, "Synchronous machine operational impedances from low voltage measurements at the stator terminals," *IEEE Trans. Power App. Syst.*, vol. 93, no. 3, pp. 777–784, May/June 1974.

[152] P. L. Dandeno and A. T. Poray, "Development of detailed turbogenerator equivalent circuits from standstill frequency response measurements," *IEEE Trans. Power App. Syst.*, vol. 100, no. 4, pp. 1646–1655, Apr. 1981.

[153] S. Sriharan and K. W. Hiong, "Synchronous machine modelling by standstill frequency response tests," *IEEE Trans. Energy Conversion*, vol. 2, no. 2, pp. 239–245, June 1987.

[154] F. P. de Mello, L. N. Hannett, and J. R. Willis, "Determination of synchronous machine stator and field leakage inductances from standstill frequency response tests," *IEEE Trans. Power Syst.*, vol. 3, no. 4, pp. 1625–1632, Nov. 1988.

[155] A. Keyhani, S. Hao, and G. Dayal, "Maximum likelihood estimation of solid-rotor synchronous machine parameters from SSFR test data," *IEEE Trans. Energy Conversion*, vol. 4, no. 3, pp. 551–558, Sept. 1989.

[156] A. Keyhani, S. Hao, and R. P. Schulz, "Maximum likelihood estimation of generator stability constants using SSFR test data," *IEEE Trans. Energy Conversion*, vol. 6, no. 1, pp. 140–154, Mar. 1991.

[157] I. Kamwa, P. Viarouge, H. Le-Huy, and J. Dickinson, "A frequency-domain maximum likelihood estimation of synchronous machine high-order models using SSFR test data," *IEEE Trans. Energy Conversion*, vol. 7, no. 3, pp. 525–536, Sept. 1992.

[158] K. Beya, R. Pintelon, J. Schoukens, P. Guillaume, P. Lataire, B. Mpanda-Mabwe, and M. Delhaye, "Identification of synchronous machines parameters using broadband excitations," *IEEE Trans. Energy Conversion*, vol. 9, no. 2, pp. 270–280, June 1994.

[159] R. Diggle and J. L. Dineley, "Generator works testing. Sudden-short-circuit or standstill variable-frequency-response method," *IEE Proc., Part C*, vol. 128, no. 4, pp. 177–182, July 1981.

[160] P. L. Dandeno, P. Kundur, A. T. Poray, and H. M. Z. El-Din, "Adaptation and validation of turbogenerator model parameters through on-line frequency response measurements," *IEEE Trans. Power App. Syst.*, vol. 100, no. 4, pp. 1656–1664, Apr. 1981.

[161] A. G. Jack and T. J. Bedford, "A study of the frequency response of turbogenerators with special reference to Nanticoke G. S." *IEEE Trans. Energy Conversion*, vol. 2, pp. 496–505, Sept. 1987.

[162] F. P. de Mello and L. N. Hannett, "Determination of synchronous machine electrical characteristics by test," *IEEE Trans. Power App. Syst.*, vol. 102, no. 12, pp. 3810–3815, Dec. 1983.

[163] C. P. Coelho, J. R. Phillips, and L. M. Silveira, "Robust rational function approximation algorithm for model generation," in *Proc.* 36^{th} *Design Automation Conference*, New Orleans, June 1999.

[164] K. Kristinsson and G. A. Dumont, "System identification and control using genetic algorithms," *IEEE Trans. Syst., Man, Cybern.*, vol. 22, no. 5, pp. 1033–1046, Sept./Oct. 1992.

[165] W. J. Wilson and J. D. Aplevich, "Dynamic equivalent power system models," *IEEE Trans. Power App. Syst.*, vol. 102, no. 12, pp. 3753–3760, Dec. 1983.

[166] D. C. Aliprantis, S. D. Sudhoff, and B. T. Kuhn, "A synchronous machine model with saturation and arbitrary rotor network representation," *IEEE Trans. Energy Conversion*, submitted for publication.

[167] ——, "Experimental characterization procedure for a synchronous machine model with saturation and arbitrary rotor network representation," *IEEE Trans. Energy Conversion*, submitted for publication.

[168] R. W. Ferguson, R. Herbst, and R. W. Miller, "Analytical studies of the brushless excitation system," *AIEE Transactions, Part III-B, Power Apparatus and Systems*, vol. 79, pp. 1815–1821, Feb. 1960.

[169] E. C. Whitney, D. B. Hoover, and P. O. Bobo, "An electric utility brushless excitation system," *AIEE Transactions, Part III-B, Power Apparatus and Systems*, vol. 79, pp. 1821–1828, Feb. 1960.

[170] H. W. Gayek, "Behavior of brushless aircraft generating systems," *IEEE Trans. Aerosp.–Support Conference Procedures*, vol. 1, no. 2, pp. 594–621, Aug. 1963.

[171] ——, "Transfer characteristics of brushless aircraft generator systems," *IEEE Trans. Aerosp.*, vol. 2, no. 2, pp. 913–928, Apr. 1964.

[172] T. Zouaghi and M. Poloujadoff, "Modeling of polyphase brushless exciter behavior for failing diode operation," *IEEE Trans. Energy Conversion*, vol. 13, no. 3, pp. 214–220, Sept. 1998.

[173] M. A. Abdel-Halim and C. D. Manning, "Modelling a laminated brushless exciter–alternator unit in all modes of operation," *IEE Proc., Part B*, vol. 138, no. 2, pp. 87–94, Mar. 1991.

[174] A. Darabi and C. Tindall, "Brushless exciter modeling for small salient pole alternators using finite elements," *IEEE Trans. Energy Conversion*, vol. 17, no. 3, pp. 306–312, Sept. 2002.

[175] T. H. Warner and J. G. Kassakian, "Transient characteristics and modeling of large turboalternator driven rectifier/inverter systems based on field test data," *IEEE Trans. Power App. Syst.*, vol. 104, no. 7, pp. 1804–1811, July 1985.

[176] P. W. Franklin, "Theory of the three phase salient pole type generator with bridge rectified output—Parts I and II," *IEEE Trans. Power App. Syst.*, vol. 91, no. 5, pp. 1960–1975, Sept./Oct. 1972.

[177] W. J. Bonwick and V. H. Jones, "Performance of a synchronous generator with a bridge rectifier," *IEE Proc.*, vol. 119, no. 9, pp. 1338–1342, Sept. 1972.

[178] ——, "Rectifier-loaded synchronous generators with damper windings," *IEE Proc.*, vol. 120, no. 6, pp. 659–666, June 1973.

[179] W. J. Bonwick, "Characteristics of a diode-bridge-loaded synchronous generator without damper windings," *IEE Proc.*, vol. 122, no. 6, pp. 637–642, June 1975.

[180] I. Jadrić, D. Borojević, and M. Jadrić, "Modeling and control of a synchronous generator with an active DC load," *IEEE Trans. Energy Conversion*, vol. 15, no. 2, pp. 303–311, Mar. 2000.

[181] *Recommended Practice for Excitation System Models for Power System Stability Studies*, IEEE Std. 421.5, Mar. 1992.

[182] S. M. L. Kabir and R. Shuttleworth, "Brushless exciter model," *IEE Proc., Part C*, vol. 141, no. 1, pp. 61–67, Jan. 1994.

[183] S. D. Sudhoff and O. Wasynczuk, "Analysis and average-value modeling of line-commutated converter–synchronous machine systems," *IEEE Trans. Energy Conversion*, vol. 8, no. 1, pp. 92–99, Mar. 1993.

[184] R. L. Witzke, J. V. Kresser, and J. K. Dillard, "Influence of A-C reactance on voltage regulation of 6-phase rectifiers," *AIEE Transactions, Part I, Communication and Electronics*, vol. 72, pp. 244–253, July 1953.

[185] F. Preisach, "Über die magnetische Nachwirkung," *Zeitschrift für Physik*, vol. 94, pp. 277–302, Mar./May 1935.

[186] R. M. D. Vecchio, "An efficient procedure for modeling complex hysteresis processes in ferromagnetic materials," *IEEE Trans. Magn.*, vol. 16, no. 5, pp. 809–811, Sept. 1980.

[187] I. D. Mayergoyz and G. Friedman, "Generalized Preisach model of hysteresis (invited)," *IEEE Trans. Magn.*, vol. 24, no. 1, pp. 212–217, Jan. 1988.

[188] I. D. Mayergoyz, "Dynamic Preisach models of hysteresis," *IEEE Trans. Magn.*, vol. 24, no. 6, pp. 2925–2927, Nov. 1988.

[189] E. Della Torre, *Magnetic Hysteresis*, 1st ed. New York: IEEE Press, 1999.

[190] S. R. Naidu, "Simulation of the hysteresis phenomenon using Preisach's theory," *IEE Proc., Part A*, vol. 137, no. 2, pp. 73–79, Mar. 1990.

[191] ——, "Time domain model for the ferromagnetic core, including the effects of hysteresis and eddy currents," *IEE Proc., Part A*, vol. 138, no. 1, pp. 44–50, Jan. 1991.

[192] J. G. Zhu, S. Y. R. Hui, and V. S. Ramsden, "A dynamic equivalent circuit model for solid magnetic cores for high switching frequency operations," *IEEE Trans. Power Electron.*, vol. 10, no. 6, pp. 791–795, Nov. 1995.

[193] ——, "A generalized dynamic circuit model of magnetic cores for low- and high-frequency applications—Part I: theoretical calculation of the equivalent core loss resistance," *IEEE Trans. Power Electron.*, vol. 11, no. 2, pp. 246–250, Mar. 1996.

[194] S. Y. R. Hui, J. G. Zhu, and V. S. Ramsden, "A generalized dynamic circuit model of magnetic cores for low- and high-frequency applications—Part II: circuit model formulation and implementation," *IEEE Trans. Power Electron.*, vol. 11, no. 2, pp. 251–259, Mar. 1996.

[195] J.-T. Hsu and K. D. T. Ngo, "A Hammerstein-based dynamic model for hysteresis phenomenon," *IEEE Trans. Power Electron.*, vol. 12, no. 3, pp. 406–413, May 1997.

[196] P. Tenant and J. J. Rousseau, "Dynamic model of magnetic materials applied on soft ferrites," *IEEE Trans. Power Electron.*, vol. 13, no. 2, pp. 372–379, Mar. 1998.

[197] A. A. Adly, "Performance simulation of hysteresis motors using accurate rotor media models," *IEEE Trans. Magn.*, vol. 31, no. 6, pp. 3542–3544, Nov. 1995.

[198] L. R. Dupré, R. V. Keer, and J. A. A. Melkebeek, "An iron loss model for electrical machines using the Preisach theory," *IEEE Trans. Magn.*, vol. 33, no. 5, pp. 4158–4160, Sept. 1997.

[199] H.-K. Kim, H.-Y. Jung, and S.-K. Hong, "Finite element analysis of hysteresis motor using the vector magnetization-dependent model," *IEEE Trans. Magn.*, vol. 34, no. 5, pp. 3495–3498, Sept. 1998.

[200] J. H. Lee and D. S. Hyun, "Hysteresis analysis for the permanent magnet assisted synchronous reluctance motor by coupled FEM & Preisach modeling," *IEEE Trans. Magn.*, vol. 35, no. 3, pp. 1203–1206, May 1999.

[201] ——, "Hysteresis characteristics computation on PWM fed synchronous reluctance motor using coupled FEM and Preisach modeling," *IEEE Trans. Magn.*, vol. 36, no. 4, pp. 1209–1213, July 2000.

[202] J. Saitz, "Magnetic field analysis of induction motors combining Preisach hysteresis modeling and finite element techniques," *IEEE Trans. Magn.*, vol. 37, no. 5, pp. 3693–3697, Sept. 2001.

[203] O. Bottauscio, M. Chiampi, and M. Zucca, "Experimental and numerical investigations on rotational fluxes in stator cores of three-phase motors," *IEEE Trans. Magn.*, vol. 38, no. 5, pp. 3294–3296, Sept. 2002.

[204] Members of the Staff of the Department of Electrical Engineering—Massachusetts Institute of Technology, *Magnetic Circuits and Transformers*, 15th ed. Cambridge, Massachusetts: M.I.T. Press, 1965.

[205] E. P. Dick and W. Watson, "Transformer models for transient studies based on field measurements," *IEEE Trans. Power App. Syst.*, vol. 100, no. 1, pp. 409–419, Jan. 1981.

[206] J. G. Frame, N. Mohan, and T. Liu, "Hysteresis modeling in an electromagnetic transients program," *IEEE Trans. Power App. Syst.*, vol. 101, no. 9, pp. 3404–3412, Sept. 1982.

[207] D. C. Jiles and D. L. Atherton, "Ferromagnetic hysteresis," *IEEE Trans. Magn.*, vol. 19, no. 5, pp. 2183–2185, Sept. 1983.

[208] ——, "Theory of ferromagnetic hysteresis (invited)," *Journal of Applied Physics*, vol. 55, no. 6, pp. 2115–2120, Mar. 1984.

[209] ——, "Theory of ferromagnetic hysteresis," *Journal of Magnetism and Magnetic Materials*, vol. 61, no. 1–2, pp. 48–60, Sept. 1986.

[210] K. H. Carpenter, "A differential equation approach to minor loops in the Jiles–Atherton hysteresis model," *IEEE Trans. Magn.*, vol. 27, no. 6, pp. 4404–4406, Nov. 1991.

[211] K. H. Carpenter and S. Warren, "A wide bandwidth, dynamic hysteresis model for magnetization in soft ferrites," *IEEE Trans. Magn.*, vol. 28, no. 5, pp. 2037–2041, Sept. 1992.

[212] D. C. Jiles, "A self consistent generalized model for the calculation of minor loop excursions in the theory of hysteresis," *IEEE Trans. Magn.*, vol. 28, no. 5, pp. 2602–2604, Sept. 1992.

[213] P. L. Chapman and S. D. Sudhoff, "Dynamic lossy inductor model for power converter simulation," in *Proc. Applied Power Electronics Conference and Exposition*, vol. 1. IEEE, Mar. 2002, pp. 137–143.

[214] D. Jiles, *Introduction to Magnetism and Magnetic Materials*, 2nd ed. London: Chapman & Hall, 1998.

[215] W. Gautschi, *Numerical Analysis, An Introduction*, 1st ed. Boston: Birkhäuser, 1997.

[216] C.-S. Liu, Y.-Y. Hsu, L.-H. Jeng, C.-J. Lin, C.-T. Huang, A.-H. Liu, and T.-H. Li, "Identification of exciter constants using a coherence function based weighted least squares approach," *IEEE Trans. Energy Conversion*, vol. 8, no. 3, pp. 460–467, Sept. 1993.

[217] E. Ludwig, M. L. Crow, K. Erickson, and K. Shah, "A feasibility study of on-line excitation system parameter estimation," *IEEE Trans. Power Syst.*, vol. 13, no. 3, pp. 910–916, Aug. 1998.

[218] C. C. Lee and O. T. Tan, "A weighted-least-squares parameter estimator for synchronous machines," *IEEE Trans. Power App. Syst.*, vol. 96, no. 1, pp. 97–101, Jan./Feb. 1977.

[219] J. J. Sanchez-Gasca, C. J. Bridenbaugh, C. E. J. Bowler, and J. S. Edmonds, "Trajectory sensitivity based identification of synchronous generator and excitation system parameters," *IEEE Trans. Power Syst.*, vol. 3, no. 4, pp. 1814–1822, Nov. 1988.

[220] J.-C. Wang, H.-D. Chiang, C.-T. Huang, Y.-T. Chen, C.-L. Chang, and C.-Y. Huang, "Identification of excitation system models based on on-line digital measurements," *IEEE Trans. Power Syst.*, vol. 10, no. 3, pp. 1286–1293, Aug. 1995.

[221] D. C. Aliprantis, S. D. Sudhoff, and B. T. Kuhn, "A brushless exciter model incorporating multiple rectifier modes and Preisach's hysteresis theory," *IEEE Trans. Energy Conversion*, submitted for publication.

[222] ——, "Genetic algorithm-based parameter identification of a hysteretic brushless exciter model," *IEEE Trans. Energy Conversion*, submitted for publication.

[223] W. H. Hayt, Jr. and J. E. Kemmerly, *Engineering Circuit Analysis*, 4th ed. New York: McGraw–Hill, 1986.

[224] L. Davis, Ed., *Genetic Algorithms and Simulated Annealing.* Pitman, London; Morgan Kaufmann, Los Altos, California, 1987.

APPENDIX

APPENDIX A
REALIZATION ALGORITHM WITH DIAGONAL SYSTEM MATRIX

The following algorithm produces a realization with matrix **A** diagonal [83]. It is valid only for the case where the roots of the minimal polynomial are distinct. It is assumed that the transfer function matrix elements are given by (4.19)–(4.21), in page 69.

1. Compute the roots of the minimal polynomial:

$$m_Y(s) = s(s-\lambda_1)\cdots(s-\lambda_{N_d-1})\,. \tag{A.1}$$

2. Expand $\mathbf{Y}_d(s)$ into partial fractions:

$$\mathbf{Y}_d(s) = \frac{1}{s}\mathbf{R}_0 + \sum_{k=1}^{N_d-1}\frac{1}{s-\lambda_k}\mathbf{R}_k\,. \tag{A.2}$$

The 2×2 residue matrices may be computed by

$$\mathbf{R}_k = \lim_{s\to\lambda_k}(s-\lambda_k)\mathbf{Y}_d(s) \tag{A.3}$$

and are of full rank; however,

$$\mathbf{R}_0 = Y_{d0}\begin{bmatrix} 1 & -1 \\ -1 & 1 \end{bmatrix} \tag{A.4}$$

is a matrix of rank 1.

3. Write

$$\mathbf{R}_k = \mathbf{C}_k\mathbf{B}_k\,, \tag{A.5}$$

for example by computing the LU decomposition. The matrices $\mathbf{C}_k, \mathbf{B}_k$ are 2×2. $\mathbf{R}_0$ may be factored as

$$\mathbf{R}_0 = \mathbf{C}_0\mathbf{B}_0 = \left(Y_{d0} \begin{bmatrix} 1 \\ -1 \end{bmatrix} \right) \begin{bmatrix} 1 & -1 \end{bmatrix} . \tag{A.6}$$

4. The realization is given by

$$\mathbf{A} = \begin{bmatrix} \lambda_1 & & & \\ & \lambda_2\mathbf{I}_2 & & \\ & & \ddots & \\ & & & \lambda_{N_d-1}\mathbf{I}_2 \end{bmatrix},$$

$$\mathbf{B} = \begin{bmatrix} \mathbf{B}_0 \\ \mathbf{B}_1 \\ \vdots \\ \mathbf{B}_{N_d-1} \end{bmatrix}, \mathbf{C} = \begin{bmatrix} \mathbf{C}_0 & \mathbf{C}_1 & \cdots & \mathbf{C}_{N_d-1} \end{bmatrix} . \tag{A.7}$$

APPENDIX B
SYNCHRONOUS GENERATOR PARAMETER SET UNIQUENESS PROOFS

The input–output characteristics of the d-axis may be conveniently expressed using transmission matrix descriptions of three series-connected two-port networks. The d-axis transmission matrix is the product of these three matrices [223]. Specifically,

$$\begin{bmatrix} \tilde{v}_{md} \\ \tilde{i}_{dr} \end{bmatrix} = \begin{bmatrix} 1 & -(r_s + sL_{lds}) \\ -\frac{1}{sL_{md}} & \frac{r_s + s(L_{lds}+L_{md})}{sL_{md}} \end{bmatrix} \begin{bmatrix} \tilde{v}_{ds} \\ \tilde{i}_{ds} \end{bmatrix}, \tag{B.1}$$

$$\begin{bmatrix} \tilde{v}_{d2} \\ -\tilde{i}'_{fdr} \end{bmatrix} = \begin{bmatrix} t_{11}(s) & t_{12}(s) \\ t_{21}(s) & t_{22}(s) \end{bmatrix} \begin{bmatrix} \tilde{v}_{md} \\ \tilde{i}_{dr} \end{bmatrix}, \tag{B.2}$$

and

$$\begin{bmatrix} \tilde{v}_{fdr} \\ -\tilde{i}_{fdr} \end{bmatrix} = \begin{bmatrix} \frac{1}{TR} & -\frac{3}{2} r_{fdr} TR \\ 0 & \frac{3}{2} TR \end{bmatrix} \begin{bmatrix} \tilde{v}_{d2} \\ -\tilde{i}'_{fdr} \end{bmatrix}. \tag{B.3}$$

The rotor transmission parameters are related to the admittance parameters (4.19)–(4.21) by

$$\begin{bmatrix} t_{11}(s) & t_{12}(s) \\ t_{21}(s) & t_{22}(s) \end{bmatrix} = \frac{1}{y_{12}(s)} \begin{bmatrix} -y_{11}(s) & 1 \\ y_{11}(s)y_{22}(s) - y_{12}^2(s) & -y_{22}(s) \end{bmatrix}. \tag{B.4}$$

It is important to note that

$$[t_{22}(s)]_{s=0} = 1\,, \tag{B.5}$$

$$[st_{21}(s)]_{s=0} = 0\,. \tag{B.6}$$

These relations are verified by substituting the functional forms of (4.19)–(4.21) in (B.4) and evaluating them at zero.

Hence, the terminal characteristics of the d-axis are given by

$$\begin{bmatrix} \tilde{v}_{fdr} \\ -\tilde{i}_{fdr} \end{bmatrix} = [\mathbf{T}(s)] \begin{bmatrix} \tilde{v}_{ds} \\ \tilde{i}_{ds} \end{bmatrix}, \tag{B.7}$$

where

$$[\mathbf{T}(s)] = \begin{bmatrix} \frac{1}{TR} & -\frac{3}{2} r_{fdr} TR \\ 0 & \frac{3}{2} TR \end{bmatrix} \cdot \begin{bmatrix} t_{11}(s) & t_{12}(s) \\ t_{21}(s) & t_{22}(s) \end{bmatrix} \cdot \begin{bmatrix} 1 & -(r_s + sL_{lds}) \\ -\frac{1}{sL_{md}} & \frac{r_s + s(L_{lds}+L_{md})}{sL_{md}} \end{bmatrix}. \tag{B.8}$$

Proof [of Theorem 3] The proof is based on equating the transmission parameters of the two networks, i.e. $\mathbf{T}$=$\mathbf{T}^\star$. By means of (B.8), it is possible to solve for the transmission parameters of the second network:

$$t^\star_{11}(s) = \frac{TR^\star}{s\,TR\,L_{md}L^\star_{md}}[st_{11}(s)L_{md}(L^\star_{lds} + L^\star_{md} - L_{lds}) + \\ + t_{12}(s)(L_{lds} + L_{md} - L^\star_{lds} - L^\star_{md})], \tag{B.9}$$

$$t^\star_{12}(s) = \frac{TR^\star}{TR\,L_{md}}[st_{11}(s)L_{md}(L^\star_{lds} - L_{lds}) + t_{12}(s)(L_{lds} + L_{md} - L^\star_{lds})], \tag{B.10}$$

$$t^\star_{21}(s) = \frac{TR}{s\,TR^\star\,L_{md}L^\star_{md}}[st_{21}(s)L_{md}(L^\star_{lds} + L^\star_{md} - L_{lds}) + \\ + t_{22}(s)(L_{lds} + L_{md} - L^\star_{lds} - L^\star_{md})], \tag{B.11}$$

$$t^\star_{22}(s) = \frac{TR}{TR^\star\,L_{md}}[st_{21}(s)L_{md}(L^\star_{lds} - L_{lds}) + t_{22}(s)(L_{lds} + L_{md} - L^\star_{lds})]. \tag{B.12}$$

It is also true that $[st_{21}(s)]_{s=0} = [st^\star_{21}(s)]_{s=0} = 0$, and $[t_{22}(s)]_{s=0} = [t^\star_{22}(s)]_{s=0} = 1$, for the selected form of rotor transfer functions. Multiplying both sides of (B.11) by s, and evaluating at zero yields (4.85). By substituting this result in (B.12), and again evaluating at zero, (4.84) is obtained. These two conditions allow the simplification of the transmission parameters expressions, which now become:

$$t^\star_{11}(s) = t_{11}(s), \tag{B.13}$$

$$t^\star_{12}(s) = st_{11}(s)\tfrac{TR^\star}{TR}(L^\star_{lds} - L_{lds}) + \left(\tfrac{TR^\star}{TR}\right)^2 t_{12}(s), \tag{B.14}$$

$$t^\star_{21}(s) = \left(\tfrac{TR}{TR^\star}\right)^2 t_{12}(s), \tag{B.15}$$

$$t^\star_{22}(s) = st_{21}(s)\tfrac{TR}{TR^\star}(L^\star_{lds} - L_{lds}) + t_{22}(s). \tag{B.16}$$

The new impedance matrix, $\mathbf{Z}_d^\star(s)$, is computed by using the transformation

$$\mathbf{Z}_d^\star(s) = -\frac{1}{t_{21}^\star(s)} \begin{bmatrix} t_{22}^\star(s) & 1 \\ 1 & t_{11}^\star(s) \end{bmatrix}, \tag{B.17}$$

and (4.86) is obtained. ■

Proof [of Theorem 4] The input–output behavior of the q-axis is characterized by its input impedance, which is

$$Z_{qs}(s) = r_s + sL_{lqs} + \frac{sL_{mq}Z_q(s)}{sL_{mq}+Z_q(s)}, \tag{B.18}$$

where $Z_q(s) = 1/Y_q(s)$. If two networks are equivalent, then

$$\left[\frac{Z_{qs}(s) - r_s}{s}\right]_{s=0} = \left[\frac{Z_{qs}^\star(s) - r_s}{s}\right]_{s=0}, \tag{B.19}$$

which implies (4.88). Then,

$$\begin{aligned} Z_{qs}(s) &= r_s + s(L_{lqs}^\star + L_{mq}^\star - L_{mq}) + \frac{sL_{mq}Z_q(s)}{sL_{mq}+Z_q(s)} = \\ &= r_s + sL_{lqs}^\star + \frac{sL_{mq}^\star Z_q^\star(s)}{sL_{mq}^\star+Z_q^\star(s)}, \end{aligned} \tag{B.20}$$

which can be solved for $Z_q^\star(s)$ to yield (4.89). ■

APPENDIX C
SYNCHRONOUS GENERATOR PRIME MOVER MODEL

The generator's prime mover is a Dyne Systems 110-kW, 590-Nm, 3600-rpm, four-quadrant, vector-controlled, induction motor-based dynamometer. Its mathematical model is shown in Fig. C.1. The parameters' values are: $J = 8.40\,\mathrm{Kg \cdot m^2}$, $srl = 20.94\,\mathrm{rad/s^2}$, $\tau_{srl} = 49.8\,\mathrm{ms}$, $\delta_{\mathrm{lm}} = 402.1\,\mathrm{rad}$, $K_\delta = 91.5\,\mathrm{N \cdot m}$, $\tau_{\mathrm{ld}} = 0.255\,\mathrm{s}$, $\tau_{\mathrm{lg}} = 3.51\,\mathrm{ms}$, $K_\omega = 406.0\,\mathrm{N \cdot m \cdot s}$, $\tau_\omega = 0.803\,\mathrm{s}$, $\omega_{\mathrm{err,\,thr}} = 10.0\,\mathrm{rad/s}$, $T_{e,\mathrm{min}} = -600\,\mathrm{N \cdot m}$, $T_{e,\mathrm{max}} = 600\,\mathrm{N \cdot m}$.

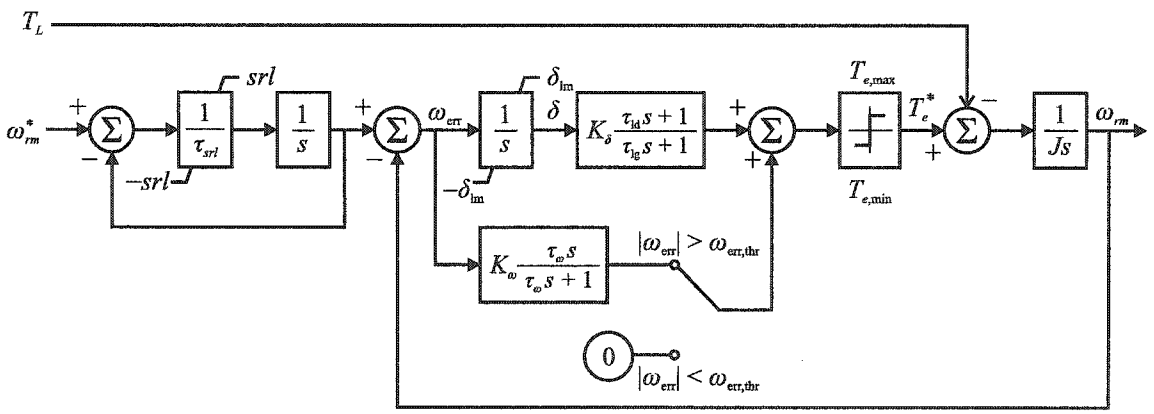

Fig. C.1. Prime mover block diagram.

The prime mover control parameters were obtained using evolutionary optimization. A genetic algorithm minimized a root-mean-square error between estimated and measured speeds. The GA fitness function involved two studies: (1) a sud-

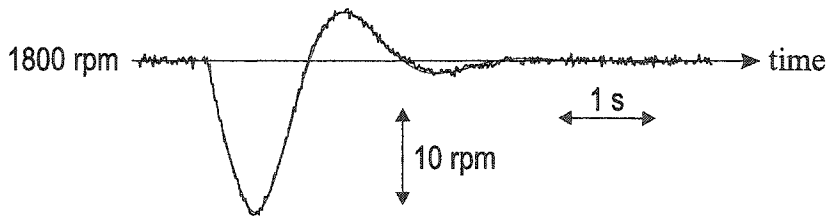

Fig. C.2. Speed variation during a torque change.

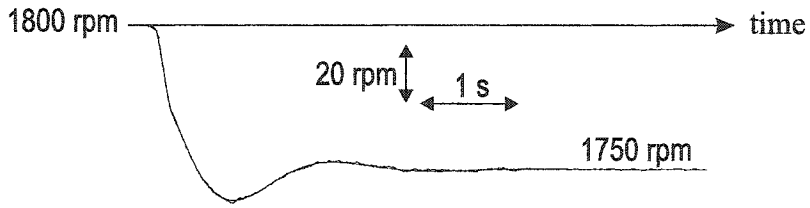

Fig. C.3. Speed variation during a change in speed reference.

den torque change from 10 Nm to 80 Nm, with a constant commanded speed of $\omega^*_{rm} = 1800$ rpm; (2) a change in speed reference from $\omega^*_{rm,0} = 1800$ rpm to $\omega^*_{rm,1} = 1750$ rpm, at no load. The measured and predicted (with the optimal parameter set) speeds are superimposed in Figs. C.2, C.3. The generator's torque, denoted by T_L in Fig. C.1, was computed from terminal voltage and current. The exciter's torque was ignored.

APPENDIX D
SYNCHRONOUS GENERATOR VOLTAGE REGULATOR COMPONENTS

The voltage regulator was custom built at Purdue University, and is using a Digital Signal Processor to apply the control logic.

The measured voltages and currents are pre-processed to remove low- and high-frequency noise. Any dc measuring offset is subtracted by the high-pass filter; the computed peak is filtered again with a second-order low-pass filter. The filtering process in block diagram form is shown in Fig. D.1.

Both peak voltage and current are monitored by the system's supervisory control. If they are within specified limits, the control signal o_{vr} enables the operation of the voltage regulator, depicted in Fig. D.2. Normally, the controller operates as a Proportional-Integral control, outputting a commanded field current. A hysteresis controller that is implemented in hardware maintains the actual current within a hysteresis band, whose peak-to-peak amplitude was set equal to $2\Delta i_{\max} = 36$ mA.

The hardware configuration of the exciter drive is shown in Fig. D.3. The switches are controlled by the hysteresis modulator. For simulation purposes, the single-phase rectifier is modeled as a constant dc voltage source, $v_{\text{rect}} = 172$ V. Also, the hysteresis modulator is modeled by an average-value representation; if

$$\Delta i = i_{fds} - i^*_{fds}\,, \tag{D.1}$$

$$v_{\text{on}} = v_{\text{rect}} - r_{\text{sw}} i_{fds}\,, \tag{D.2}$$

$$v_{\text{off}} = -v_{\text{rect}} - v_{\text{d}} - r_{\text{d}} i_{fds}\,, \tag{D.3}$$

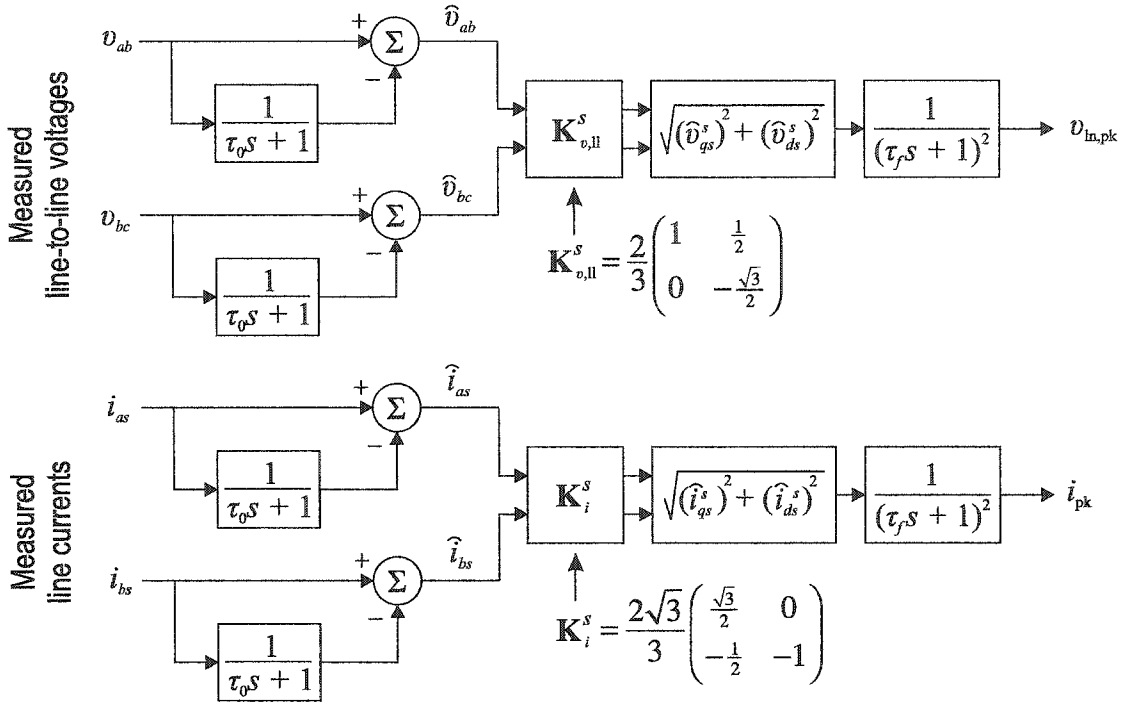

Fig. D.1. Pre-processing of measured voltages and currents.

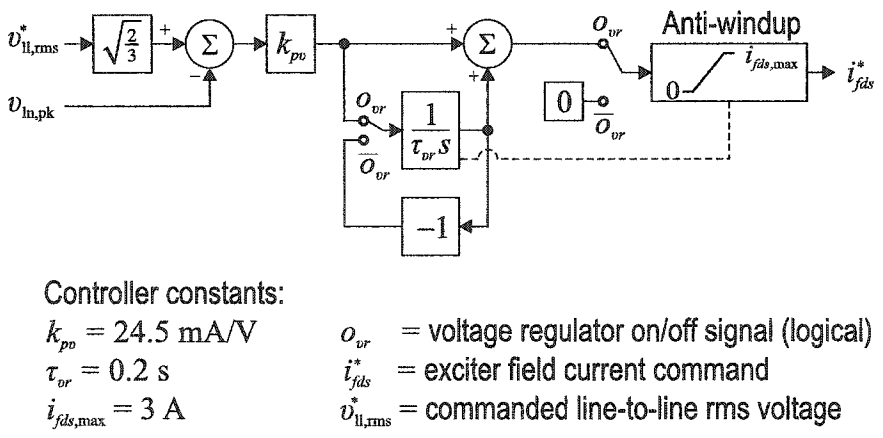

Fig. D.2. Voltage controller logic.

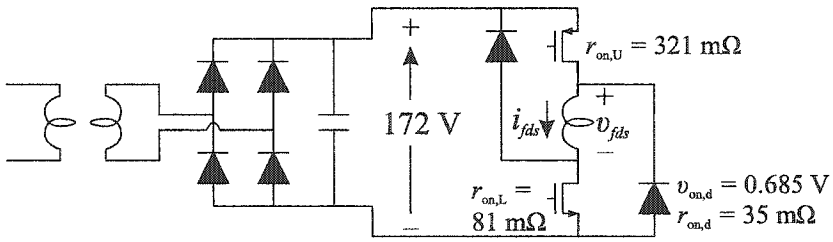

Total switch-on resistance: $r_{sw} = r_{on,U} + r_{on,L} = 402\ \text{m}\Omega$
Total diode-on resistance: $r_d = 2r_{on,d} = 70\ \text{m}\Omega$
Total diode-on voltage drop: $v_d = 2v_{on,d} = 1.37\ \text{V}$

Fig. D.3. Exciter's field winding drive circuit.

then

$$v_{fds} = \begin{cases} \min\left\{v_{\text{on}}, v_{\text{on}} \frac{|\Delta i|}{\Delta i_{\max}}\right\} & \text{for } \Delta i < 0\,, \\ \max\left\{v_{\text{off}}, v_{\text{off}} \frac{\Delta i}{\Delta i_{\max}}\right\} & \text{for } \Delta i \geq 0\,. \end{cases} \tag{D.4}$$

VITA

VITA

Dionysios C. Aliprantis was born in Athens, Greece on July 15, 1976. He received the Diploma in electrical and computer engineering from the National Technical University of Athens, Greece, in July, 1999. His specialization was in the areas of power systems, electric machines, and telecommunications.

Since August, 1999 he has been a graduate assistant at Purdue University, West Lafayette, IN, conducting research in the area of electromechanical energy conversion. His interests include the modeling and simulation of electric machines and power systems, evolutionary optimization methods, and power electronics.